Development and Application of a Comprehensive Simulation for Modeling Helicopter Ship Landing

by

Abhinav Sharma

A dissertation submitted in partial fulfillment
of the requirements for the degree of
Doctor of Philosophy
(Aerospace Engineering)
in the University of Michigan
2019

Doctoral Committee:

Professor Peretz P. Friedmann, Chair
Professor Carlos E. Cesnik
Associate Professor Karthik Duraisamy
Professor Bogdan Epureanu
Assistant Research Scientist Ashwani K. Padthe

Abhinav Sharma

absharma@umich.edu

ORCID iD: 0000-0002-1856-7633

To my family, for always being my rock.

Acknowledgments

The journey that has led to me to this point has been arduous and challenging, but at the same time, very rewarding. I wish to thank all those who made it possible. First and foremost, I would like to express my sincerest gratitude to my adviser, Prof. Friedmann, for giving me an opportunity to pursue my doctoral studies under his wing, as well as for his continual support and guidance throughout the project. Prof. Friedmann's high standards of research, with emphasis on clarity and quality, have enabled me to become a more adept researcher and communicator. I am forever grateful for his mentorship. I would also like to thank Dr. Ashwani Padthe, for his patience, support and insights throughout the project. His expertise was invaluable. I would like to acknowledge David Xu and Prof. Karthik Duraisamy, for providing the wind over deck model used in this work. In addition, I would like to thank Prof. Roberto Celi from the University of Maryland for providing the HeliUM2 source code for modifications. I am grateful to Prof. Carlos Cesnik, Prof. Bogdan Epureanu, Prof. Karthik Duraisamy and Dr. Ashwani Padthe for serving on my committee.

This research was funded by the Office of Naval Research under ONR grant N00014-16-1-2728 with Dr. Brian Holm-Hansen as project monitor.

I would like to acknowledge Prof. Albert Ratner, from the University of Iowa, for he is the one who convinced me to apply to the University of Michigan (UM), his alma mater, for graduate school.

During my time at UM, I have been fortunate to develop strong and lasting friendships with several people. I would like to thank my colleagues Puneet Singh and Ryan Patterson in Prof. Friedmann's group for their humorous and lively company, as well as Dr. Daning Huang. I would like to further thank Puneet for his technical insight at various stages in the project. I am thankful for Shamsheer Singh Chauhan, John Jasa and all my aerospace department friends. I am also grateful for my friends from Graduate Rackham International (GRIN), notably Dr. Natacha Bohin, and Dr. Janis Lai, and for my Muay Thai family at Final Round Training Center.

I would like to express my gratitude to Denise Phelps, for her relentless help and positivity throughout my time at UM, and Dave McLean for the fun conversations we had, and for providing me with the spare computer I used throughout my Master's and PhD studies.

I am very much indebted to my girlfriend, Olivia Liao, for her companionship, humor and love, which have propelled me in the last phases of my PhD studies with greater appreciation of the journey that led me here.

Finally, I am forever grateful to my parents and brother for their unconditional and never ending love and support in every phase of life.

TABLE OF CONTENTS

Dedication ii

Acknowledgments iii

List of Figures viii

List of Tables xiii

List of Appendices xiv

List of Abbreviations xv

List of Symbols xvi

Abstract xxvii

Chapter

1 Introduction, Background, and Objectives 1

1.1 Review of Helicopter-Ship Dynamic Interface Modeling 4
1.2 Review of Trajectory Tracking Control Strategies 8
1.3 Review of Helicopter Landing Gear Modeling 9
1.4 Review of Ground Effect Modeling 11
1.5 Objectives of this Dissertation 13
1.6 Dissertation Outline 15

2 Flight Dynamics Model (HeliUM2) 16

2.1 Coordinate Systems 17
2.1.1 Earth-fixed coordinate system 17
2.1.2 Helicopter body-fixed coordinate system 18
2.1.3 Wind coordinate system 19
2.1.4 Shaft coordinate system 19
2.1.5 Nonrotating hub coordinate system 20
2.1.6 Rotating hub coordinate system 21
2.1.7 Undeformed, preconed blade coordinate system 22
2.1.8 Deformed blade coordinate system 23
2.1.9 Blade sectional aerodynamic coordinate system 26
2.2 Main Assumptions 27
2.2.1 Aerodynamic assumptions 27

2.2.2 Inertial and structural assumptions . . . 28
2.2.3 UH-60A helicopter modeling assumptions . . . 29
2.3 Main Rotor Model . . . 29
2.3.1 Main rotor aerodynamic loads . . . 30
2.3.2 Main rotor inertia loads . . . 37
2.3.3 Main rotor structural loads . . . 38
2.3.4 Main rotor tensile loads . . . 41
2.3.5 Main rotor lag damper loads . . . 41
2.3.6 Finite element discretization . . . 43
2.3.6.1 Beam finite element model . . . 44
2.3.6.2 Assembly of global load vectors . . . 46
2.3.7 Rotating blade mode shapes . . . 48
2.3.8 Modal coordinate transformation . . . 49
2.3.9 Main rotor equations of motion . . . 49
2.4 Fuselage Equations of Motion . . . 50
2.4.1 Main rotor loads . . . 51
2.4.2 Fuselage aerodynamic loads . . . 53
2.4.3 Empennage aerodynamic loads . . . 55
2.4.4 Tail rotor loads . . . 58
2.5 Final Equations . . . 60
2.6 Helicopter Trim Analysis . . . 61
2.6.1 Trim unknowns . . . 62
2.6.2 Trim equations . . . 63
2.7 Linearization . . . 67

3 Approach Trajectory and its Control . . . 69

3.1 Approach Trajectory . . . 69
3.1.1 Velocity profile during descent . . . 69
3.2 Controller Design . . . 73
3.2.1 LQR formulation . . . 73
3.2.2 Trajectory tracking . . . 75
3.2.3 Landing . . . 75

4 Wind Over Deck . . . 77

4.1 Description of CFD Method . . . 77
4.2 Mesh and Boundary Conditions . . . 79
4.3 Comparison with Literature . . . 81
4.4 Integration of WOD Model into Flight Dynamics Code . . . 83
4.4.1 Coordinate transformation . . . 84
4.4.2 Calculation and integration of WOD velocities . . . 87

5 Landing Gear and Ground Effect Modeling . . . 89

5.1 Landing Gear Model . . . 89
5.2 Ground Effect Model . . . 95
5.2.1 Simple ground effect model . . . 95

5.2.2 Finite-state ground effect model . . . 96
5.2.2.1 Review of He-Peters dynamic inflow model . . . 96
5.2.2.2 Ground effect model for static case . . . 102
5.2.2.3 Ground effect model for dynamic case . . . 108
5.2.2.4 Implementation . . . 112

6 Ship Motion . . . 115

6.1 Description of SCONE Data . . . 115
6.2 Combination of SCONE and Flight Dynamics Model . . . 118

7 Results and Discussion . . . 122

7.1 Results for Approach Segment . . . 123
7.1.1 Influence of WOD during approach . . . 124
7.1.1.1 WOD effects on rotor alone . . . 125
7.1.1.2 WOD effects on the entire vehicle . . . 127
7.1.2 Combined WOD and ground effect during hover and landing . . . 128
7.1.3 Approach and landing simulation with combined WOD and ground effects . . . 135
7.2 Ground Effect from Inclined and Moving Decks . . . 136
7.2.1 Comparison with results from literature . . . 138
7.2.2 Effect of deck inclination . . . 138
7.2.2.1 Hover . . . 139
7.2.2.2 Landing . . . 143
7.2.3 Influence of isolated ground motion . . . 147
7.2.3.1 Hover . . . 149
7.2.3.2 Landing . . . 159
7.2.4 Influence of combined SCONE motion . . . 165
7.2.5 Combined motion and WOD . . . 166

8 Conclusions, Original Contributions, and Recommendations for Future Research . . . 176

8.1 Conclusions . . . 177
8.2 Original Contributions Made in this Dissertation . . . 179
8.3 Recommendations for Future Research . . . 180

Appendices . . . 181

Bibliography . . . 190

LIST OF FIGURES

FIGURE

1.1 Illustration of a typical helicopter ship landing environment. 1
1.2 A typical SHOL diagram. 2
1.3 Flow topology behind a simplified ship geometry. 4
1.4 External and internal view of HELIFLIGHT-R simulator 6
1.5 Ship geometries used in airwake generation: a) Simple Frigate Shape Version 2 (SFS2), b) Type 23 frigate, and c) Wave class auxiliary oiler. 7
1.6 Massless 3D landing gear model. 10
1.7 Landing gear model with an unsprung mass. 11
1.8 Experimental data showing the influence of ground effect on power requirements for constant thrust. 12
1.9 Illustration of the image rotor model. 12
1.10 Illustration of ground source. 13

2.1 Earth-fixed and helicopter body-fixed coordinate systems. 18
2.2 Illustration of fuselage sideslip angle, angle of attack, and wind acess. 20
2.3 Illustration of a) lateral and b) longitudinal shaft tilt angles, exaggerated for clarity. 21
2.4 Relationship between shaft frame and nonrotating hub coordinate system. . . . 22
2.5 Relationship between nonrotating and rotating hub frames. 23
2.6 Relationship between rotating hub frame, undeformed, preconed frame and deformed preconed frames. 24
2.7 DOFs of blade with four FEs. 47

3.1 Side view (left), and top view (right) illustrations of the approach and landing trajectory, figure not to scale. 70
3.2 Helicopter (a) speed and (b) deceleration profiles during descent to hover position. 73

4.1 SFS2 ship geometry—(a) 3D view and (b) top, side and rear views with dimensions. 78
4.2 Illustration of CFD domain with SFS2 ship outline. 80
4.3 Near-body mesh and domain of interest for WOD. 80
4.4 Definition of positive sideslip angle β_{WOD}. 81
4.5 The SFS1 and SFS2 ship geometries—dimensions are in feet 81
4.6 The SFS1 mesh. 82

4.7 Contours of velocity magnitude over ship for a headwind at 197 ft/s. 82
4.8 Horizontal WOD velocity distribution over ship for a headwind at 197 ft/s. . . 83
4.9 Straight blade approximation used to obtain WOD velocities for main rotor blades. 86
4.10 Flowchart depicting integration of WOD model into HeliUM2. 88

5.1 Landing gear geometry. 89
5.2 Landing gear model. 90
5.3 Illustration of heights used to determine gear deflection. 91
5.4 Illustration of the different height contributions to z_{deck}. 92
5.5 Illustration of ground effect. 95
5.6 Rotor coordinate system and freestream coordinate. 98
5.7 An illustration of the elliptic coordinate system around the rotor disk. 101
5.8 Coordinate systems for a hovering flight in ground effect. 104

6.1 Flowchart illustrating decomposition of SCONE data. 116
6.2 Frequency spectrum of roll angle ϕ_D for "high" amplitude roll dominant simulations. 117
6.3 Frequency spectrum of roll angle ϕ_D, pitch angle θ_D, and heave displacement z_D for a "high" amplitude roll dominant simulation. 117
6.4 Coordinate system used in SCONE data. 118
6.5 Roll angle ϕ_D, pitch angle θ_D, heave displacement z_D, heave velocity V_{zD} and heave acceleration A_{zD} time histories for (a) "low" and (b) "high" heave excitation. 119
6.6 Time histories of roll angle ϕ_D, pitch angle θ_D, and heave displacement z_D used in simulations. 120

7.1 UH-60A cant angle. 122
7.2 Rotating mode shapes used in modal coordinate transformation. 124
7.3 Horizontal x, lateral y, and vertical z positions of helicopter CG during approach to a stationary deck, WOD included in main rotor model. 126
7.4 Roll ϕ_f, pitch θ_f, and yaw ψ_f angles of fuselage during approach to a stationary deck, WOD included in main rotor model. 127
7.5 Control inputs generated by FCS during the approach to a stationary deck, WOD included in main rotor model. 128
7.6 WOD velocity components at hub location during approach to a stationary deck, WOD included in main rotor model. 129
7.7 Roll ϕ_f, pitch θ_f, and yaw ψ_f angles of fuselage during approach to a stationary deck, WOD included on entire helicopter. 130
7.8 Control inputs generated by FCS during approach to a stationary deck, WOD included on entire helicopter. 131
7.9 Horizontal x, lateral y, and vertical z positions of helicopter CG during hover and landing flight segments with simple ground effect model and WOD included on the entire helicopter, stationary deck. 132

7.10 Roll ϕ_f, pitch θ_f, and yaw ψ_f angles of fuselage during hover and landing phases with simple ground effect model and WOD included on the entire helicopter, stationary deck. . . . 132
7.11 Right, left and tail gear deflections during hover and landing phases with simple ground effect model and WOD included on the entire helicopter, stationary deck. . . . 133
7.12 Control inputs generated by FCS during hover and landing phases with simple ground effect model and WOD included on the entire helicopter, stationary deck. 133
7.13 Rotor thrust, total vertical gear reaction force, and tail rotor contribution to lift during hover and landing phases with simple ground effect model and WOD included on the entire helicopter, stationary deck. . . . 134
7.14 Power required during hover and landing phases with simple ground effect model and WOD included on the entire helicopter, stationary deck. . . . 135
7.15 Roll ϕ_f, pitch θ_f, and yaw ψ_f angles of fuselage during approach and landing phases with simple ground effect model and WOD included on entire helicopter, stationary deck. . . . 136
7.16 Control inputs generated by FCS during approach and landing phases with simple ground effect model and WOD included on entire helicopter, stationary deck. . . . 137
7.17 Rotor power reduction due to static and level ground effect as a function of height. . . . 138
7.18 Hover configuration during static deck inclination simulations. . . . 139
7.19 Time histories of effective inflow coefficients during hover over a deck inclined at a static roll angle. . . . 140
7.20 Control inputs generated by FCS during hover over a deck inclined at a static roll angle. . . . 141
7.21 Time histories of power required during hover over a deck inclined at a static roll angle. . . . 141
7.22 Time histories of CG position coordinates relative to the deck frame during hover over a deck inclined at a static roll angle. . . . 142
7.23 Rotor thrust during hover over a deck inclined at a static roll angle. . . . 142
7.24 Time histories of effective inflow coefficients during hover over a deck inclined at a static pitch angle. . . . 143
7.25 Control inputs generated by FCS during hover over a deck inclined at a static pitch angle. . . . 144
7.26 Time histories of power required during hover over a deck inclined at a static pitch angle. . . . 144
7.27 Illustration of landing on an inclined deck at a constant roll or pitch angle. . . . 145
7.28 Roll, pitch and yaw attitudes during hover and landing flight segments with the deck inclined at a constant roll angle of 10°. . . . 146
7.29 Vertical gear positions during hover and landing flight segments with the deck inclined at a constant roll angle of 10°. . . . 147
7.30 Vertical gear positions during hover and landing flight segments with the deck inclined at a constant roll angle of 10°. . . . 148

7.31 Control input time histories during hover and landing flight segments with the deck inclined at a constant roll angle of 10°. 148
7.32 Roll, pitch and yaw attitudes during hover and landing flight segments with the deck inclined at a constant pitch angle of 8°. 149
7.33 Vertical gear positions during hover and landing flight segments with the deck inclined at a constant pitch angle of 8°. 150
7.34 Control input time histories during hover and landing flight segments with the deck inclined at a constant pitch angle of 8°. 150
7.35 Time histories of effective inflow coefficients during hover over a deck excited by roll motion alone. 151
7.36 Control inputs generated by FCS during hover over a deck excited by roll motion alone. 152
7.37 Frequency spectra of control inputs during hover over a deck excited by roll motion alone. 153
7.38 Time histories of power required during hover over a deck excited by roll motion alone. 154
7.39 Time histories of CG position coordinates relative to the deck frame during hover over a deck excited by roll motion alone. 154
7.40 Rotor thrust during hover over a deck excited by roll motion alone. 155
7.41 Time histories of effective inflow coefficients during hover over a deck excited by pitch motion alone. 155
7.42 Control inputs generated by FCS during hover over a deck excited by pitch motion alone. 156
7.43 Frequency spectra of control inputs during hover over a deck excited by pitch motion alone. 157
7.44 Time histories of power required during hover over a deck excited by pitch motion alone. 157
7.45 Time histories of effective inflow coefficients during hover over a deck excited by heave motion alone. 159
7.46 Control inputs generated by FCS during hover over a deck excited by heave motion alone. 160
7.47 Frequency spectra of control inputs during hover over a deck excited by heave motion alone. 161
7.48 Time histories of power required during hover over a deck excited by heave motion alone. 161
7.49 Roll, pitch and yaw attitudes during hover and landing flight segments with the deck excited by roll motion alone. 162
7.50 Vertical gear positions during hover and landing flight segments with the deck excited by roll motion alone. 163
7.51 Vertical gear positions during hover and landing flight segments with the deck excited by roll motion alone. 164
7.52 Control input time histories during hover and landing flight segments with the deck excited by roll motion alone. 165
7.53 Horizontal, lateral and vertical position coordinates of CG during hover and landing flight segments with the deck excited by roll motion alone. 166

7.54 Roll, pitch and yaw attitudes during hover and landing flight segments with the deck excited by pitch motion alone. 167
7.55 Vertical gear positions during hover and landing flight segments with the deck excited by pitch motion alone. 168
7.56 Control input time histories during hover and landing flight segments with the deck excited by pitch motion alone. 168
7.57 Vertical gear positions during hover and landing flight segments with the deck excited by heave motion alone. 169
7.58 Vertical gear positions during hover and landing flight segments with the deck excited by heave motion alone. 169
7.59 Control input time histories during hover and landing flight segments with the deck excited by heave motion alone. 170
7.60 Time histories of power required during hover and landing flight segments; deck excited by combined roll, pitch and heave motion using SCONE data for a "moderate" heave condition. 170
7.61 Vertical gear positions during hover and landing flight segments; deck excited by combined roll, pitch and heave motion using SCONE data for a "moderate" heave condition. 171
7.62 Control input time histories during hover and landing flight segments; deck excited by combined roll, pitch and heave motion using SCONE data for a "moderate" heave condition. 172
7.63 Horizontal, lateral and vertical position coordinates of CG during hover and landing flight segments; deck excited by combined roll, pitch and heave motion using SCONE data for a "moderate" heave condition, together with the $\beta_{WOD} = -30^\circ$ WOD condition. 173
7.64 Control input time histories during hover and landing flight segments; deck excited by combined roll, pitch and heave motion using SCONE data for a "moderate" heave condition, together with the $\beta_{WOD} = -30^\circ$ WOD condition. 174
7.65 WOD velocity components at hub location during hover and landing flight segments for the $\beta_{WOD} = -30^\circ$ WOD condition. 175

C.1 Illustration of the DDG-51 ship with different parts labeled. 189

LIST OF TABLES

TABLE

3.1 Approach trajectory parameters 70

5.1 Landing gear parameters 94

6.1 Ship motion parameters for roll excitation 118
6.2 Ship motion parameters for heave excitation 118

7.1 HeliUM2-umich setup parameters 123

A.1 Values of K_n^m 182

C.1 SCONE ship geometry parameters 188

LIST OF APPENDICES

APPENDIX

A Associated Legendre Functions 181

B General Form of Ground Effect Matrices 184

C DDG-51 Ship Geometry 187

LIST OF ABBREVIATIONS

AC	Aerodynamic Center
AGARD	Advisory Group for Aerospace Research and Development
BC	Boundary Condition
CFD	Computational Fluid Dynamics
CG	Center of Gravity
COP	Center of Pressure
DES	Detached Eddy Simulation
DI	Dynamic Interface
DIMSS	Dynamic Interface Modeling and Simulation System
DOF	Degree Of Freedom
FCS	Flight Control System
FE	Finite Element
GE	Ground Effect
IGE	In-Ground-Effect
JSHIP	Joint Shipboard Helicopter Integration Process
LES	Large Eddy Simulation
LHA	Landing Helicopter Assault
LQR	Linear-Quadratic Regulator
LTI	Linear Time-Invariant
LTP	Linear Time-Periodic
MPPI	Model Predictive Path Integral
NATO	North Atlantic Treaty Organization
ODE	Ordinary Differential Equation
OGE	Out-of-Ground-Effect
PDE	Partial Differential Equation
POD	Proper Orthogonal Decomposition
RANS	Reynold-Averaged Navier-Stokes
ROM	Reduced Oder Model
SDOF	Single Degree Of Freedom
SFS2	Simple Frigate Shape Version 2
SCONE	Systematic Characterization Of the Naval Environment
SHOL	Ship Helicopter Operating Limit
TTCP	Tripartite Technical Cooperation Program
VSTOL	Vertical Short Take-Off and Landing
WOD	Wind Over Deck

LIST OF SYMBOLS

a	main rotor blade lift curve slope
$\mathbf{a}_P$	absolute acceleration of a point on blade elastic axis
A_b	blade cross section area
A_t	effective size of the object being viewed, used in the approach trajectory calculation
A_{zD}	heave acceleration from SCONE data
$\mathbf{A}_0$	linearized-time invariant state matrix
$\mathbf{A}_{LTP}(t)$	linearized time-periodic state matrix
$\mathbf{A}_G$	matrix that relates ground rotor inflow coefficients $\boldsymbol{\beta}$ to ground pressure coefficients $\boldsymbol{\sigma}$
b	nondimensional half-chord length, $b = c/2R$
$\mathbf{B}_0$	linearized time-invariant control matrix
$\mathbf{B}_{LTP}(t)$	linearized time-periodic control matrix
$\mathbf{B}_G$	matrix that relates ground rotor pressure coefficients $\boldsymbol{\sigma}$ to rotor pressure coefficients $\boldsymbol{\tau}$
c	blade chord
c_1	empirical constant used in approach trajectory calculation
C_n^m, D_n^m	pressure potential expansion coefficients used in dynamic inflow model
C_L, C_D, C_M	blade sectional lift, drag and moment coefficients
C_{Lf}, C_{Df}, C_{Yf}	fuselage lift, drag and lateral force coefficients, respectively
C_{LH}, C_{DH}	horizontal tail lift and drag coefficients
C_{LV}, C_{DV}	vertical tail lift and drag coefficients
C_P	main rotor power coefficient
C_{Q_t}	tail rotor torque coefficient
C_{Rf}, C_{Mf}, C_{Nf}	fuselage rolling, pitching and yawing moment coefficients, respectively
C_T	main rotor thrust coefficient
C_W	helicopter weight coefficient
$\mathbf{C}_G$	dynamic ground influence matrix
$d, \dot{d}$	gear deflection and deflection rate
d_1, d_2, d_3, d_4, d_5	lag damper geometry constants
$D, \dot{D}, \ddot{D}$	horizontal distance, velocity, and deceleration to target point
$\ddot{D}_{peak}$	peak deceleration used in the approach trajectory calculation
D_p	blade sectional drag force
e	blade hinge offset
$\hat{\mathbf{e}}_T, \hat{\mathbf{e}}_P, \hat{\mathbf{e}}_R$	unit vectors of blade sectional aerodynamic frame
$\hat{\mathbf{e}}_x, \hat{\mathbf{e}}_y, \hat{\mathbf{e}}_z$	unit vectors of undeformed, preconed blade coordinate system
$\hat{\mathbf{e}}_{x_{tip}}, \hat{\mathbf{e}}_{y_{tip}}, \hat{\mathbf{e}}_{z_{tip}}$	unit vectors of the rigid blade coordinate system used for WOD model

$\hat{\mathbf{e}}'_x, \hat{\mathbf{e}}'_y, \hat{\mathbf{e}}'_z$	unit vectors of deformed, preconed blade coordinate system
$\mathbf{e}(\boldsymbol{\beta})$	error function used in Newton-Raphson method
E	Young's Modulus
$E_I[\,]$	differentiation operator used in dynamic inflow model
EI_2, EI_3	flap and lag bending stiffnesses
$\mathbf{E}(t), \mathbf{F}(t), \mathbf{G}(t)$	Jacobian matrices used in linearization
f_T, f_P, f_R	tangential, perpendicular and radial aerodynamic loads, per unit span, in blade sectional aerodynamic frame
$\mathbf{f}(\dot{\mathbf{x}}, \mathbf{x}, \mathbf{u}; t)$	combined system of ordinary differential equations
$\mathbf{f}_q(\dot{\mathbf{q}}, \mathbf{q})$	main rotor system of ordinary differential equations using generalized coordinates
$F(\nu_R, \eta_R, \psi_R)$	transformation between the rotor and ground ellipsoidal coordinate systems
F_{gx}, F_{gy}, F_{gz}	landing gear reaction forces
F_{sx}, F_{sy}, F_{sz}	components of the blade structural force vector $\mathbf{F}_{ss}$
F_{LD}	lag damper force
$\mathbf{F}_{ss}$	blade structural force vector per unit span
$\mathbf{F}_t$	tail rotor force vector
$\mathbf{F}_{wF}$	fuselage aerodynamic force vector in wind axes
$\mathbf{F}_{wH}$	horizontal tail aerodynamic force vector in wind axes
$\mathbf{F}_{wV}$	vertical tail aerodynamic force vector in wind axes
$\mathbf{F}_A, \mathbf{F}_D, \mathbf{F}_I, \mathbf{F}_S, \mathbf{F}_T$	assembled FE aerodynamic, damping, inertial, structural and tension load vectors, respectively
$\mathbf{F}_{Am}, \mathbf{F}_{Dm}, \mathbf{F}_{Im},$	generalized aerodynamic, damping, inertial, structural and tension
$\mathbf{F}_{Sm}, \mathbf{F}_{Tm}$	forces obtained after modal coordinate transformation
$\mathbf{F}_{A_v}, \mathbf{F}_{A_w}, \mathbf{F}_{A_\phi}$	assembled FE aerodynamic load vectors associated with lag, flap and torsional DOFs, respectively
$\mathbf{F}_{LG}$	landing gear reaction force vector
$\mathbf{F}(\boldsymbol{\Theta})$	system of trim equations
g	acceleration due to gravity
g_z	normal component of ground plane velocity
g_{z0}, g_{zc}, g_{zs}	average, cosine and sine components of g_z
$\mathbf{g}(\mathbf{x}, \hat{\mathbf{x}}; t)$	system of algebraic equations
G	landing gear damping constant
G_s	shear modulus
GJ	torsional stiffness
$\mathbf{G}_G$	ground influence matrix
$\dot{h}$	plunge rate of a point on blade elastic axis
H_n^m	ratio of factorials used in dynamic inflow model
$\mathbf{H}_v, \mathbf{H}_w, \mathbf{H}_\phi$	Hermite interpolation polynomials
$\hat{\mathbf{i}}_{deck}, \hat{\mathbf{j}}_{deck}, \hat{\mathbf{k}}_{deck}$	unit vectors of the stationary deck frame
$\hat{\mathbf{i}}'_{deck}, \hat{\mathbf{j}}'_{deck}, \hat{\mathbf{k}}'_{deck}$	unit vectors of the moving deck frame
$\hat{\mathbf{i}}_{hel}, \hat{\mathbf{j}}_{hel}, \hat{\mathbf{k}}_{hel}$	unit vectors of the helicopter body-fixed frame
$\hat{\mathbf{i}}_{sh}, \hat{\mathbf{j}}_{sh}, \hat{\mathbf{k}}_{sh}$	unit vectors of the shaft frame

$\hat{\mathbf{i}}_t, \hat{\mathbf{j}}_t, \hat{\mathbf{k}}_t$	unit vectors of the tail rotor frame
$\hat{\mathbf{i}}_I, \hat{\mathbf{j}}_I, \hat{\mathbf{k}}_I$	unit vectors of the inertial earth-fixed frame
$\hat{\mathbf{i}}_H, \hat{\mathbf{j}}_H, \hat{\mathbf{k}}_H$	unit vectors of the horizontal tail wind frame
$\hat{\mathbf{i}}_{H_{NR}}, \hat{\mathbf{j}}_{H_{NR}}, \hat{\mathbf{k}}_{H_{NR}}$	unit vectors of the nonrotating hub frame
$\hat{\mathbf{i}}_{H_R}, \hat{\mathbf{j}}_{H_R}, \hat{\mathbf{k}}_{H_R}$	unit vectors of the rotating hub frame
$\hat{\mathbf{i}}_S, \hat{\mathbf{j}}_S, \hat{\mathbf{k}}_S$	unit vectors of the ship frame
$\hat{\mathbf{i}}_V, \hat{\mathbf{j}}_V, \hat{\mathbf{k}}_V$	unit vectors of the vertical tail wind frame
$\hat{\mathbf{i}}_W, \hat{\mathbf{j}}_W, \hat{\mathbf{k}}_W$	unit vectors of the fuselage wind frame
I_{xx}, I_{yy}, I_{zz}	mass moments of inertia about the helicopter body-fixed axes
I_{xy}, I_{xz}, I_{yz}	products of inertia about the helicopter body-fixed axes
J	cost function in LQR algorithm
k_t	proportionality constant used to define velocity profile during approach
k_G	ground effect correction factor
K	landing gear stiffness constant
K_{blk}	empirical factor used to compute tail rotor thrust
K_H	empirical factor used to compute effective velocities at horizontal tail COP
K_V	empirical factor used to compute effective velocities at vertical tail COP
$[K]$	blade stiffness matrix
$\mathbf{K}_{LQR}$	control gain matrix
l	length of blade element
L_{circ}	blade sectional circulatory lift used in the dynamic inflow model
L_{deck}	length of ship deck
L_p	lift force per unit span at blade section
L, M, N	effective x, y, z moments at CG
L_F, M_F, N_F	x, y, z moments at CG due to fuselage aerodynamic loads
L_H, M_H, N_H	x, y, z moments at CG due to horizontal tail aerodynamic loads
$L_I[\,]$	integration operator used in dynamic inflow model
L_{LG}, M_{LG}, N_{LG}	x, y, z moments at CG due to landing gear reaction forces
L_{MR}, M_{MR}, N_{MR}	x, y, z moments at CG due to main rotor loads
L_Q	quasi-steady lift per unit span in Theodorsen's theory
L_R	pressure discontinuity across the rotor in dynamic inflow model
L_{TR}, M_{TR}, N_{TR}	x, y, z moments at CG due to tail rotor loads
L_V, M_V, N_V	x, y, z moments at CG due to vertical tail aerodynamic loads
$[L_{DI}]$	dynamic inflow gain matrix
m	fuselage mass
m_0	main rotor blade mass
Ma	Mach number
M_p	aerodynamic moment at blade section
M_x, M_y, M_z	components of structural moment vector $\mathbf{M}_{ss}$
M_{Dx}, M_{Dy}, M_{Dz}	component of lag damper moment vector
$M_{LD\beta}$	flap moment about blade hinge due to lag damper
$M_{LD\zeta}$	lag moment about blade hinge due to lag damper
$[M]$	blade mass matrix

$[M_{DI}]$	dynamic inflow apparent mass matrix
$\mathbf{M}_{ss}$	structural moment vector at blade section
$\mathbf{M}_t$	tail rotor moment vector at tail rotor hub center
$\mathbf{M}_{wF}$	fuselage aerodynamic moment vector in wind axes
$\mathbf{M}_D$	lag damper moment vector
n_1	empirical constant used in approach trajectory calculation
N_b	number of main rotor blades
N_{dof}	total number of DOFs in the blade FE representation
N_e	number of blade finite elements
N_h	number of harmonics included in Fourier expansions of blade generalized coordinates
N_m	number of blade normal modes used for modal transformation
N_F	number of fuselage rigid body states
N_G	number of Gaussian quadrature points used
p, q, r	pitch, roll, and yaw angular rates of the fuselage, respectively
$p_{\mathrm{A}x}, p_{\mathrm{A}y}, p_{\mathrm{A}z}$	components of distributed blade aerodynamic load vector
$p_{\mathrm{I}x}, p_{\mathrm{I}y}, p_{\mathrm{I}z}$	components of distributed blade inertial load vector
$\mathbf{p}_A$	distributed blade aerodynamic load vector
$\mathbf{p}_I$	distributed blade inertial load vector
$\mathbf{p}_T$	distributed blade tensile load vector
P	main rotor power
P_b	point on blade elastic axis
P_n^m, Q_n^m	associated Legendre functions of the first and second kind, respectively
P_{IGE}, P_{OGE}	rotor power in-ground-effect and out-of-ground-effect, respectively
$\bar{P}_n^m, \bar{Q}_n^m$	normalized Legendre functions of the first and second kind
q^k	normal mode coordinate for kth blade mode
q_{app}^k	approximation of normal blade coordinate q^k
$q_0^j, q_{1c}^j, q_{1s}^j, q_2^j$	multiblade coordinates corresponding to the jth normal mode
$q_{\mathrm{A}x}, q_{\mathrm{A}y}, q_{\mathrm{A}z}$	components of distributed blade aerodynamic moment vector
$q_{\mathrm{I}x}, q_{\mathrm{I}y}, q_{\mathrm{I}z}$	components of distributed blade inertial moment vector
q_F	dynamic pressure at the fuselage AC
q_H	dynamic pressure at the horizontal tail AC
q_V	dynamic pressure at the vertical tail AC
$\mathbf{q}$	vector of blade normal mode coordinates
$\mathbf{q}_{app}$	vector of approximated blade normal mode coordinates
$\mathbf{q}_v$	nondimensional perturbations in flow velocity vector used in dynamic inflow model
$\mathbf{q}_A$	distributed blade aerodynamic moment vector
$\mathbf{q}_I$	distributed blade inertial moment vector
Q_{TR}	nondimensional tail rotor torque
$\mathbf{Q}, \mathbf{R}$	weight matrices used in the LQR algorithm
r_{gx}, r_{gy}	horizontal and lateral position coordinates of the gear relative to the target landing location, respectively
r_x, r_y, r_z	position coordinates of gear relative to the helicopter CG frame

$r_{LDx}, r_{LDy}, r_{LDz}$	position coordinates of lag damper relative to shaft frame
$\bar{r}$	nondimensional radial coordinate used in dynamic inflow model
$\mathbf{r}_g$	position vector of landing gear relative to CG
$\mathbf{r}_{LD}$	position vector of lag damper location relative to hub center
R	main rotor radius
R_t	tail rotor radius
$\mathbf{R}_{CG}$	position vector of helicopter CG with respect to inertial frame
$\mathbf{R}_B$	position vector of point on blade elastic axis relative to hub center
$\mathbf{R}_C$	position vector of point on elastic axis relative to the hinge location
$\mathbf{R}_e$	position vector of blade hinge relative to hub center
$\mathbf{R}_H$	position vector of hub center relative to helicopter CG
$\mathbf{R}_P$	position vector of a point on blade elastic axis relative to the inertial frame
S_H	area of horizontal tail
S_{ij}	elements of the transformation matrix between undeformed and deformed blade coordinate systems $[T_{DP}]$
S_V	area of vertical tail
t	time
t_0, t_f	initial and final time, used in the LQR algorithm
$\bar{t}$	nondimensional time used in dynamic inflow model
$\mathbf{t}$	vector of stress components used to compute structural loads at a blade section
T_p	tensile force at a blade section
T	rotor thrust
T_{IGE}, T_{OGE}	rotor thrust in-ground-effect and out-of-ground-effect, respectively
T_{TR}	tail rotor thrust
$\boldsymbol{T}$	Jacobian matrix used in Newton-Raphson iteration
$[T_{AP}]$	transformation matrix from undeformed, preconed frame to blade sectional aerodynamic frame
$[T_{BI}]$	transformation matrix from earth-fixed inertial frame to fuselage body-fixed frame
$[T_{DP}]$	transformation matrix from blade undeformed, preconed frame to deformed, preconed frame
$[T_{FH_R}]$	transformation matrix from hub rotating frame to rigid blade coordinate system used for WOD model
$[T_{HB}]$	transformation matrix from fuselage body-fixed frame to horizontal tail wind frame
$[T_{H_{NR}Sh}]$	transformation matrix from main rotor shaft frame to hub nonrotating frame
$[T_{H_RH_{NR}}]$	transformation matrix from hub nonrotating frame to hub rotating frame
$[T_{PH_R}]$	transformation matrix from hub rotating frame to blade undeformed, preconed frame
$[T_{ShB}]$	transformation matrix from fuselage body-fixed frame to shaft frame
$[T_{SB}]$	transformation matrix from fuselage body-fixed frame to ship frame

$[T_{TB}]$	transformation matrix from fuselage body-fixed frame to tail rotor frame
$[T_{VB}]$	transformation matrix from helicopter body-fixed frame to vertical tail wind frame
$[T_{WB}]$	transformation matrix from helicopter body-fixed frame to fuselage wind coordinate system
u, v, w	helicopter horizontal, lateral and vertical velocities at the CG, in the fuselage body-fixed frame
u_H, v_H, w_H	velocity components at horizontal tail COP
u_p, v_p, w_p	axial, lag, and flap deflections, respectively, of a point on the blade elastic axis
u_{tl}, v_{tl}, w_{tl}	velocity components at tail rotor hub center, in the tail rotor frame
u_{TR}, v_{TR}, w_{TR}	velocity components at tail rotor hub center, in the fuselage body-fixed frame
u_V, v_V, w_V	velocity components at COP of vertical tail
$\mathbf{u}$	helicopter control vector consisting of $\theta_{1c}, \theta_{1s}, \theta_0$ and θ_{0t}
$\mathbf{u}_{eq}$	helicopter control vector at a trim condition
U_T, U_P, U_R	velocity components at a blade section, in the sectional aerodynamic frame
v_{It}	tail rotor inflow velocity
v_t	velocity magnitude at tail rotor COP
v_{LD}	blade lag deflection at lag damper position
$\mathbf{v}_n$	vector of assembled FE lag DOFs
V	helicopter speed
V_0, V_f	initial and final helicopter speeds, respectively, during approach to deck
V_m	nondimensional mass flow parameter used in dynamic inflow model
V_{p0}	velocity magnitude at a point on blade elastic axis
V_{11}, V_{12}, V_{13}	velocity components of a point on the blade elastic axis
V_{WOD}	root mean square of WOD velocity vector
V_{zD}	heave velocity from SCONE data
$[V]$	matrix used to perform modal coordinate transformation
$\mathbf{V}_p$	velocity of a point on blade elastic axis
$\mathbf{V}_A$	blade sectional velocity vector in local aerodynamic frame
$\mathbf{V}_{CG}$	velocity of the helicopter CG
$\mathbf{V}_F$	freestream velocity at fuselage AC
$\mathbf{V}_H$	freestream velocity at COP of horizontal tail
$\mathbf{V}_I$	inflow velocity vector
$\mathbf{V}_T$	effective velocity of a point on blade elastic axis including inflow
$\mathbf{V}_{TR}$	freestream velocity at tail rotor hub center
$\mathbf{V}_V$	freestream velocity at COP of vertical tail
$\mathbf{V}_{WOD}$	wind over deck velocity
$\mathbf{V}_\infty$	freestream velocity used in dynamic inflow model
w_{tip}	blade tip flap deflection
w_G	induced velocity due to ground effect
w_{LD}	blade flap deflection at lag damper position

w^{IGE}	effective in-ground-effect induced velocity
$\mathbf{w}_n$	vector of assembled FE blade flapping DOFs
x, y, z	horizontal, lateral and vertical displacements of the vehicle CG, respectively
x_0	initial horizontal distance of helicopter from the ship deck center
x_d	horizontal distance to be covered by helicopter during the descent phase of approach
x_{deck}	horizontal position of the ship deck center relative to the origin of ship frame
x_e	spanwise distance of a point on the blade element
$x_{off}, y_{off}, z_{off}$	coordinates of helicopter CG relative to the origin of ship frame
x_{p0}	spanwise distance of a point on blade elastic axis from the blade hinge location
x_A	blade cross sectional aerodynamic center offset from the elastic axis
x_H, y_H, z_H	coordinates of the main rotor hub center relative to the CG in the fuselage body-fixed frame
x_{LD}	span location of the lag damper position on blade
$\mathbf{x}, \dot{\mathbf{x}}$	state and state derivative vectors, respectively
$\mathbf{x}_{act}, \mathbf{x}_{des}$	actual and desired state vectors, respectively, used in the controller
$\mathbf{x}_e$	error between the actual and desired state vectors
$\mathbf{x}_{eq}, \dot{\mathbf{x}}_{eq}$	state and state derivative vectors at trim
$\mathbf{x}_p$	span location of a blade point on the representative rigid blade used for WOD model
$\mathbf{x}_F$	fuselage rigid body state vector
$\mathbf{x}_{FAC}$	position vector of fuselage AC relative to CG
$\mathbf{x}_H$	position vector of COP of horizontal tail relative to CG
$\mathbf{x}_I$	inflow state vector
$\mathbf{x}_{NR}$	main rotor state vector in the nonrotating frame
$\mathbf{x}_R$	main rotor state vector in the rotating frame
$\hat{x}_d, \hat{y}_d, \hat{z}_d$	stationary deck coordinate system
$\hat{x}'_d, \hat{y}'_d, \hat{z}'_d$	moving deck coordinate system
$\hat{x}_{hel}, \hat{y}_{hel}, \hat{z}_{hel}$	Fuselage body-fixed coordinate system
$\hat{x}_{sh}, \hat{y}_{sh}, \hat{z}_{sh}$	shaft coordinate system
$\hat{x}_G, \hat{y}_G, \hat{z}_G$	coordinate system of ground plane
$\hat{x}_{H_R}, \hat{y}_{H_R}, \hat{z}_{H_R}$	hub rotating coordinate system
$\hat{x}_I, \hat{y}_I, \hat{z}_I$	earth-fixed inertial coordinate system
$\hat{x}_R, \hat{y}_R, \hat{z}_R$	coordinate system of main rotor used in finite-state ground effect model
$\hat{x}_S, \hat{y}_S, \hat{z}_S$	ship coordinate frame
$\mathbf{x}_{TR}$	position vector of tail rotor hub center relative to CG
$\mathbf{x}_V$	position vector of vertical tail COP relative to CG
$\hat{x}_W, \hat{y}_W, \hat{z}_W$	fuselage wind coordinate system
X, Y, Z	effective loads acting at CG
X_F, Y_F, Z_F	aerodynamic loads at CG due to fuselage
X_H, Y_H, Z_H	aerodynamic loads at CG due to horizontal tail
X_{LG}, Y_{LG}, Z_{LG}	loads at CG due to landing gears

X_{MR}, Y_{MR}, Z_{MR}	loads at CG due to main rotor
X_{TR}, Y_{TR}, Z_{TR}	loads at CG due to tail rotor
X_V, Y_V, Z_V	aerodynamic loads at CG due to vertical tail
y_{p0}, z_{p0}	coordinates of a generic point on blade cross section
$\mathbf{y}_i$	vector containing nodal DOFs of a blade FE
$\mathbf{y}_n$	assembled FE vector of blade DOFs
$\mathbf{y}_v$	assembled FE vector of blade lag DOFs
$\mathbf{y}_w$	assembled FE vector of blade flapping DOFs
$\mathbf{y}_\phi$	assembled FE vector of blade torsional DOFs
$\bar{\mathbf{y}}_n$	eigenvectors corresponding to rotating blade mode shapes
z_0, z_f	initial and final vehicle altitudes, respectively, during approach
z_{ang}	vertical displacement of a point on the deck due to deck rotation
z_{deck}	height of ship deck relative to stationary deck frame
z_{dyn}	deck heave displacement
z_g	height of gear contact point relative to stationary deck frame
z_h	height of rotor hub center above ground plane
z_{loss}	loss in altitude due to transition from level flight to descent during approach
z_{stat}	height of ship deck from waterline when it is level and stationary
z_D	heave displacement from SCONE data
z_{D0}	stationary deck height in SCONE data

Greek Symbols

$\alpha_0^{IGE}, \alpha_c^{IGE}, \alpha_s^{IGE}$	average, cosine and sine in-ground-effect inflow coefficients, respectively
α_f	fuselage angle of attack
α_x, α_y	longitudinal and lateral shaft tilt angles, respectively
α_H	horizontal tail angle of attack
α_T	Effective angle of attack at a blade section
α_{TPP}	angle of attack of the rotor tip path plane
α_V	vertical tail angle of attack
$\boldsymbol{\alpha}$	vector of main rotor inflow coefficients
$\boldsymbol{\alpha}^{IGE}$	vector of in-ground-effect inflow coefficients
$\beta_j^{rc}, \beta_j^{rs}$	cosine and sine ground rotor inflow coefficients
β_f	fuselage sideslip angle
β_p	blade precone angle
β_{tip}	flapping angle of the representative rigid blade used for WOD modeling
β_H	sideslip angle of horizontal tail
β_{WOD}	ship sideslip angle used for WOD calculations
β_V	sideslip angle of vertical tail
$\boldsymbol{\beta}$	vector of inflow coefficients due to a static ground source distribution
$\boldsymbol{\beta}^D$	vector of inflow coefficients due to a dynamic ground
γ	flight path angle

γ_I	sideslip angle at blade section
γ_R	main rotor lock number
$\boldsymbol{\gamma}$	vector of dynamic ground pressure coefficients
Γ	roll inclination of the ground plane
Γ_{deck}	deck roll angle
Γ_{TR}	tail rotor cant angle
δ	ground plane pitch angle
δ_0, θ_{GLD}	lag damper constants
δ_{deck}	deck pitch angle
δ_{flap}	effective blade flapping angle
δ_{lag}	effective blade lag angle
Δh	local grid spacing
Δ_{sp}	azimuthal lag in the swash plate due to hinge offsets
Δt	time step used in the DASSL time-marching solver
$\Delta\mathbf{x}, \Delta\dot{\mathbf{x}}$	perturbations in state and state derivative vectors, respectively
$\Delta\mathbf{u}$	perturbations in control vector
$\Delta\Phi_G^D$	pressure discontinuity across the ground source distribution plane
$\boldsymbol{\varepsilon}(\psi), \boldsymbol{\varepsilon}^k$	vector of residuals used in helicopter trim procedure
$\epsilon_{xx}, \epsilon_{yy}, \epsilon_{zz}$	blade normal strain components
$\epsilon_{xy}, \epsilon_{xz}, \epsilon_{yz}$	blade shear strain components
$\zeta_0^k, \zeta_{jc}^k, \zeta_{js}^k$	Fourier expansion coefficients of the kth blade normal mode
η_x	nondimensional span location of an arbitrary point on a blade element
$\theta_0, \theta_{1c}, \theta_{1s}$	main rotor collective, lateral cyclic and longitudinal cyclic inputs, respectively
θ_{0H}	geometric pitch angle of the horizontal tail
θ_{0t}	tail rotor collective input
θ_{0V}	geometric pitch angle of the vertical tail
θ_D	deck pitch angle from SCONE data
θ_G	geometric pitch angle of the blade section
θ_{TW}	built-in twist at a blade section
$\boldsymbol{\Theta}$	vector of trim unknowns
$\boldsymbol{\Theta}_B$	vector of fuselage trim unknowns
$\boldsymbol{\Theta}_I$	vector of inflow trim unknowns
$\boldsymbol{\Theta}_R$	vector of main rotor trim unknowns
λ	main rotor inflow
$\lambda_0, \lambda_{1c}, \lambda_{1s}$	main rotor inflow states (3 state He-Peters model)
λ_t	tail rotor inflow
$\lambda_x, \lambda_y, \lambda_z$	components of inflow velocity vector in undeformed, preconed frame
$\lambda_{IGE}, \lambda_{OGE}$	main rotor inflow in-ground-effect and out-of-ground-effect, respectively
Λ_{TR}	tail rotor yaw angle
μ	advance ratio
μ_x, μ_y	friction coefficients in the landing gear model

ν_R, η_R, ψ_R	ellipsoidal coordinates used in the dynamic inflow model for the main rotor
ν_t	eddy viscosity
ν_G, η_G, ψ_G	ellipsoidal coordinates used in the dynamic inflow model for the ground rotor
ξ	nondimensional streamline coordinate used in the dynamic inflow model, positive upstream
ρ	air density
ρ_b	mass density of the blade
ρ_n^m	nondimensionalizing factor for P_n^m
$\sigma_k^{lc}, \sigma_k^{ls}$	cosine and sine parts of ground pressure coefficients
$\sigma_{xx}, \sigma_{yy}, \sigma_{zz}$	blade normal stress components
$\sigma_{xy}, \sigma_{xz}, \sigma_{yz}$	blade shear stress components
$\boldsymbol{\sigma}$	vector of ground pressure coefficients
$\boldsymbol{\tau}$	vector of main rotor pressure coefficients
$\tau_n^{0c}, \tau_n^{mc}, \tau_n^{ms}$	average, cosine, sine components of $\boldsymbol{\tau}$
ϕ_f, θ_f, ψ_f	fuselage Euler angles
ϕ_n^m	dynamic inflow expansion functions, $\phi_n^m = \bar{P}_n^m/\nu$
ϕ_p	elastic twist of a point on the blade
ϕ_D	deck roll angle from SCONE data
$\boldsymbol{\phi}_n$	vector of assembled FE blade torsional DOFs
Φ_G	nondimensional pressure potential due to ground source distribution
Φ_G^D	dynamic part of Φ_G
Φ_G^S	static part of Φ_G
Φ_R	nondimensional acceleration or pressure potential
$\Phi_R^{(t)}, \Phi_R^{(c)}$	unsteady and convective parts of the acceleration potential Φ_R, respectively
χ	rotor wake skew angle used in the dynamic inflow model
ψ	$= \Omega t$ azimuth angle
Ψ	Azimuthal offset between the main rotor and the ground rotor axes used in the ground effect model
ω_n	blade natural frequency
$\boldsymbol{\omega}$	fuselage angular velocity vector
Ω	main rotor angular speed
Ω_t	angular speed of tail rotor
$\boldsymbol{\Omega}$	angular velocity vector of the main rotor
∇	vector gradient
∇^2	Laplacian operator

Superscripts and Subscripts

$(\ )^{-1}$	inverse
$(\ )^T$	transpose
$\dot{(\ )}$	derivative with respect to time

$\ddot{(\ )}$	second derivative with respect to time
$(\ )_{pi}$	quantity associated with ith point in a given blade finite element
$(\ )_{,x}$	partial derivative with respect to x spatial coordinate
$(\ )_{,xx}$	second partial derivative with respect to x spatial coordinate

ABSTRACT

This work presents a comprehensive first principles physics-based simulation capability for helicopter ship landing, denoted as "HeliUM2-umich." The simulation incorporates key components of the ship-helicopter dynamic interface including: 1) a high fidelity flight dynamics model with coupled rotor-fuselage-landing gear dynamics, 2) an aerodynamic model for the complex Wind Over Deck (WOD) that results from wind interacting with the superstructure of a moving ship, 3) a ground effect model that captures aerodynamics in proximity of the deck, 4) a ship deck motion model for a given sea condition, and 5) a Linear-Quadatric Regulator (LQR) based Flight Control System (FCS) to stabilize the vehicle dynamics and maintain a desired approach trajectory.

Initial portion of the work was focused on developing a WOD model and integrating it into the flight dynamics code in order to examine the influence of WOD on the UH-60A helicopter response during approach and landing flight segments. The WOD velocities were generated using unsteady Detached Eddy Simulation of flow over a full-scale Simple Frigate Shape Version 2 ship. The flight trajectory consisted of steady level flight followed by descent along a straight inclined trajectory to a specified hover position. Subsequently, the main rotor collective is gradually decreased to enable vertical descent and landing. Gain scheduling was used to track the approach trajectory. The effect of the WOD on vehicle response was examined for two cases: WOD affecting the rotor only, and WOD affecting the entire helicopter including the fuselage, empennage and tail rotor. The controller was shown to be effective in maintaining the desired approach and landing trajectory. However, additional control effort was needed in the presence of WOD. High frequency oscillations were noted in the CG position coordinates and attitude angles due to WOD. Oblique WOD

conditions required greater control effort than the headwind case. A larger effort was also required when WOD affected the entire helicopter as compared to the rotor alone. The combined influence of WOD and ground effect during approach and landing was also examined. The ground effect, which was modeled using a simple scaling factor, caused a decrease of approximately 11.3% in power consumption.

Next, a finite-state ground effect model was implemented to study the influence of static deck inclination and deck motion on helicopter dynamics. Rotor performance predictions showed good agreement with results from literature for hover over a level and stationary ground plane. Hover and landing simulations were performed with the deck inclined at constant roll and pitch angles, as well as with the deck excited in isolated roll, pitch and heave motions. For hover over a deck with constant roll inclination, an increase in the lateral inflow coefficient and the longitudinal cyclic control input was noted. Deck heaving motion produced an additional 7.5% change in power requirements relative to static ground effect, thus highlighting the importance of modeling dynamic ground effect. Simulations were also performed to examine the combined influence of WOD and deck motion. The representative ship motion data was extracted from the Systematic Characterization of the Naval Environment (SCONE) database. The controller was capable of maintaining a stable landing on level, inclined and moving decks in the presence of WOD and ground effect.

CHAPTER 1

Introduction, Background, and Objectives

Due to several unique aspects of the naval environment, illustrated in Fig. 1.1, shipboard landing of a helicopter is a challenging task for pilots. Pilots have to track a moving ship

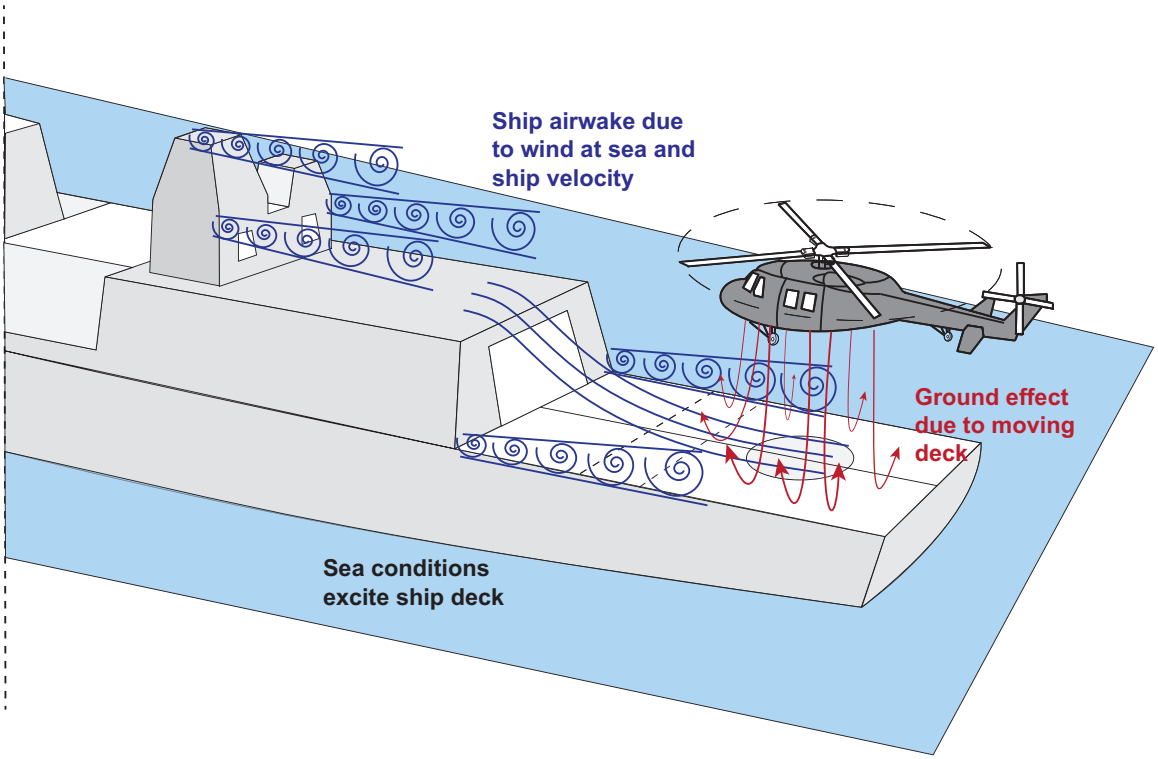

Figure 1.1: Illustration of a typical helicopter ship landing environment.

deck excited by sea conditions, as well as ensure vehicle stability in the presence of unsteady airwake from the ship structure, which interacts with the main rotor airwake. The ambient wind interacting with the ship structure, combined with the ship velocity, is re-

ferred to as "wind-over-deck" (WOD). The WOD introduces unsteady aerodynamic loads on the helicopter affecting take-off, landing, and hover over the ship deck. Furthermore, when operating close to the deck, the surface acts as an impermeable boundary condition (BC) producing a ground effect that causes helicopter downwash to turn back towards the vehicle modifying rotor thrust. Such conditions result in deteriorated handling qualities and increased pilot workload. It is thus important to design accurate launch and recovery envelopes, or Ship-Helicopter Operating Limits (SHOLs), to maximize safety. A typical SHOL is illustrated in Fig. 1.2, where the limits of wind strength and direction, relative to the deck, are indicated on a polar chart. The highlighted region indicates combinations of wind speed and direction in which the helicopter can safely operate. The SHOL diagram

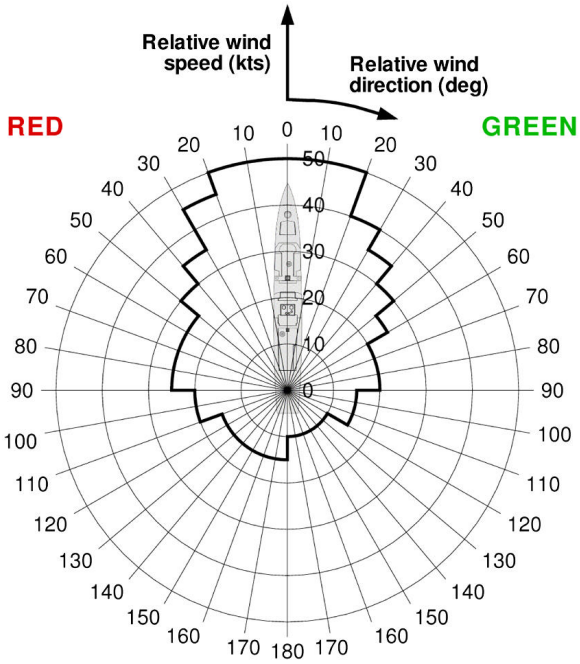

Figure 1.2: A typical SHOL diagram; winds from the portside are called "red" winds while starboard winds are called "green" winds [1]; region within the thick line is safe to operate.

for a given helicopter-ship combination is established during First of Class Flight Trials (FOCFTs) which involve test pilots carrying out numerous launch and recovery tasks for winds of different strength and direction at sea. However, the flight tests are expensive, and often incomplete since it is difficult to obtain a full range of wind conditions [2]. Simula-

tions provide a cost-effective alternative. For the ship landing problem, a comprehensive first principles physics-based simulation capability that includes all relevant components is needed. Required components include:

1. a high fidelity rotorcraft flight dynamic model that accounts for coupled rotor-fuselage-landing gear dynamics, combined with a rotor model based on flexible blades with coupled flap-lag-torsional dynamics;

2. an aerodynamic model for the WOD;

3. a ground effect model to capture the influence of the moving deck on the rotor; and

4. a robust flight control system (FCS) to maintain the desired position and attitude of the helicopter in the presence of WOD and ground effect.

Such a simulation capability has the potential to augment flight test programs by providing *a priori* understanding of the ship-helicopter dynamic interface (DI) for specified ship and helicopter configurations. The capability with some additional improvements can also be integrated into flight simulator environments to train pilots.

Numerous studies have been performed to characterize the ship-helicopter dynamic interface as described in Ref. 3. However, they have several shortcomings. Firstly, helicopter rotor models were based on rigid blade assumption. It is important to model blade flexibility in order to accurately capture the effects of WOD, ground effect and disturbances such as atmospheric gusts in the vehicle response. Secondly, numerous studies employ low fidelity airwake models. Airwake due to WOD is a critical component of the ship-helicopter DI and accurate modeling involves capturing flow features that have time stamps ranging from $O(10s)$ to several orders of magnitude smaller, as illustrated in Fig. 1.3. Thirdly, most studies ignored landing gear dynamics and were limited to simulating hover over the deck instead of an actual touchdown. Undesired and dangerous effects such as dynamic rollover [4] can result when the landing gears make contact with the ship deck. Finally, none of the studies accounted for ground effect.

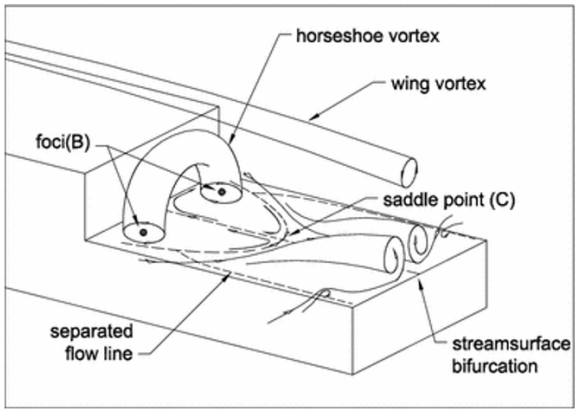

Figure 1.3: Flow topology behind a simplified ship geometry [5].

The objective of this study is the development of a comprehensive simulation capability that accounts for all the components mentioned previously. Section 1.1 reviews literature devoted to modeling ship airwake and the coupled helicopter-ship DI. Various control strategies employed to simulate pilot activity during helicopter launch and recovery operations are reviewed in Section 1.2. Section 1.3 contains a literature review of landing gear modeling, and Section 1.4 covers literature on ground effect modeling. The objectives of this dissertation are presented in Sections 1.5. Section 1.6 presents an outline of this dissertation.

1.1 Review of Helicopter-Ship Dynamic Interface Modeling

During the past two decades, several studies have addressed the modeling and simulation of the helicopter-ship DI [1, 2, 6–13]. Early efforts on the topic surfaced during the Advisory Group for Aerospace Research and Development (AGARD) Flight Mechanics Panel Symposium in 1991 [6]. The AGARD program was a joint initiative by member nations of the North Atlantic Treaty Organization (NATO) aimed at furthering science and technology related to aerospace. The symposium in 1991 focused on the deployment of fixed-winged

aircraft, Vertical Short Take-Off and Landing (VSTOL) aircraft, and helicopters near or on board ships. The papers examined the ship environment in terms of wind and deck motion [14], guidance and control methods [15], as well as flight tests and simulation techniques [16]. It was noted in Ref. 14 that typical ship superstructures are not aerodynamically efficient and generate recirculation zones with steep velocity gradients from the sharp edges of the superstructure, which are not readily predicted using time-averaged computational fluid dynamics (CFD) techniques. The author advocated for integration of aerodynamics in the ship design process. Ship airwake can be obtained from full-scale tests, wind tunnel testing, and CFD as described in Ref. 17. Airwake obtained from full-scale tests of flow over the deck of HMAS Darwin, an FFG-7 class frigate, was compared against wind tunnel results in Ref. 16. While the mean vertical velocities showed good agreement, significant differences were observed in the horizontal and lateral velocities due to atmospheric turbulence, which was not replicated in the wind tunnel tests. An inverse power model was fitted onto the spectral density of the airwake data in a subsequent study [18] to obtain a turbulence model that could be integrated into a flight simulation code. The model showed promise but required further examination. In Ref. 19, ship deck motion was shown to greatly impact on-deck stability of the vehicle. The use of restraining devices was recommended to increase the on-deck operating limits of the vehicle. A comprehensive discussion of the different challenges associated with helicopter ship landing was presented in Ref. 20.

Further research on the topic was performed under the Joint Shipboard Helicopter Integration Process (JSHIP) program [7, 8, 21, 22]. It was shown in Ref. 7 that steady-state CFD calculations do not accurately predict the time-average of the turbulent flowfield in the ship airwake. Furthermore, turbulence modeling adds too much dissipation to Reynold-Averaged Navier-Stokes (RANS) based CFD calculations. Time-accurate Large Eddy Simulation (LES) emerged as the preferred approach for simulating the ship airwake, albeit at a significant computational cost. For WOD speeds ranging from 15 to 30 knots, it was also found that flow over a Landing Helicopter Assault (LHA) class ship can be assumed to be

incompressible and independent of Reynolds number [7]. As a consequence, the flowfield obtained for a given velocity can be scaled to any other velocity, without having to repeat the simulation. As part of the JSHIP program, the Dynamic Interface Modeling and Simulation System (DIMSS) was developed so as to define a process for expanding WOD flight envelopes for any ship-helicopter combination [21]. The DIMMS tool was integrated into the NASA Ames Vertical Motion Simulator and pilot workload was assessed for a UH-60 helicopter operating near an LHA class ship. Flight tests were performed to validate the predictions [8, 22].

A substantial amount of research work on the helicopter-ship DI has been carried out by the Flight Science and Technology research group at the University of Liverpool [1, 2, 11, 23, 24]. The main tool used is the HELIFLIGHT-R reconfigurable flight simulator shown in Fig. 1.4 [2]. The importance of visual aids in shipboard operations was demon-

Figure 1.4: External (left) and internal (right) view of HELIFLIGHT-R simulator [2].

strated in Ref. 23, where a test pilot's ability to perform a landing task using different visual

aid models was assessed. Higher fidelity visual aid models made the pilot feel confident in their ability to land at night, when vision was degraded. The effect of WOD on pilot workload using the simulator integrated with a CFD based ship airwake and experiment based fuselage loading models was examined in Ref. 11. For the headwind case, a minor difference in pilot workload was noted when fuselage loading was included. For oblique winds however, pilot workload increased significantly. More recently, time-accurate CFD simulations using Detached Eddy Simulation (DES) based turbulence modeling were used to construct airwake models on three different ship structures, shown in Fig. 1.5 [1]. Note

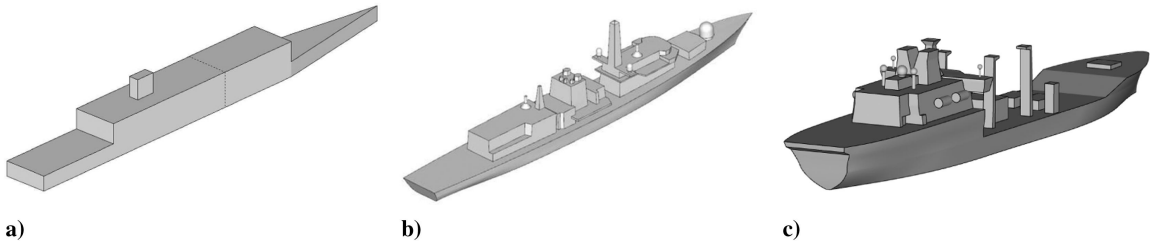

Figure 1.5: Ship geometries used in airwake generation: a) Simple Frigate Shape Version 2 (SFS2), b) Type 23 frigate, and c) Wave class auxiliary oiler [1].

that the Simple Frigate Shape Version 2 (SFS2) ship shown in Fig. 1.5a was conceived and extensively studied under the Tripartite Technical Cooperation Program (TTCP) [25], which sought to create a simple ship to be used as basis for comparison by different research groups. The DES method used in Ref. 1 provided a good compromise between the computationally expensive LES and lower-fidelity unsteady RANS solution, and had also been validated using wind tunnel and full-scale experimental data in a prior study [24]. Therefore, in this study, a model for WOD is obtained using DES. The airwake models in Ref. 1 were incorporated in a FLIGHTLAB [26] based simulator which was operated by an experienced test pilot to determine operating limits. Deck motion due to sea state was modeled. The airwake had a significant impact on pilot workload, with oblique WOD conditions requiring the greatest effort relative to the headwind case.

In Ref. 9, wind tunnel measurements of time-averaged rotor thrust coefficient for a rotor operating in ship airwake were presented. A 10-15% decrease in available thrust

was measured on a rotor placed 9-15 m above the deck in the presence of an airwake. A GENHEL model of UH-60A Blackhawk helicopter was combined with time-accurate CFD solutions of a LHA class ship airwake in Ref. 10. However, the rotor model was based on a simple rigid blade rotor. Pilot workload increased substantially with WOD effects, especially during the hover segment of the trajectory [10]. Approach and landing simulations were performed in Ref. 27 using FLIGHTLAB. Deck motion and landing gear dynamics were included, however an empirical stochastic airwake model was employed. The airwake in these studies [1, 10, 11] is obtained offline and accounts only for the effect of ship airwake on the helicopter, implying a one-way coupling. A complete coupled CFD based WOD simulation with helicopter flight dynamics in real-time was attempted in Ref. 12. However, this study was preliminary and far from real-time. Furthermore, it was based on the GENHEL model with rigid rotor blades, which is deemed inadequate for the problem. A similar attempt for fully coupled-simulations was made in Ref. 13. The solution was far from real-time and deck motion was ignored.

In Ref. 28, a Proper Orthogonal Decomposition (POD) based Reduced Order Model (ROM) was generated to approximate the dynamics of the flow over an SFS2 ship geometry. The goal of the study was to develop an airwake model that is not limited by computer memory, as is generally the case when CFD data is imported in the form of table look-up in rotorcraft simulations. The ROM predictions showed good agreement with CFD data.

1.2 Review of Trajectory Tracking Control Strategies

Helicopters are inherently unstable, and require an FCS for stable operation. In Ref. 10, a simplified optimal control model of a human pilot was used to simulate pilot control activity for a prescribed trajectory. The model was based on a linear-quadratic regulator (LQR) and developed such that tracking performance could be readily tuned based on a desired crossover frequency in each control axis. Dynamic inversion control was used to

carry out autonomous approach and landing simulations on a moving deck in Ref. 27. The controller was tested in FLIGHTLAB [26] based simulations. Although the controller was effective in tracking straight and oblique approach trajectories, it produced unnecessary displacements while tracking a heaving deck in the landing phase. It was also noted that for the controller to perform effectively, the trajectory path had to be smooth and not overly aggressive. A gain-scheduled LQR controller was used in Ref. 29 in an optimization framework to obtain an approach trajectory that minimized brownout. Two optimal paths were identified. In the first optimum, the vehicle approached the landing spot at a small flight path angle, effectively keeping the cloud of dust in its trail; in the second, the vehicle followed a steep trajectory, keeping the wake vortices above ground. A Model Predictive Path Integral (MPPI) method based on an implicit stochastic optimal control framework was recently examined in Ref. 30. The method was shown to be viable for real-time applications as it provided optimal control at a fraction of the computation cost associated with explicit optimal control techniques. Control strategies to mitigate the effects of ship airwake on pilot workload have also been developed [31, 32]. It was recommended in Ref. 20 that such control augmentation system be designed based on the handling requirements set forth in the Aeronautical Design Standard (ADS)-33 [33].

1.3 Review of Helicopter Landing Gear Modeling

Landing gear modeling generally focuses on two parts: (1) a shock absorbing oleo strut and (2) a rubber tire that provides surface traction and transfers the loads between the deck and aircraft. The strut consists of an air spring and oil damper. Vertical motion of the strut pushes oil into an air-filled chamber through an orifice, producing spring and damping resistances [34]. Two landing gear models were presented in Ref. 35. In the first model, the strut was represented by a nonlinear spring damper system and the tire by a linear undamped spring. Both were assumed to be massless and produced reaction

forces in the vertical direction only. In the second model, the strut was represented by a two stage nonlinear spring damper system which produced stiffer restoring forces once gear deflection exceeded a prescribed threshold. The study was rudimentary and modeled the helicopter as a large mass connected to one strut and tire. A subsequent study [36] considered three landing gears, each based on a three-dimensional nonlinear spring-damper system, illustrated in Fig. 1.6. The planar stiffness coefficients used in the model were

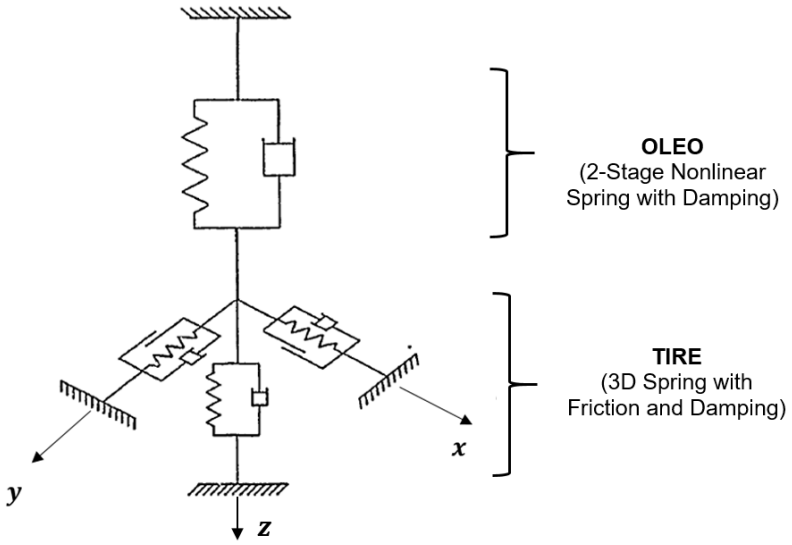

Figure 1.6: Massless 3D landing gear model [36].

based on actual tire properties provided in Ref. 37. The landing gears successfully brought the vehicle to rest in drop test simulations performed on inclined and sinusoidal rolling decks. However, the study ignored rotor aerodynamics. A model that accounts for the inertial effects due to strut deflection, shown in Fig. 1.7, was introduced in Refs. 38 and 39. When the ground reaction force exceeded the preload setting of the strut, the unsprung mass experienced an acceleration, generating a restoring force in the strut. In other cases, the tire reaction force was transferred directly onto the airframe with zero strut deflection. More sophisticated tire models have been developed to study on-deck maneuvers [40, 41]. These are however beyond the scope of this dissertation.

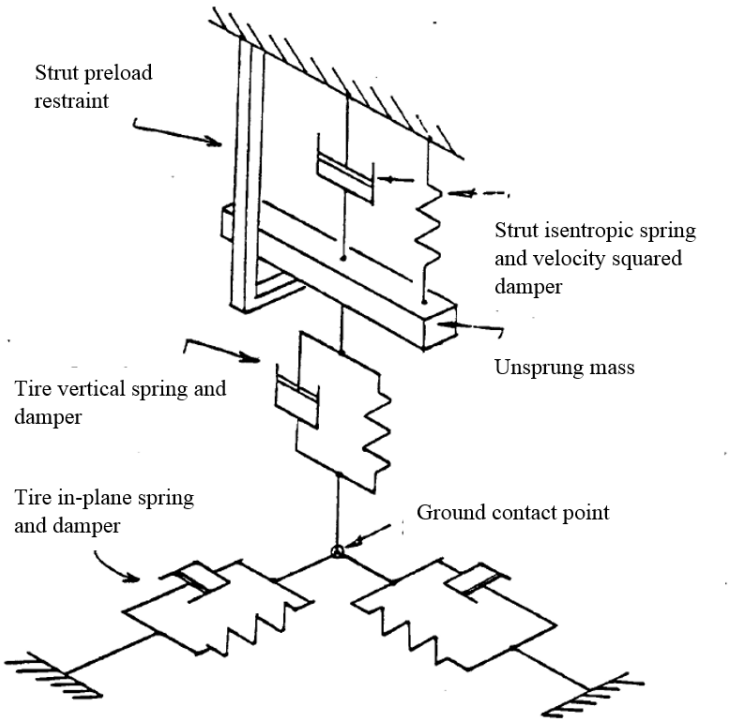

Figure 1.7: Landing gear model with an unsprung mass [38, 39].

1.4 Review of Ground Effect Modeling

The influence of a level ground on rotor performance has been extensively studied through experiments [42–49], shown in Fig. 1.8, with power reductions as high as 30-60% noted during hover close to ground. More recently, the influence of an inclined or a moving ground plane on rotor performance was examined through flight tests and laboratory-scale experiments [50, 51]. Rotor performance was found to be sensitive to disc loading, in addition to the hub height above the ground plane and the thrust/power setting. For low disc loadings, inclined ground resulted in lower power consumption, when compared to a level ground. For high disc loadings, ground inclination caused rotor power to exceed out-of-ground-effect (OGE) power requirements, a trend not observed in previous conventional ground effect studies. Experiments in Ref. 51 showed that sinusoidal pitching of the ground plane generated sinusoidal fluctuations in the hub pitching moment, and a sinusoidal heaving ground motion resulted in variations as high as 20% in rotor thrust.

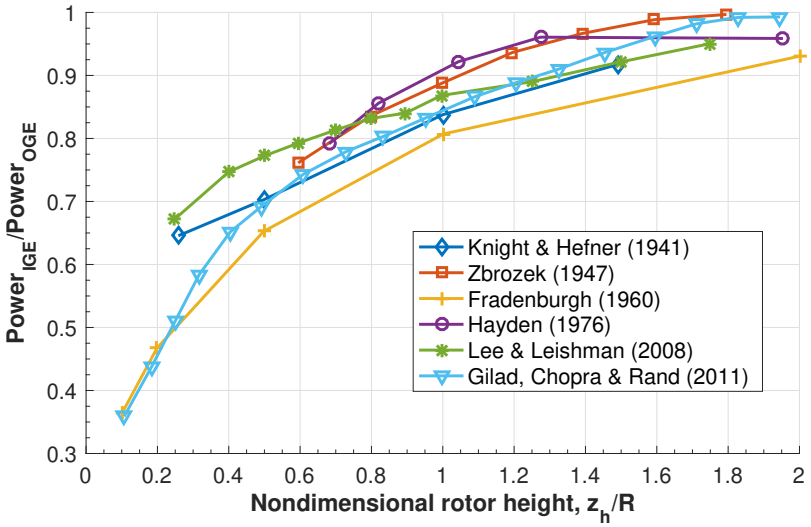

Figure 1.8: Experimental data showing the influence of ground effect on power requirements for constant thrust; adapted from Fig. 4 of Ref. 49.

Ground effect is traditionally modeled using a simple empirical correction factor k_G, which is a function of rotor height from the ground z_h, and rotor thrust or power [48]. The factor is readily amenable to incorporation in flight dynamic models, but is not accurate for $z_h/R < 0.5$, where R is the rotor radius. Accurate ground effect modeling can be achieved using CFD [52, 53] or free-wake models [54, 55], but these tend to be computationally expensive. In Ref. 56, ground effect was modeled using dynamic inflow models and an image rotor to satisfy the impermeable surface BC as illustrated in Fig. 1.9. The primary

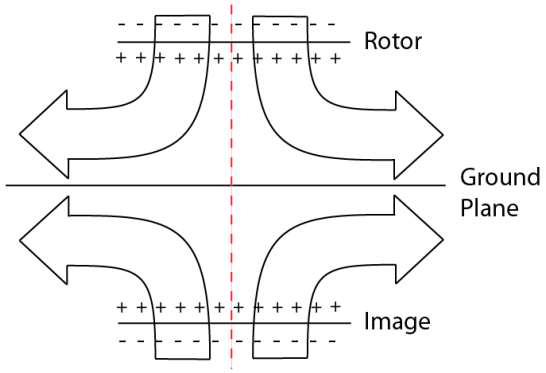

Figure 1.9: Illustration of the image rotor model.

advantage of using an image rotor method is its simplicity and the fact that the BC is satisfied at any given instant of time. However, for hover, the two rotors are placed in each other's wake, which cannot be modeled using the usual state-space dynamic inflow models. Furthermore, superposition of pressures from the actual and image rotors is based on an implicit assumption that the two rotors share a common free stream direction, which is not accurate. Also, the image rotor method cannot be used to model inclined and dynamic surfaces. To overcome these shortcomings, a new approach based on a ground source rotor was developed in Refs. [57, 58]. The ground is represented by a source distribution that produces pressure equal and opposite to that exerted by the main rotor on the ground as shown in Fig. 1.10. The model combines the He-Peters dynamic inflow model [59] with an additional set of ordinary differential equations (ODE's) that represent the influence of ground on the rotor inflow velocity, and accounts for inclined, partial, and dynamic ground planes. This model has never been applied to the helicopter ship landing problem.

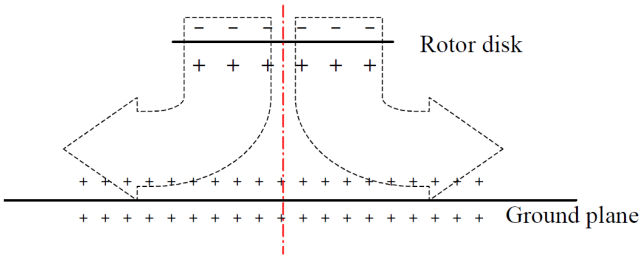

Figure 1.10: Illustration of ground source [58].

1.5 Objectives of this Dissertation

The literature review provided in the previous sections indicates the need for a comprehensive first principles based simulation capability for helicopter approach and landing on a ship deck in the presence of WOD and ground effect. Developing such a capability is the overall objective of this thesis. An extensively modified version of the HeliUM2 flight

dynamics simulation code [60], referred to as the "HeliUM2-umich" code, is used. The specific objectives are to:

1. Document improvements made to the HeliUM2 flight dynamic simulation code to account for WOD effects on the helicopter components (main rotor, fuselage, empennage and tail rotor), and the inclusion of a ground effect model, a landing gear model, and a flight control system.

2. Develop a time-accurate DES based WOD model, and integrate it into the flight dynamic simulation.

3. Develop an FCS capable of stabilizing helicopter dynamics and maintaining a prescribed approach and landing trajectory.

4. Describe the inclusion of a dynamic finite-state ground effect model into the simulation code.

5. Describe the integration of Systematic Characterization Of the Naval Environment (SCONE) data for simulating ship deck motion into HeliUM2-umich.

6. Simulate complete approach and landing to examine the influence of WOD on helicopter response for two cases: WOD affecting the rotor only, and WOD affecting the entire helicopter.

7. Determine the influence of dynamic ground effect on rotor performance in the presence of level, inclined, and moving decks.

8. Determine the combined influence of WOD and ground effect on helicopter response during approach and landing on a moving deck.

1.6 Dissertation Outline

The thesis is organized as follows: Chapter 2 contains an overview of the baseline HeliUM2 flight dynamics model; Chapter 3 provides details on the approach and landing trajectory considered in this study, together with a description of the controller design; Chapter 4 describes the WOD model and its integration into the flight dynamic simulation; landing gear and ground effect models are described in Chapter 5; Chapter 6 describes the incorporation of the SCONE data; Chapter 7 presents all the simulation results; and Chapter 8 contains conclusions and recommendations for future research.

CHAPTER 2

Flight Dynamics Model (HeliUM2)

A detailed description of the HeliUM2 flight dynamics model is provided for completeness, and background on the integration of components that were incorporated as part of this study. The HeliUM2 flight dynamics code [60, 61], developed and maintained at the University of Maryland, is a replacement for the GENHEL flight simulation capability [62] with improvements such as flexible blade model [63] and the Maryland Free Wake model [64]. The capability has been used to examine the dynamic response of a UH-60A helicopter, which has articulated rotor blades, as well as a BO-105 helicopter with hingeless blades in steady turns, climb and descent. Vehicle response predictions have been validated against flight test data [60]. HeliUM2 has also been used for dynamic analysis of the XV-15 tilt rotor aircraft, coaxial rotors, and helicopters towing submerged bodies [60].

The equations of motion representing helicopter dynamics are formulated as a set of nonlinear first order ODEs in implicit form, given by

$$\mathbf{f}(\dot{\mathbf{x}}, \mathbf{x}, \mathbf{u}; t) = \mathbf{0}, \tag{2.1}$$

where $\mathbf{x}$ is the state vector and $\mathbf{u}$ the control input vector. The implicit formulation, used in this study, allows for a solution to be obtained without explicit algebraic manipulations.

The state vector $\mathbf{x}$ is given by

$$\mathbf{x} = \{\mathbf{x}_F, \mathbf{x}_I, \mathbf{x}_{NR}\}^T, \tag{2.2}$$

where $\mathbf{x}_F$ contains fuselage rigid body states, $\mathbf{x}_I$ contains main and tail rotor inflow states, and $\mathbf{x}_{NR}$ contains generalized coordinates representing the main rotor blade motion.

The control input vector consists of main rotor collective, cyclic, and tail rotor collective inputs and is given by

$$\mathbf{u} = \{\theta_0, \theta_{1c}, \theta_{1s}, \theta_{0t}\}^T. \tag{2.3}$$

The various coordinate systems used in the model are described next, followed by a list of assumptions made. The formulation of the main rotor equations of motions and fuselage rigid body equations, as well as empennage and tail rotor equations is described subsequently. This is followed by a description of the final equations of motion and the DASSL solver [65], used in time-marching. Finally, trim and linearization procedures are described.

2.1 Coordinate Systems

The different coordinate systems and transformations between them are described next.

2.1.1 Earth-fixed coordinate system

The earth-fixed or gravity coordinate system has its origin at the waterline directly below the center of gravity (CG) of the helicopter at $t = 0$ s, with the $\hat{z}_I$ axis aligned parallel to the direction of gravity. The $\hat{x}_I$ and $\hat{y}_I$ axes are usually taken pointing North and East, respectively. The coordinate system is illustrated in Fig. 2.1.

2.1.2 Helicopter body-fixed coordinate system

The helicopter body-fixed frame, shown in Fig. 2.1, is obtained from the earth-fixed frame using three translations to shift the origin to the CG, followed by three Euler rotations ψ_f, θ_f, ϕ_f, which represent the yaw, pitch and roll angular attitudes, respectively, of the CG. The rotation matrix from gravity to helicopter axes $[T_{BI}]$ is given by

$$[T_{BI}] = \begin{bmatrix} 1 & 0 & 0 \\ 0 & \cos\phi_f & \sin\phi_f \\ 0 & -\sin\phi_f & \cos\phi_f \end{bmatrix} \begin{bmatrix} \cos\theta_f & 0 & -\sin\theta_f \\ 0 & 1 & 0 \\ \sin\theta_f & 0 & \cos\theta_f \end{bmatrix} \begin{bmatrix} 1 & 0 & 0 \\ 0 & \cos\phi_f & \sin\phi_f \\ 0 & -\sin\phi_f & \cos\phi_f \end{bmatrix}. \quad (2.4)$$

Therefore,

$$\begin{Bmatrix} \hat{\mathbf{i}}_{hel} \\ \hat{\mathbf{j}}_{hel} \\ \hat{\mathbf{k}}_{hel} \end{Bmatrix} = [T_{BI}] \begin{Bmatrix} \hat{\mathbf{i}}_I \\ \hat{\mathbf{j}}_I \\ \hat{\mathbf{k}}_I \end{Bmatrix}. \quad (2.5)$$

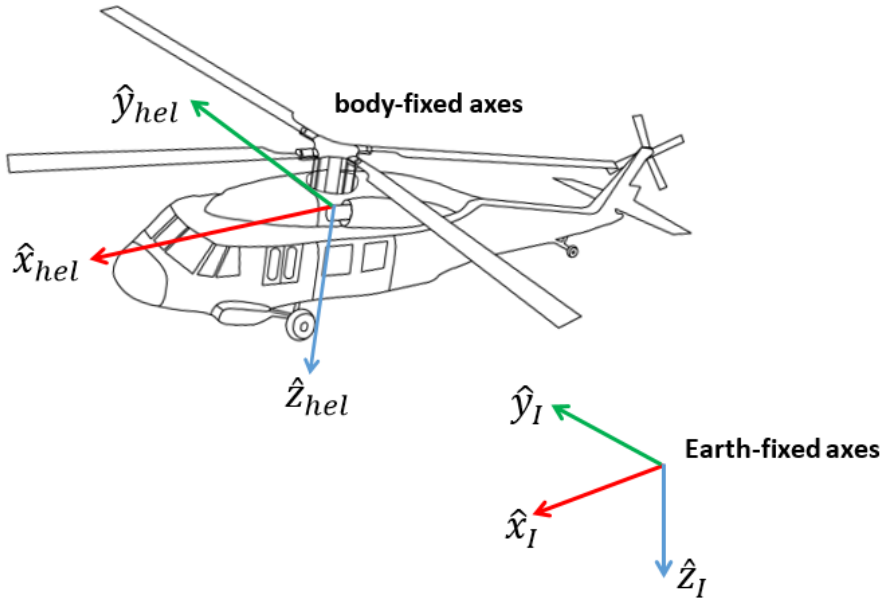

Figure 2.1: Earth-fixed and helicopter body-fixed coordinate systems.

2.1.3 Wind coordinate system

The wind coordinate system has its center at the CG and its orientation is determined by the freestream air flow. The $\hat{x}_W$ axis points forward, aligned with the freestream velocity. The $\hat{y}_W$ and $\hat{z}_W$ axes are perpendicular $\hat{x}_W$ and point to starboard and downwards, respectively. The body-fixed frame is related to the wind axes by the fuselage angle of attack α_f and fuselage sideslip angle β_f as shown in Fig. 2.2. The transformation between the two frames is given by

$$[T_{WB}] = \begin{bmatrix} \cos\alpha_f & 0 & \sin\alpha_f \\ 0 & 1 & 0 \\ -\sin\alpha_f & 0 & \cos\alpha_f \end{bmatrix} \begin{bmatrix} \cos\beta_f & \sin\beta_f & 0 \\ -\sin\beta_f & \cos\beta_f & 0 \\ 0 & 0 & 1 \end{bmatrix}, \tag{2.6}$$

and thus,

$$\begin{Bmatrix} \hat{\mathbf{i}}_W \\ \hat{\mathbf{j}}_W \\ \hat{\mathbf{k}}_W \end{Bmatrix} = [T_{WB}] \begin{Bmatrix} \hat{\mathbf{i}}_{hel} \\ \hat{\mathbf{j}}_{hel} \\ \hat{\mathbf{k}}_{hel} \end{Bmatrix}. \tag{2.7}$$

In this study, aerodynamic coefficients of fuselage are defined relative to the wind coordinate system and obtained using table look-up.

2.1.4 Shaft coordinate system

The rotor shaft is tilted slightly relative to the $\hat{z}_{hel}$ body axis. The purpose of the shaft tilt angle is to minimize drag in forward flight. The shaft coordinate system has its origin at the hub with the $\hat{z}_{sh}$ pointing downward along the shaft, the $\hat{x}_{sh}$ axis pointing forward, and the $\hat{y}_{sh}$ pointing starboard. The shaft tilt is defined by the longitudinal and lateral tilt angles α_x and α_y, respectively, illustrated in Fig. 2.3. The transformation matrix between the shaft

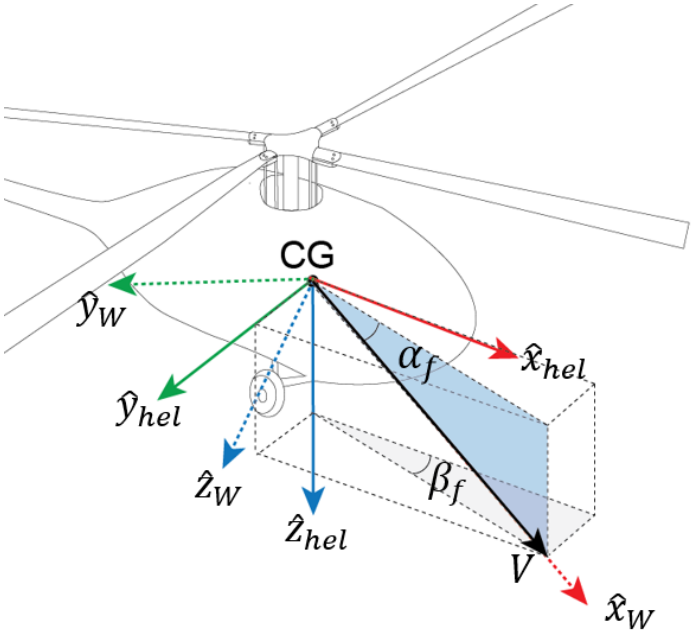

Figure 2.2: Illustration of fuselage sideslip angle, angle of attack, and wind acess.

frame and the body-fixed frame is given by

$$[T_{ShB}] = \begin{bmatrix} \cos\alpha_x & 0 & -\sin\alpha_x \\ 0 & 1 & 0 \\ \sin\alpha_x & 0 & \cos\alpha_x \end{bmatrix} \begin{bmatrix} 1 & 0 & 0 \\ 0 & \cos\alpha_y & \sin\alpha_y \\ 0 & -\sin\alpha_y & \cos\alpha_y \end{bmatrix}, \tag{2.8}$$

implying,

$$\begin{Bmatrix} \hat{\mathbf{i}}_{sh} \\ \hat{\mathbf{j}}_{sh} \\ \hat{\mathbf{k}}_{sh} \end{Bmatrix} = [T_{ShB}] \begin{Bmatrix} \hat{\mathbf{i}}_{hel} \\ \hat{\mathbf{j}}_{hel} \\ \hat{\mathbf{k}}_{hel} \end{Bmatrix}. \tag{2.9}$$

2.1.5 Nonrotating hub coordinate system

The nonrotating hub system has its origin at the hub and is obtained by rotating the shaft coordinate system by 180° about the positive $\hat{y}_{sh}$ axis, as illustrated in Fig. 2.4. The

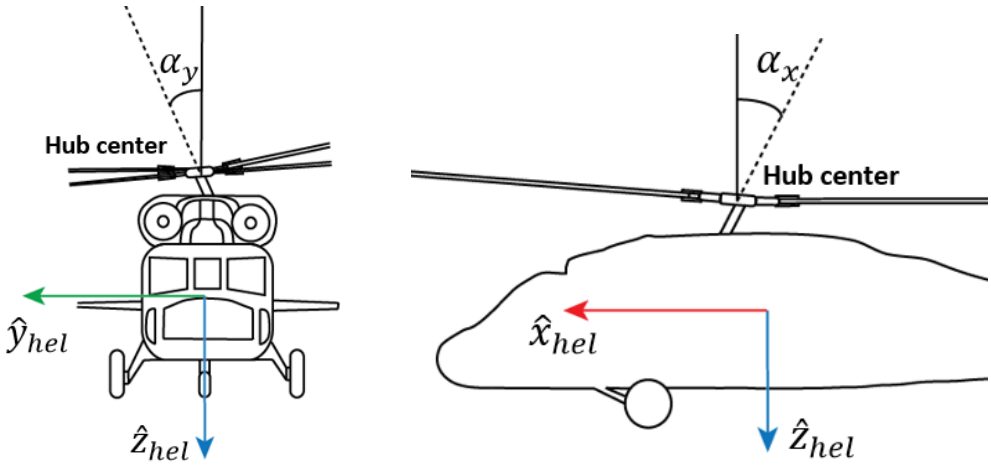

(a) (b)

Figure 2.3: Illustration of a) lateral and b) longitudinal shaft tilt angles, exaggerated for clarity.

transformation between the two frames is given by

$$[T_{H_{NR}Sh}] = \begin{bmatrix} -1 & 0 & 0 \\ 0 & 1 & 0 \\ 0 & 0 & -1 \end{bmatrix}. \tag{2.10}$$

Therefore,

$$\begin{Bmatrix} \hat{\mathbf{i}}_{H_{NR}} \\ \hat{\mathbf{j}}_{H_{NR}} \\ \hat{\mathbf{k}}_{H_{NR}} \end{Bmatrix} = [T_{H_{NR}Sh}] \begin{Bmatrix} \hat{\mathbf{i}}_{sh} \\ \hat{\mathbf{j}}_{sh} \\ \hat{\mathbf{k}}_{sh} \end{Bmatrix}. \tag{2.11}$$

2.1.6 Rotating hub coordinate system

The hub rotating system has its origin at the hub, with the $\hat{z}_{H_R}$ axis parallel to the $\hat{z}_{H_{NR}}$ axis. The $\hat{x}_{H_R}$ axis is coincident with the elastic axis of the undeformed blade, and is located at an azimuth angle ψ, measured from the aft of the rotor disk and positive counterclockwise when the disk is viewed from the top, as illustrated in Fig. 2.5. The $\hat{y}_{H_R}$ axis is a chordwise

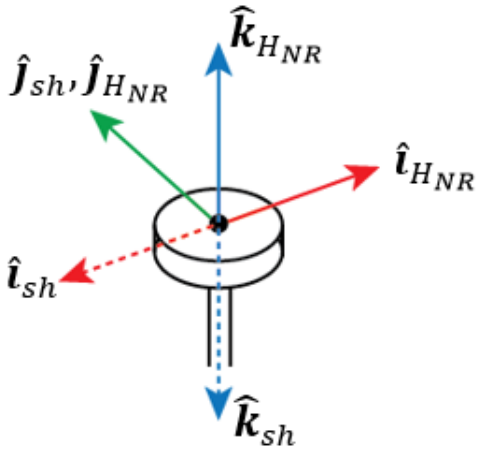

Figure 2.4: Relationship between shaft frame and nonrotating hub coordinate system.

axis positive towards the leading edge. The transformation between the nonrotating and rotating hub frames is given by

$$[T_{H_R H_{NR}}] = \begin{bmatrix} \cos\psi & \sin\psi & 0 \\ -\sin\psi & \cos\psi & 0 \\ 0 & 0 & 1 \end{bmatrix}. \tag{2.12}$$

Thus,

$$\begin{Bmatrix} \hat{\mathbf{i}}_{H_R} \\ \hat{\mathbf{j}}_{H_R} \\ \hat{\mathbf{k}}_{H_R} \end{Bmatrix} = [T_{H_R H_{NR}}] \begin{Bmatrix} \hat{\mathbf{i}}_{H_{NR}} \\ \hat{\mathbf{j}}_{H_{NR}} \\ \hat{\mathbf{k}}_{H_{NR}} \end{Bmatrix}. \tag{2.13}$$

2.1.7 Undeformed, preconed blade coordinate system

The undeformed, preconed blade coordinate system is a rotating system that accounts for the blade precone angle β_p. The origin of the frame is at the blade root. The $\hat{\mathbf{e}}_x$ unit vector is aligned along the blade span and positive outwards, the $\hat{\mathbf{e}}_y$ vector is oriented in the blade chordwise direction, and the $\hat{\mathbf{e}}_z$ vector is perpendicular to the the undeformed elastic axis

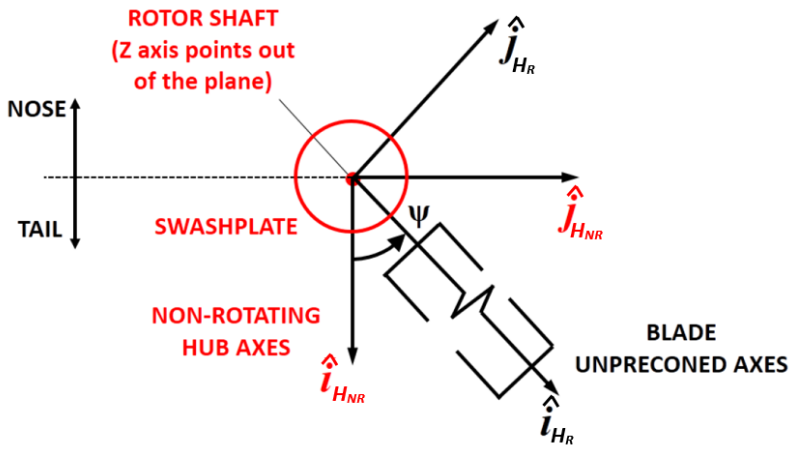

Figure 2.5: Relationship between nonrotating and rotating hub frames; adapted from Fig. 2.3 of Ref. 66.

and positive upwards. The relationship between the hub rotating frame and the undeformed, preconed frame is depicted in Fig. 2.6. The transformation matrix between the frames is given by

$$[T_{PH_R}] = \begin{bmatrix} \cos\beta_p & 0 & \sin\beta_p \\ 0 & 1 & 0 \\ -\sin\beta_p & 0 & \cos\beta_p \end{bmatrix}. \tag{2.14}$$

Thus,

$$\begin{Bmatrix} \hat{\mathbf{e}}_x \\ \hat{\mathbf{e}}_y \\ \hat{\mathbf{e}}_z \end{Bmatrix} = [T_{PH_R}] \begin{Bmatrix} \hat{\mathbf{i}}_{H_R} \\ \hat{\mathbf{j}}_{H_R} \\ \hat{\mathbf{k}}_{H_R} \end{Bmatrix}. \tag{2.15}$$

2.1.8 Deformed blade coordinate system

The deformed blade coordinate system is a rotating frame unique to each point on the deformed elastic axis as illustrated in Fig. 2.6. The corresponding unit vectors are $\hat{\mathbf{e}}'_x, \hat{\mathbf{e}}'_y$ and $\hat{\mathbf{e}}'_z$, where $\hat{\mathbf{e}}'_x$ is tangent to the deformed elastic axis, $\hat{\mathbf{e}}'_y$ is aligned with the blade chord and positive towards the leading edge, and $\hat{\mathbf{e}}'_z$ is normal to the $\hat{\mathbf{e}}'_x$-$\hat{\mathbf{e}}'_y$ plane and positive

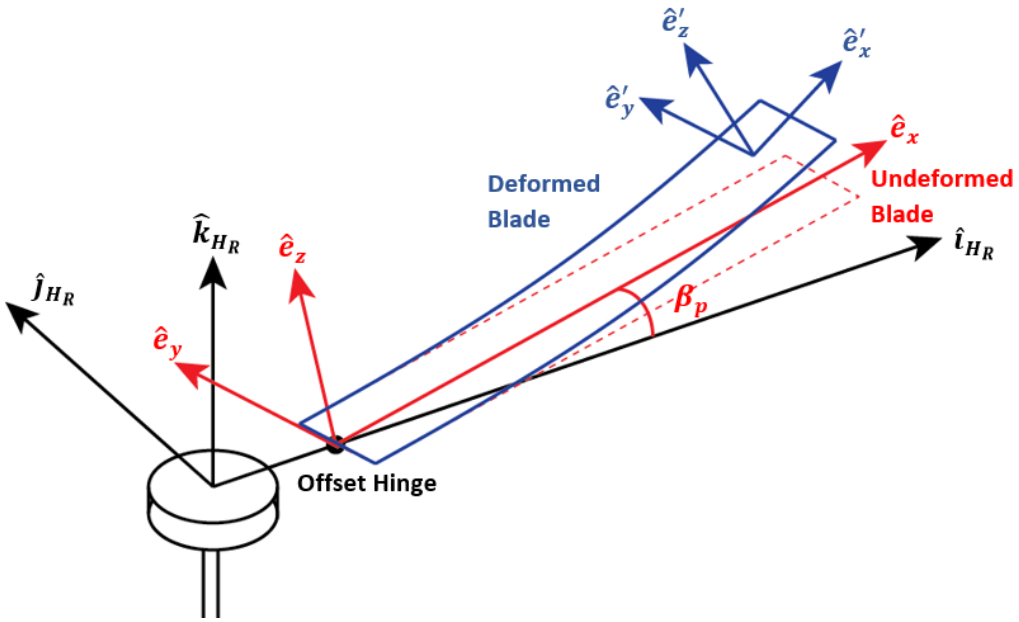

Figure 2.6: Relationship between rotating hub frame, undeformed, preconed frame and deformed preconed frames.

upward. The transformation from undeformed to deformed blade coordinates is given by

$$[T_{DP}] = \begin{bmatrix} S_{11} & S_{12} & S_{13} \\ S_{21} & S_{22} & S_{23} \\ S_{31} & S_{32} & S_{33} \end{bmatrix}, \tag{2.16}$$

where,

$$\begin{aligned} S_{11} &= \cos\theta_y \cos\theta_z, \\ S_{12} &= \cos\theta_y \sin\theta_z, \\ S_{13} &= -\sin\theta_y, \\ S_{21} &= \sin\theta_x \sin\theta_y \cos\theta_z - \cos\theta_x \sin\theta_z, \\ S_{22} &= \cos\theta_x \cos\theta_z + \sin\theta_x \sin\theta_y \sin\theta_z, \\ S_{23} &= \sin\theta_x \cos\theta_y, \\ S_{31} &= \cos\theta_x \sin\theta_y \cos\theta_z + \sin\theta_x \sin\theta_z, \end{aligned} \tag{2.17}$$

$$
\begin{aligned}
S_{32} &= -\left(\sin\theta_x \cos\theta_z - \cos\theta_x \sin\theta_y \sin\theta_z\right), \\
S_{33} &= \cos\theta_x \cos\theta_y,
\end{aligned}
$$

and where,

$$
\begin{aligned}
\theta_x &= \phi_p, \\
\sin\theta_y &= -\frac{w_{p,x}}{\sqrt{1 + 2u_{p,x} + u_{p,x}^2 + v_{p,x}^2 + w_{p,x}^2}}, \\
\cos\theta_y &= \frac{\sqrt{1 + 2u_{p,x} + u_{p,x}^2 + v_{p,x}^2}}{\sqrt{1 + 2u_{p,x} + u_{p,x}^2 + v_{p,x}^2 + w_{p,x}^2}}, \\
\sin\theta_z &= \frac{v_{p,x}}{\sqrt{1 + 2u_{p,x} + u_{p,x}^2 + v_{p,x}^2 + w_{p,x}^2}}, \\
\cos\theta_z &= \frac{1 + u_{p,x}}{\sqrt{1 + 2u_{p,x} + u_{p,x}^2 + v_{p,x}^2 + w_{p,x}^2}}.
\end{aligned}
\tag{2.18}
$$

The blades in HeliUM2 are assumed to undergo small strains and moderate deflections, implying finite rotations. Thus the expressions in Eq. (2.18) simplify to [67]

$$
\begin{aligned}
\theta_x &= \phi_p, \\
\sin\theta_y &= -w_{p,x}, \\
\cos\theta_y &= 1, \\
\sin\theta_z &= v_{p,x}, \\
\cos\theta_z &= 1.
\end{aligned}
\tag{2.19}
$$

The deformed and undeformed blade coordinate systems are related as follows

$$
\begin{Bmatrix} \hat{\mathbf{e}}'_x \\ \hat{\mathbf{e}}'_y \\ \hat{\mathbf{e}}'_z \end{Bmatrix} = [T_{DP}] \begin{Bmatrix} \hat{\mathbf{e}}_x \\ \hat{\mathbf{e}}_y \\ \hat{\mathbf{e}}_z \end{Bmatrix}. \tag{2.20}
$$

2.1.9 Blade sectional aerodynamic coordinate system

The blade sectional aerodynamic coordinate system is a local coordinate system with its origin on the deformed elastic axis. The airflow velocity components at the blade section are represented using this coordinate system. Its unit vectors are $\mathbf{e}_T, \mathbf{e}_P$ and $\mathbf{e}_R$, defined such that $\mathbf{e}_T$ points aft towards the trailing edge, $\mathbf{e}_R$ is tangent to the elastic axis and points towards the blade tip, and $\mathbf{e}_P$ is normal to the $\mathbf{e}_T$-$\mathbf{e}_R$ plane and positive up.

The total blade sectional velocity in the undeformed, preconed coordinate system is given as

$$\mathbf{V}_T = V_x\hat{\mathbf{e}}_x + V_y\hat{\mathbf{e}}_y + V_z\hat{\mathbf{e}}_z. \tag{2.21}$$

For aerodynamic calculations, $\mathbf{V}_T$ in Eq. (2.21) is transformed to the blade sectional aerodynamics coordinate system yielding

$$\mathbf{V}_A = U_T\hat{\mathbf{e}}_T + U_P\hat{\mathbf{e}}_P + U_R\hat{\mathbf{e}}_R. \tag{2.22}$$

The transformation is achieved using the following matrix

$$[T_{AP}] = \begin{bmatrix} \sin v_{p,x} & -\cos v_{p,x} & 0 \\ \sin w_{p,x}\cos v_{p,x} & \sin w_{p,x}\sin v_{p,x} & -\cos w_{p,x} \\ \cos w_{p,x}\cos v_{p,x} & \cos w_{p,x}\sin v_{p,x} & \sin w_{p,x} \end{bmatrix}, \tag{2.23}$$

where $w_{p,x}$ and $v_{p,x}$ are the local flap and lag slopes of the blade elastic axis relative to the undeformed, preconed blade coordinate system, respectively.

The relationship between the undeformed, preconed coordinate system and the blade

sectional aerodynamics coordinate system is given as

$$\left\{ \begin{array}{c} \hat{\mathbf{e}}_T \\ \hat{\mathbf{e}}_P \\ \hat{\mathbf{e}}_R \end{array} \right\} = [T_{AP}] \left\{ \begin{array}{c} \hat{\mathbf{e}}_x \\ \hat{\mathbf{e}}_y \\ \hat{\mathbf{e}}_z \end{array} \right\}. \tag{2.24}$$

2.2 Main Assumptions

The main assumptions used in the formulation of the mathematical model are summarized next.

2.2.1 Aerodynamic assumptions

1. Aerodynamic coefficients of the main rotor blade sections are provided in the form of look-up tables derived from wind tunnel tests. Lift, drag and moment coefficients are tabulated as a function of angle of attack, for Mach numbers ranging from 0.3 to 1.0 in 0.1 increments. The aerodynamic coefficients vary linearly between angle of attack and Mach number data points.

2. Effects of dynamic stall are not included. Static stall is modeled through table look-up of lift, drag and moment coefficients.

3. A two-dimensional quasi-steady aerodynamics model is used to calculate the main rotor aerodynamics loads. The main rotor inflow is modeled by the He-Peters dynamic inflow model [59]. Tip losses due to 3D effects are approximated by assuming the outboard 3% of the blade to be ineffective aerodynamically.

4. Aerodynamic forces and moments on the blade section are based on airflow velocity at the elastic axis of the blade.

5. The influence of rotor downwash on fuselage and empennage is not modeled.

6. Fuselage and empennage aerodynamics are derived from wind tunnel tests performed without the main rotor. Aerodynamic coefficients are tabulated as functions of angle of attack and sideslip. Stall, compressibility, and unsteady aerodynamic effects are neglected for the fuselage and empennage.

2.2.2 Inertial and structural assumptions

1. The airframe is a rigid body with a constant mass and the $\hat{x}_{hel}$-$\hat{z}_{hel}$ plane is a plane of symmetry.

2. The undeformed blade is straight with no sweep, droop or torque offsets.

3. Flap, lag and pitch hinges when present are coincident.

4. Blade cross sections are symmetric with respect to the major principal axes.

5. The blade cross sectional area centroid and elastic axis are coincident, thus the tension center is also coincident with the elastic axis. However, cross sectional centers of gravity, aerodynamic centers, and elastic axes need not be coincident.

6. Blade chord, built-in twist, stiffness and mass properties, and cross-sectional offsets are defined at discrete spanwise stations, and vary linearly in between.

7. It is assumed that the blades are linearly elastic.

8. All blades have identical mass, stiffness, and geometric properties.

9. Euler-Bernoulli beam theory is used, and thus plane cross sections remain plane and perpendicular to the elastic axis after deforming. Effects of shear deformation are ignored.

10. The blade undergoes small strains and moderate deflections, implying finite rotations.

11. The main rotor operates at a constant angular speed Ω. Engine and engine control system dynamics are not modeled.

12. The blade pitch control system is infinitely stiff. Freeplay in the control linkages is ignored. The swashplate and tail rotor collective controls are attached rigidly to pilot controls.

2.2.3 UH-60A helicopter modeling assumptions

1. The blade is assumed to be rigid in flap, lag and torsion inboard of the flap and lag hinges.

2. The pitch angle of the horizontal stabilizer is fixed for a given flight condition, and control logic for automatic positioning of the stabilizer is not modeled.

2.3 Main Rotor Model

Each rotor blade is modeled as an isotropic Euler-Bernoulli beam undergoing small strains and moderate deflections with coupled nonlinear flap-lag-torsional dynamics. The blade can have both rigid and flexible degrees of freedom (DOFs). The flexible DOFs are discretized using finite elements (FEs). The flap and lag bending DOFs are modeled using cubic Hermite interpolation, and the torsional DOF is based on quadratic Hermite interpolation. The beam elements are assumed to be inextensional, thus eliminating the axial DOF. Each element has 11 DOFs: flap, lag bending displacements and slopes at each end, and torsional deflection at each end and midpoint of the element. The FE DOFs are reduced using a modal transformation. The global aerodynamic, inertial, structural and tensile load vectors $\mathbf{F}_A$, $\mathbf{F}_I$, $\mathbf{F}_S$ and $\mathbf{F}_T$, respectively, are calculated using Gaussian quadrature. For articulated rotors, the effect of lag dampers is modeled as moments acting at the hinge location, represented by the damping load vector $\mathbf{F}_D$. The final rotor equations of motion are

obtained by combining the various load vectors.

2.3.1 Main rotor aerodynamic loads

The aerodynamic load formulation begins with the position vector $\mathbf{R}_p$ of a point P_b on the elastic axis of the blade

$$\mathbf{R}_p = \mathbf{R}_{CG} + \mathbf{R}_H + \mathbf{R}_B, \tag{2.25}$$

where $\mathbf{R}_{CG}$ is the position vector of the vehicle CG with respect to the inertial frame, $\mathbf{R}_H$ is the position vector of the hub relative to the body-fixed frame, and $\mathbf{R}_B$ is the position vector of the point on the elastic axis of the blade, relative to the rotating hub frame. The position vector $\mathbf{R}_H$ is given by

$$\mathbf{R}_H = x_H \hat{\mathbf{i}}_{hel} + y_H \hat{\mathbf{j}}_{hel} + z_H \hat{\mathbf{k}}_{hel}, \tag{2.26}$$

where x_H, y_H and z_H are the components of the position vector from the CG to the hub. The position vector $\mathbf{R}_B$, is given by

$$\mathbf{R}_B = e\hat{\mathbf{i}}_{H_R} + (x_{p0} + u_p)\hat{\mathbf{e}}_x + v_p\hat{\mathbf{e}}_y + w_p\hat{\mathbf{e}}_z, \tag{2.27}$$

where e is the hinge offset from the axis of rotation, $\hat{\mathbf{i}}_{H_R}$ is a unit vector of the hub rotating system and $\hat{\mathbf{e}}_x, \hat{\mathbf{e}}_y$ and $\hat{\mathbf{e}}_z$ are unit vectors of the undeformed, preconed frame. The elastic portion of the blade starts at the hinge, and inboard from this point the blade is assumed rigid. The term x_{p0} is the distance from the hinge location to the point P_b on the elastic axis of the undeformed section and u_p, v_p and w_p are the elastic deflections of the point from the undeformed blade coordinate system. Equation (2.27) is expressed in the undeformed, preconed coordinate system using the transformation in Eq. (2.14) as

$$\mathbf{R}_B = (e\cos\beta_p + x_{p0} + u_p)\hat{\mathbf{e}}_x + v_p\hat{\mathbf{e}}_y + (w_p - \sin\beta_p)\hat{\mathbf{e}}_z, \tag{2.28}$$

where β_p is the blade precone angle.

The absolute velocity $\mathbf{V}_P$ of the point P_b is given by:

$$\mathbf{V}_p = \frac{d\mathbf{R}_P}{dt} = \frac{d\mathbf{R}_{CG}}{dt} + \frac{d\mathbf{R}_H}{dt} + \frac{d\mathbf{R}_B}{dt}. \tag{2.29}$$

where

$$\frac{d\mathbf{R}_{CG}}{dt} = u\hat{\mathbf{i}}_{hel} + v\hat{\mathbf{j}}_{hel} + w\hat{\mathbf{k}}_{hel}, \tag{2.30}$$

$$\frac{d\mathbf{R}_H}{dt} = \frac{\partial \mathbf{R}_H}{\partial t} + \boldsymbol{\omega} \times \mathbf{R}_H, \tag{2.31}$$

$$\frac{d\mathbf{R}_B}{dt} = \frac{\partial \mathbf{R}_B}{\partial t} + \boldsymbol{\omega} \times \mathbf{R}_B, \tag{2.32}$$

and where u, v and w represent the CG velocity components in the body-fixed frame, and $\boldsymbol{\omega}$ is the angular velocity vector of the CG given by

$$\boldsymbol{\omega} = p\hat{\mathbf{i}}_{hel} + q\hat{\mathbf{j}}_{hel} + r\hat{\mathbf{k}}_{hel}, \tag{2.33}$$

with p, q and r representing the roll, pitch and yaw rates, respectively.

The term $\partial \mathbf{R}_H/\partial t$ in Eq. (2.31) is zero since the hub is rigidly connected to the fuselage. The $\partial \mathbf{R}_B/\partial t$ term in Eq. (2.32) is the velocity vector of the blade point as seen by an observer moving with the body-fixed axes, and is given by

$$\frac{\partial \mathbf{R}_B}{\partial t} = \left(\frac{\partial \mathbf{R}_B}{\partial t}\right)_R + \boldsymbol{\Omega} \times \mathbf{R}_B \tag{2.34}$$

where $\left(\frac{\partial \mathbf{R}_B}{\partial t}\right)_R$ is the velocity vector of the point relative to the hub rotating frame and $\boldsymbol{\Omega}$ is the angular velocity vector of the main rotor

$$\boldsymbol{\Omega} = \Omega\hat{\mathbf{k}}_{sh}, \tag{2.35}$$

where Ω is the rotor speed.

The absolute velocity of the point on the elastic axis of the blade in Eq. (2.29) therefore becomes

$$\mathbf{V}_p = \frac{d\mathbf{R}_{CG}}{dt} + \left(\frac{d\mathbf{R}_B}{dt}\right)_R + \Omega \times \mathbf{R}_B + \omega \times [\mathbf{R}_H + \mathbf{R}_B]. \tag{2.36}$$

The total velocity $\mathbf{V}_T$ at the blade section is obtained by subtracting the inflow velocity $\mathbf{V}_I$

$$\mathbf{V}_T = \mathbf{V}_p - \mathbf{V}_I. \tag{2.37}$$

The inflow velocity $\mathbf{V_I}$ is subtracted because it represents the velocity of flow with respect to the blade, as opposed to the velocity of blade point. The absolute velocity $\mathbf{V}_p$ in Eq. (2.36) is expressed in the undeformed, preconed coordinate system as

$$\mathbf{V}_p = V_{11}\hat{\mathbf{e}}_x + V_{12}\hat{\mathbf{e}}_y + V_{13}\hat{\mathbf{e}}_z, \tag{2.38}$$

where V_{11}, V_{12} and V_{13} represent the components of the velocity vector of the point P_b on the blade elastic axis. The inflow velocity $\mathbf{V}_I$ is similarly expressed in the undeformed preconed coordinate system as

$$\mathbf{V}_I = \lambda_x\hat{\mathbf{e}}_x + \lambda_y\hat{\mathbf{e}}_y + \lambda_z\hat{\mathbf{e}}_z \tag{2.39}$$

with $\lambda_x = \lambda_y = 0$ in this study. Using Eqs. (2.38) and (2.39), the total velocity $\mathbf{V}_T$ in Eq. (2.37) is given by

$$\mathbf{V}_T \;=\; V_{11}\hat{\mathbf{e}}_x + V_{12}\hat{\mathbf{e}}_y + (V_{13} - \lambda_z)\hat{\mathbf{e}}_z. \tag{2.40}$$

The velocity vector $\mathbf{V}_T$ represents the total velocity of the blade section as it moves through air. For aerodynamic calculations however, the velocity of air at the blade point is

needed. The expression for $\mathbf{V}_T$ in Eq. (2.40) is thus negated

$$\begin{aligned} \mathbf{V}_{TF} &= -\left[V_{11}\hat{\mathbf{e}}_x + V_{12}\hat{\mathbf{e}}_y + (V_{13} - \lambda_z)\hat{\mathbf{e}}_z\right], & (2.41) \\ &= V_x\hat{\mathbf{e}}_x + V_y\hat{\mathbf{e}}_y + V_z\hat{\mathbf{e}}_z, & (2.42) \end{aligned}$$

and transformed to the blade sectional aerodynamics coordinate system using Eq. (2.23), yielding

$$\mathbf{V}_A = U_T\hat{\mathbf{e}}_T + U_P\hat{\mathbf{e}}_P + U_R\hat{\mathbf{e}}_R, \tag{2.43}$$

where $\mathbf{V}_A$ is the resultant velocity of the airflow at the 1/4-chord location, U_T is positive for flow from the leading edge to the trailing edge, U_P is positive upwards, and U_R is positive radially outwards.

Following a legacy convention from GENHEL [62], a flight simulation program that HeliUM2 is replacing, the flow yaw angle γ_I and angle of attack α_Y at the blade section are determined as

$$\cos(\gamma_I) = \frac{|U_T|}{\sqrt{U_T^2 + U_R^2}}, \tag{2.44}$$

$$\tan(\alpha_Y) = \frac{(U_T\tan(\theta_G) + U_P)\cos(\gamma_I)}{U_T - U_P\tan(\theta_G)\cos^2(\gamma_I)}, \tag{2.45}$$

where θ_G is the total blade section geometric pitch given by

$$\theta_G = \theta_0 + \theta_{1c}\cos(\psi + \Delta_{sp}) + \theta_{1s}\sin(\psi + \Delta_{sp}) + \theta_{TW} + \phi_p, \tag{2.46}$$

and where θ_0 is the blade collective pitch angle, θ_{1c} and θ_{1s} are the lateral and longitudinal cyclic pitch components, respectively, ψ is the blade azimuth angle, Δ_{sp} is the swash plate phase angle, θ_{TW} is the built-in twist at the blade section, and ϕ_p is the elastic twist at the blade section. The swash plate phase angle is an azimuth offset used to correct the phase response of articulated rotor blades with offset hinges [39].

A two-dimensional quasi-steady aerodynamic model is used to compute the aerodynamic loads at the blade point. Lift, drag, and moment coefficients are obtained from table look-up [39] as a function of local Mach number Ma and corrected angle of attack α_T, which is computed using α_Y in Eq. (2.45) as

$$\alpha_T = \alpha_Y \cos(\gamma_I). \tag{2.47}$$

Thus,

$$C_L = C_L(Ma, \alpha_T), \tag{2.48}$$

$$C_D = C_D(Ma, \alpha_T), \tag{2.49}$$

$$C_M = C_M(Ma, \alpha_T). \tag{2.50}$$

The sectional lift force is given by [68]

$$L_p = L_Q + \frac{1}{2} a \rho (bR)^2 V_{p0} \dot{\alpha} \tag{2.51}$$

where a is the lift curve slope, ρ is the air density, b is the nondimensional half-chord length, R is the blade radius, and $\dot{\alpha}$ is the time rate of change of the total blade section pitch angle θ_G from Eq. (2.46). The velocity magnitude of the incoming flow V_{p0} is calculated as

$$V_{p0} = \sqrt{U_T^2 + U_P^2 + U_R^2}, \tag{2.52}$$

and the quasi-steady lift L_Q is given by

$$L_Q = a \rho b R V_{p0}^2 \left[\alpha + \frac{\dot{h}}{V_{p0}} + \frac{\dot{\alpha}}{V_{p0}} (bR - x_A) \right] \tag{2.53}$$

where x_A is the cross sectional aerodynamic center offset from the elastic axis, c is the blade

chord, and $\dot{h}$ is the plunge rate of the point on the blade elastic axis. The term $\alpha + \dfrac{\dot{h}}{V_{p0}}$ represents the angle of attack α_T used to obtain the lift coefficient C_L in Eq. (2.48). Thus, the HeliUM2 implementation of the quasi-steady lift equation is [61]

$$\begin{aligned} L_Q &= a\rho bRV_{p0}^2\left[\alpha_T + \frac{\dot{\alpha}}{V_{p0}}(bR - x_A)\right] \\ &= \rho bRV_{p0}^2\left[\alpha_T a + \frac{a\dot{\alpha}}{V_{p0}}(bR - x_A)\right] \\ &= \rho bRV_{p0}^2\left[C_L + \frac{a\dot{\alpha}}{V_{p0}}(bR - x_A)\right] \\ &= \frac{1}{2}\rho cV_{p0}^2\left[C_L + \frac{a\dot{\alpha}}{V_{p0}}\left(\frac{c}{2} - x_A\right)\right], \end{aligned} \tag{2.54}$$

where $C_L = \alpha_T a$, and $c/2 = bR$.

The blade sectional moment about the elastic axis is given by

$$M_p = \frac{1}{2}C_M\rho V_{p0}^2c^2 + L_Q x_A - \frac{1}{2}a\rho V_{p0}\dot{\alpha}(bR - x_A)(bR)^2 \tag{2.55}$$

The first component represents the steady pitching moment resulting due to C_M from table look-up, the second is due to the quasi-steady lift in Eq. (2.53), and the third represents the non-circulatory pitch damping contribution. Note that the Theodorsen's lift deficiency function $C(k) = 1$ in Eqs. (2.51) and (2.55) [68], and apparent mass terms are not included.

The blade sectional drag force is given by

$$D_p = \frac{1}{2}C_D\rho V_{p0}^2c \tag{2.56}$$

where C_D is obtained from table look-up.

The aerodynamic lift L_p and drag D_p forces in Eqs. (2.51) and (2.56), respectively, are transformed to the local blade sectional aerodynamics coordinate system following a

GENHEL convention as follows:

$$f_T = \frac{1}{V_{p0}} \left[D_p U_T - L_p U_P \cos\gamma_I \right], \tag{2.57}$$

$$f_P = \frac{1}{V_{p0}} \left[L_p \frac{U_T}{\cos\gamma_I} + D_p U_P \right], \tag{2.58}$$

$$f_R = \frac{1}{V_{p0}} \left[D_p U_R - L_p \frac{U_P \cos\gamma_I U_R}{U_T} \right], \tag{2.59}$$

where f_T, f_P and f_R represent the tangential, perpendicular, and radial aerodynamic loads per unit span, along the $\mathbf{e}_T, \mathbf{e}_P$ and $\mathbf{e}_R$ unit vectors, respectively. Similarly, the aerodynamic moment in the blade sectional aerodynamics frame is given by

$$M_p = \frac{1}{2} C_M \rho V_{p0}^2 c^2 + f_P \frac{L_Q}{L} x_A \cos\theta_G + f_T \frac{L_Q}{L} x_A \sin\theta_G - \frac{1}{8} a \rho V_{p0} c^2 \dot{\alpha} \left(\frac{c}{2} - x_A \right). \tag{2.60}$$

The distributed aerodynamic loads are obtained by converting the force components f_P, f_T and f_R to the undeformed preconed blade coordinate system using the inverse of matrix $[T_{AP}]$, shown in Eq. (2.23). The resulting distributed aerodynamic forces are given by

$$\begin{aligned} \mathbf{p}_{\mathrm{A}} &= \left(f_P \cos\zeta \sin\beta - f_T \sin\zeta - f_R \cos\zeta \cos\beta \right) \hat{\mathbf{e}}_x \\ &\quad + \left(f_P \sin\zeta \sin\beta + f_T \cos\zeta - f_R \sin\zeta \cos\beta \right) \hat{\mathbf{e}}_y \\ &\quad + \left(-f_P \cos\beta - f_R \sin\beta \right) \hat{\mathbf{e}}_z \\ &= p_{\mathrm{A}x} \hat{\mathbf{e}}_x + p_{\mathrm{A}y} \hat{\mathbf{e}}_y + p_{\mathrm{A}z} \hat{\mathbf{e}}_z, \end{aligned} \tag{2.61}$$

and the distributed aerodynamic moments by

$$\begin{aligned} \mathbf{q}_{\mathrm{A}} &= \left(-M_p \cos\zeta \cos\beta \right) \hat{\mathbf{e}}_x - \left(M_p \sin\zeta \cos\beta \right) \hat{\mathbf{e}}_y - \left(M_p \sin\beta \right) \hat{\mathbf{e}}_z \\ &= q_{\mathrm{A}x} \hat{\mathbf{e}}_x + q_{\mathrm{A}y} \hat{\mathbf{e}}_y + q_{\mathrm{A}z} \hat{\mathbf{e}}_z. \end{aligned} \tag{2.62}$$

2.3.2 Main rotor inertia loads

The distributed inertial forces and moments are given by

$$\begin{aligned}\mathbf{p}_{\mathrm{I}} &= -\int_{A_b} \rho_b(\mathbf{a}_P + g\hat{\mathbf{k}}_{\mathrm{I}})dA_b \\ &= p_{\mathrm{I}x}\hat{\mathbf{e}}_x + p_{\mathrm{I}y}\hat{\mathbf{e}}_y + p_{\mathrm{I}z}\hat{\mathbf{e}}_z, \qquad (2.63)\\ \mathbf{q}_{\mathrm{I}} &= -\int_{A_b} \rho_b \left[(y_{p0}\hat{\mathbf{e}}'_x + z_{p0}\hat{\mathbf{e}}'_y) \times (\mathbf{a}_P + g\hat{\mathbf{k}}_{\mathrm{I}})\right] dA_b \\ &= q_{\mathrm{I}x}\hat{\mathbf{e}}_x + q_{\mathrm{I}y}\hat{\mathbf{e}}_y + q_{\mathrm{I}z}\hat{\mathbf{e}}_z \qquad (2.64)\end{aligned}$$

where ρ_b is the mass density of the blade, y_{p0} and z_{p0} are coordinates of a generic mass point on the cross section A_b, and $g\hat{\mathbf{k}}_I$ is the contribution due to gravity with $\hat{\mathbf{k}}_I$ being the z-component of the inertial coordinate system described in Section 2.1.1. Note that the contribution due to gravity is usually ignored.

The inertia loads in Eqs. (2.63) and (2.64) depend on the absolute acceleration of the current blade point, $\mathbf{a}_P$ which is calculated by taking time derivatives of the position vector $\mathbf{R}_B$ of the point P_b, given by

$$\mathbf{R}_B = e\hat{\mathbf{i}}_{H_R} + (x_{p0} + u_p)\hat{\mathbf{e}}_x + v_p\hat{\mathbf{e}}_y + w_p\hat{\mathbf{e}}_z \underline{+ y_{p0}\hat{\mathbf{e}}'_y + z_{p0}\hat{\mathbf{e}}'_z}, \qquad (2.65)$$

where the underlined terms represent the distance of the point from the elastic axis.

The position vector $\mathbf{R}_B$ in Eq. (2.65) is expresssed in the undeformed preconed coordinate system using the transformation matrices in Eqs. (2.14) and (2.16)

$$\begin{aligned}\mathbf{R}_B &= \left[(e\cos\beta_p + u_p) + x_0 \underline{+ S_{21}y_{p0} + S_{31}z_{p0}}\right]\hat{\mathbf{e}}_x + \\ &\quad \left[v_p \underline{+ S_{22}y_{p0} + S_{32}z_{p0}}\right]\hat{\mathbf{e}}_y + \left[w_p - \sin\beta_{\mathrm{P}} \underline{+ S_{23}y_{p0} + S_{33}z_{p0}}\right]\hat{\mathbf{e}}_z. \qquad (2.66)\end{aligned}$$

The absolute velocity of the blade point $\mathbf{V}_p$ is that same as that in Eq. (2.29), with the exception of the $\mathbf{R}_B$ vector which is defined in Eq. (2.66). The acceleration of the blade

point $\mathbf{a}_P$ is thus given by

$$\mathbf{a}_P = \frac{d^2\mathbf{R}_{CG}}{dt^2} + \frac{\partial^2\mathbf{R}_B}{\partial t^2} + 2\boldsymbol{\omega} \times \frac{\partial \mathbf{R}_B}{\partial t} + \dot{\boldsymbol{\omega}} \times (\mathbf{R}_B + \mathbf{R}_H) + \boldsymbol{\omega} \times [\boldsymbol{\omega} \times (\mathbf{R}_B + \mathbf{R}_H)], \tag{2.67}$$

where

$$\frac{d^2\mathbf{R}_{CG}}{dt^2} = \dot{u}\hat{\mathbf{i}}_{hel} + \dot{v}\hat{\mathbf{j}}_{hel} + \dot{w}\hat{\mathbf{k}}_{hel}, \tag{2.68}$$

and

$$\frac{\partial^2\mathbf{R}_B}{\partial t^2} = \left(\frac{\partial^2\mathbf{R}_B}{\partial t^2}\right)_R + \dot{\Omega} \times \mathbf{R}_B + 2\Omega \times \left(\frac{\partial \mathbf{R}_B}{\partial t}\right)_R + \Omega \times (\Omega \times \mathbf{R}_B). \tag{2.69}$$

2.3.3 Main rotor structural loads

Each rotor blade is modeled as an isotropic Euler-Bernoulli beam undergoing small strains and moderate deflections with coupled nonlinear flap-lag-torsional dynamics. The strain components for a point on the blade section are given by

$$\epsilon_{xx} = \frac{1}{2}(\mathbf{G}_x \cdot \mathbf{G}_x - 1), \tag{2.70}$$

$$\epsilon_{yy} = \frac{1}{2}(\mathbf{G}_y \cdot \mathbf{G}_y - 1), \tag{2.71}$$

$$\epsilon_{zz} = \frac{1}{2}(\mathbf{G}_z \cdot \mathbf{G}_z - 1), \tag{2.72}$$

$$\epsilon_{xy} = \frac{1}{2}(\mathbf{G}_x \cdot \mathbf{G}_y) = 0, \tag{2.73}$$

$$\epsilon_{xz} = \frac{1}{2}(\mathbf{G}_x \cdot \mathbf{G}_z) = 0, \tag{2.74}$$

$$\epsilon_{yz} = \frac{1}{2}(\mathbf{G}_y \cdot \mathbf{G}_z) = 0, \tag{2.75}$$

where the vectors $\mathbf{G}_x$, $\mathbf{G}_y$ and $\mathbf{G}_z$ represent spatial derivatives of the position vector of a generic point on the deformed blade $\mathbf{R}_B$ in Eq. (2.65). The shear stresses ϵ_{xy}, ϵ_{xz}, and ϵ_{yz} in Eqs. (2.73) to (2.75) are zero due to the Euler-Bernoulli assumption. The expressions

for $\mathbf{G}_x$, $\mathbf{G}_y$ and $\mathbf{G}_z$, assuming a rigid cross section, are given by

$$\begin{aligned}
\mathbf{G}_x = \frac{\partial \mathbf{R}_B}{\partial x} &= (1+u_{p,x})\hat{\mathbf{e}}_x + v_{p,x}\hat{\mathbf{e}}_y + w_{p,x}\hat{\mathbf{e}}_z + \\
&\quad y_{p0}(-\kappa_y \hat{\mathbf{e}}'_x + \tau \hat{\mathbf{e}}'_z) + z_{p0}(-\kappa_z \hat{\mathbf{e}}'_x + \tau \hat{\mathbf{e}}'_y), \qquad (2.76)\\
\mathbf{G}_y = \frac{\partial \mathbf{R}_B}{\partial y} &= \hat{\mathbf{e}}'_y, \qquad (2.77)\\
\mathbf{G}_z = \frac{\partial \mathbf{R}_B}{\partial z} &= \hat{\mathbf{e}}'_z, \qquad (2.78)
\end{aligned}$$

where κ_y and κ_z are the blade curvatures and τ is the elastic twist of the deformed blade section. These, in turn, are given by

$$\begin{aligned}
\kappa_y &= -\hat{\mathbf{e}}'_x \cdot \hat{\mathbf{e}}'_{y,x} = -(S_{11}S_{21,x} + S_{12}S_{22,x} + S_{13}S_{23,x}), \qquad (2.79)\\
\kappa_z &= -\hat{\mathbf{e}}'_x \cdot \hat{\mathbf{e}}'_{z,x} = -(S_{11}S_{31,x} + S_{12}S_{32,x} + S_{13}S_{33,x}), \qquad (2.80)\\
\tau &= -\hat{\mathbf{e}}'_y \cdot \hat{\mathbf{e}}'_{y,x} = -(S_{21}S_{21,x} + S_{22}S_{22,x} + S_{23}S_{23,x}), \qquad (2.81)
\end{aligned}$$

where the S_{ij} operators are given in Eq. (2.16).

The stress-strain relationship for the linearly elastic and isotropic blade is given by

$$\begin{Bmatrix} \sigma_{xx} \\ \sigma_{yy} \\ \sigma_{zz} \\ \sigma_{xy} \\ \sigma_{xz} \\ \sigma_{yz} \end{Bmatrix} = \begin{bmatrix} E & 0 & 0 & 0 & 0 & 0 \\ 0 & E & 0 & 0 & 0 & 0 \\ 0 & 0 & E & 0 & 0 & 0 \\ 0 & 0 & 0 & 2G_s & 0 & 0 \\ 0 & 0 & 0 & 0 & 2G_s & 0 \\ 0 & 0 & 0 & 0 & 0 & 2G_s \end{bmatrix} \begin{Bmatrix} \epsilon_{xx} \\ \epsilon_{yy} \\ \epsilon_{zz} \\ \epsilon_{xy} \\ \epsilon_{xz} \\ \epsilon_{yz} \end{Bmatrix} \qquad (2.82)$$

where E is Young's Modulus, G_s is the shear modulus of the material, and the strains are given in Eqs. (2.70) to (2.75). Following the Euler-Bernoulli hypothesis, flap and lag bending do not contribute to the shear stresses σ_{xy} and σ_{xz} in Eq. (2.82). However, small contributions due to torsion are present [67].

The stress-force relationship is given by

$$\mathbf{F}_{ss} = T_p\hat{\mathbf{e}}'_x + F_{sy}\hat{\mathbf{e}}'_y + F_{sz}\hat{\mathbf{e}}'_z = \int\int_{A_b} \mathbf{t}\, dA_b, \tag{2.83}$$

$$\mathbf{M}_{ss} = M_x\hat{\mathbf{e}}'_x + M_y\hat{\mathbf{e}}'_y + M_z\hat{\mathbf{e}}'_z = \int\int_{A_b} \mathbf{d}\times\mathbf{t}\, dA_b, \tag{2.84}$$

where

$$\mathbf{d} = y_{p0}\hat{\mathbf{e}}'_y + z_{p0}\hat{\mathbf{e}}_z, \tag{2.85}$$

$$\mathbf{t} = \sigma_{xx}\hat{\mathbf{e}}'_x + \sigma_{xy}\hat{\mathbf{e}}'_y + \sigma_{xz}\hat{\mathbf{e}}'_y. \tag{2.86}$$

Equations (2.83) and (2.84) are used to establish force and moment equilibrium expressions for a slender rod [67], from which the structural moment $\mathbf{M}_{ss}$ at the blade point is obtained

$$\mathbf{M}_{ss} = M_T\hat{\mathbf{e}}_\mathbf{x} + M_F\hat{\mathbf{e}}_\mathbf{y} + M_L\hat{\mathbf{e}}_\mathbf{z}, \tag{2.87}$$

where M_T, M_F and M_L represent torsional, flap, and lag structural operators, respectively, and are given by

$$M_T(v_p, w_p, \phi_p) = M_{t1} - M_{t0}, \tag{2.88}$$

$$M_F(v_p, w_p, \phi_p) = M_{f2} - M_{f1}, \tag{2.89}$$

$$M_L(v_p, w_p, \phi_p) = M_{l2} - M_{l1}, \tag{2.90}$$

with

$$M_{t1} = GJ\left(\phi_{p,x} + v_{p,xx}w_{p,x}\right), \tag{2.91}$$

$$M_{t0} = -\frac{1}{2}\left(EI_2 - EI_3\right)\sin 2\theta_G\left(v^2_{p,xx} - w^2_{p,xx}\right) + \left(EI_2 - EI_3\right)\cos 2\theta_G\left(v_{p,xx} + 2\phi_p w_{p,xx}\right), \tag{2.92}$$

$$M_{f2} = \left(EI_2 - EI_3\right)\sin 2\theta_G\left(v_{p,xx} + 2\phi_p w_{p,xx}\right) + \left(EI_2 - EI_3\right)\cos 2\theta_G\phi_p v_{p,xx} +$$

$$\left(EI_2 \sin^2\theta_G + EI_3 \cos^2\theta_G\right) w_{p,xx}, \tag{2.93}$$

$$M_{f1} = GJ\phi_{p,x} v_{p,xx}, \tag{2.94}$$

$$M_{l2} = \left(EI_2 \cos^2\theta_G + EI_3 \sin^2\theta_G\right) v_{p,xx} + (EI_2 - EI_3) \sin 2\theta_G \left(w_{p,xx} + 2\phi_p v_{p,xx}\right) + (EI_2 - EI_3) \cos 2\theta_G \phi_p w_{,pxx}, \tag{2.95}$$

$$M_{l1} = GJ\phi_{p,x} w_{p,xx}. \tag{2.96}$$

The quantities EI_2, EI_3 and GJ represent flap bending, lag bending and torsional stiffnesses, respectively. The subscripts 0, 1, and 2 indicate the number of times the structural moment operators in Eqs. (2.91) to (2.96) have to be integrated by parts. Note that Eqs. (2.91) to (2.96) were derived using an ordering scheme [67].

2.3.4 Main rotor tensile loads

Similar to the components of the stuctural moment in Eq. (2.87), the tension-induced loads are based on the equations of equilibrium of a deformed rod [67], and are given by

$$\mathbf{p}_T = T_p S_{12} \hat{\mathbf{e}}_y + T_p S_{13} \hat{\mathbf{e}}_z, \tag{2.97}$$

where T_p is the tension along the $\hat{\mathbf{e}}_x$ unit vector, and S_{12} and S_{13} are elements of the transformation matrix from the undeformed preconed frame to the deformed preconed frame given in Eq. (2.16). Since the blades are assumed to be inextensional, axial dynamics along $\hat{\mathbf{e}}_x$ are not considered. Note that the components of $\mathbf{p}_T$ in Eq. (2.97) have to integrated by parts once to yield the actual tensile forces [67].

2.3.5 Main rotor lag damper loads

A lag damper model based on the actual lag damper of a UH-60A helicopter [39] is employed in this study. Loads generated by the lag damper are dependent on the rate of

change of the relative position of the damper's pick-up, which refers to the location where the damper connects with the blade. For a flexible blade, an effective flap and lag angle is defined, based on the location of the lag damper pick-up

$$\delta_{flap} = \frac{w_{LD}}{x_{LD}}, \tag{2.98}$$

$$\delta_{lag} = \frac{v_{LD}}{x_{LD}}, \tag{2.99}$$

where x_{LD} is the span location of the lag damper pick-up and w_{LD} and v_{LD} are the elastic deflections at the lag damper pick-up.

The moments about the blade flapping and lagging hinges are given by:

$$M_{LD\beta} = -\frac{F_{LD}}{|\mathbf{r}_{LD}|}\left(r_{LDz}d_3 + r_{LDx}d_5\sin\theta_{LD}\right), \tag{2.100}$$

$$M_{LD\zeta} = -\frac{F_{LD}}{|\mathbf{r}_{LD}|}\left[d_5\cos\theta_{LD}\left(r_{LDx}\cos\delta_{flap} - r_{LDz}\sin\delta_{flap}\right) + r_{LDy}\left(d_3\cos\delta_{flap} + d_5\sin\theta_{LD}\sin\delta_{flap}\right)\right], \tag{2.101}$$

where F_{LD} represents the axial damping force, which is a nonlinear function of the rate of change of extension or contraction of the lag damper [39], and is given by

$$F_{LD} = F_{LD}\left(|\dot{\mathbf{r}}_{LD}|\right). \tag{2.102}$$

The position vector of the lag damper pick-up, relative to the shaft coordinate system described in Section 2.1.4, is given as

$$\mathbf{r}_{LD} = \left\{ \begin{array}{c} r_{LDx} \\ r_{LDy} \\ r_{LDz} \end{array} \right\}, \tag{2.103}$$

where

$$
\begin{aligned}
r_{LDx} &= d_1 \sin\delta_{flap} + d_2 \cos\left(\delta_{lag}+\delta_0\right)\cos\delta_{flap} + d_3 + d_4 \sin\left(\delta_{lag}+\delta_0\right)\cos\delta_{flap}, \\
r_{LDy} &= -d_5 \cos\theta_{LD} - d_2 \sin\left(\delta_{lag}+\delta_0\right) + d_4 \cos\left(\delta_{lag}+\delta_0\right), \\
r_{LDz} &= d_1 \cos\delta_{flap} - d_5 \sin\theta_{LD} - d_2 \sin\delta_{flap}\cos\left(\delta_{lag}+\delta_0\right) \\
&\quad -d_4 \sin\delta_{flap}\sin\left(\delta_{lag}+\delta_0\right), \qquad (2.104)
\end{aligned}
$$

and where δ_0, d_1, d_2, d_3, d_4 and d_5 are lag damper geometry constants, and δ_{flap} and δ_{lag} are the effective flap and lag angles of the blade from Eqs. (2.98) and (2.99), respectively. The lag damper pitch angle, θ_{LD} is given by

$$\theta_{LD} = \theta_0 + \theta_{1c}\cos\psi + \theta_{1s}\sin\psi + \theta_{GLD}, \qquad (2.105)$$

where θ_0, θ_{1c} and θ_{1s} are control input angles and θ_{GLD} is an additional lag damper geometry constant.

The effect of the lag damper is considered to be the application of a pure moment at the root of the blade where the hinge is loacted. The moment $\mathbf{M}_D$ generated by the damper is given by

$$\mathbf{M}_D = M_{Dx}\hat{\mathbf{e}}_x + M_{Dy}\hat{\mathbf{e}}_y + M_{Dz}\hat{\mathbf{e}}_z, \qquad (2.106)$$

where the individual components are obtained after transforming the expressions in Eqs. (2.100) and (2.101) from the shaft coordinate system to the undeformed, preconed coordinate system.

2.3.6 Finite element discretization

Blade flexible DOFs are discretized using FEs. The blade loads described in the previous sections are nonlinear partial differential equations (PDEs). A finite element procedure

based on the Galerkin method of weighted residuals [69] is implemented to transform the equations to ODEs, which are subsequently coupled with the rest of the flight dynamic model. The Galerkin FE method allows for the spatial discretization of the governing PDEs directly, without resorting to energy based approaches which can require a significant amount of algebraic manipulations [69]. The method is combined with the HeliUM2 implicit formulation to obtain the governing nonlinear blade equations of motion.

2.3.6.1 Beam finite element model

Each blade is divided into N_e finite elements, each with 11 degrees of freedom: flap and lag bending displacements and slopes at each end of the element, and torsional deflection at the two ends and midpoint of the element, represented symbolically as

$$\mathbf{y}_i = \begin{bmatrix} \mathbf{y}_v \\ \mathbf{y}_w \\ \mathbf{y}_\phi \end{bmatrix}, \tag{2.107}$$

where

$$\mathbf{y}_v = \{v_{p0}, v_{p0,x}, v_{p1}, v_{p1,x}\}^T, \tag{2.108}$$

$$\mathbf{y}_w = \{w_{p0}, w_{p0,x}, w_{p1}, w_{p1,x}\}^T, \tag{2.109}$$

$$\mathbf{y}_\phi = \{\phi_{p0}, \phi_{p\frac{1}{2}}, \phi_{p1}\}^T, \tag{2.110}$$

with v_p, w_p and ϕ_p representing the lag, flap and torsional deflections at the nodes, respectively, "$,x$" terms representing slopes of the deflections, and "0", "$1/2$" and "1" representing the start tip, midpoint and end tip of the element, respectively. Axial DOF is not modeled.

The deflections and slopes at any spanwise location x_e within the element are computed

using Hermite interpolation polynomials, given, for flap and lag bending, by

$$\mathbf{H}_v(x_e) = \mathbf{H}_w(x_e) = \left\{ \begin{array}{c} 1 - 3\eta_x^2 + 2\eta_x^3 \\ \eta_x(1 - 2\eta_x + \eta_x^2)l \\ 3\eta_x^2 - 2\eta_x^3 \\ \eta_x(-\eta_x + \eta_x^2)l \end{array} \right\}^T , \tag{2.111}$$

and for torsion by

$$\mathbf{H}_\phi(x_e) = \left\{ \begin{array}{c} 1 - 3\eta_x + 2\eta_x^2 \\ 4\eta_x - 4\eta_x^2 \\ -\eta_x + 2\eta_x^2 \end{array} \right\}^T , \tag{2.112}$$

where l is the length of the element, and $\eta_x = x_e/l$.

The deflections at location x_e are calculated as

$$v_p(x_e) = \mathbf{H}_v(x_e)\mathbf{y}_v(t) \tag{2.113}$$

$$w_p(x_e) = \mathbf{H}_w(x_e)\mathbf{y}_w(t) \tag{2.114}$$

$$\phi_p(x_e) = \mathbf{H}_\phi(x_e)\mathbf{y}_\phi(t) \tag{2.115}$$

where $\mathbf{y}_v$, $\mathbf{y}_w$ and $\mathbf{y}_\phi$ are the nodal lag, flap and torsional deflection and slope vectors from Eq. (2.107). Spatial and temporal derivatives of the deflections at x_e are readily obtained using Eqs. (2.113) to (2.115), which employ separation of variables.

Using the Hermite polynomials, the nodal inertia load vector associated with the ith element is calculated as

$$\mathbf{p}_{\mathrm{I}i} = \int_0^{l_i} \left\{ \begin{array}{c} p_{\mathrm{I}y}\mathbf{H}_v(x_e) \\ p_{\mathrm{I}z}\mathbf{H}_w(x_e) \\ q_{\mathrm{I}x}\mathbf{H}_\phi(x_e) \end{array} \right\} dx \tag{2.116}$$

where $p_{\mathrm{I}y}$, $p_{\mathrm{I}z}$ and $q_{\mathrm{I}x}$ are components of the distributed inertial loads $\mathbf{p}_{\mathrm{I}}$ and $\mathbf{q}_{\mathrm{I}}$ defined in Eqs. (2.63) and (2.64) in Section 2.3.2. The nodal aerodynamic, structural, tensile and

damping load vectors, $\mathbf{p}_{\mathrm{A}i}$, $\mathbf{p}_{\mathrm{S}i}$, $\mathbf{p}_{\mathrm{T}i}$, and $\mathbf{p}_{\mathrm{D}_i}$, respectively, are obtained in a similar manner. Note that the integrations are performed using Gaussian weighted summation [70] in the HeliUM2 code.

2.3.6.2 Assembly of global load vectors

The global aerodynamic, inertial, structural, tensile, and damping nodal load vectors $\mathbf{F}_A$, $\mathbf{F}_I$, $\mathbf{F}_S$, $\mathbf{F}_T$ and $\mathbf{F}_D$, respectively, are obtained using the conventional FE assembly procedure [70], described next.

A blade with $N_e = 4$ FEs is shown in Fig. 2.7. There are $N_{dof} = 5N_{st} + N_e = 29$ DOFs in the blade, with elements 1-2, 2-3, and 3-4 sharing the $\{v_{p1}, v_{p1,x}, w_{p1}, w_{p1,x}, \phi_{p1}\}$, $\{v_{p2}, v_{p2,x}, w_{p2}, w_{p2,x}, \phi_{p2}\}$, and $\{v_{p3}, v_{p3,x}, w_{p3}, w_{p3,x}, \phi_{p3}\}$ DOFs, respectively. The DOFs are assembled in a global vector $\mathbf{y}_n$ as

$$\mathbf{y}_n = \begin{bmatrix} \mathbf{v}_n \\ \mathbf{w}_n \\ \phi_n \end{bmatrix}, \tag{2.117}$$

where

$$\mathbf{v}_n = \{v_{p0}, v_{p0,x}, v_{p1}, v_{1,x}, \ldots, v_{pN_e}, v_{pN_e,x}\}^T, \tag{2.118}$$

$$\mathbf{w}_n = \{w_{p0}, w_{p0,x}, w_{p1}, w_{p1,x}, \ldots, w_{pN_e}, w_{pN_e,x}\}^T, \tag{2.119}$$

$$\phi_n = \{\phi_{p0}, \phi_{p\frac{1}{2}}, \phi_{p1}, \ldots, \phi_{pN_e}\}^T. \tag{2.120}$$

The global load vectors are expressed in a similar form to the DOFs in Eq. (2.117). For

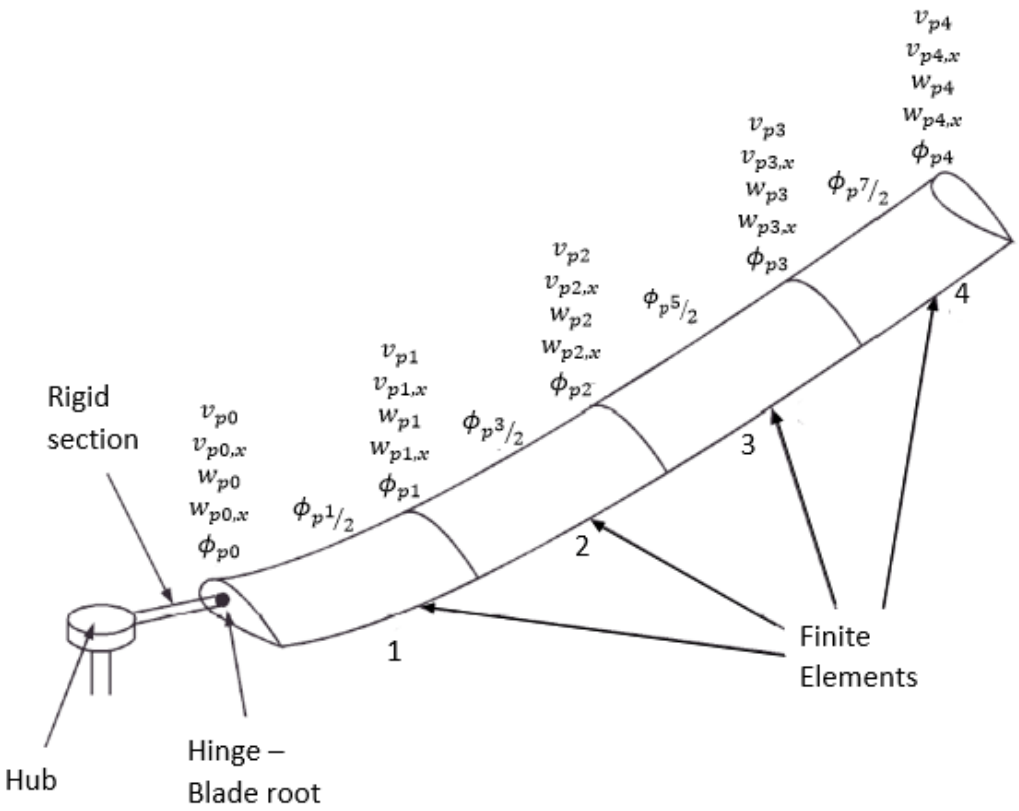

Figure 2.7: DOFs of blade with four FEs; adapted from Fig. 1.15 of [61].

example, the global aerodynamic load vector is given by

$$\mathbf{F}_A = \left\{ \begin{array}{c} \mathbf{F}_{A_v} \\ \mathbf{F}_{A_w} \\ \mathbf{F}_{A_\phi} \end{array} \right\}, \tag{2.121}$$

where $\mathbf{F}_{A_v}$, $\mathbf{F}_{A_w}$ and $\mathbf{F}_{A_\phi}$ contain the aerodynamic loads corresponding to $\mathbf{v}_n$, $\mathbf{w}_n$ and ϕ_n, respectively.

2.3.7 Rotating blade mode shapes

The blade mode shapes and corresponding natural frequencies are calculated using the rotating blade *in vacuo*. The blade governing equations in this case are given by

$$[K]\,\mathbf{y}_n = \omega_n^2\,[M]\,\mathbf{y}_n, \tag{2.122}$$

where $[M]$ is the blade mass matrix, $[K]$ is the blade stiffness matrix and $\mathbf{y}_n$ is the vector of nodal displacements from Eq. (2.117). The $[M]$ and $[K]$ in Eq. (2.122) are calculated using finite difference approximation.

The mass matrix is obtained using the global inertial load vector $\mathbf{F}_{\mathrm{I}}$, which is represented symbolically as $\mathbf{F}_{\mathrm{I}}(\ddot{\mathbf{y}}_n, \dot{\mathbf{y}}_n, \mathbf{y}_n)$, where $\dot{\mathbf{y}}_n$ and $\ddot{\mathbf{y}}_n$ are, respectively, the first and second time derivatives of the global vector of DOFs $\mathbf{y}_n$ given in Eq. (2.117). Taking advantage of the implicit formulation employed in HeliUM2, the ith column of the mass matrix is calculated as

$$\mathbf{M}_i = \frac{\mathbf{F}_{\mathrm{I}}(\ddot{\mathbf{y}}_i, \mathbf{0}, \mathbf{0}) - \mathbf{F}_{\mathrm{I}}(\mathbf{0}, \mathbf{0}, \mathbf{0})}{\delta_{pert}}, \tag{2.123}$$

where $\ddot{\mathbf{y}}_i = \delta_{pert}\ \mathbf{e}_i$, δ_{pert} is the perturbation size, and $\mathbf{e}_i$ is a unit vector with the only nonzero element in the ith row. The complete mass matrix is obtained by successively perturbing each element of the nodal acceleration vector.

The stiffness matrix is obtained using the structural, inertial and tension load vectors $\mathbf{F}_S$, $\mathbf{F}_I$, and $\mathbf{F}_T$, respectively. The ith column of the stiffness matrix is obtained by perturbing the ith component of the nodal vector $\mathbf{y}_n$ as follows

$$\begin{aligned}\mathbf{K}_i \;=\; & \frac{\mathbf{F}_{\mathrm{I}}(\mathbf{0}, \mathbf{0}, \mathbf{y}_i) - \mathbf{F}_{\mathrm{I}}(\mathbf{0}, \mathbf{0}, \mathbf{0})}{\delta_{pert}} + \frac{\mathbf{F}_{\mathrm{S}}(\mathbf{0}, \mathbf{0}, \mathbf{y}_i) - \mathbf{F}_{\mathrm{S}}(\mathbf{0}, \mathbf{0}, \mathbf{0})}{\delta_{pert}} \\ & + \frac{\mathbf{F}_{\mathrm{T}}(\mathbf{0}, \mathbf{0}, \mathbf{y}_i) - \mathbf{F}_{\mathrm{T}}(\mathbf{0}, \mathbf{0}, \mathbf{0})}{\delta_{pert}}.\end{aligned} \tag{2.124}$$

The blade mode shapes are calculated by solving the eigen problem given in Eq. (2.3.7).

All eigenvectors contain a combination of flap, lag and torsion. This is due to the elastic coupling. In this study however, each mode will be referred as a flap, lag or torsion mode, depending on which one is dominant at the blade tip.

2.3.8 Modal coordinate transformation

The vector $\mathbf{y}_n$ in Eq. (2.117) contains $N_{dof} = 5N_{st} + N_e$ DOFs. A modal transformation is employed to reduce the number of DOFs. The vector is projected onto a modal space as follows:

$$\mathbf{y}_n = [V]\mathbf{q}, \tag{2.125}$$

where $[V]$ is the modal coordinate transformation matrix whose columns contain the rotating mode shapes of the blade, and $\mathbf{q}$ is the vector of generalized coordinates in modal space. Note that $[V]$ has dimensions $N_{dof} \times N_m$, where N_m is the number of modes retained for the transformation, with $N_m \ll N_{dof}$. The vector of generalized coordinates $\mathbf{q}$ becomes the unknown of the problem. The number of unknowns effectively reduces form N_{dof} to N_m for each blade.

2.3.9 Main rotor equations of motion

The final rotor equations of motion are obtained by combining the global vectors $\mathbf{F}_A$, $\mathbf{F}_I$, $\mathbf{F}_S$, $\mathbf{F}_T$ and $\mathbf{F}_D$. The vectors are first transformed into modal load vectors using the same modal coordinate transformation used to reduce the number of degrees of freedom [61]

$$\mathbf{F}_{\mathrm{A}m} = [V]^{\mathrm{T}} \mathbf{F}_{\mathrm{A}}, \tag{2.126}$$

$$\mathbf{F}_{\mathrm{I}m} = [V]^{\mathrm{T}} \mathbf{F}_{\mathrm{I}}, \tag{2.127}$$

$$\mathbf{F}_{\mathrm{S}m} = [V]^{\mathrm{T}} \mathbf{F}_{\mathrm{S}}, \tag{2.128}$$

$$\mathbf{F}_{\mathrm{T}m} = [V]^{\mathrm{T}} \mathbf{F}_{\mathrm{T}}, \tag{2.129}$$

$$\mathbf{F}_{\mathrm{D}m} = [V]^{\mathrm{T}} \mathbf{F}_{\mathrm{D}}. \tag{2.130}$$

The transformed load vectors are subsequently summed, yielding the ODEs representing blade dynamics [61]

$$\mathbf{F}_{\mathrm{A}} + \mathbf{F}_{\mathrm{I}} + \mathbf{F}_{\mathrm{S}} + \mathbf{F}_{\mathrm{T}} + \mathbf{F}_{\mathrm{D}} = \mathbf{0}. \tag{2.131}$$

The total number of equations is obtained by multiplying the number of blades N_b by the number of mode shapes in the modal transformation N_m.

2.4 Fuselage Equations of Motion

The fuselage has 6 rigid body DOFs, where fuselage rotations are represented by Euler angles. The mathematical model represents the six force and moment equations of equilibrium, expressed in the body-fixed frame described in Section 2.1.2,

$$X = m\dot{u} + m(qw - rv) + mg\sin\theta_f, \tag{2.132}$$

$$Y = m\dot{v} + m(ru - pw) + mg\cos\theta_f\sin\phi_f, \tag{2.133}$$

$$Z = m\dot{w} + m(pv - qu) - mg\cos\theta_f\cos\phi_f, \tag{2.134}$$

$$L = I_{xx}\dot{p} - I_{xy}\dot{q} - I_{xz}\dot{r} - I_{yz}(q^2 - r^2) - I_{xz}pq + I_{xy}pr - (I_{yy} - I_{zz})qr, \tag{2.135}$$

$$M = I_{yy}\dot{q} - I_{xy}\dot{p} - I_{yz}\dot{r} - I_{xz}(r^2 - p^2) - I_{xy}qr + I_{yz}pq - (I_{zz} - I_{xx})pr, \tag{2.136}$$

$$N = I_{zz}\dot{r} - I_{xz}\dot{p} - I_{yz}\dot{q} - I_{xy}(p^2 - q^2) - I_{yz}pr + I_{xz}qr - (I_{xx} - I_{yy})pq, \tag{2.137}$$

combined with the appropriate kinematic relations

$$\dot{\phi}_f = p + q\tan\theta_f\sin\phi_f + r\tan\theta_f\cos\phi_f, \tag{2.138}$$

$$\dot{\theta}_f = q\cos\phi_f - r\sin\phi_f, \tag{2.139}$$

$$\dot{\psi}_f = r\frac{\cos\phi_f}{\cos\theta_f} + q\frac{\sin\phi_f}{\cos\theta_f}. \tag{2.140}$$

The force and moment components on the left hand side of Eqs. (2.132) to (2.137) are the externally applied loads at the CG, while the right hand side represents inertial forces and moments due to the rigid body motion of the fuselage in response to the applied loads.

The applied forces and moments are the sum of contributions from the main rotor, tail rotor, fuselage and empennage and are given by

$$X = X_{MR} + X_{TR} + X_F + X_V + X_H, \tag{2.141}$$

$$Y = Y_{MR} + Y_{TR} + Y_F + Y_V + Y_H, \tag{2.142}$$

$$Z = Z_{MR} + Z_{TR} + Z_F + Z_V + Z_H, \tag{2.143}$$

$$L = L_{MR} + L_{TR} + L_F + L_V + L_H, \tag{2.144}$$

$$M = M_{MR} + M_{TR} + M_F + M_V + M_H, \tag{2.145}$$

$$N = N_{MR} + N_{TR} + N_F + N_V + N_H, \tag{2.146}$$

where the subscript MR denotes the main rotor, TR the tail rotor, F the fuselage, H the horizontal tail, and V the vertical tail loads.

The following subsections describe the components of the external forces and moments that appear in Eqs. (2.141) through (2.146).

2.4.1 Main rotor loads

The contributions from the main rotor to the fuselage loads consists of the sum of the distributed aerodynamic and inertial loads, integrated along the span of the blade. The integrated loads are formulated in the undeformed, preconed coordinate system described in Section 2.1.7. These forces and moments are given by

$$\mathbf{F}_R = \int_e^1 (\mathbf{p}_\mathrm{A} + \mathbf{p}_\mathrm{I}) dx_0, \tag{2.147}$$

$$\mathbf{M}_R = \int_e^1 (\mathbf{q}_\mathrm{A} + \mathbf{q}_\mathrm{I}) dx_0 + \int_e^1 \mathbf{R}_C \times (\mathbf{p}_\mathrm{A} + \mathbf{p}_\mathrm{I}) dx_0 + \mathbf{M}_\mathrm{D}, \tag{2.148}$$

where $\mathbf{p}_{\mathrm{A}}$, $\mathbf{p}_{\mathrm{I}}$, $\mathbf{q}_{\mathrm{A}}$, $\mathbf{q}_{\mathrm{I}}$ and $\mathbf{M}_{\mathrm{D}}$ are defined by Eqs. (2.61), (2.63), (2.62), (2.64) and (2.106), respectively, and e is the hinge offset. The position vector $\mathbf{R}_C$ contains the position coordinates of the deflected elastic axis from the offset hinge, and is given by

$$\mathbf{R}_C = x_{p0}\hat{\mathbf{e}}_x + u_p\hat{\mathbf{e}}'_x + v_p\hat{\mathbf{e}}'_y + w_p\hat{\mathbf{e}}'_z. \tag{2.149}$$

The main rotor loads are transformed to equivalent loads at the CG in the body-fixed frame. For a single rotor blade, the forces are [61]

$$\begin{aligned}\mathbf{F}_{MR} &= \left\{\begin{array}{c} X_{MR} \\ Y_{MR} \\ Z_{MR} \end{array}\right\} \\ &= [T_{ShB}]^{-1}[T_{H_{NR}Sh}]^{-1}[T_{H_RH_{NR}}]^{-1}[T_{PH_R}]^{-1} \times \left\{\begin{array}{c} \int_e^1 (p_{\mathrm{A}x} + p_{\mathrm{I}x})dx_0 \\ \int_e^1 (p_{\mathrm{A}y} + p_{\mathrm{I}y})dx_0 \\ \int_e^1 (p_{\mathrm{A}z} + p_{\mathrm{I}z})dx_0 \end{array}\right\},\end{aligned} \tag{2.150}$$

where the transformation matrices $[T_{ShB}]$, $[T_{H_{NR}Sh}]$, $[T_{H_RH_{NR}}]$, and $[T_{PH_R}]$ are defined in Eqs. (2.8), (2.10), (2.12), and (2.14), respectively.

For an articulated rotor configuration, flap and lag moments due to distributed aerodynamic and inertia loads are not transferred through the hinge. The moment vector at the CG for a single blade is given by [61]

$$\begin{aligned}\mathbf{M}_{MR} &= \left\{\begin{array}{c} L_{MR} \\ M_{MR} \\ N_{MR} \end{array}\right\} \\ &= [T_{ShB}]^{-1}[T_{H_{NR}Sh}]^{-1}[T_{H_RH_{NR}}]^{-1}[T_{PH_R}]^{-1} \left\{\begin{array}{c} M_{\mathrm{D}x} \\ M_{\mathrm{D}y} \\ \int_0^1 (q_{\mathrm{A}z} + q_{\mathrm{I}z})dx_0 + M_{\mathrm{D}z} \end{array}\right\} \\ &+ [T_{ShB}]^{-1}[T_{H_{NR}Sh}]^{-1}[T_{H_RH_{NR}}]^{-1}[T_{PH_R}]^{-1} \{\mathbf{R}_e \times \mathbf{F}_R\} \\ &+ \mathbf{R}_H \times \mathbf{F}_{MR}.\end{aligned} \tag{2.151}$$

The first term in Eq. (2.151) represents the contribution from the distributed moments at the various blade sections. The second term introduces contributions due to the hinge offset from the hub. The position vector from the hub to the hinge $\mathbf{R}_e$ is given by

$$\mathbf{R}_e = e\hat{\mathbf{i}}_{H_{NR}}. \tag{2.152}$$

The final term in Eq. (2.151) transforms the forces at the hub into moments at the CG using the position vector of the hub relative to the CG, $\mathbf{R}_H$, defined in Eq. (2.26).

2.4.2 Fuselage aerodynamic loads

Aerodynamic loads on the fuselage are based on empirical coefficients obtained from table look-up [39]. The coefficients are specific to the UH-60A helicopter and are assumed to act at a specified point referred to as the "aerodynamic center" (AC). The freestream velocities at the AC are given by

$$\mathbf{V}_F = \mathbf{V}_{CG}, \tag{2.153}$$

where $\mathbf{V}_{CG}$ is the velocity vector of the CG with components u, v, w along the body-fixed frame. Note that main rotor downwash is not accounted for in Eq. (2.153). Furthermore, the offset between the CG and AC is assumed to be small and thus, angular rate velocities due to the offset are not included.

The dynamic pressure at the AC is given by

$$q_F = \frac{1}{2}\rho(u^2 + v^2 + w^2), \tag{2.154}$$

where ρ is the air density.

The components of the velocity vector $\mathbf{V}_F$ in Eq. (2.153) are used to determine the

fuselage angle of attack α_f and sideslip angle β_f as follows:

$$\alpha_f = \tan^{-1}\frac{w}{|u|}, \tag{2.155}$$

$$\beta_f = \tan^{-1}\frac{v}{\sqrt{v^2+w^2}}. \tag{2.156}$$

Nonlinear aerodynamic coefficients, defined in the wind coordinate system described in Section 2.1.3, are obtained from table look-up as a function of α_f and β_f.

The fuselage aerodynamic loads in the wind axes system are given by [61]

$$\mathbf{F}_{wF} = -q_F C_{Df}\hat{\mathbf{i}}_{\mathrm{W}} - q_F C_{Yf}\hat{\mathbf{j}}_{\mathrm{W}} - q_F C_{Lf}\hat{\mathbf{k}}_{\mathrm{W}}, \tag{2.157}$$

$$\mathbf{M}_{wF} = q_F C_{Rf}\hat{\mathbf{i}}_{\mathrm{W}} - q_F C_{Mf}\hat{\mathbf{j}}_{\mathrm{W}} + q_F C_{Nf}\hat{\mathbf{k}}_{\mathrm{W}}, \tag{2.158}$$

where the lift, drag and lateral force coefficients C_{Lf}, C_{Df}, and C_{Yf}, respectively, have units of ft^2, while the rolling, pitching and yawing moment coefficients C_{Rf}, C_{Mf}, and C_{Nf}, respectively, have units of ft^3 [39].

The forces and moments due to the fuselage aerodynamics, when resolved at the CG, are given by

$$\mathbf{F}_F = \begin{Bmatrix} X_F \\ Y_F \\ Z_F \end{Bmatrix} = [T_{WB}]^{-1}\mathbf{F}_{wF} = [T_{WB}]^{-1}\begin{Bmatrix} -q_F C_{Df} \\ -q_F C_{Yf} \\ -q_F C_{Lf} \end{Bmatrix}, \tag{2.159}$$

and

$$\mathbf{M}_F = \begin{Bmatrix} L_F \\ M_F \\ N_F \end{Bmatrix} = [T_{WB}]^{-1}\mathbf{M}_{wF} + \mathbf{x}_{FAC} \times \mathbf{F}_F, \tag{2.160}$$

where $[T_{WB}]$ is the transformation matrix from the body-fixed frame to the wind frame given in Eq. (2.6), and $\mathbf{x}_{FAC}$ is the position vector of the fuselage AC relative to the CG.

2.4.3 Empennage aerodynamic loads

The empennage consists of horizontal and vertical tail surfaces. The aerodynamic load formulation is based on empirical aerodynamic coefficients obtained from table look-up [39]. The coefficients are specific to the UH-60A helicopter and were determined from wind tunnel tests of isolated tail surfaces. The load formulation requires the velocities at the centers of pressure (COPs) of the surfaces

$$\mathbf{V}_H = K_H \mathbf{V}_{CG} + \omega \times \mathbf{x}_H, \tag{2.161}$$

$$\mathbf{V}_V = K_V \mathbf{V}_{CG} + \omega \times \mathbf{x}_V, \tag{2.162}$$

where K_H and K_V are empirical factors that define the extent of dynamic pressure losses at the horizontal and vertical tails, respectively, $\mathbf{x}_H$ and $\mathbf{x}_V$ are the positions vectors of the COPs, and ω is the vector of CG angular rates with components p, q, r. Note that sidewash and downwash contributions from the main rotor and fuselage are not included in Eqs. (2.161) and (2.162).

The dynamic pressure at the horizontal and vertical tail surfaces are

$$q_H = \frac{1}{2}\rho(u_H^2 + v_H^2 + w_H^2), \tag{2.163}$$

$$q_V = \frac{1}{2}\rho(u_V^2 + v_V^2 + w_V^2), \tag{2.164}$$

where u_H, v_H, w_H and u_V, v_V, w_V are the components of the velocity vectors $\mathbf{V}_H$ and $\mathbf{V}_V$ defined in Eqs. (2.161) and (2.162), respectively.

The velocities in Eqs. (2.161) and (2.162) are used to determine the angles of attack and sideslip of the tail surfaces as follows:

$$\alpha_H = \tan^{-1}\frac{w_H}{|u_H|} + \theta_{0H}, \tag{2.165}$$

$$\beta_H = \tan^{-1}\frac{v_H}{\sqrt{v_H^2 + w_H^2}}, \tag{2.166}$$

$$\alpha_V = \tan^{-1}\frac{w_V}{|u_V|}, \tag{2.167}$$

$$\beta_V = \tan^{-1}\frac{v_V}{\sqrt{v_V^2+w_V^2}} + \theta_{0V},, \tag{2.168}$$

where θ_{0H} and θ_{0V} are the initial angles of incidence of the horizontal and vertical tail surfaces, respectively. The angles in Eqs. (2.165) to (2.168) are, in turn, used to obtain the nondimensional lift and drag coefficients of the tail surfaces from table look-up.

The aerodynamic loads at the tail surfaces are obtained using the dynamic pressure expressions in Eqs. (2.163) and (2.164) and the coefficients from table look-up [61],

$$\mathbf{F}_{wH} = -q_H C_{DH} S_H \hat{\mathbf{i}}_H - q_H C_{LH} S_H \hat{\mathbf{k}}_H, \tag{2.169}$$

$$\mathbf{F}_{wV} = -q_V C_{DV} S_V \hat{\mathbf{i}}_V - q_V C_{LV} S_V \hat{\mathbf{k}}_V, \tag{2.170}$$

where S_H and S_V are the surface areas of horizontal and vertical tail, respectively.

The forces in Eqs. (2.169) and (2.170) are defined in local wind coordinate systems and need to be transformed to the body fixed frame. The transformation from the horizontal tail wind coordinate system, with unit vectors $(\hat{\mathbf{i}}_H, \hat{\mathbf{j}}_H, \hat{\mathbf{k}}_H)$, to the body-fixed frame is given by

$$[T_{HB}] = \begin{bmatrix} \cos(\alpha_H - \theta_{0H})\cos\beta_H & \cos(\alpha_H - \theta_{0H})\sin\beta_H & -\sin(\alpha_H - \theta_{0H}) \\ \sin\beta_H & -\cos\beta_H & 0 \\ \sin(\alpha_H - \theta_{0H})\cos\beta_H & \sin(\alpha_H - \theta_{0H})\sin\beta_H & \cos(\alpha_H - \theta_{0H}) \end{bmatrix}, \tag{2.171}$$

such that

$$\begin{Bmatrix} \hat{\mathbf{i}}_{hel} \\ \hat{\mathbf{j}}_{hel} \\ \hat{\mathbf{k}}_{hel} \end{Bmatrix} = [T_{HB}]^{-1} \begin{Bmatrix} \hat{\mathbf{i}}_H \\ \hat{\mathbf{j}}_H \\ \hat{\mathbf{k}}_H \end{Bmatrix}. \tag{2.172}$$

Similarly, the transformation from the vertical tail wind coordinate system to the body-fixed

frame is given by

$$[T_{VB}] = \begin{bmatrix} \cos(\alpha_V - \theta_{0V})\cos\beta_V & \cos(\alpha_V - \theta_{0V})\sin\beta_V & -\sin(\alpha_V - \theta_{0V}) \\ \sin\beta_V & -\cos\beta_V & 0 \\ \sin(\alpha_V - \theta_{0V})\cos\beta_V & \sin(\alpha_V - \theta_{0V})\sin\beta_V & \cos(\alpha_V - \theta_{0V}) \end{bmatrix}, \quad (2.173)$$

and thus,

$$\begin{Bmatrix} \hat{\mathbf{i}}_{hel} \\ \hat{\mathbf{j}}_{hel} \\ \hat{\mathbf{k}}_{hel} \end{Bmatrix} = [T_{VB}]^{-1} \begin{Bmatrix} \hat{\mathbf{i}}_V \\ \hat{\mathbf{j}}_V \\ \hat{\mathbf{k}}_V \end{Bmatrix}. \quad (2.174)$$

The aerodynamic forces and moments at the CG due to the horizontal tail are thus given by

$$\mathbf{F}_H = \begin{Bmatrix} X_H \\ Y_H \\ Z_H \end{Bmatrix} = [T_{HB}]^{-1} \mathbf{F}_{wH}, \quad (2.175)$$

$$\mathbf{M}_H = \begin{Bmatrix} L_H \\ M_H \\ N_H \end{Bmatrix} = \mathbf{x}_H \times \mathbf{F}_H, \quad (2.176)$$

and those due to the vertical tail by

$$\mathbf{F}_V = \begin{Bmatrix} X_V \\ Y_V \\ Z_V \end{Bmatrix} = [T_{VB}]^{-1} \mathbf{F}_{wV}, \quad (2.177)$$

$$\mathbf{M}_V = \begin{Bmatrix} L_V \\ M_V \\ N_V \end{Bmatrix} = \mathbf{x}_V \times \mathbf{F}_V. \quad (2.178)$$

2.4.4 Tail rotor loads

The tail rotor loads are determined using a simplified model where the blades are rigid, rectangular and linearly twisted from root to tip. The velocity vector at the tail rotor is given by

$$\mathbf{V}_{TR} = \mathbf{V}_{CG} + \omega \times \mathbf{x}_{TR}, \tag{2.179}$$

where $\mathbf{x}_{TR}$ is the position vector of the tail rotor hub center relative to the CG. The velocities in Eq. (2.179) are transformed from the body-fixed frame to the local tail rotor coordinate system using two rotations, one about the $\hat{x}_{hel}$ axis by the tail rotor cant angle Γ_{TR}, and the second about the new $\hat{z}$ axis by the tail rotor yaw angle Λ_{TR}. The resulting coordinate transformation is given by

$$[T_{TB}] = \begin{bmatrix} \cos\Lambda_{TR} & -\sin\Gamma_{TR}\sin\Lambda_{TR} & \cos\Gamma_{TR}\sin\Lambda_{TR} \\ 0 & \cos\Gamma_{TR} & \sin\Gamma_{TR} \\ -\sin\Lambda_{TR} & -\sin\Gamma_{TR}\cos\Lambda_{TR} & \cos\Gamma_{TR}\cos\Lambda_{TR} \end{bmatrix}, \tag{2.180}$$

and thus, the velocity components of $\mathbf{V}_{TR}$ in Eq. (2.179) are obtained in the local tail rotor coordinate system as

$$\begin{Bmatrix} u_{tl} \\ v_{tl} \\ w_{tl} \end{Bmatrix} = [T_{TB}] \begin{Bmatrix} u_{TR} \\ v_{TR} \\ w_{TR} \end{Bmatrix}. \tag{2.181}$$

The nondimensional tail rotor thrust is expressed as [61]

$$T_{TR} = \frac{2\rho\pi R_t^2 v_{It} v_t \left(\Omega_t R_t\right)^2 K_{blk}}{m_0(\Omega R)^2}, \tag{2.182}$$

where R_t is the tail rotor radius, Ω_t is the angular velocity of the tail rotor, m_0 is a reference mass per unit length, and K_{blk} is an empirical blockage factor that accounts for the presence of the vertical tail. The inflow velocity v_{It} is determined using the Pitt-Peters dynamic

inflow model [71], with the sine and cosine components of the inflow assumed to be zero. The nondimensional air velocity magnitude at the tail rotor hub center v_t is obtained using the velocity components from Eq. (2.181) as follows:

$$v_t = \frac{\sqrt{u_{tl}^2 + v_{tl}^2 + (w_{tl} - v_{It}\Omega_t R_t)^2}}{\Omega_t R_t}. \tag{2.183}$$

The nondimensional tail rotor torque is given by

$$Q_{TR} = \frac{C_{Qt}\rho\pi R_t^2 \left(\Omega_t R_t\right)^2 R_t}{m_0(\Omega R)^2 R}, \tag{2.184}$$

where the torque coefficient C_{Q_t} is a function of the tail rotor blade solidity, advance ratio, tip loss factor, lock number, lift curve slope, and twist angle.

The thrust and torque loads in the local tail rotor coordinate system are

$$\mathbf{F}_t = -T_{TR}\hat{\mathbf{j}}_t, \tag{2.185}$$

$$\mathbf{M}_t = -Q_{TR}\hat{\mathbf{j}}_t. \tag{2.186}$$

The tail rotor loads, when resolved at the CG, are

$$\mathbf{F}_{TR} = \left\{ \begin{array}{c} X_{TR} \\ Y_{TR} \\ Z_{TR} \end{array} \right\} = [T_{TB}]^{-1} \mathbf{F}_t, \tag{2.187}$$

$$\mathbf{M}_{TR} = \left\{ \begin{array}{c} L_{TR} \\ M_{TR} \\ N_{TR} \end{array} \right\} = [T_{TB}]^{-1} \mathbf{M}_t + \mathbf{x}_{TR} \times \mathbf{F}_{TR}. \tag{2.188}$$

2.5 Final Equations

The final equations are formulated as a set of nonlinear first-order differential equations, given by

$$\mathbf{f}(\dot{\mathbf{x}}, \mathbf{x}, \mathbf{u}; t) = \mathbf{0}. \tag{2.189}$$

The formulation is implicit and thus, no ordering scheme or explicit algebraic manipulation is required.

For an articulated four-bladed helicopter model with N_m DOFs, the main rotor state vector is given by

$$\begin{aligned}\mathbf{x}_R = \{&q^1_{1_R},\ q^1_{2_R},\ q^1_{3_R},\ q^1_{4_R},\ \dot{q}^1_{1_R},\ \dot{q}^1_{2_R},\ \dot{q}^1_{3_R},\ \dot{q}^1_{4_R},\ \ldots, q^{N_m}_{1_R},\ q^{N_m}_{2_R},\ q^{N_m}_{3_R},\ q^{N_m}_{4_R},\\ &\dot{q}^{N_m}_{1_R},\ \dot{q}^{N_m}_{2_R},\ \dot{q}^{N_m}_{3_R},\ \dot{q}^{N_m}_{4_R}\}^T.\end{aligned} \tag{2.190}$$

The states in Eq. (2.190) represent blade DOFs in a rotating coordinate frame. A multi-blade coordinate transformation [72] is used to transform the rotating states to a nonrotating frame. The resulting rotor states are given by

$$\begin{aligned}\mathbf{x}_{NR} = \{&q^1_0,\ q^1_{1c},\ q^1_{1s},\ q^1_2,\ \dot{q}^1_0,\ \dot{q}^1_{1c},\ \dot{q}^1_{1s},\ \dot{q}^1_2,\ \ldots, q^{N_m}_1,\ q^{N_m}_{1c},\ q^{N_m}_{1s},\ q^{N_m}_2,\\ &\dot{q}^{N_m}_1,\ \dot{q}^{N_m}_{1c},\ \dot{q}^{N_m}_{1s},\ \dot{q}^{N_m}_2\}^T,\end{aligned} \tag{2.191}$$

where $q^j_0, q^j_{1c}, q^j_{1s}$, and q^j_2 represent, respectively, the collective, cosine, sine and differential portions of the jth generalized coordinates.

Assuming a 3-state dynamic inflow model for the main rotor, the final state vector for the helicopter model is given by

$$\mathbf{x} = \{\mathbf{x}_F, \mathbf{x}_I, \mathbf{x}_{NR}\}^T, \tag{2.192}$$

where the fuselage rigid body and inflow states, respectively, are given by

$$\mathbf{x}_F = \{x,\ y,\ z,\ u,\ v,\ w,\ p,\ q,\ r,\ \phi_f,\ \theta_f,\ \psi_f\}^T, \tag{2.193}$$

$$\mathbf{x}_I = \{\lambda_0,\ \lambda_{1c},\ \lambda_{1s},\ \lambda_t\}^T. \tag{2.194}$$

The control input vector consists of main rotor collective, cyclic, and tail rotor collective inputs and is given by

$$\mathbf{u} = \{\theta_0, \theta_{1c}, \theta_{1s}, \theta_{0t}\}^T. \tag{2.195}$$

HeliUM2 uses the DASSL differential-algebraic equation (DAE) solver [65]. Traditional ODE solvers require acceleration terms to be on one side of the equations. The algebraic manipulations involved to obtain such a structure are cumbersome, requiring simplifying approximations. This issue is avoided using DAE solvers. A DAE system is expressed as

$$\begin{aligned} \mathbf{f}(\dot{\mathbf{x}}, \mathbf{x}, \hat{\mathbf{x}}; t) &= \mathbf{0}, \\ \mathbf{g}(\mathbf{x}, \hat{\mathbf{x}}; t) &= \mathbf{0}, \end{aligned} \tag{2.196}$$

where $\mathbf{g}$ represents a system of algebraic equations, and $\hat{\mathbf{x}}$ represent algebraic variables that do not have a time-dependent counterpart [65]. Comparing Eqs. (2.189) and (2.196), a system of ODEs forms a special case of the DAE system in which no algebraic equations $\mathbf{g}$ are present. Given initial conditions for $\mathbf{x}$, $\dot{\mathbf{x}}$ and $\mathbf{u}$, the DASSL solver iteratively updates $\mathbf{x}$, and $\dot{\mathbf{x}}$ until they converge and the residual in Eq. (2.189) approaches zero.

2.6 Helicopter Trim Analysis

The trim state is computed for a specified flight condition, defined by the weight coefficient C_W, vehicle speed V, flight path angle γ, and turn rate $\dot{\psi}_f$. Since only straight flight is considered in this work, $\dot{\psi}_f = 0$. The trim problem is formulated as a coupled system

of nonlinear algebraic equations, which enforce force and moment equilibrium about the body axes, kinematic conditions, and steady state inflow equations.

2.6.1 Trim unknowns

The vector of trim variables is split into three parts [61]

$$\boldsymbol{\Theta} = \{\boldsymbol{\Theta}_B, \boldsymbol{\Theta}_R, \boldsymbol{\Theta}_I\}^T, \tag{2.197}$$

where $\boldsymbol{\Theta}_B, \boldsymbol{\Theta}_R$ and $\boldsymbol{\Theta}_I$ contain, respectively, trim unknowns associated with the entire helicopter, main rotor, and the inflow.

The trim variables associated with the entire helicopter $\boldsymbol{\Theta}_B$ are given by

$$\boldsymbol{\Theta}_B = \{\theta_0, \theta_{1c}, \theta_{1s}, \theta_t, \alpha_f, \beta_f, \phi_f, \theta_f, \lambda_t\}^T, \tag{2.198}$$

where θ_f is the fuselage pitch angle, ϕ_f is the fuselage roll angle, and λ_t is a constant tail rotor inflow and is included in the $\boldsymbol{\Theta}_B$ partition for convenience.

The angles of attack α_f and sideslip β_f, together with the vehicle speed V are used to calculate the velocities u, v, and w along the body axes

$$u = V \cos\alpha_f \cos\beta_f, \tag{2.199}$$

$$v = V \sin\beta_f, \tag{2.200}$$

$$w = V \sin\alpha_f \cos\beta_f. \tag{2.201}$$

The angular velocities p, q, r are zero at trim since $\dot{\psi}_f = 0$.

The blade motion is assumed to be periodic in trim and thus, is approximated by a truncated Fourier series. The Fourier expansion coefficients of the generalized coordinates

given in Eq. (2.190) form the main rotor trim unknowns $\mathbf{\Theta}_R$

$$q^k(\psi) \approx q^k_{app}(\psi) = \zeta^k_0 + \sum_{j=1}^{N_\mathrm{h}} \left(\zeta^k_{jc} \cos j\psi + \zeta^k_{js} \sin j\psi\right), \tag{2.202}$$

where ζ^k_0 is the constant expansion coefficient of the kth mode, ζ^k_{jc} and ζ^k_{js} are the coefficients of the jth harmonic cosine and sine for the kth mode, N_h is the number of harmonics included in the expansion for each mode, and N_m is the number of modes retained for the modal coordinate transformation described in Section 2.3.8. The vector of main rotor trim unknowns $\mathbf{\Theta}_R$ is thus given by

$$\begin{aligned}\mathbf{\Theta}_R = \{&\zeta^1_0,\ \zeta^1_{1c},\ \zeta^1_{1s},\ \zeta^1_{2c},\ \zeta^1_{2s},\ \ldots \zeta^1_{N_hc},\ \zeta^1_{N_hs},\ \ldots,\ \zeta^{N_m}_0,\ \zeta^{N_m}_{1c},\ \zeta^{N_m}_{1s},\ \zeta^{N_m}_{2c},\\ &\zeta^{N_m}_{2s},\ \ldots,\ \zeta^{N_m}_{N_hc},\ \zeta^{N_m}_{N_hs}\}^T.\end{aligned} \tag{2.203}$$

The main rotor blades are assumed to be identical and therefore, only one blade is taken into account in trim analysis.

The Θ_I partition contains the values of the dynamic inflow coefficients representing main rotor inflow

$$\mathbf{\Theta}_I = \{\lambda_0, \lambda_{1s}, \lambda_{1c}\}^T, \tag{2.204}$$

where a 3-state dynamic inflow model is assumed.

2.6.2 Trim equations

The trim equations for steady maneuvering flight represent a system of nonlinear algebraic equations

$$\mathbf{F}(\mathbf{\Theta}) = \mathbf{0}, \tag{2.205}$$

which can be divided into body, main rotor and inflow parts as

$$\mathbf{F}(\boldsymbol{\Theta}) = \{\mathbf{F}_{\Theta B}, \mathbf{F}_{\Theta R}, \mathbf{F}_{\Theta I}\}^T. \tag{2.206}$$

The vector $\mathbf{F}_{\Theta B}$ represents a set of nine algebraic equations, which enforce the conditions described next.

1. *Force and moment equilibrium*

   Force and moment equilibrium is enforced by requiring that the translational and rotational accelerations of the aircraft be zero when averaged over one rotor revolution. For instance,

   $$\int_0^{2\pi} \dot{u}\, d\psi = 0, \tag{2.207}$$

   and similarly for $\dot{v}, \dot{w}, \dot{p}, \dot{q}$, and $\dot{r}$.

2. *Turn coordination equation*

   The turn coordination condition requires the Y component of the forces acting on the CG, shown in Eq. (2.133), be zero when averaged over one rotor revolution [73]. That is,

   $$\int_0^{2\pi} \left[\sin\phi_f - \frac{\dot{\psi}V}{g}\left(\cos\alpha_f \cos\phi_f + \sin\alpha_f \tan\theta_f\right)\cos\beta_f\right] d\psi = 0. \tag{2.208}$$

   Since $\dot{\psi} = 0$ in this study, Eq. (2.208) becomes

   $$\int_0^{2\pi} \sin\phi_f\, d\psi = 0. \tag{2.209}$$

   This equation is valid for an advance ratio $\mu > 0.1$, where the lateral force and yaw moment from the vertical tail enforces the condition that the average roll angle be zero [61]. For $\mu < 0.1$, the turn coordination is replaced by an equation which

enforces a zero average sideslip angle [61]

$$\int_0^{2\pi} \beta_f \, d\psi = 0. \tag{2.210}$$

3. *Relationship between angle of attack and Euler pitch angle*

   The flight path angle γ, angle of attack α_f, sideslilp angle β_f, roll angle ϕ_f and pitch angle θ_f need to satisfy the following equation [73]:

$$\int_0^{2\pi} [\cos\alpha_f \cos\beta_f \sin\theta_f - (\sin\beta_f \sin\phi_f + \sin\alpha_f \cos\beta_f \cos\phi_f) \cos\theta_f - \sin\gamma] \, d\psi = 0. \tag{2.211}$$

4. *Tail rotor inflow*

   The tail rotor equation enforces the condition that the tail rotor inflow be constant when averaged over one rotor revolution

$$\int_0^{2\pi} \dot{\nu}_t \, d\psi = 0. \tag{2.212}$$

For trim analysis, the main rotor equations of motion, from Eq. (2.131) in Section 2.3.9, are formulated such that acceleration terms appear on the left hand side as follows [61]:

$$\ddot{\mathbf{q}} = \mathbf{f}_q(\dot{\mathbf{q}}, \mathbf{q}), \tag{2.213}$$

where $\mathbf{q}$ are the blade generalized displacements, and $\dot{\mathbf{q}}$ and $\ddot{\mathbf{q}}$ the first and second time derivatives, respectively.

The truncated Fourier series in Eq. (2.202) is used to approximate the first and second

time derivatives of the generalized coordinates as follows:

$$\dot{q}^k(\psi) \approx \dot{q}^k_{app}(\psi) = \Omega \sum_{j=1}^{N_\mathrm{h}} \left(-\zeta^k_{jc} \sin j\psi + \zeta^k_{js} \cos j\psi\right), \tag{2.214}$$

$$\ddot{q}^k(\psi) \approx \ddot{q}^k_{app}(\psi) = -\Omega^2 \sum_{j=1}^{N_\mathrm{h}} \left(\zeta^k_{jc} \cos j\psi + \zeta^k_{js} \sin j\psi\right). \tag{2.215}$$

A nonzero residual vector is obtained if the vector of approximate solutions $\mathbf{q}_{app}$ is substituted into Eq. (2.213),

$$\boldsymbol{\varepsilon}(\psi) = \ddot{\mathbf{q}}_{app} - \mathbf{f}_\mathrm{q}(\dot{\mathbf{q}}_{app}, \mathbf{q}_{app}). \tag{2.216}$$

Following Galerkin's method, the Fourier coefficients ζ^k_0, ζ^k_{jc} and ζ^k_{js} are chosen such that the following equations are satisfied [74]

$$\int_0^{2\pi} \boldsymbol{\varepsilon}^k(\psi)\, d\psi = 0, \tag{2.217}$$

$$\int_0^{2\pi} \boldsymbol{\varepsilon}^k(\psi) \cos j\psi,\ d\psi = 0; \quad j = 1, \ldots, N_\mathrm{h} \tag{2.218}$$

$$\int_0^{2\pi} \boldsymbol{\varepsilon}^k(\psi) \sin j\psi\ d\psi = 0; \quad j = 1, \ldots, N_\mathrm{h}. \tag{2.219}$$

The resulting set of algebraic equations make up the $\mathbf{F}_{\Theta R}$ partition of the vector of trim equations given in Eq. (2.206).

The $\mathbf{F}_{\Theta I}$ partition of the vector of trim equations, given in Eq. (2.206), consists of a set of equations that ensure the derivative of each dynamic inflow coefficient is zero when averaged over one rotor revolution. That is,

$$\int_0^{2\pi} \dot{\lambda}_0\, d\psi = 0, \tag{2.220}$$

$$\int_0^{2\pi} \dot{\lambda}_{1s}\, d\psi = 0, \tag{2.221}$$

$$\int_0^{2\pi} \dot{\lambda}_{1c}\, d\psi = 0. \tag{2.222}$$

2.7 Linearization

The equations of motion are linearized about a trim state using a Taylor series expansion of Eq. (2.189)

$$\mathbf{f}(\dot{\mathbf{x}}, \mathbf{x}, \mathbf{u}; t) \approx \mathbf{f}(\dot{\mathbf{x}}_{eq}, \mathbf{x}_{eq}, \mathbf{u}_{eq}; t) + \frac{\partial \mathbf{f}}{\partial \dot{\mathbf{x}}}\Delta\dot{\mathbf{x}} + \frac{\partial \mathbf{f}}{\partial \mathbf{x}}\Delta\mathbf{x} + \frac{\partial \mathbf{f}}{\partial \mathbf{u}}\Delta\mathbf{u} = \mathbf{0}, \tag{2.223}$$

where $\Delta\dot{\mathbf{x}} = \dot{\mathbf{x}} - \dot{\mathbf{x}}_{eq}$, $\Delta\mathbf{x} = \mathbf{x} - \mathbf{x}_{eq}$ and $\Delta\mathbf{u} = \mathbf{u} - \mathbf{u}_{eq}$, and all the derivatives are computed using finite difference approximations.

Since $\mathbf{f}(\dot{\mathbf{x}}_{eq}, \mathbf{x}_{eq}, \mathbf{u}_{eq}; t) = \mathbf{0}$, Eq. (2.223) becomes

$$\mathbf{E}(t)\Delta\dot{\mathbf{x}} + \mathbf{F}(t)\Delta\mathbf{x} + \mathbf{G}(t)\Delta\mathbf{u} = \mathbf{0}, \tag{2.224}$$

where

$$\mathbf{E}(t) = \frac{\partial \mathbf{f}}{\partial \dot{\mathbf{x}}}, \quad \mathbf{F}(t) = \frac{\partial \mathbf{f}}{\partial \mathbf{x}}, \quad \mathbf{G}(t) = \frac{\partial \mathbf{f}}{\partial \mathbf{u}}. \tag{2.225}$$

Solving Eq. (2.224) for $\Delta\dot{\mathbf{x}}$ yields

$$\Delta\dot{\mathbf{x}} = \mathbf{A}_{LTP}(t)\Delta\mathbf{x} + \mathbf{B}_{LTP}(t)\Delta\mathbf{u}, \tag{2.226}$$

where

$$\mathbf{A}_{LTP}(t) = -\mathbf{E}(t)^{-1}\mathbf{F}(t), \quad \mathbf{B}_{LTP}(t) = -\mathbf{E}(t)^{-1}\mathbf{G}(t). \tag{2.227}$$

Equation (2.226) represents a linearized time-periodic (LTP) system where the matrices $\mathbf{A}(t)$ and $\mathbf{B}(t)$ are periodic with respect to t. In order to obtain a linear time-invariant (LTI) system, needed to construct the FCS, the matrices are averaged over one rotor revolution

as follows:

$$\mathbf{A}_0 = \frac{1}{2\pi}\int_0^{2\pi} \mathbf{A}_{LTP}(t)\, d\psi, \tag{2.228}$$

$$\mathbf{B}_0 = \frac{1}{2\pi}\int_0^{2\pi} \mathbf{B}_{LTP}(t)\, d\psi. \tag{2.229}$$

The final LTI approximation of the system at a trim state is therefore given as

$$\Delta\dot{\mathbf{x}} = \mathbf{A}_0\Delta\mathbf{x} + \mathbf{B}_0\Delta\mathbf{u}. \tag{2.230}$$

CHAPTER 3

Approach Trajectory and its Control

Several capabilities were added to the HeliUM2 flight dynamic code described in Chapter 2. The modified code is referred to as "HeliUM2-umich" and includes provision for a flight control system (FCS), wind over deck (WOD), landing gear, ground effect, and the SCONE ship motion data. These components are described in the next four chapters. The present chapter describes the approach and landing trajectory considered in this dissertation, as well as the FCS. The trajectory is fixed and established *a priori* during simulations.

3.1 Approach Trajectory

The helicopter approach trajectory consists of three segments shown in Fig. 3.1: a) steady level flight, b) descent to a hover position, and c) hover over the ship deck. In this study, segments (a), (b), and (c) are simulated for 20 s, 76 s, and 10 s, respectively. The steady level flight speed is denoted as V_0 and the altitude as z_0.

3.1.1 Velocity profile during descent

In the descent phase of the approach, the vehicle is assumed to follow a straight trajectory with a constant flight path angle γ shown in Fig. 3.1. The descent begins at an altitude z_0, with velocity V_0, and ends in hover at an altitude z_f over a specified location on the ship deck. Table 3.1 provides the values used based on Refs. [10], [12] and [75]. The altitudes

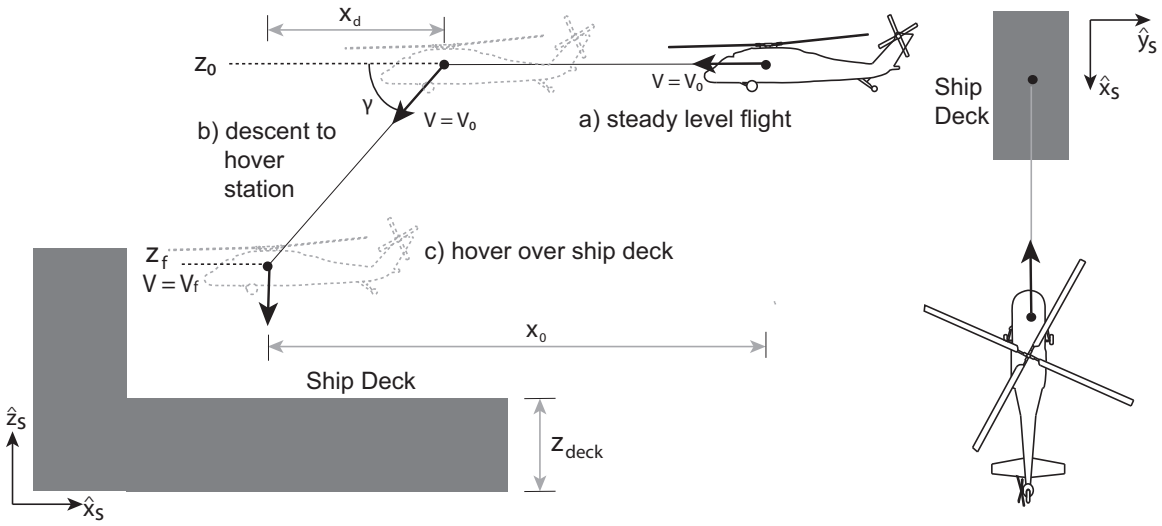

Figure 3.1: Side view (left), and top view (right) illustrations of the approach and landing trajectory, figure not to scale.

are relative to sea level and velocities are relative to a stationary ship. Note that the ship deck is assumed to be 15 ft. above sea level as a result of the ship configuration used.

Table 3.1: Approach trajectory parameters

Parameter	Value
z_0	300 ft.
V_0	60 kts.
z_f	30 ft.
V_f	0 kts.
γ	6°
x_d	2570 ft.
x_0	4830 ft.
z_{deck}	15 ft.

The analytical model developed by Heffley [76] is used to determine the velocity profile of the vehicle during the descent phase. Heffley's model provides a guidance law that is based on a human pilot's perception of the visual field during a deceleration maneuver from forward flight to hover, and has been validated against flight data [76]. During such a maneuver, peak deceleration occurs when the helicopter is at a horizontal distance of

approximately 300 ft. from the target hover position. From there on, the helicopter approaches the deck at slow speeds. Heffley's model has been used previously in several studies [29, 77–79]. The horizontal velocity is given by

$$\dot{D} = \frac{-k_t D}{1 + D/A_t}, \tag{3.1}$$

where D is the horizontal distance from the target, k_t is a proportionality constant, and A_t is the effective size of the region in the pilot's visual field. The deceleration profile is obtained by differentiating Eq. (3.1) with respect to time

$$\begin{aligned}
\ddot{D} = \frac{d\dot{D}}{dt} &= \frac{d}{dt}\left(\frac{-k_t D}{1 + D/A_t}\right) \\
&= \frac{(1 + D/A_t)(-k_t)\dot{D} - (-k_t D)(1/A_t)\dot{D}}{(1 + D/A_t)^2} \\
&= \frac{-k_t - k_t D/A_t + k_t D/A_t}{(1 + D/A_t)^2}\dot{D} \\
&= \frac{-k_t}{(1 + D/A_t)^2}\dot{D} \\
&= \frac{k_t^2 D}{(1 + D/A_t)^3}.
\end{aligned} \tag{3.2}$$

This model is convenient to use since only two parameters, namely the effective size A_t and the proportionality constant k_t, are needed to define the velocity profile.

To determine A_t, an analytical expression for the ratio of the squared horizontal velocity $\dot{D}^2$ to the horizontal deceleration $\ddot{D}$ is needed [76]. This is obtained using Eqs. (3.1) and (3.2) as follows:

$$\frac{\dot{D}^2}{\ddot{D}} = \frac{\left(\dfrac{-k_t D}{1 + D/A_t}\right)}{\dfrac{k_t^2 D}{(1 + D/A_t)^3}} = \frac{\dfrac{k_t^2 D^2}{(1 + D/A_t)^2}}{\dfrac{k_t^2 D}{(1 + D/A_t)^3}} = D\left(1 + \frac{D}{A_t}\right). \tag{3.3}$$

An empirical expression for the ratio is provided in Ref. 80 as

$$\frac{\dot{D}^2}{\ddot{D}} = c_1 D^{n_1}, \tag{3.4}$$

where $c_1 = 0.23$ ft.$^{-0.36}$ and $n_1 = 1.36$ are empirical constants. Note that the units for the empirical constant c_1 were not specified in Refs. [76] and [80] and are given here for dimensional consistency.

The effective size A_t is determined by matching the $\dot{D}^2/\ddot{D}$ ratio values from Eqs. (3.3) and (3.4) over a desired distance D. In this study, the matching was performed using a MATHEMATICA [81] script. Using $D = x_d$ from Table 3.1 , and an initial value of $A_t = 600$ ft., the value used in Ref. [76], an iterative method was used to obtain a final value of $A_t = 661.72$ ft.

The value for k_t is determined by substituting the final value for A_t and the values $D = x_d$, and $\dot{D}_0 = V_0 \cos\gamma$ from Table 3.1 into Eq. (3.1)

$$k_t = \frac{-\dot{D}_0(1 + x_d/A_t)}{x_d}, \tag{3.5}$$

which yields $k_t = 0.19$/s. Note that this approach differs from the one suggested in Ref. [76] where a theoretical peak deceleration $\ddot{D}_{peak}$ is used to compute k_t as follows:

$$k_t = \sqrt{\frac{27\ddot{D}_{peak}}{4A_t}}. \tag{3.6}$$

The method used in this study directly relates the horizontal velocity $\dot{D}$ in Eq. (3.1) to the initial vehicle speed V_0. The resulting velocity and deceleration profiles are shown in Figs. 3.2a and 3.2b.

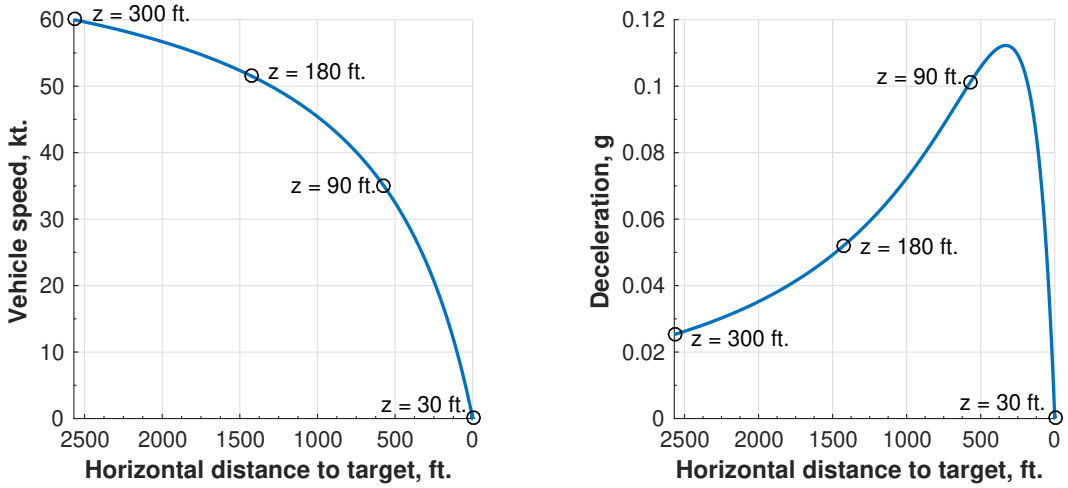

(a) (b)

Figure 3.2: Helicopter (a) speed and (b) deceleration profiles during descent to hover position.

3.2 Controller Design

A Linear-Quadratic Regulator (LQR) based Flight Control System is used to stablize the inherently unstable UH-60A helicopter model. The FCS generates control inputs at each time step based on the control law

$$\mathbf{u} = \mathbf{K}_{LQR}(\mathbf{x}_{des} - \mathbf{x}_{act}) \tag{3.7}$$

where $\mathbf{x}_{des}$ and $\mathbf{x}_{act}$ are the desired and actual state values, respectively. The LQR formulation is described next.

3.2.1 LQR formulation

The gain matrix $\mathbf{K}_{LQR}$ is determined by minimizing a cost function

$$J(\mathbf{u}) = \int_{t_0}^{t_f} (\mathbf{x}_e^T \mathbf{Q} \mathbf{x}_e + \mathbf{u}^T \mathbf{R} \mathbf{u})\, dt, \tag{3.8}$$

where the **Q** matrix penalizes magnitude of errors in the system states, $\mathbf{x}_e = \mathbf{x}_{des} - \mathbf{x}_{act}$, and the **R** matrix penalizes magnitude of the control inputs.

In this study, **R** is chosen to be a 4×4 identity matrix, and **Q** a diagonal matrix of size $N_F \times N_F$ corresponding to the N_F rigid body DOFs shown in the $\mathbf{x}_F$ vector from Eq. (2.193), rewritten here for convenience

$$\mathbf{x}_F = \{x,\ y,\ z,\ u,\ v,\ w,\ p,\ q,\ r,\ \phi_f,\ \theta_f,\ \psi_f\}^T. \tag{3.9}$$

The diagonal elements of the **Q** matrix are determined by trial and error. As an initial guess, it was assumed that 0.1 ft. and 0.1 ft/s were acceptable errors for states with units of length and length/time in Eq. (3.9), respectively. The corresponding Q_i weight was given by

$$Q_i = \left(\frac{1}{0.1}\right)^2, \tag{3.10}$$

such that when $x_{e,i} = 0.1$, $x_{e,i}^2 Q_i$ from Eq. (3.8) equals unity, and when $x_{e,i} > 0.1$, the value of $x_{e,i}^2 Q_i$, and thus that of $J(\mathbf{u})$, is greater than one. For the angular and angular rate states in Eq. (3.9), errors of magnitude 0.01 rad and 0.01 rad/s were assumed to be acceptable. The **Q** weights were tuned to minimize errors between the actual and desired state values throughout the approach segment of trajectory described in Section 3.1. With the initial weights, the converged yaw angle had an error of approximately 54°. After tuning, the yaw angle error was less than 10°. The final **Q** and **R** matrices were found to be

$$\mathbf{Q} = \text{diag}(1\ \ 3\ \ 2\ \ 1\ \ 3\ \ 2\ \ 100\ \ 100\ \ 2500\ \ 100\ \ 100\ \ 2500), \tag{3.11}$$

$$\mathbf{R} = \text{diag}(1\ \ 1\ \ 1\ \ 1). \tag{3.12}$$

In this study, the gain matrix $\mathbf{K}_{LQR}$ is determined using the standard LQR formulation implemented in MATLAB, where an LTI approximation of the helicopter dynamics model,

shown in Eq. (2.230), is used.

3.2.2 Trajectory tracking

The controller is used to track the desired approach profile described in Section 3.1. As mentioned earlier, the approach trajectory is divided into three segments: a) steady level flight, b) descent to a hover position, and c) hover over the ship deck. Gain scheduling is used to update the $\mathbf{K}_{LQR}$ matrix during the transition from segment (a), where $\gamma = 0^\circ$, to segment (b), where $\gamma = 6^\circ$, and also to track the trajectory during segment (b). During the transition from steady level flight to descent, the controller gains are updated with respect to γ in 1° increments. The process is described next:

1. Linearized models corresponding to trim at V_0 and $\gamma = \{0^\circ, 1^\circ, 2^\circ, 3^\circ, 4^\circ, 5^\circ, 6^\circ\}$ are constructed. The changing approach angle creates a progressive loss in altitude that needs to be taken into account when generating the linear models. From Fig. 3.1, the loss is determined as follows:

$$z_{loss} = V_0 \sin(\gamma)\Delta t. \tag{3.13}$$

2. The $\mathbf{K}_{LQR}$ matrix corresponding to each linearized system is computed.

3. At every time step, $\mathbf{K}_{LQR}$ for the current γ is determined by interpolation.

The controller gains for descent segment (b) are updated with respect to V in 2 knot decrements from V_0 to V_f. The gain scheduling methodology is similar to that used in Ref. [29].

3.2.3 Landing

Landing is performed by gradually reducing the main rotor collective input to a value that produces zero thrust, similar to the approach used in Ref. [4]. This results in a gradual

axial descent of the helicopter on to the deck. In this phase, since the collective is manually decreased, the FCS uses only the main rotor cyclic and tail rotor collective inputs to ensure stability.

CHAPTER 4

Wind Over Deck

Wind over deck is a critical component of the ship landing problem. The aerodynamics involved are complex and include energetic flow features with widely varying time scales. A time-accurate model is therefore necessary. This chapter describes the WOD model used and its integration into the flight dynamic simulation.

4.1 Description of CFD Method

Airwake due to WOD is obtained from DES of flow over a full-scale Simple Frigate Shape V2 (SFS2) ship model, depicted in Fig. 4.1. The DES was selected because it provides a good compromise between the computationally expensive Large Eddy Simulation, and the lower-fidelity unsteady RANS solution. The CFD simulation is performed using a commercial finite-volume solver FLUENT [82], executed in the pressure-based mode. A second-order spatial discretization and a second-order implicit time-integration scheme are used.

A RANS simulation with the $k-\omega$ turbulence model [83] is first carried out to provide the initial conditions for the subsequent unsteady DES [84]. The RANS equations are obtained by averaging the Navier-Stokes equations with respect to time. The process yields a set of equations that can be decomposed into two parts: a mean part and a fluctuating part. The fluctuating part of the equations, known as the "Reynolds stress", introduces additional unknowns, requiring further modeling before the equations can be solved. This is known

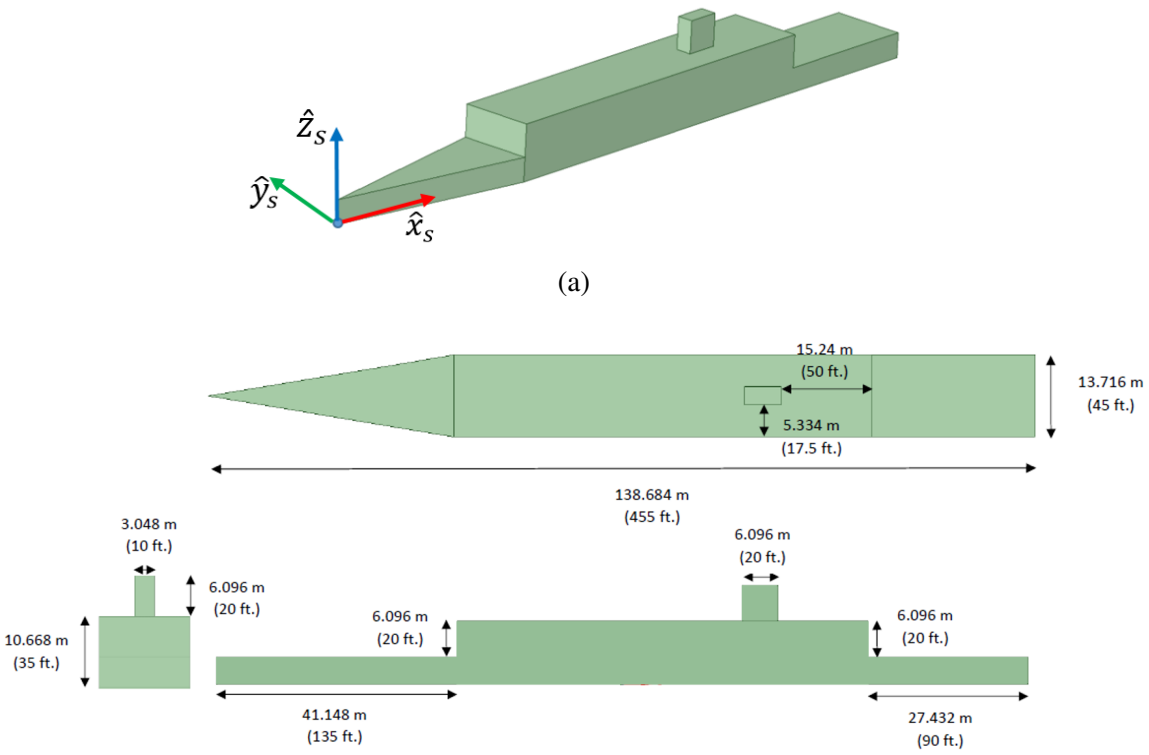

Figure 4.1: SFS2 ship geometry—(a) 3D view and (b) top, side and rear views with dimensions.

as the "closure problem". With the standard $k-\omega$ turbulence model, the Reynolds stresses are related to velocity gradients of the flow through a proportionality constant ν_t, known as the "eddy viscosity", which in turn is a function of turbulent kinetic energy k and the specific rate of dissipation of the turbulent kinetic energy ω [83]

$$\nu_t = \frac{\rho k}{\omega}, \tag{4.1}$$

where ρ is the density of the flow. Values for k and ω in Eq. (4.1) are obtained by solving two PDEs. The simulation is carried out for 15 s with a time step of 0.01 s. Note that dominant features in the ship airwake have time scales larger than 0.2 s [28]. Upon completion of the simulation, the solution method is changed from RANS to DES.

The DES formulation augments the RANS model by allowing for medium to large-scale turbulent structures to be resolved using LES in regions of high grid resolution. The LES solution is obtained using a low-pass filter that removes turbulence of the smallest length scales. The modification in DES relates the turbulent length scale L_T to the local grid size Δh, such that LES is used when $L_T > \Delta h$ and RANS is used when $L_T \leq \Delta h$. The shear stress transport (SST) $k - \omega$ turbulence model is employed for closure since it provides accurate predictions of the onset and amount of flow separation under adverse pressure gradients [85]. The dissipation of the turbulent kinetic energy k is governed by a term which includes a parameter f_{β^*}. In the standard model, $f_{\beta^*} = 1$, but in the SST model [24],

$$f_{\beta^*} = \max\left(\frac{L_T}{C_{DES}\Delta h}\right), \tag{4.2}$$

where $C_{DES} = 0.61$ is a constant in the DES model. When $f_{\beta^*} > 1$, there is an increase in the dissipation of k, which in turn causes a decrease in the eddy viscosity ν_t given in Eq. (4.1).

After the switch from RANS to DES, the first 2000 steps allow for transition from steady to time-accurate simulation. The subsequent 120 seconds of simulation data is stored in tabular form and used for the ship airwake simulation in "HeliUM2-umich". Twenty-five iterations are performed per time step. A similar approach was used and validated in Ref. 24.

4.2 Mesh and Boundary Conditions

A hexahedral mesh is used with a near-body cell resolution of $(2.25, 1, 2)$ ft., relative to the ship frame. The mesh coarsens 40 times in each direction towards the outer boundary. Taking the height of double-level structure above the deck, which is 40 ft., as the characteristic length L_c, the farfield covers a computational domain of $(75, 50, 18.5)L_c$. The final mesh, shown in Fig. 4.2, has 1.95 million cells. The near-body mesh is shown in Fig. 4.3.

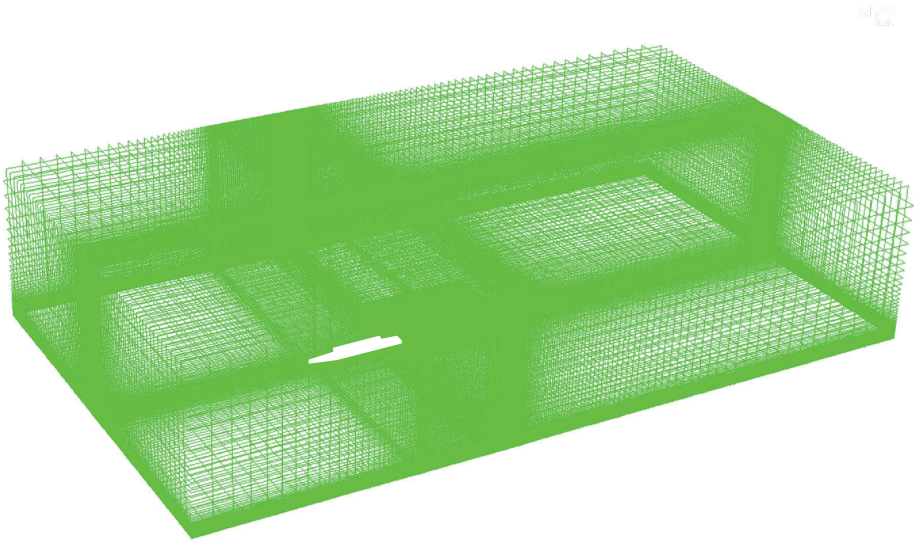

Figure 4.2: Illustration of CFD domain with SFS2 ship outline.

A velocity inlet BC is used due to the incompressible nature of the flow ($Ma \approx 0.05$). A pressure outlet BC is used to ensure the flowfield pressure remains unchanged in the farfield. The bottom surface is specified as a translational moving wall with the same velocities used in the inlet BC. The specification of the portside and starboard surfaces depends on the flow being simulated. Currently, three simulations are performed. These include a headwind case and two sideslip cases $\beta_{WOD} = \{-30°, 30°\}^T$, where β_{WOD} is considered to be positive for winds which come from the starboard side as shown in Fig. 4.4. For the headwind case, a symmetry BC is specified for both portside and starboard surfaces of the

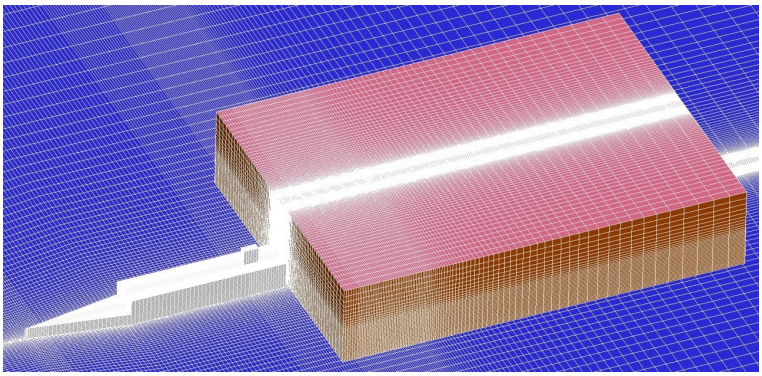

Figure 4.3: Near-body mesh and domain of interest for WOD.

Figure 4.4: Definition of positive sideslip angle β_{WOD}.

domain. For the $\beta_{WOD} = -30°$ case, the portside surface BC is set to velocity inlet and the starboard BC to pressure outlet. For the $\beta_{WOD} = 30°$ case, a pressure outlet BC is specified for the portside surface and a velocity inlet BC for the starboard surface. A symmetry BC is imposed for the top surface and the ship is modeled as a wall with a no-slip BC.

4.3 Comparison with Literature

Initial tests to validate the DES approach were performed using the SFS1 ship, a predecessor to the SFS2 ship, shown by the shaded region in Fig. 4.5 [11]. Following the methodol-

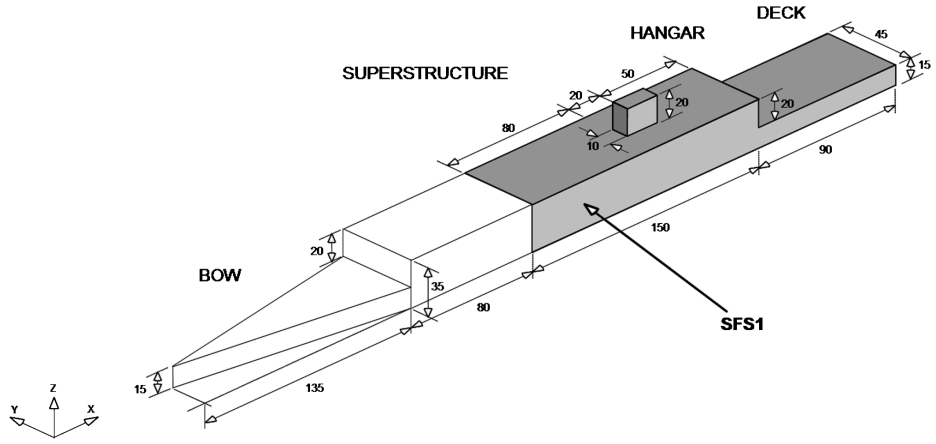

Figure 4.5: The SFS1 and SFS2 ship geometries—dimensions are in feet [11].

ogy from Ref. 86, a rectangular domain that is 14.3 L_c units long, 7.5 L_c units wide and 3.5 L_c units high was used, where L_c was taken to be the ship length. The upstream boundary was placed 3.9 ship lengths ahead of the bow [86]. A hybrid structured/unstructured mesh was employed. Cells close to the ship structure were modeled using hexahedral blocks, which transitioned into tetrahedral blocks further away from the ship as illustrated in Fig.

4.6. The final mesh had 1.1 million cells. A headwind with a speed of 197 ft/s was consid-

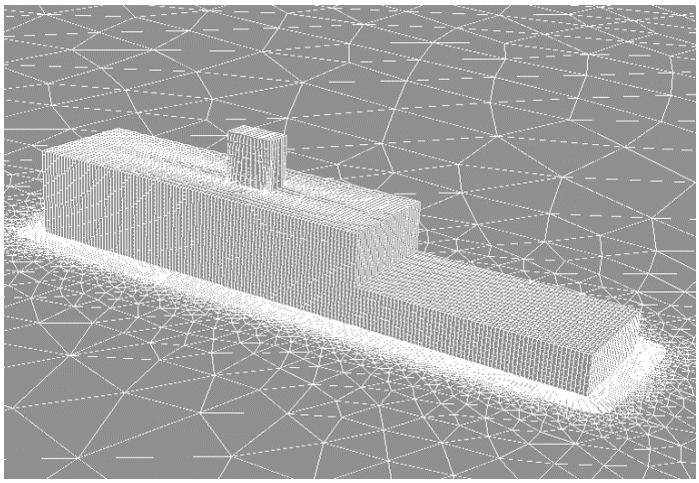

Figure 4.6: The SFS1 mesh.

ered [87]. Velocity magnitude contours over the ship are shown in Fig. 4.7. Separation due to the sharp edges of the structure are apparent. The nondimensional horizontal velocity distribution across slice A from Fig. 4.7 is shown in Fig. 4.8a, for $z = 25$ ft. Results from Ref. 88, which showed good agreement of flow distribution with water tunnel tests, are also plotted in the figure. The horizontal velocity distribution obtained using DES closely matches that from Ref. 88. The streamwise velocity distribution shows similar agreement in Fig. 4.8b. These results give confidence in the DES methodology employed in this study.

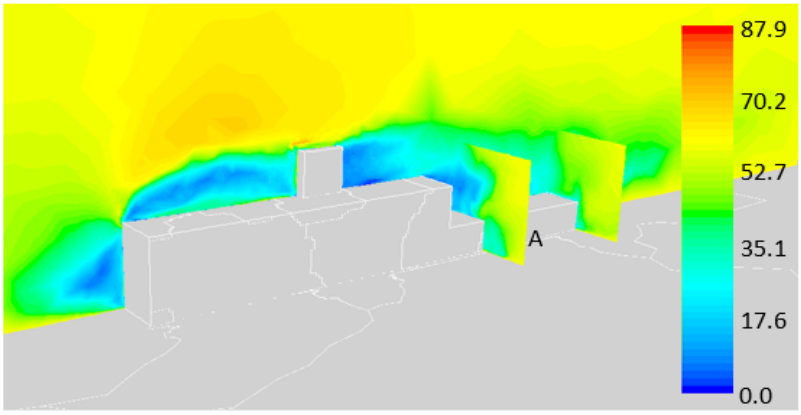

Figure 4.7: Contours of velocity magnitude over ship for a headwind at 197 ft/s.

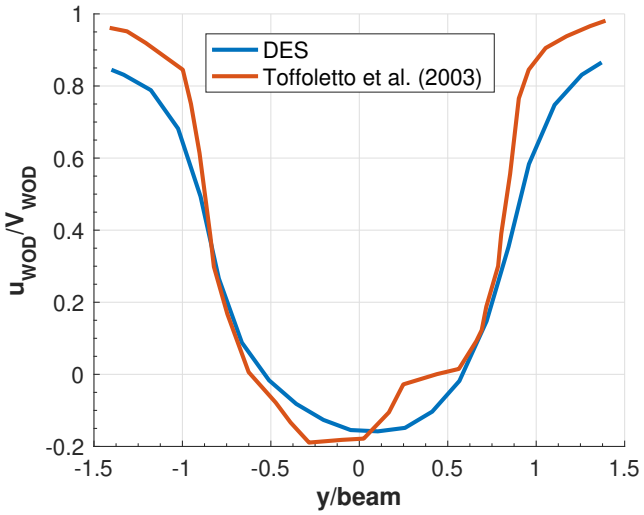

(a) Transverse distribution of horizontal velocity

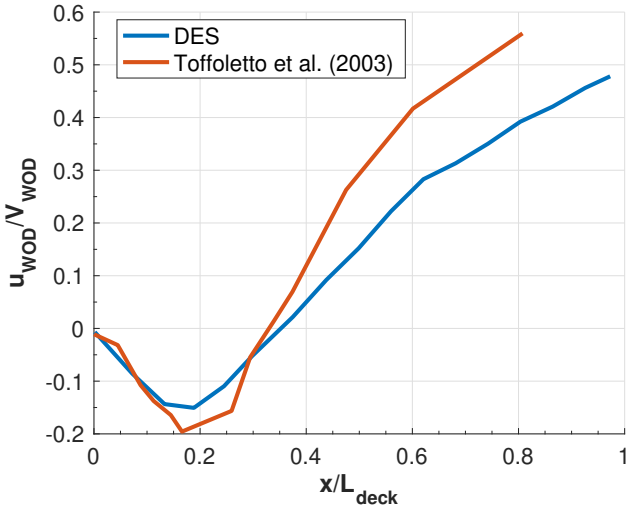

(b) Streamwise distribution of horizontal velocity; L_{deck} is the length of the deck.

Figure 4.8: Horizontal WOD velocity distribution over ship for a headwind at 197 ft/s.

4.4 Integration of WOD Model into Flight Dynamics Code

The WOD solution is mapped onto a uniformly distributed grid, shown as the red colored domain in Fig. 4.3. This domain is 360 ft. long, 315 ft. wide, and 80 ft. high, and is selected based on work presented in Refs. 1 and 10 . The result of the mapping is a dataset containing the coordinates of the grid points and the corresponding WOD velocities as a

function of time. The WOD tables are loaded into the computer memory at the beginning of the simulation, and the WOD velocities at the helicopter components are calculated via linear interpolation at each time step during the time-marching simulation.

4.4.1 Coordinate transformation

To access the WOD model, the position coordinates of the helicopter components need to be expressed relative to the ship frame shown in Fig. 4.1a. The ship frame is obtained from the helicopter body-fixed coordinate system, described in Section 2.1.2, using three translations to shift the origin from the helicopter CG to the bottom of the ship bow, followed by a 180° rotation about the positive $\hat{y}_{hel}$ axis. Thus,

$$\begin{Bmatrix} \hat{\mathbf{i}}_S \\ \hat{\mathbf{j}}_S \\ \hat{\mathbf{k}}_S \end{Bmatrix} = [T_{SB}] \begin{Bmatrix} \hat{\mathbf{i}}_{hel} \\ \hat{\mathbf{j}}_{hel} \\ \hat{\mathbf{k}}_{hel} \end{Bmatrix}, \tag{4.3}$$

where

$$[T_{SB}] = \begin{bmatrix} -1 & 0 & 0 \\ 0 & 1 & 0 \\ 0 & 0 & -1 \end{bmatrix}, \tag{4.4}$$

and $\hat{\mathbf{i}}_S, \hat{\mathbf{j}}_S$, and $\hat{\mathbf{k}}_S$ are unit vectors of the ship frame. Since the trajectory considered in this work is known beforehand (see Chapter 3), the initial values for the translational offsets between the CG and origin of the ship frame are given by

$$x_{off} = x_0 + x_{deck}, \tag{4.5}$$

$$y_{off} = 0, \tag{4.6}$$

$$z_{off} = z_0, \tag{4.7}$$

where $x_0 = 4830$ ft. and $z_0 = 300$ ft. from Table 3.1, and x_{deck} represents the horizontal position of the center of the ship deck, which is 410 ft. in this study as evident from Fig. 4.1b. During time-marching, the offsets are updated by taking the distance traveled by the vehicle into account as follows

$$\begin{bmatrix} x_{off} \\ y_{off} \\ z_{off} \end{bmatrix} = \begin{bmatrix} x_0 + x_{deck} \\ 0 \\ z_0 \end{bmatrix} + [T_{BH}] \begin{bmatrix} x \\ y \\ z \end{bmatrix}, \tag{4.8}$$

where x, y, and z are the horizontal, lateral, and vertical displacements of the CG from Eq. (2.193), respectively.

Position coordinates of the fuselage, empennage and tail rotor COPs, relative to the body-fixed frame, are given by the vectors $\mathbf{x}_{FAC}$, $\mathbf{x}_H$, $\mathbf{x}_V$ and $\mathbf{x}_{TR}$, respectively. For the main rotor blades, a rigid blade assumption is used to reduce computational cost when retrieving WOD velocities. The HeliUM2 code is setup such that the deformations at the various blade span locations are determined individually inside a nested loop, requiring a total of $N_b \times N_e \times N_G$ calls to the WOD model to obtain the corresponding airwake velocities, where N_G represents the number of Gauss points in each element. With the rigid blade assumption, all blade point positions are stored in a vector and the WOD model is invoked only once, significantly reducing cost. The blade tip deflection is used to establish an "equivalent" flapping angle β_{tip} for the rigid blade

$$\beta_{tip} = \frac{w_{tip}}{R - e} + \beta_p, \tag{4.9}$$

illustrated in Fig. 4.9.

The position vector $\mathbf{x}_p$ of a blade point along the span of the rigid blade is expressed in

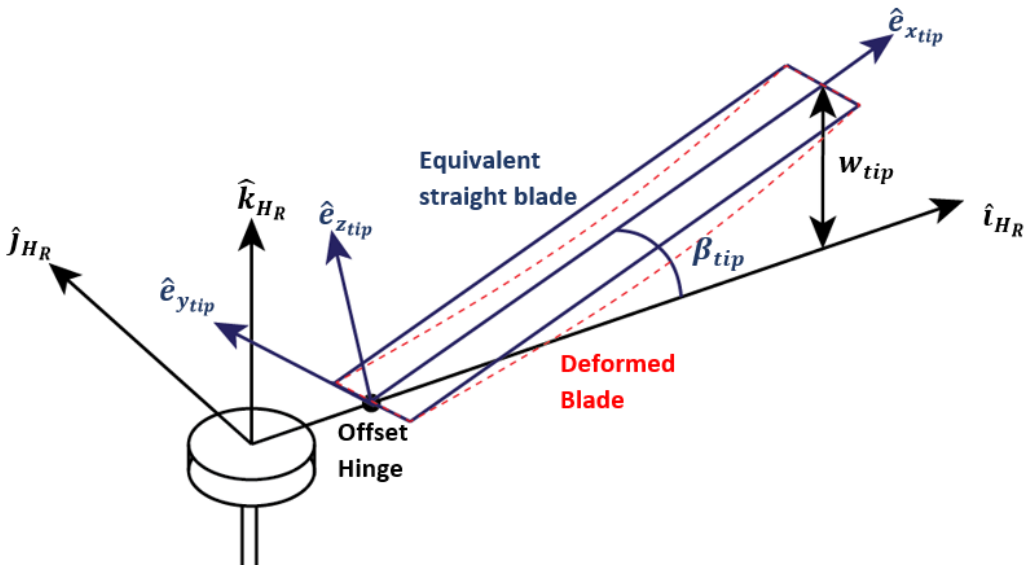

Figure 4.9: Straight blade approximation used to obtain WOD velocities for main rotor blades.

the body-fixed frame as

$$\mathbf{x}_{p_{hel}} = [T_{ShB}]^{-1}[T_{H_{NR}Sh}]^{-1}[T_{H_RH_{NR}}]^{-1}[T_{FH_R}]^{-1}\,\mathbf{x}_p, \tag{4.10}$$

where the transformation matrices $[T_{ShB}]$, $[T_{H_{NR}Sh}]$, and $[T_{H_RH_{NR}}]$ are defined in Eqs. (2.8), (2.10), and (2.12), respectively, and $[T_{FH_R}]$ represents the transformation matrix from the hub rotating frame to the straight blade axes, and is given by

$$[T_{FH_R}] = \begin{bmatrix} \cos\beta_{tip} & 0 & \sin\beta_{tip} \\ 0 & 1 & 0 \\ -\sin\beta_{tip} & 0 & \cos\beta_{tip} \end{bmatrix}. \tag{4.11}$$

Thus,

$$\begin{Bmatrix} \hat{\mathbf{e}}_{x_{tip}} \\ \hat{\mathbf{e}}_{y_{tip}} \\ \hat{\mathbf{e}}_{z_{tip}} \end{Bmatrix} = [T_{FH_R}] \begin{Bmatrix} \hat{\mathbf{i}}_{H_R} \\ \hat{\mathbf{j}}_{H_R} \\ \hat{\mathbf{k}}_{H_R} \end{Bmatrix}. \tag{4.12}$$

4.4.2 Calculation and integration of WOD velocities

The position coordinates of the various blade sections and helicopter components are expressed in the ship coordinate system using the relation given in Eq. (4.3). The corresponding WOD velocities at these coordinates are obtained from the preloaded WOD velocity tables using linear interpolation. The resulting velocities are transformed to the component's local coordinate system.

The WOD velocity is incorporated into the total velocity at the individual blade sections in a manner similar to the inflow velocity in Eq. (2.37)

$$\mathbf{V}_T = \mathbf{V}_{CG} + \left(\frac{d\mathbf{R}_B}{dt}\right)_R + \Omega \times \mathbf{R}_B + \omega \times [\mathbf{R}_H + \mathbf{R}_B] - \mathbf{V}_I - \mathbf{V}_{WOD}. \tag{4.13}$$

Note that although a rigid blade assumption is used to access the WOD model, the resulting WOD velocities are taken into account in the flexible blade model. The actual WOD velocities at the blade sections may thus differ slightly from the WOD velocities used. The WOD is included in the fuselage, empennage and tail rotor models by a similar modification of the velocities at the respective COPs. For the fuselage, Eq. (2.153) becomes

$$\mathbf{V}_F = \mathbf{V}_{CG} - \mathbf{V}_{WOD}. \tag{4.14}$$

For the tail surfaces, Eqs. (2.161) and (2.162) become

$$\mathbf{V}_H = K_H \mathbf{V}_{CG} + \omega \times \mathbf{x}_H - \mathbf{V}_{WOD}, \tag{4.15}$$

$$\mathbf{V}_V = K_V \mathbf{V}_{CG} + \omega \times \mathbf{x}_V - \mathbf{V}_{WOD}, \tag{4.16}$$

respectively, and for the tail rotor, Eq. (2.179) becomes

$$\mathbf{V}_{TR} = \mathbf{V}_{CG} + \omega \times \mathbf{x}_{TR} - \mathbf{V}_{WOD}. \tag{4.17}$$

Using the approach described above, the HeliUM2 code is modified such that the helicopter experiences WOD velocities as it enters the domain of interest, shown in Fig. 4.3. Integration of the WOD model into the HEliUM2 time-marching routine is depicted in Fig. 4.10. The helicopter is trimmed at a given flight condition using the propulsive trim procedure described in Section 2.6. The trim solution is used as an initial condition for time-marching. At each time step, the FCS is engaged to maintain the flight condition. Gain scheduling is employed for changing flight conditions. Values for the current state vector $\mathbf{x}$, state derivative vector $\dot{\mathbf{x}}$, and control input vector $\mathbf{u}$ are fed to the DASSL solver which then iterates to achieve convergence and advance the simulation by one time step. Only one-way coupling between the flight mechanics code and WOD components is considered. Thus, the downwash from the helicopter is assumed to have no influence on the ship airwake.

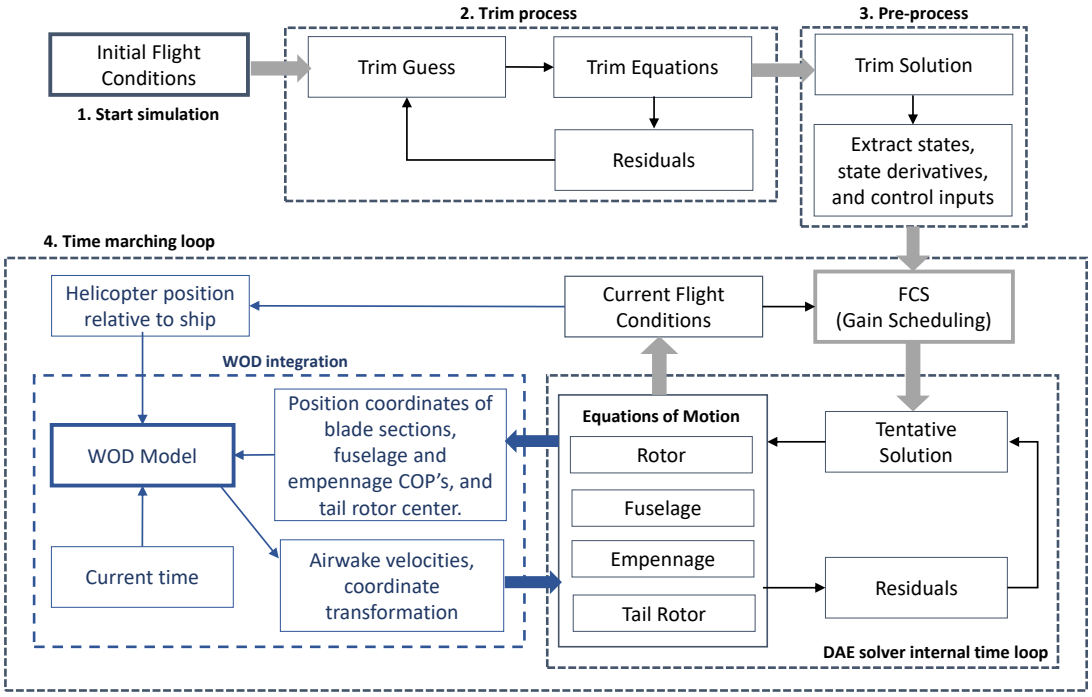

Figure 4.10: Flowchart depicting integration of WOD model into HeliUM2.

CHAPTER 5

Landing Gear and Ground Effect Modeling

It is important to account for landing dynamics and the influence of ground effect on helicopter response in the ship landing problem. This chapter describes the spring-damper based landing gear model employed in this study, as well as the two ground effect models considered.

5.1 Landing Gear Model

A standard UH-60A configuration with two main gears and one tail gear, shown in Fig. 5.1, is used in the simulations. The two main gears are referred to as the 'right' and 'left' gears when the helicopter is viewed from the rear. The dimensions in Fig. 5.1 are representative of the full-scale UH-60A helicopter [38]. Each gear is modeled as a massless spring-

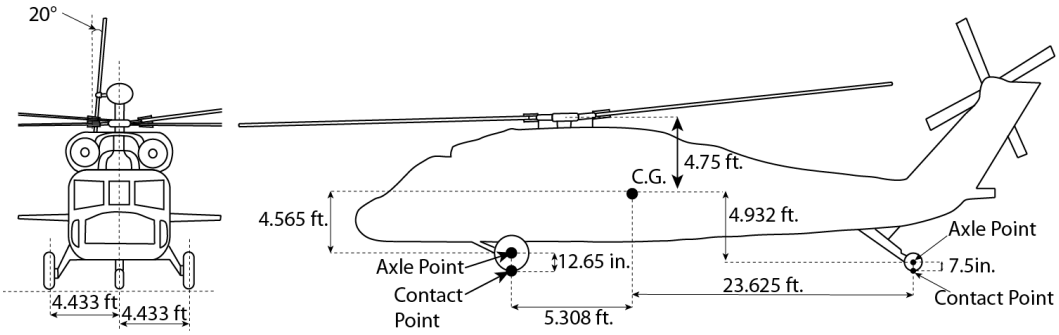

Figure 5.1: Landing gear geometry.

damper system in vertical direction, shown in Fig. 5.2. The vertical reaction force is given

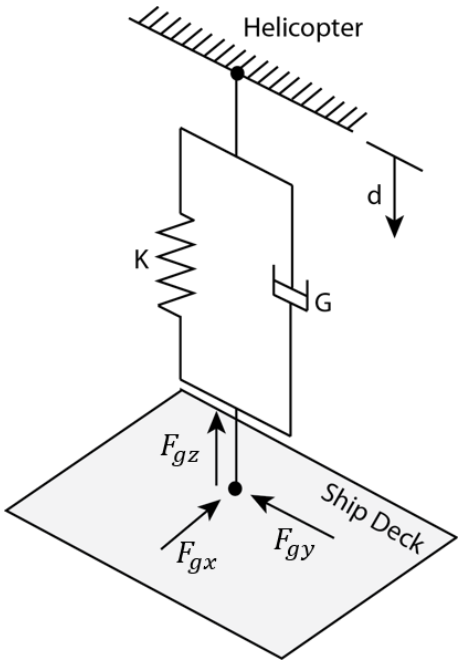

Figure 5.2: Landing gear model.

by

$$F_{gz} = Kd + G\dot{d}. \tag{5.1}$$

The gear deflection d is calculated as

$$d = z_{deck} - z_g, \tag{5.2}$$

where z_g is the height of the gear contact point, and z_{deck} is the height of the point directly below the gear on the ship deck as shown in Fig. 5.3. Both heights are relative to the inertial deck frame shown in the figure. Note that the deck axes are parallel to the ship axes shown in Fig. 4.1a. The height z_{deck} in Eq. (5.2) also depends on ship deck motion as shown in Fig. 5.3, and is determined as follows:

$$z_{deck} = z_{stat} + z_{dyn} + z_{ang}, \tag{5.3}$$

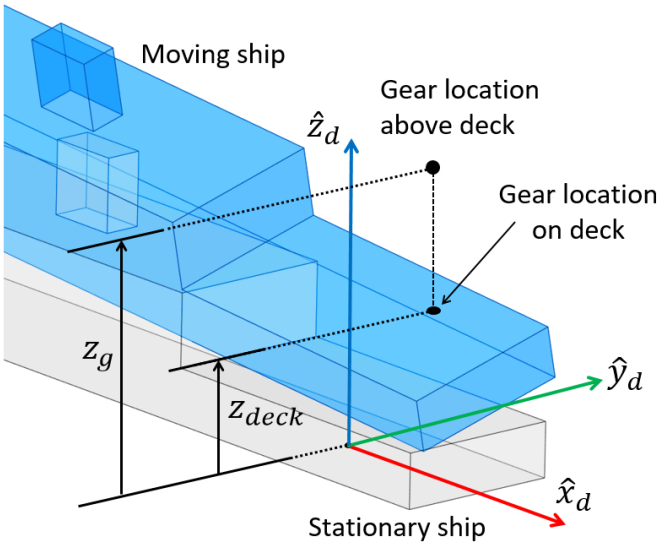

Figure 5.3: Illustration of heights used to determine gear deflection.

where $z_{stat} = 15$ ft. represents the height of the ship deck when it is level and stationary, z_{dyn} represents heave displacement, z_{ang} is the height contribution due to deck roll and pitch attitudes. Note that yaw attitude does not produce a height contribution, and is therefore not included. The different height contributions are illustrated in Fig. 5.4.

To determine z_{ang}, an order of rotation where the deck is allowed to roll and then pitch is assumed. The transformation for case is given by

$$\begin{bmatrix} x'_{ang} \\ y'_{ang} \\ z'_{ang} \end{bmatrix} = \begin{bmatrix} \cos\delta_{deck} & 0 & -\sin\delta_{deck} \\ 0 & 1 & 0 \\ \sin\delta_{deck} & 0 & \cos\delta_{deck} \end{bmatrix} \begin{bmatrix} 1 & 0 & 0 \\ 0 & \cos\Gamma_{deck} & \sin\Gamma_{deck} \\ 0 & -\sin\Gamma_{deck} & \cos\Gamma_{deck} \end{bmatrix} \begin{bmatrix} x_{ang} \\ y_{ang} \\ z_{ang} \end{bmatrix}, \tag{5.4}$$

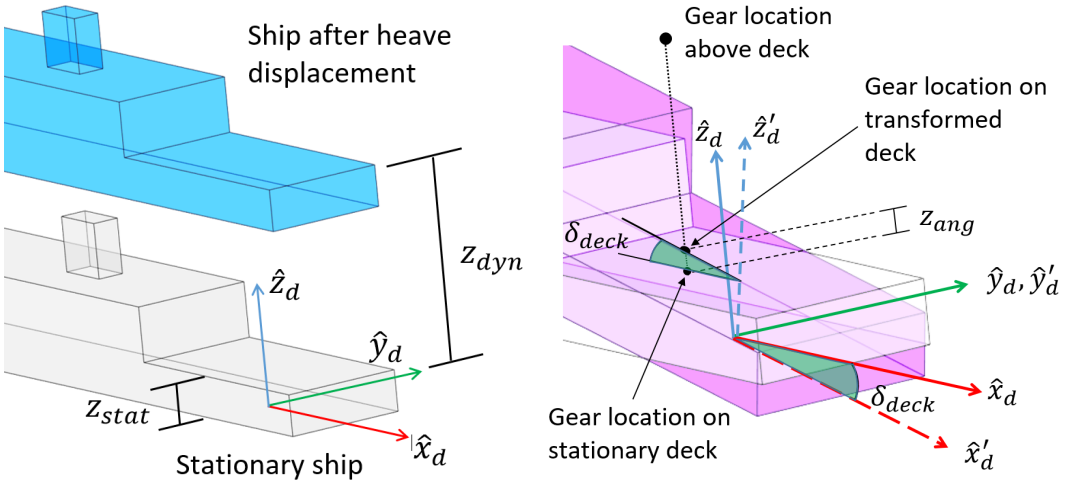

(a) Static deck height and heave displacement contributions to z_{deck}.

(b) Height contribution due to deck pitch attitude.

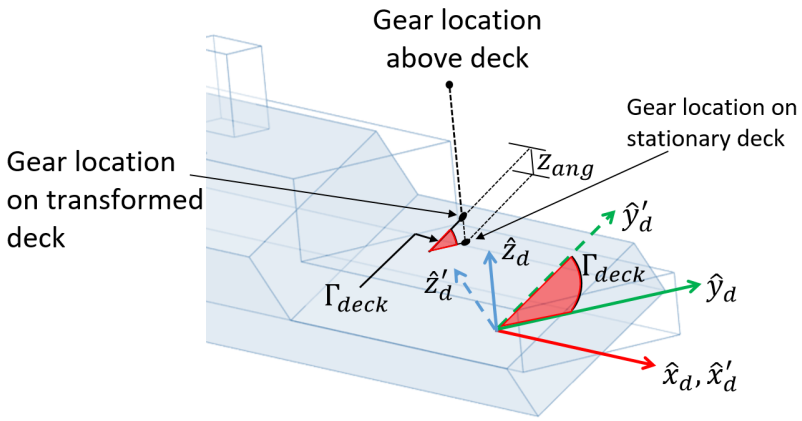

(c) Height contribution due to deck roll attitude.

Figure 5.4: Illustration of the different height contributions to z_{deck}.

or,

$$\begin{bmatrix} x'_{ang} \\ y'_{ang} \\ z'_{ang} \end{bmatrix} = \begin{bmatrix} \cos\delta_{deck} & \sin\delta_{deck}\sin\Gamma_{deck} & -\sin\delta_{deck}\cos\Gamma_{deck} \\ 0 & \cos\Gamma_{deck} & \sin\Gamma_{deck} \\ \sin\delta_{deck} & -\cos\delta_{deck}\sin\Gamma_{deck} & \cos\delta_{deck}\cos\Gamma_{deck} \end{bmatrix} \begin{bmatrix} x_{ang} \\ y_{ang} \\ z_{ang} \end{bmatrix}, \quad (5.5)$$

where Γ_{deck} is the roll angle about the positive $\hat{x}_d$ axis, δ_{deck} is the pitch angle about the

intermediate $\hat{y}_d$ axis, and

$$x_{ang} = r_{gx}, \tag{5.6}$$

$$y_{ang} = r_{gy}, \tag{5.7}$$

where r_{gx} and r_{gy} are the horizontal and lateral position coordinates of the gear from the target landing location, respectively, relative to the inertial deck frame. Since $z'_{ang} = 0$, the third row of the transformation in Eq. (5.5) yields

$$z'_{ang} = x_{ang}(\sin\delta_{deck}) - y_{ang}(\cos\delta_{deck}\sin\Gamma_{deck}) + z_{ang}(\cos\delta_{deck}\cos\Gamma_{deck}) = 0. \tag{5.8}$$

The height contribution due to deck rotation z_{ang} is thus given by

$$z_{ang} = \frac{r_{gy}\cos\delta_{deck}\sin\Gamma_{deck} - r_{gx}\sin\delta_{deck}}{\cos\delta_{deck}\cos\Gamma_{deck}}. \tag{5.9}$$

The deflection rate is given by

$$\dot{d} = \dot{z}_{deck} - \dot{z}_g. \tag{5.10}$$

For simplicity, it is assumed that $\dot{z}_{deck} = 0$ for all ship conditions. Assuming that the landing gear is rigidly connected to the fuselage, $\dot{z}_g$ represents the vertical component of the velocity at the gear contact point, given by

$$\begin{aligned}\mathbf{V}_g &= \mathbf{V}_{CG} + \Omega \times \mathbf{r}_g \\ &= \begin{bmatrix} u \\ v \\ w \end{bmatrix} + \begin{bmatrix} p \\ q \\ r \end{bmatrix} \times \begin{bmatrix} r_x \\ r_y \\ r_z \end{bmatrix} = \begin{bmatrix} u + qr_z - rr_y \\ v - pr_z + rr_x \\ w + pr_y - qr_x \end{bmatrix},\end{aligned} \tag{5.11}$$

where $\mathbf{r}_g$ is the position vector of the gear relative to the CG with components r_x, r_y, and r_z. The gear deflection rate $\dot{d}$ is thus given as

$$\dot{d} = w + pr_y - qr_x. \tag{5.12}$$

When the gear is **not** in contact with the deck (that is, d from Eq. (5.2) is negative), the reaction force F_{gz} in Eq. (5.1) is set to zero.

Gear reaction forces in the plane of the deck are due to surface friction and are given by

$$F_{gx} = \mu_x F_N, \tag{5.13}$$

$$F_{gy} = \mu_y F_N, \tag{5.14}$$

where μ_x and μ_y are the friction coefficients, and F_N is the normal reaction force from the deck, set equal to F_{gz} in this study. The values for the stiffness and damping constants in Eq. (5.1) were determined by modifying those given in Ref. 38. The final values are given in Table 5.1, together with the surface friction coefficients. The friction coefficients given in Ref. 38 were reduced by 30% to account for surface wetness [89].

Table 5.1: Landing gear parameters

	K (lbf/ft)	G (lbf-s/ft)	μ_x	μ_y
Main gears	2.54×10^4	3.42×10^3	0.42	0.42
Tail gear	6.06×10^4	1.05×10^3	0.042	0.42

The gear reaction forces and the resulting moments contribute to the fuselage external loads in Eqs. (2.132) to (2.137)

$$\mathbf{F}_{LG} = \left\{ \begin{array}{c} X_{LG} \\ Y_{LG} \\ Z_{LG} \end{array} \right\} = \left\{ \begin{array}{c} F_{gx} \\ F_{gy} \\ F_{gz} \end{array} \right\}, \tag{5.15}$$

$$\mathbf{M}_{LG} = \left\{ \begin{array}{c} L_{LG} \\ M_{LG} \\ N_{LG} \end{array} \right\} = \mathbf{r}_g \times \mathbf{F}_{LG}. \tag{5.16}$$

5.2 Ground Effect Model

During helicopter shipboard operations, the deck represents an impermeable surface that causes the helicopter downwash to turn back towards the vehicle thus modifying the rotor thrust, as shown in Fig. 5.5. For accurate and realistic modeling of helicopter dynamics

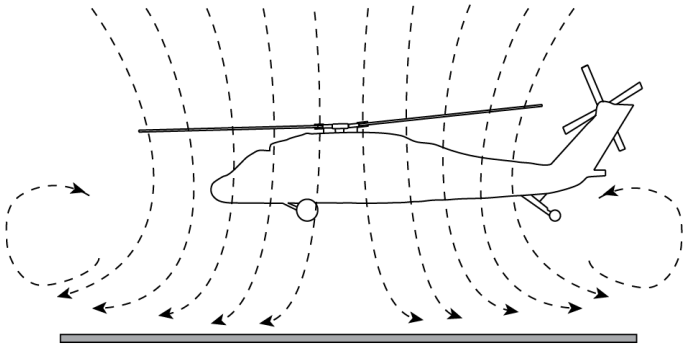

Figure 5.5: Illustration of ground effect.

during ship landing, the ground effect must be taken into account. Two different ground effect models, a simple correction factor model and a dynamic inflow based finite-state model used, are used in this study.

5.2.1 Simple ground effect model

The Cheeseman and Bennett model [44, 48] was used first. It is based on the image rotor concept, illustrated in Fig. 1.9, to satisfy the impermeable surface BC. The model provides a scaling factor that accounts for the increased thrust due to ground effect during hover at

constant power,

$$\left[\frac{T_{IGE}}{T_{OGE}}\right]_{P=const} = \frac{1}{1-\left(\frac{R}{4z_h}\right)^2} = \frac{1}{k_G}. \tag{5.17}$$

From momentum theory, $C_P = C_T\lambda$. Thus, the influence of ground effect also corresponds to a reduction in rotor power at constant thrust

$$\left[\frac{P_{OGE}}{P_{IGE}}\right]_{T=const} = \left[\frac{\lambda_{OGE}}{\lambda_{IGE}}\right] = \left[\frac{T_{IGE}}{T_{OGE}}\right]_{P=const} = \frac{1}{k_G}. \tag{5.18}$$

The ground effect is used to modify the local inflow at the individual rotor blade stations by multiplying the inflow velocity vector $\mathbf{V}_I$ in Eq. (2.37) by the scaling factor k_G. However, this model is not accurate for $z_h/R < 0.5$ [48]. Furthermore, it is a static model and does not account for ground motion. Therefore, a more sophisticated model based on dynamic inflow was implemented as described next.

5.2.2 Finite-state ground effect model

The finite-state ground effect model developed in Ref. 58 is based on the He-Peters dynamic inflow model [59]. The model can be used for partial, inclined and dynamic ground planes. Furthermore, since it is based on a dynamic inflow model formulated in state-space form, the model can be readily integrated into the flight simulation. A description of the He-Peters dynamic inflow model [59] is provided first, followed by a description of the finite-state ground effect model and its implementation.

5.2.2.1 Review of He-Peters dynamic inflow model

The He-Peters dynamic inflow model is based on the following assumptions:

- Flow is inviscid, and thus governed by Euler equations with an acceleration potential (or a pressure potential) Φ_R.

- Pressure distribution over the rotor disc is continuous but has a discontinuity across the disc.
- Flow is incompressible and as such, density is constant and continuity is satisfied.
- The rotor disc is considered to be a flat orientable disc.

Based on these assumptions the dynamic inflow model is derived from a linearized conservation of momentum equation

$$\frac{\partial \mathbf{q}_v}{\partial \bar{t}} + \mathbf{V}_\infty.(\nabla \mathbf{q}_v) = -\nabla \Phi_R, \tag{5.19}$$

where $\mathbf{q}_v$ is the vector containing perturbations in the flow velocity vector, and $\mathbf{V}_\infty$ is the freestream velocity. Taking advantage of the superposition principle of linear equations, Eq. (5.19) is divided into unsteady and convective parts as follows:

$$\frac{\partial \mathbf{q}_v}{\partial \bar{t}} = -\nabla \Phi_R^{(t)}, \tag{5.20}$$

$$\mathbf{V}_\infty.(\nabla \mathbf{q}_v) = \nabla \Phi_R^{(c)}, \tag{5.21}$$

where $\nabla \Phi_R^{(t)}$ and $\nabla \Phi_R^{(c)}$ represent the unsteady and convective parts of $\nabla \Phi_R$, respectively.

The vertical component of $\mathbf{q}_v$ is conventionally referred to as the 'induced' or 'inflow' velocity, and the horizontal, lateral components are generally neglected. From Eq. (5.21), an expression for the inflow velocity w is obtained by integrating along a non-dimensional streamline coordinate ξ

$$w_R = -\frac{1}{V_\infty} \int_0^\infty \frac{\partial \Phi_R^{(c)}}{\partial z_R} d\xi. \tag{5.22}$$

Note that ξ is positive upstream while freestream flows downwards [90], as illustrated in Fig. 5.6, hence the negative sign in Eq. (5.22). The freestream velocity vector $\mathbf{V}_\infty$ also becomes a scalar quantity along the streamline coordinate.

An expression for the rate of change of the induced velocity $\dot{w}$ is obtained from Eq.

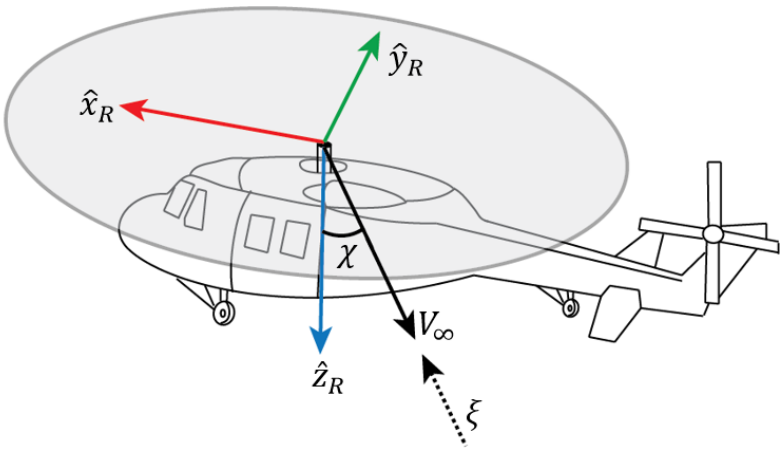

Figure 5.6: Rotor coordinate system and freestream coordinate.

(5.20)

$$\dot{w_R} = \frac{\partial w_R}{\partial \bar{t}} = -\frac{\partial \Phi_R^{(t)}}{\partial z_R}. \tag{5.23}$$

The actions of integration and differentiation in Eqs. (5.22) and (5.23) are then represented as linear transformations that yield w and $\dot{w}$ when applied on $\Phi_R^{(c)}$ and $\Phi_R^{(t)}$, respectively. That is,

$$w_R = L_I[\Phi_R^{(c)}], \tag{5.24}$$

$$\dot{w}_R = E_I[\Phi_R^{(t)}]. \tag{5.25}$$

The formulation further assumes that the L and E transformations are invertible, such that the following relations hold

$$L_I^{-1}[w_R] = \Phi_R^{(c)}, \tag{5.26}$$

$$E_I^{-1}[\dot{w}_R] = \Phi_R^{(t)}. \tag{5.27}$$

The expressions in Eqs. (5.26) and (5.27) allow for the momentum equations in Eq. (5.19) to be rewritten as

$$E_I^{-1}[\dot{w}_R] + L_I^{-1}[w_R] = \Phi_R^{(c)} + \Phi_R^{(t)} = \Phi_R. \tag{5.28}$$

A pressure potential satisfying the momentum equations in Eq. (5.28) is obtained by

solving the Laplace's equation

$$\nabla^2 \Phi_R^{(t)} = 0, \tag{5.29}$$

$$\nabla^2 \Phi_R^{(c)} = 0, \tag{5.30}$$

$$\nabla^2 \Phi_R = \nabla^2 \Phi_R^{(t)} + \nabla^2 \Phi_R^{(c)} = 0, \tag{5.31}$$

for two boundary conditions [90]: a) Φ_R becomes zero at infinity and b) Φ_R becomes zero at the edge of the rotor. Using an ellipsoidal coordinate system with origin at the rotor disk center, solutions to the Laplace's equation in rotorcraft applications are conveniently given by the associated Legendre functions as follows [90, 91]

$$\begin{aligned}\Phi_R(\nu_R, \eta_R, \psi_R, \bar{t}) \;&= \sum_{m=0}^{\infty} \sum_{n=m+1,m+3,..}^{\infty} P_n^m(\nu_R) Q_n^m(i\eta_R)[C_n^m(\bar{t}) \cos(m\psi_R) \\ &\qquad + D_n^m(\bar{t}) \sin(m\psi_R)],\end{aligned} \tag{5.32}$$

where $P_n^m(\nu_R)$ and $Q_n^m(i\eta_R)$ are associated Legendre functions of the first and second kinds, respectively. Sets of these functions with $n = m+1, m+3, m+5, ...$ satisfy the two boundary conditions and are suitable for representing the pressure gap between the upper and lower surfaces of the disc. An illustration of the elliptical coordinate system is given in Fig. 5.7. The entire 3-D space can be covered once if the coordinates are restricted as follows

$$-1 \leq \nu_R \leq +1, \tag{5.33}$$

$$0 \leq \eta_R \leq \infty, \tag{5.34}$$

$$0 \leq \psi_R \leq 2\pi. \tag{5.35}$$

On the rotor disc, $\eta_R = 0$ and $\nu_R = \sqrt{1 - \bar{r}^2}$, where $\bar{r}$ is a nondimensional radial coordinate. Also, ν_R is positive above the rotor disk and negative below the rotor disk. The rotor

lift can thus be expressed as

$$\begin{aligned} L_R(\bar{r},\psi_R,\bar{t}) &= \Phi_R(\nu_R<0,\eta_R=0,\psi_R,\bar{t}) - \Phi_R(\nu_R>0,\eta_R=0,\psi_R,\bar{t}) \\ &= \sum_{m=0}^{\infty}\sum_{n=m+1,m+3,..}^{\infty} \bar{P}_n^m(\nu_R)[\tau_n^{mc}(\bar{t})\cos(m\psi_R)+\tau_n^{ms}(\bar{t})\sin(m\psi_R)], \end{aligned} \tag{5.36}$$

where

$$\bar{P}_n^m(\nu_R) = (-1)^m\left(\frac{P_n^m(\nu_R)}{\rho_n^m}\right), \tag{5.37}$$

$$\rho_n^m = \sqrt{\frac{1}{2n+1}\frac{(n+m)!}{(n-m)!}}, \tag{5.38}$$

$$\tau_n^{mc} = (-1)^{m+1}2Q_n^m(i0)\rho_n^m C_n^m, \tag{5.39}$$

$$\tau_n^{ms} = (-1)^{m+1}2Q_n^m(i0)\rho_n^m D_n^m, \tag{5.40}$$

with $\bar{P}_n^m(\nu_R)$ representing the normalized associated Legendre function of the first kind.

For consistency with the lift function defined in Eq. (5.36), the pressure potential given in Eq. (5.32) is normalized to yield

$$\begin{aligned} \Phi_R(\nu_R,\eta_R,\psi_R,\bar{t}) \;\; = -\tfrac{1}{2}\sum_{m=0}^{\infty}\sum_{n=m+1,m+3,..}^{\infty} \bar{P}_n^m(\nu_R)\bar{Q}_n^m(i\eta_R)[\tau_n^{mc}(\bar{t})\cos(m\psi_R) \\ +\tau_n^{ms}(\bar{t})\sin(m\psi_R)], \end{aligned} \tag{5.41}$$

where $\bar{Q}_n^m = Q_n^m(i\eta_R)/Q_n^m(i0)$.

The induced flow distribution at the rotor disk is expressed by

$$w_R(\bar{r},\psi_R,\bar{t}) = \sum_{r=0}^{\infty}\sum_{j=r+1,r+3,..}^{\infty} \phi_j^r(\bar{r})[\alpha_j^{rc}(\bar{t})\cos(r\psi_R)+\alpha_j^{rs}(\bar{t})\sin(r\psi_R)], \tag{5.42}$$

where $\phi_n^m = \bar{P}_n^m(\nu_R)/\nu_R$ represent a complete set of orthogonal functions, and are simple

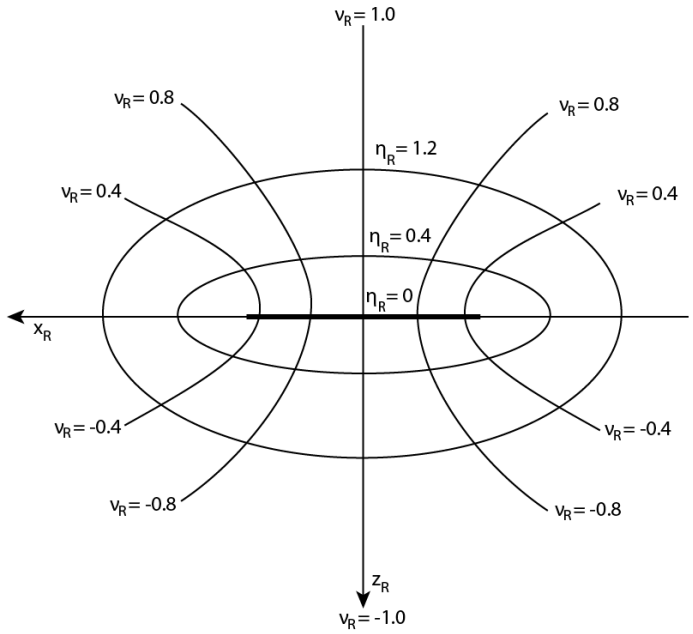

Figure 5.7: An illustration of the elliptic coordinate system around the rotor disk [58].

radial polynomials given by

$$\phi_n^m(\bar{r}) = \sqrt{(2n+1)H_n^m} \sum_{q=m,m+2,\ldots}^{n-1} \bar{r}^2 (-1)^{(q-m)/2} \frac{(n+q)!!}{(q-m)!!(q+m)!!(n-q-1)!!}, \tag{5.43}$$

with

$$H_n^m \equiv \frac{(n+m-1)!!(n-m-1)!!}{(n+m)!!(n-m)!!}. \tag{5.44}$$

A relation between the unknown coefficients $\alpha_j^{rc}(\bar{t})$ and $\alpha_j^{rs}(\bar{t})$ in Eq. (5.42) and the lift coefficients $\tau_n^{mc}(\bar{t})$ and $\tau_n^{ms}(\bar{t})$ in Eq. (5.41) is established using Eq. (5.28). The process yields a set of first-order ODEs

$$[M_{DI}]\{\dot{\alpha}\} + 2V_m[L_{DI}]^{-1}\{\alpha\} = \{\tau\}, \tag{5.45}$$

where $[M_{DI}]$ is the apparent mass matrix, V_m is the mass flow parameter, and $[L_{DI}]$ is referred to as the gain matrix. Closed form expressions for the $[M_{DI}]$ and $[L_{DI}]$ in Eq.

(5.45) have been derived in Ref. 92. The vector $\boldsymbol{\tau}$ in Eq. (5.45) contains the pressure coefficients given in Eq. (5.36), which can be expressed as [93]

$$\tau_n^{0c} = \frac{1}{2\pi} \sum_{k=1}^{N_b} \left[\int_0^1 \frac{L_{circ}(\bar{r}, \bar{t})}{\rho \Omega^2 R^3} \phi_n^0 d\bar{r} \right], \tag{5.46}$$

$$\tau_n^{mc} = \frac{1}{\pi} \sum_{k=1}^{N_b} \left[\int_0^1 \frac{L_{circ}(\bar{r}, \bar{t})}{\rho \Omega^2 R^3} \phi_n^m d\bar{r} \right] \cos(m\psi_k), \tag{5.47}$$

$$\tau_n^{ms} = \frac{1}{\pi} \sum_{k=1}^{N_b} \left[\int_0^1 \frac{L_{circ}(\bar{r}, \bar{t})}{\rho \Omega^2 R^3} \phi_n^m d\bar{r} \right] \sin(m\psi_k), \tag{5.48}$$

where L_{circ} represents the blade sectional circulatory lift. In this study, L_{circ} is determined by transforming the distributed aerodynamic loads $\mathbf{p}_{\mathrm{A}}$ in Eq. (2.61) from the undeformed, preconed coordinate frame to the rotating hub frame using the transformation from Eq. (2.14), and retaining *only the resulting vertical component*. Thus,

$$L_{circ} = \mathbf{p}_{\mathrm{A}}(1) \sin \beta_p + \mathbf{p}_{\mathrm{A}}(3) \cos \beta_p, \tag{5.49}$$

where $\mathbf{p}_{\mathrm{A}}(1)$ and $\mathbf{p}_{\mathrm{A}}(3)$ represent the distributed aerodynamic load components along the $\mathbf{e}_x$ and $\mathbf{e}_z$ directions of the undeformed, preconed coordinate frame, respectively.

5.2.2.2 Ground effect model for static case

The ground plane is modeled as a distributed plane of source terms as shown in Fig. 1.10. The effect of the source plane is modeled as an additional pressure distribution Φ_G in the flowfield satisfying the boundary condition

$$\Phi_G(z = z_h) = \Phi_R(z = z_h), \tag{5.50}$$

where Φ_R represents the pressure from main rotor. Thus, Φ_G is expressed as

$$\Phi_G(\nu_G, \eta_G, \psi_G, \bar{t}) = -\frac{1}{2}\sum_{l=0}^{\infty}\sum_{k=l,l+2,..}^{\infty} \bar{P}_k^l(\nu_G)\bar{Q}_k^l(\imath\eta_G)[\sigma_k^{lc}(t)\cos(l\psi_G) + \sigma_k^{ls}(t)\sin(l\psi_G)], \tag{5.51}$$

where the Legendre functions $\bar{P}_k^l(\nu_G)$ and $\bar{Q}_k^l(\imath\eta_G)$ are expressed in a different ellipsoidal coordinate system $(\hat{\nu}_G, \hat{\eta}_G, \hat{\psi}_G)$ with its origin at the center of the rotor wake footprint on the ground plane. Note that in contrast to the $(n+m)$ = odd terms used in Eq. (5.41) to represent the main rotor pressure discontinuity, $(k+l)$ = even terms are used to represent the source distribution. Transformation between the rotor and the ground ellipsoidal coordinate systems

$$(\nu_G, \eta_G, \psi_G) = F(\nu_R, \eta_R, \psi_R), \tag{5.52}$$

is dependent on the flight condition and parameters such as the height of the rotor above the ground z_h, pitch inclination angle of the ground plane δ, roll inclination angle of the ground plane Γ, angle of attack of the rotor tip path plane α_{TPP}, angle Ψ between the rotor and ground x axes, and the rotor wake skew angle χ. An illustration of the two coordinate systems in a hovering flight is given in Fig. 5.8.

The Cartesian coordinates are related to the elliptic coordinates as follows:

$$\begin{aligned} x_R &= -\sqrt{1-\nu_R^2}\sqrt{1+\eta_R^2}\cos\psi_R, \\ y_R &= \sqrt{1-\nu_R^2}\sqrt{1+\eta_R^2}\sin\psi_R, \\ z_R &= -\nu_R\eta_R, \end{aligned} \tag{5.53}$$

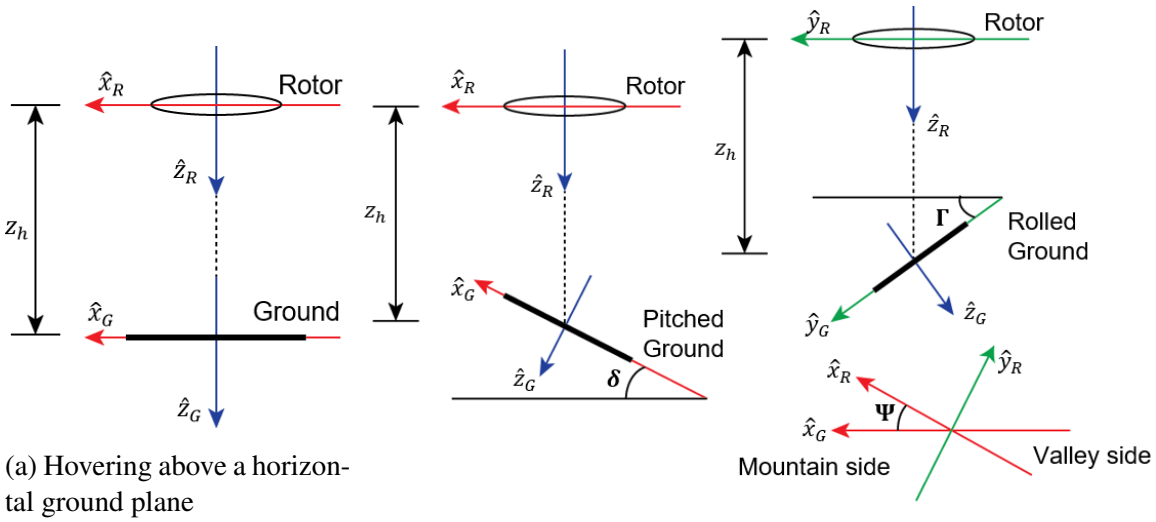

(a) Hovering above a horizontal ground plane

(b) Hovering above an inclined ground plane

Figure 5.8: Coordinate systems for a hovering flight in ground effect.

or

$$\begin{aligned}
\nu_R &= -\frac{1}{\sqrt{2}}\,\mathrm{sign}(z_R)\sqrt{(1-S)+\sqrt{(1-S)^2+4z_R^2}},\\
\eta_R &= \frac{1}{\sqrt{2}}\sqrt{(S-1)+\sqrt{(1-S)^2+4z_R^2}},\\
\psi_R &= \arctan\left(-\frac{y_R}{x_R}\right),
\end{aligned} \tag{5.54}$$

where $S = x_R^2 + y_R^2 + z_R^2$. Transformation from rotor to ground Cartesian coordinate systems is given as

$$\begin{bmatrix} x_G \\ y_G \\ z_G \end{bmatrix} = \begin{bmatrix} 1 & 0 & 0 \\ 0 & \cos\Gamma & \sin\Gamma \\ 0 & -\sin\Gamma & \cos\Gamma \end{bmatrix} \begin{bmatrix} \cos\delta & 0 & -\sin\delta \\ 0 & 1 & 0 \\ \sin\delta & 0 & \cos\delta \end{bmatrix} \begin{bmatrix} \cos\Psi & -\sin\Psi & 0 \\ \sin\Psi & \cos\Psi & 0 \\ 0 & 0 & 1 \end{bmatrix} \times \left(\begin{bmatrix} \cos\alpha_{TPP} & 0 & -\sin\alpha_{TPP} \\ 0 & 1 & 0 \\ \sin\alpha_{TPP} & 0 & \cos\alpha_{TPP} \end{bmatrix} \begin{bmatrix} x_R \\ y_R \\ z_R \end{bmatrix} - \begin{bmatrix} \Delta x \\ 0 \\ \Delta z \end{bmatrix} \right), \tag{5.55}$$

where

$$\Delta z = \frac{z_h}{1 - \tan(\alpha_{TPP} + \chi)\tan\delta},$$

$$\Delta x = -\Delta z \tan(\alpha_{TPP} + \chi),$$

$$\chi = \arctan\left(\frac{\pi^2 \mu}{4\lambda}\right).$$

The transformation function F in Eq. (5.52) is derived using Eqs. (5.53), (5.54), and (5.55) for a given flight condition. Note that the roll inclination of the ground plane Γ was not included in Ref. 58.

Since the source-like pressure distribution of the ground does not alter the mass flow but only redirects it, the main rotor and ground pressure distributions can share a common freestream. The total pressure distribution is then the superposition of the two

$$\Phi = \Phi_R + \Phi_G. \tag{5.56}$$

By applying the pressure boundary condition on the ground surface

$$\Phi_G|_{\eta_G=0} = \Phi_R|_{\eta_G=0}, \tag{5.57}$$

the ground pressure coefficients can be related to the rotor pressure coefficients in a matrix form as

$$\{\sigma\} = [B_G]\{\tau\}, \tag{5.58}$$

where the expressions for the elements of matrix $\mathbf{B}_G$ are given by [58]:

$$\begin{aligned}
(B_{kn}^{0m})^{cc} &= \tfrac{1}{2\pi}\int_0^{2\pi}\int_0^1 \bar{P}_k^0(\nu_G)[\bar{P}_n^m(\nu_R)\bar{Q}_n^m(\iota\eta_R)\cos(m\psi_R)]_{\eta_G=0}\, d\eta_G d\psi_G \\
(B_{kn}^{0m})^{cs} &= \tfrac{1}{2\pi}\int_0^{2\pi}\int_0^1 \bar{P}_k^0(\nu_G)[\bar{P}_n^m(\nu_R)\bar{Q}_n^m(\iota\eta_R)\sin(m\psi_R)]_{\eta_G=0}\, d\eta_G d\psi_G \\
&\text{for } l = 0.
\end{aligned} \tag{5.59}$$

and

$$
\begin{aligned}
(B_{kn}^{lm})^{cc} &= \tfrac{1}{\pi}\int_0^{2\pi}\int_0^1 \bar{P}_k^l(\nu_G)\cos(l\psi_G)[\bar{P}_n^m(\nu_R)\bar{Q}_n^m(\imath\eta_R)\cos(m\psi_R)]_{\eta_G=0}\, d\eta_G d\psi_G \\
(B_{kn}^{lm})^{cs} &= \tfrac{1}{\pi}\int_0^{2\pi}\int_0^1 \bar{P}_k^l(\nu_G)\cos(l\psi_G)[\bar{P}_n^m(\nu_R)\bar{Q}_n^m(\imath\eta_R)\sin(m\psi_R)]_{\eta_G=0}\, d\eta_G d\psi_G \\
(B_{kn}^{lm})^{sc} &= \tfrac{1}{\pi}\int_0^{2\pi}\int_0^1 \bar{P}_k^l(\nu_G)\sin(l\psi_G)[\bar{P}_n^m(\nu_R)\bar{Q}_n^m(\imath\eta_R)\cos(m\psi_R)]_{\eta_G=0}\, d\eta_G d\psi_G \\
(B_{kn}^{lm})^{ss} &= \tfrac{1}{\pi}\int_0^{2\pi}\int_0^1 \bar{P}_k^l(\nu_G)\sin(l\psi_G)[\bar{P}_n^m(\nu_R)\bar{Q}_n^m(\imath\eta_R)\sin(m\psi_R)]_{\eta_G=0}\, d\eta_G d\psi_G \\
&\text{for } l > 0. \qquad (5.60)
\end{aligned}
$$

Recurrence relations used to derive the normalized associated Legendre functions $\bar{P}$ and $\bar{Q}$ are provided in Appendix A. Note that Eq. (5.57) is applied only within rotor wake footprint because most of the momentum is located inside this area [58]. The effect of ground effect on the induced flow at the rotor disk is an upward velocity, thus, the in-ground-effect induced velocity is given by

$$w^{IGE} = -\frac{1}{V_\infty}\int_0^\infty \frac{\partial \Phi_R^{(c)}}{\partial z_R} d\xi - \frac{1}{V_\infty}\int_0^\infty \frac{\partial \Phi_G}{\partial z_G} d\xi. \qquad (5.61)$$

or

$$w^{IGE} = w_R - w_G, \qquad (5.62)$$

where w is the induced velocity without any ground effect as given in Eq. (5.42), and

$$w_G = \frac{1}{V_\infty}\int_0^\infty \frac{\partial \Phi_G}{\partial z_G} d\xi, \qquad (5.63)$$

is the induced velocity due to ground effect. Similar to Eq. (5.42), the ground induced velocity is expressed as

$$w_G(\bar{r}, \psi_R, \bar{t}) = \sum_{r=0}^{\infty}\sum_{j=r+1,r+3,..}^{\infty} \phi_j^r(\bar{r})[\beta_j^{rc}(\bar{t})\cos(r\psi_R) + \beta_j^{rs}(\bar{t})\sin(r\psi_R)]. \qquad (5.64)$$

Substituting Eq. (5.64) and Eq. (5.51) into Eq. (5.63) yields a matrix equation

$$\{\beta\} = \frac{1}{2V_m}[A_G]\{\sigma\} \tag{5.65}$$

where the mass flow parameter V_m is the same as that used for the main rotor in Eq. (5.45), and the expressions for the elements of matrix $\mathbf{A}_G$ are given as [58]:

$$\begin{aligned}
(A_{jk}^{0l})^{cc} &= \frac{1}{2\pi}\int_0^{2\pi}\int_0^1 \bar{P}_j^0(\nu_R)[\bar{P}_k^l(\nu_G)\bar{Q}_k^l(\imath\eta_G)\cos(l\psi_G)]_{\eta=0}\, d\nu_R d\psi_R \\
(A_{jk}^{0l})^{cs} &= \frac{1}{2\pi}\int_0^{2\pi}\int_0^1 \bar{P}_j^0(\nu_R)[\bar{P}_k^l(\nu_G)\bar{Q}_k^l(\imath\eta_G)\sin(l\psi_G)]_{\eta=0}\, d\nu_R d\psi_R \\
&\text{for} \quad r = 0
\end{aligned} \tag{5.66}$$

and

$$\begin{aligned}
(A_{jk}^{rl})^{cc} &= \frac{1}{\pi}\int_0^{2\pi}\int_0^1 \bar{P}_j^r(\nu_R)\cos(r\psi_R)[\bar{P}_k^l(\nu_G)\bar{Q}_k^l(\imath\eta_G)\cos(l\psi_G)]_{\eta=0}\, d\nu_R d\psi_R \\
(A_{jk}^{rl})^{cs} &= \frac{1}{\pi}\int_0^{2\pi}\int_0^1 \bar{P}_j^r(\nu_R)\cos(r\psi_R)[\bar{P}_k^l(\nu_G)\bar{Q}_k^l(\imath\eta_G)\sin(l\psi_G)]_{\eta=0}\, d\nu_R d\psi_R \\
(A_{jk}^{rl})^{sc} &= \frac{1}{\pi}\int_0^{2\pi}\int_0^1 \bar{P}_j^r(\nu_R)\sin(r\psi_R)[\bar{P}_k^l(\nu_G)\bar{Q}_k^l(\imath\eta_G)\cos(l\psi_G)]_{\eta=0}\, d\nu_R d\psi_R \\
(A_{jk}^{rl})^{ss} &= \frac{1}{\pi}\int_0^{2\pi}\int_0^1 \bar{P}_j^r(\nu_R)\sin(r\psi_R)[\bar{P}_k^l(\nu_G)\bar{Q}_k^l(\imath\eta_G)\sin(l\psi_G)]_{\eta=0}\, d\nu_R d\psi_R \\
&\text{for} \quad r > 0
\end{aligned} \tag{5.67}$$

Combining Eqs. (5.65) and (5.58) yields

$$\{\beta\} = \frac{1}{2V_m}[G_G]\{\tau\}, \tag{5.68}$$

where the ground influence coefficient matrix $\mathbf{G}_G$ is defined as

$$\begin{bmatrix} (G_{jn}^{rm})^{cc} & (G_{jn}^{rm})^{cs} \\ (G_{jn}^{rm})^{sc} & (G_{jn}^{rm})^{ss} \end{bmatrix} = \begin{bmatrix} (A_{jk}^{rl})^{cc} & (A_{jk}^{rl})^{cs} \\ (A_{jk}^{rl})^{sc} & (A_{jk}^{rl})^{ss} \end{bmatrix} \begin{bmatrix} (B_{kn}^{lm})^{cc} & (B_{kn}^{lm})^{cs} \\ (B_{kn}^{lm})^{sc} & (B_{kn}^{lm})^{ss} \end{bmatrix} \tag{5.69}$$

or simply

$$[G_G] = [A_G][B_G], \tag{5.70}$$

where

$$r, l, m = 0, 1, 2, \ldots,$$

$$j = r + 1, r + 3, \ldots,$$

$$k = l, l + 2, l + 4, \ldots,$$

$$n = m + 1, m + 3, \ldots.$$

The effective inflow distribution at the rotor disk can be written as

$$w^{IGE}(\bar{r}, \psi_R, \bar{t}) = \sum_{r=0}^{\infty} \sum_{j=r+1,r+3,..}^{\infty} \phi_j^r(\bar{r}) \left[(\alpha_j^{rc}(\bar{t}))^{IGE} \cos(r\psi_R) + (\alpha_j^{rs}(\bar{t}))^{IGE} \sin(r\psi_R) \right], \tag{5.71}$$

where the in-ground-effect inflow coefficients are determined by

$$\boldsymbol{\alpha}^{IGE} = \boldsymbol{\alpha} - \boldsymbol{\beta}, \tag{5.72}$$

and where $\boldsymbol{\alpha}$ and $\boldsymbol{\beta}$ are determined from Eqs. (5.45) and (5.68), respectively. Note that the in-gound-effect dynamic inflow model is expressed as a set of ODEs that can be easily integrated into a flight simulation program.

5.2.2.3 Ground effect model for dynamic case

In the case of a dynamic ground, an additional pressure perturbation is used to capture the effect of ground plane motion on rotor inflow. The ground pressure perturbation is expressed as

$$\Phi_G = \Phi_G^S + \Phi_G^D \tag{5.73}$$

where Φ_G^S represents the static ground effect, and Φ_G^D represents the effect due to ground motion. If g_z is the normal component of the ground plane velocity, the wake footprint can

be imagined to be a fan turning with an induced velocity equal to g_z. Based on this analogy, the pressure perturbation due to ground motion must have a discontinuity across the ground plane, denoted as $\Delta\Phi_G^D$, and expanded as

$$\Delta\Phi_G^D = V_m \sum_{p=0}^{\infty} \sum_{i=p+1,p+3,..}^{\infty} \bar{P}_i^p(\nu_G)[\gamma_i^{pc}(t)\cos(p\psi_G) + \gamma_i^{ps}(t)\sin(p\psi_G)]. \tag{5.74}$$

The "ground fan" is assumed to share a common mass flow parameter V_m with the helicopter rotor, thus, the pressure perturbation

$$\Delta\Phi_G^D = V_m g_z. \tag{5.75}$$

Using Eqs. (5.74) and (5.75), the ground velocity coefficients are given as [58]

$$\gamma_i^{0c} = \frac{1}{2\pi}\int_0^{2\pi}\int_0^1 \bar{P}_i^0(\nu_G) g_z(\nu_G,\psi_G) d\nu_G d\psi_G, \qquad \text{for } p = 0, \tag{5.76}$$

and

$$\gamma_i^{pc} = \frac{1}{\pi}\int_0^{2\pi}\int_0^1 \bar{P}_i^p(\nu_G) g_z(\nu_G,\psi_G)\cos(p\psi_G)\, d\nu_G d\psi_G, \tag{5.77}$$

$$\gamma_i^{ps} = \frac{1}{\pi}\int_0^{2\pi}\int_0^1 \bar{P}_i^p(\nu_G) g_z(\nu_G,\psi_G)\sin(p\psi_G)\, d\nu_G d\psi_G, \qquad \text{for } p > 0. \tag{5.78}$$

The ground velocity of a rigid ground plane is generally given by

$$g_z = g_{z0} + g_{zc}\hat{\bar{r}}\cos\psi_G + g_{zs}\hat{\bar{r}}\sin\psi_G, \tag{5.79}$$

where g_{z0} is the ground heave velocity, g_{zc} is the ground pitching velocity, g_{zs} is the ground rolling velocity, and $\hat{\bar{r}}$ is a nondimensional radial coordinate on the ground wake footprint. With the expression of g_z given in Eq. (5.79), the ground velocity coefficients in Eqs. (5.76)

to (5.78) become

$$\gamma_i^{0c} = g_{z0} \int_0^1 \bar{P}_i^0(\nu_G) d\nu_G, \tag{5.80}$$

$$\gamma_i^{1c} = g_{zc} \int_0^1 \sqrt{1-\nu_G^2}\bar{P}_i^1(\nu_G) d\nu_G, \tag{5.81}$$

$$\gamma_i^{1s} = g_{zs} \int_0^1 \sqrt{1-\nu_G^2}\bar{P}_i^1(\nu_G) d\nu_G, \qquad \text{for } p=0 \tag{5.82}$$

and

$$\gamma_i^{pc} \quad = \gamma_i^{ps} = 0 \quad \text{for } p > 0. \tag{5.83}$$

The induced velocity due to ground at the rotor disk is similarly written as a superposition of two parts

$$w_G = w_G^S + w_G^D \tag{5.84}$$

where the static ground effect w_G^S is given by

$$w_G^S = \frac{1}{V_\infty} \int_0^\infty \frac{\partial \Phi_G^S}{\partial z_G} d\xi, \tag{5.85}$$

and the dynamic ground effect w_G^D by

$$w_G^D = \frac{1}{V_\infty} \int_0^\infty \frac{\partial \Phi_G^D}{\partial z_G} d\xi. \tag{5.86}$$

The static ground effect was accounted for in Eq. (5.68). A similar derivation is performed for the dynamic ground effect. The dynamic ground interference velocity is expressed as

$$w_G^D(\bar{r}, \psi_R, \bar{t}) = \sum_{r=0}^{\infty} \sum_{j=r+1,r+3,..}^{\infty} \phi_j^r(\bar{r})[(\beta_j^{rc}(\bar{t}))^D \cos(r\psi_R) + (\beta_j^{rs}(\bar{t}))^D \sin(r\psi_R)]. \tag{5.87}$$

Substituting Eqs. (5.74) and (5.87) into Eq. (5.86), and applying the orthogonal property of

$\bar{P}_j^r(\nu)$, yields

$$\begin{bmatrix} \beta_j^{rc} \\ \beta_j^{rs} \end{bmatrix}^D = \frac{1}{2} \begin{bmatrix} (C_{ji}^{rp})^{cc} & (C_{ji}^{rp})^{cs} \\ (C_{ji}^{rp})^{sc} & (C_{ji}^{rp})^{ss} \end{bmatrix} \begin{bmatrix} \gamma_i^{pc} \\ \gamma_i^{ps} \end{bmatrix}, \tag{5.88}$$

or

$$\{\beta\}^D = \frac{1}{2}[C_G]\{\gamma\}, \tag{5.89}$$

where

$$r, p = 0, 1, 2, \ldots, \quad j = r+1, r+3, \ldots, \quad i = p+1, p+3, \ldots,$$

and

$$\begin{aligned}
(C_{ji}^{0p})^{cc} &= \frac{1}{2\pi} \int_0^{2\pi} \int_0^1 \bar{P}_j^0(\nu_R)[\bar{P}_i^p(\nu_G)\bar{Q}_i^p(\imath\eta_G)\cos(p\psi_G)]_{\eta=0}\, d\nu_R d\psi_R, \\
(C_{ji}^{0p})^{cs} &= \frac{1}{2\pi} \int_0^{2\pi} \int_0^1 \bar{P}_j^0(\nu_R)[\bar{P}_i^p(\nu_G)\bar{Q}_i^p(\imath\eta_G)\sin(p\psi_G)]_{\eta=0}\, d\nu_R d\psi_R, \\
&\qquad\qquad \text{for} \quad r = 0, \\
(C_{ji}^{rp})^{cc} &= \frac{1}{\pi} \int_0^{2\pi} \int_0^1 \bar{P}_j^r(\nu_R)\cos(r\psi_R)[\bar{P}_i^p(\nu_G)\bar{Q}_i^p(\imath\eta_G)\cos(p\psi_G)]_{\eta=0}\, d\nu_R d\psi_R, \\
(C_{ji}^{rp})^{cs} &= \frac{1}{\pi} \int_0^{2\pi} \int_0^1 \bar{P}_j^r(\nu_R)\cos(r\psi_R)[\bar{P}_i^p(\nu_G)\bar{Q}_i^p(\imath\eta_G)\sin(p\psi_G)]_{\eta=0}\, d\nu_R d\psi_R, \\
(C_{ji}^{rp})^{sc} &= \frac{1}{\pi} \int_0^{2\pi} \int_0^1 \bar{P}_j^r(\nu_R)\sin(r\psi_R)[\bar{P}_i^p(\nu_G)\bar{Q}_i^p(\imath\eta_G)\cos(p\psi_G)]_{\eta=0}\, d\nu_R d\psi_R, \\
(C_{ji}^{rp})^{ss} &= \frac{1}{\pi} \int_0^{2\pi} \int_0^1 \bar{P}_j^r(\nu_R)\sin(r\psi_R)[\bar{P}_i^p(\nu_G)\bar{Q}_i^p(\imath\eta_G)\sin(p\psi_G)]_{\eta=0}\, d\nu_R d\psi_R, \\
&\qquad\qquad \text{for} \quad r > 0.
\end{aligned} \tag{5.90}$$

Equations (5.89), combined with Eq. (5.68), form a complete model of the effect of dynamic ground on the rotor disk. General forms of the $\mathbf{A}_G$, $\mathbf{B}_G$, $\mathbf{G}_G$ and $\mathbf{C}_G$ matrices are given in Appendix B.

5.2.2.4 Implementation

The $\boldsymbol{\beta}$ and $\boldsymbol{\tau}$ vectors in Eq. (5.68) are both unknown and interdependent. The pressure coefficients in $\boldsymbol{\tau}$ depend on the blade sectional aerodynamic loads as evident from Eqs. (5.46) to (5.49). The sectional aerodynamic loads in turn account for the effective inflow w^{IGE} as evident in Eq. (2.37). However, w^{IGE} is dependent on the pressure coefficients in $\boldsymbol{\tau}$ as indicated by Eqs. (5.64) and (5.68). Therefore, an iterative Newton-Raphson procedure is used to compute the effective inflow velocity.

Due to the interdependency between $\boldsymbol{\beta}$ and $\boldsymbol{\tau}$, Eq. (5.68) can be expressed as

$$\boldsymbol{\beta} = \mathbf{f}(\boldsymbol{\beta}), \tag{5.91}$$

or

$$\mathbf{e}(\boldsymbol{\beta}) = \boldsymbol{\beta} - \mathbf{f}(\boldsymbol{\beta}) = \mathbf{0}. \tag{5.92}$$

Starting with an initial guess $\boldsymbol{\beta}_0$ and assuming $\mathbf{e}(\boldsymbol{\beta}_0) \neq \mathbf{0}$, a value for the vector $\boldsymbol{\beta}_k$ that satisfies the condition in Eq. (5.92) is obtained using a Taylor series expansion of Eq. (5.92) about $\boldsymbol{\beta}_{k-1} = \boldsymbol{\beta}_0$,

$$\mathbf{e}(\boldsymbol{\beta}) \approx \mathbf{e}(\boldsymbol{\beta}_{k-1}) + \left.\frac{\partial \mathbf{e}(\boldsymbol{\beta})}{\partial \boldsymbol{\beta}}\right|_{\boldsymbol{\beta}=\boldsymbol{\beta}_{k-1}} \left[\boldsymbol{\beta}_k - \boldsymbol{\beta}_{k-1}\right] = \mathbf{0}. \tag{5.93}$$

Solving for $\boldsymbol{\beta}_k$ yields

$$\boldsymbol{\beta}_k = \boldsymbol{\beta}_{k-1} - \mathbf{T}^{-1}\mathbf{e}(\boldsymbol{\beta}_{k-1}), \tag{5.94}$$

where the Jacobian matrix

$$\mathbf{T} = \left.\frac{\partial \mathbf{e}(\boldsymbol{\beta})}{\partial \boldsymbol{\beta}}\right|_{\boldsymbol{\beta}=\boldsymbol{\beta}_{k-1}}, \tag{5.95}$$

and is determined by finite differencing. If the $\boldsymbol{\beta}_k$ coefficients from Eq. (5.94) do not satisfy the condition in Eq. (5.92), $\boldsymbol{\beta}_{k-1}$ is set equal to $\boldsymbol{\beta}_k$ and the coefficients are recomputed

using Eq. (5.94). The process is repeated until convergence is achieved. Note that an iterative procedure is not needed to compute the dynamic ground coefficients $\boldsymbol{\beta}^D$ from Eq. (5.89). Also, the $\boldsymbol{\beta}^D$ coefficients become constant after touchdown.

In the case of hovering above a horizontal ground plane, shown in Fig. 5.8a, the relationship between the rotor and ground coordinate systems is given by

$$\begin{bmatrix} x_G \\ y_G \\ z_G \end{bmatrix} = \begin{bmatrix} x_R \\ y_R \\ z_R - \frac{z_h}{R} \end{bmatrix}. \tag{5.96}$$

Combining Eq. (5.96) with Eqs. (5.53) and (5.54) results in a transformation between the rotor and the ground ellipsoidal coordinate systems

$$(\nu_R, \eta_R, \psi_R) = F(\nu_G, \eta_G = 0, \psi_G), \tag{5.97}$$

which is used in Eqs. (5.59) and (5.60) to evaluate elements of the **B** matrix. Similarly, the inverse transformation can also be obtained

$$(\nu_G, \eta_G, \psi_G) = F^{-1}(\nu_R, \eta_R = 0, \psi_R), \tag{5.98}$$

which is used in Eqs. (5.66) and (5.67) to evaluate elements of the **A** matrix.

In the case of hovering above an inclined ground plane, shown in Fig. 5.8b, the rotor

and ground coordinate systems are related as

$$\begin{bmatrix} x_G \\ y_G \\ z_G \end{bmatrix} = \begin{bmatrix} 1 & 0 & 0 \\ 0 & \cos\Gamma & \sin\Gamma \\ 0 & -\sin\Gamma & \cos\Gamma \end{bmatrix} \begin{bmatrix} \cos\delta & 0 & -\sin\delta \\ 0 & 1 & 0 \\ \sin\delta & 0 & \cos\delta \end{bmatrix} \begin{bmatrix} \cos\Psi & -\sin\Psi & 0 \\ \sin\Psi & \cos\Psi & 0 \\ 0 & 0 & 1 \end{bmatrix} \begin{bmatrix} x_R \\ y_R \\ z_R - \frac{z_h}{R} \end{bmatrix}. \tag{5.99}$$

Transformations between the rotor and ground ellipsoidal coordinate systems are similar to Eqs. (5.97) and (5.98).

CHAPTER 6

Ship Motion

The ship is assumed to be rigid, and its motion is based on a database developed by the US Navy Office of Naval Research and the Naval Surface Warfare Center under the Systematic Characterization of the Naval Environment (SCONE) program [94]. A description of the SCONE database is provided in Section 6.1, followed by a description of its integration into the flight simulation code in Section 6.2.

6.1 Description of SCONE Data

The current SCONE database is generated for the David Taylor Model Basin (DTMB) 5415 ship hull configuration which is representative of a DDG-51 type ship. Details on the ship dimensions, along with relevant nautical terminology, are provided in Appendix C. The Large Amplitude Motions Program (LAMP) simulation code [95], which models the ship dynamic response to wave excitation in a range of sea conditions, was used to generate the data. The deck was excited with dominant motion in either roll or heave. For each DOF, three different excitation amplitudes were employed, characterized as "low", "moderate", and "high". This characterization is different from the numbering system traditionally used to represent sea state, which is the degree of turbulence at the free surface of a large body of water at a given time and location, and is measured on a scale of 0 to 9 according to average wave height. Thirty-minute time histories of the three translational and three rotational DOFs—surge, sway, heave, roll, pitch and yaw—together with their first and second time

derivatives, are recorded at a sampling rate of 20 Hz. Each of the six deck motion cases was simulated using five different randomly generated wave disturbances, yielding a total of 30 datasets, as illustrated in Fig. 6.1.

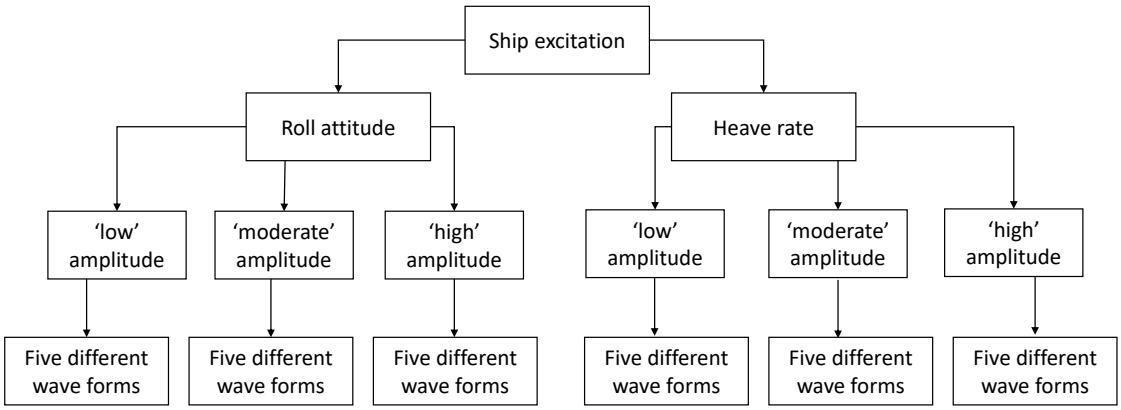

Figure 6.1: Flowchart illustrating decomposition of SCONE data.

To assess the differences in the five datasets, time histories and frequency spectra of the roll angle, pitch angle, heave displacement, heave velocity and heave acceleration for the five "high" amplitude roll dominant simulations were examined. The five sets differed mainly in the high frequency distribution, as shown in Fig. 6.2. A frequency spectra of the DOFs from one of the given sets reveals a peak in the roll, pitch and heave motion frequency distributions at approximately 0.1 Hz, 0.1 Hz, and 0.15 Hz, respectively, as shown in Fig. 6.3.

The mean, minimum, and maximum values of the ship roll attitude ϕ_D, pitch attitude θ_D, heave displacement z_D, heave rate V_{zD}, and heave acceleration A_{zD} corresponding to "low", "moderate" and "high" roll amplitude simulations are shown in Table 6.1. Roll angle is positive starboard, pitch angle is positive when the bow goes up, and heave motion is positive downward from the waterline. The coordinate system used is illustrated in Fig 6.4. Note that the mean heave displacement represents the average vertical position of the center of the ship deck during the simulation. Deck motion quantities corresponding to "low", "moderate" and "high" heave amplitude simulations are compared in Table 6.2.

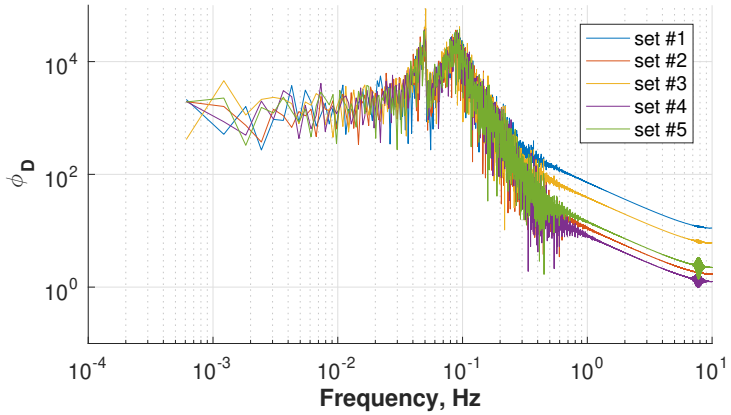

Figure 6.2: Frequency spectrum of roll angle ϕ_D for "high" amplitude roll dominant simulations.

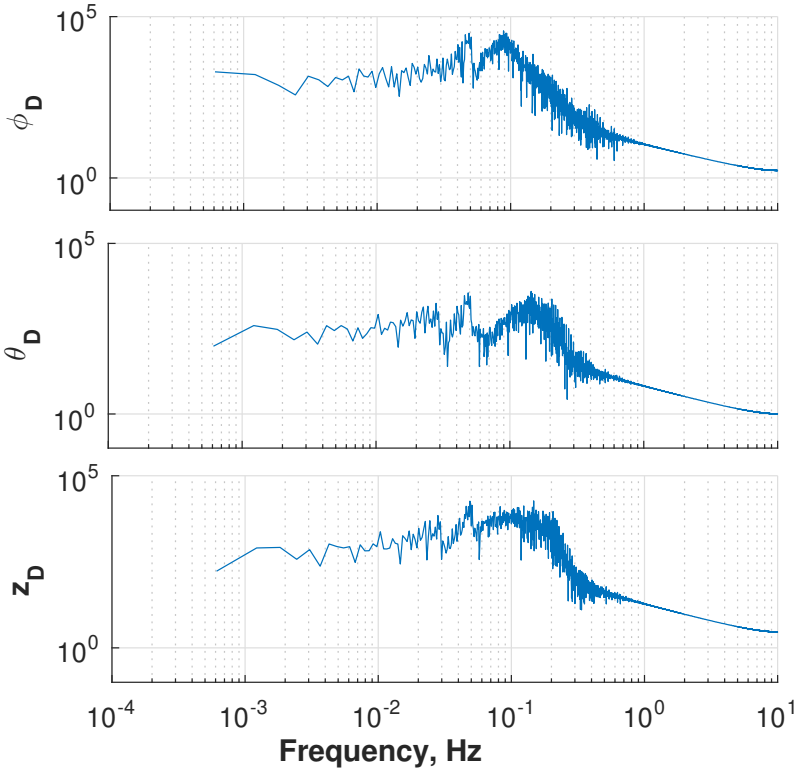

Figure 6.3: Frequency spectrum of roll angle ϕ_D, pitch angle θ_D, and heave displacement z_D for a "high" amplitude roll dominant simulation.

From Tables 6.1 and 6.2, amplitudes of the ship DOFs are significantly greater in the "high" amplitude tests compared to the "low" amplitude tests. Time histories of the ship DOFs for "low" and "high" heave amplitude tests are shown in Fig. 6.5.

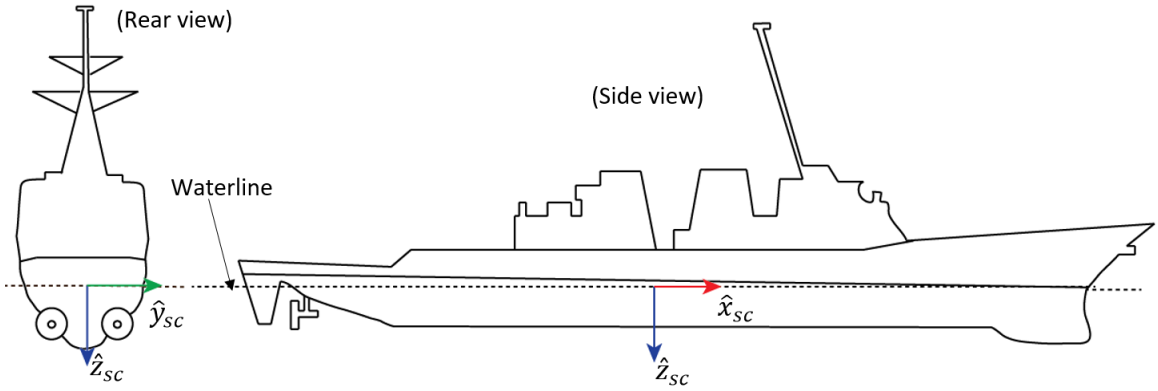

Figure 6.4: Coordinate system used in SCONE data.

Table 6.1: Ship motion parameters for roll excitation

	Low			Moderate			High		
	mean	min	max	mean	min	max	mean	min	max
ϕ_D (deg)	0.07	-5.5	5.4	0.1	-14.9	16.7	-0.15	-26.9	23.7
θ_D (deg)	-0.15	-0.79	0.70	-0.15	-1.7	1.39	-0.03	-3.24	2.59
z_D (ft.)	-16.2	-19.0	-13.0	-16.2	-23.7	-8.98	-14.8	-27.3	0.24
V_{zD} (ft/s)	0.00	-1.30	1.10	0.00	-5.93	4.37	0.00	-11.0	10.6
A_{zD} (g)	0.00	-0.03	0.03	0.00	-0.14	0.13	0.00	-0.56	0.76

Table 6.2: Ship motion parameters for heave excitation

	Low			Moderate			High		
	mean	min	max	mean	min	max	mean	min	max
ϕ_D (deg)	0.06	-3.88	3.44	0.01	-4.12	3.56	-0.15	-15.1	12.6
θ_D (deg)	-0.01	-1.50	1.36	-0.11	-3.35	3.68	0.05	-4.35	5.77
z_D (ft.)	-16.4	-22.5	-10.1	-16.1	-25.3	-3.51	-14.7	-30.3	1.93
V_{zD} (ft/s)	0.00	-5.25	4.96	0.00	-10.8	11.7	0.00	-15.6	14.7
A_{zD} (g)	0.00	-0.14	0.13	0.00	-0.40	0.32	0.00	-0.56	0.46

6.2 Combination of SCONE and Flight Dynamics Model

Each table in the SCONE database is 11 MB in size. The simulations in this study are performed using a computer with a memory capacity of 48 GB, and thus any one of the thirty available tables can be directly loaded into computer memory for helicopter ship landing

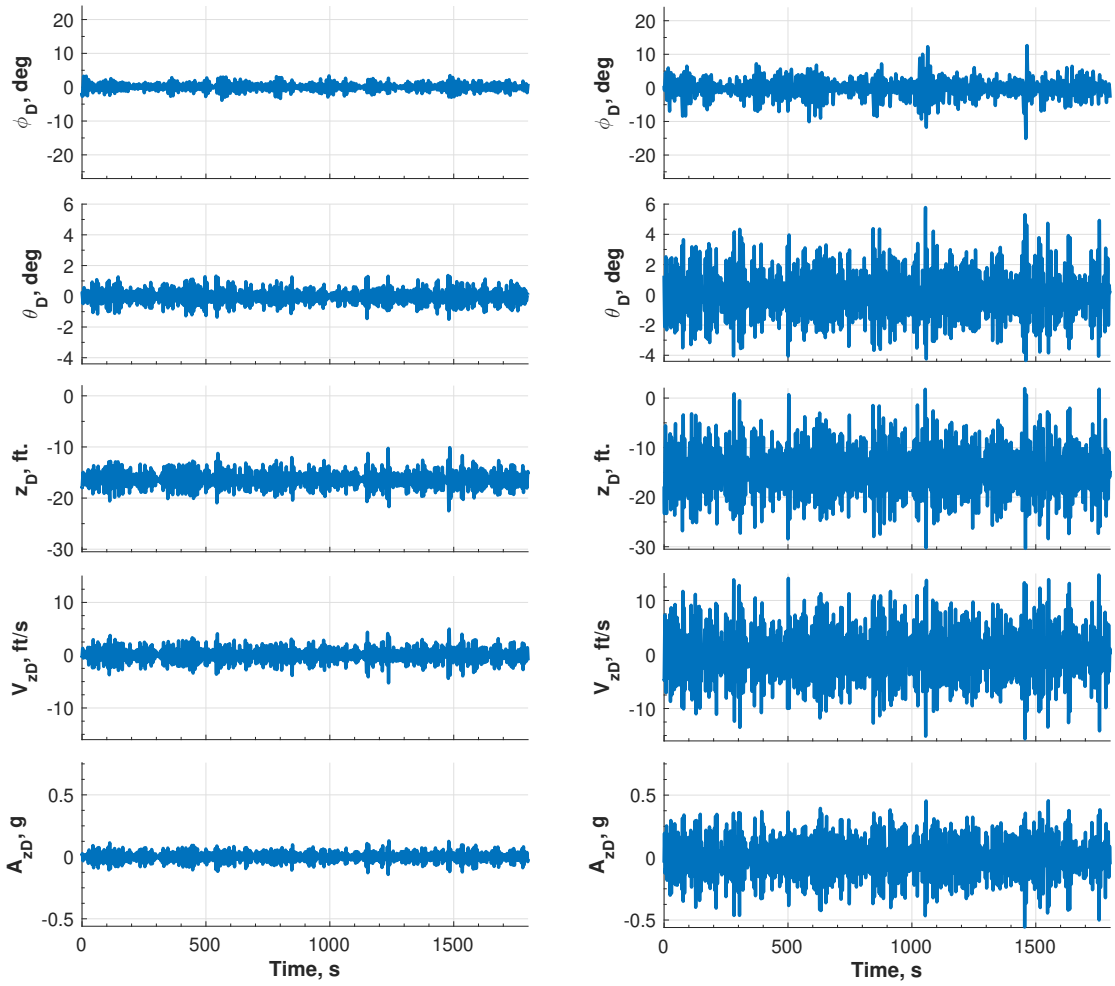

Figure 6.5: Roll angle $\boldsymbol{\phi_D}$, pitch angle $\boldsymbol{\theta_D}$, heave displacement $\boldsymbol{z_D}$, heave velocity $\boldsymbol{V_{zD}}$ and heave acceleration $\boldsymbol{A_{zD}}$ time histories for (a) "low" and (b) "high" heave excitation.

simulations. It was shown in the previous section that only a slight variance in the time histories and frequency spectra of ship DOFs was noted between the five tests associated with the "high" roll amplitude simulations. Therefore, any one of the five data sets can be used. It was also evident that the "low" amplitude excitation results in a relatively benign ship motion of approximately $\pm 5^\circ$ in roll attitude, and ± 3ft. in heave displacement, whereas the "high" amplitude case produces large ship motion of approximately $\pm 15^\circ$ in roll attitude, and ± 15 ft. in heave displacement. Therefore, for the helicopter ship land-

ing problem, the "moderate" amplitude case, which produces intermediate ship motion of approximately $\pm 4^\circ$ in roll attitude, and ± 9 ft. in heave displacement, is chosen.

Data set #2 of the chosen case is loaded into computer memory at the beginning of the simulation. Ship motion data is then extracted for two minutes, from $t = 1250$ s to $t = 1370$ s since ship response is fully developed in this window. In this study, only the roll attitude ϕ_D, pitch attitude θ_D, and heave displacement z_D are considered. The time histories used are shown in Fig. 6.6. Note that the initial heave displacement $z_{D0} = -16$ ft., which represents the deck height at $t = 0$ s, was subtracted from z_D in Fig. 6.6.

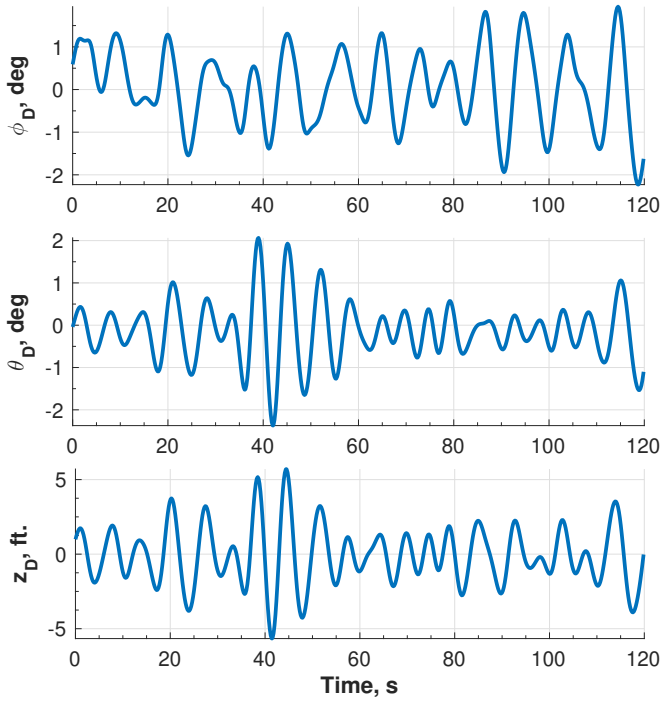

Figure 6.6: Time histories of roll angle $\boldsymbol{\phi_D}$, pitch angle $\boldsymbol{\theta_D}$, and heave displacement $\boldsymbol{z_D}$ used in simulations.

Ship motion is included in the landing gear model through the calculation of z_{deck} from Eq. (5.3). The contribution due to heave displacement z_{dyn} is determined as follows:

$$z_{dyn} = -\Delta z_D = -(z_D - z_{D0}), \tag{6.1}$$

where the leading negative sign converts the displacement from the SCONE data coordinate frame, shown in Fig. 6.4, to the inertial deck frame. The roll and pitch angles, Γ_{deck} and δ_{deck}, respectively, used to determine z_{ang} in Eq. (5.9), are related to ϕ_D and θ_D as follows:

$$\Gamma_{deck} = -\phi_D, \tag{6.2}$$

$$\delta_{deck} = \theta_D. \tag{6.3}$$

In the ground effect model, Δz_D from Eq. (6.1) is used to update the height of the rotor hub center from ground z_h, and the ground inclination angles Γ and δ are related to ϕ_D and θ_D as follows:

$$\Gamma = \phi_D, \tag{6.4}$$

$$\delta = \theta_D. \tag{6.5}$$

The ground heaving, pitching, and rolling velocities g_{z0}, g_{zc}, and g_{zc}, respectively, from Eq. (5.79) are determined using finite differencing with respect to time. Ship dynamics do not influence WOD velocities in this study.

CHAPTER 7

Results and Discussion

Approach and landing simulations were performed for a 4-bladed UH-60A helicopter configuration using the modified flight dynamics code, HeliUM2-umich. Relevant vehicle and rotor parameters are provided in Table 7.1. Note that the UH-60A helicopter has a 20° cant angle [39], shown in Fig. 7.1, that causes the tail rotor to generate a vertical thrust component that contributes to lift. Inflow velocity was determined from a 3-state He-Peters dynamics inflow model [59]. Each main rotor blade was modeled using four FEs, each with 8 Gaussian points. The number of FE DOFs was reduced using a modal coordinate transformation based on five rotating modes: rigid flap, rigid lag, and the first flexible flap, lag and torsional modes, plotted in Fig. 7.2. The corresponding natural frequencies are given in Table 7.1.

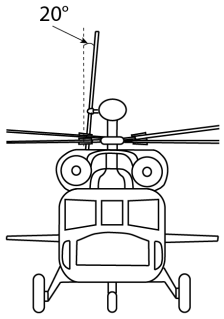

Figure 7.1: UH-60A cant angle.

Table 7.1: HeliUM2-umich setup parameters

Main Rotor Data	
Main rotor speed	258 RPM (27 rad/s)
Individual blade weight	116.5 kg (256.9 lbs.)
Blade radius	8.18 m (26.83 ft.)
Hinge offset	0.381 m (1.25 ft.)
Airfoil section	SC 1095
Blade chord (constant)	0.527 m (1.73 ft)
Blade precone, β_p	0°
lock number, γ_R	5.11
Rigid lag frequency	0.268 /rev
Rigid flap frequency	1.035 /rev
1st flap frequency	2.823 /rev
1st torsion frequency	4.632 /rev
1st lag frequency	12.408 /rev
Helicopter Data	
Longitudinal shaft tilt angle α_x	0°
Lateral shaft tilt angleα_y	0°
Swash plate phase Δ_{sp}	-9.7°
Fuselage weight	7779.1 kg (17150 lbs.)
Number of tail rotor blades	4
Tail rotor blade radius R_t	1.68 m (5.5 ft.)
Tail rotor speed Ω_t	1190 RPM (124.6 rad/s)
Taill rotor cant angle Γ_{TR}	20°
Simulation Data	
Time marching step size	0.0032 s (5 azimuthal deg.)
Trim Type	Propulsive

7.1 Results for Approach Segment

Simulations for the approach segment, shown in Fig. 3.1, were conducted to determine the effect of WOD on the helicopter dynamic response. Actual landing on a stationary deck from a hover position was also simulated, so as to understand the combined effects of landing gear, ground effect, and WOD.

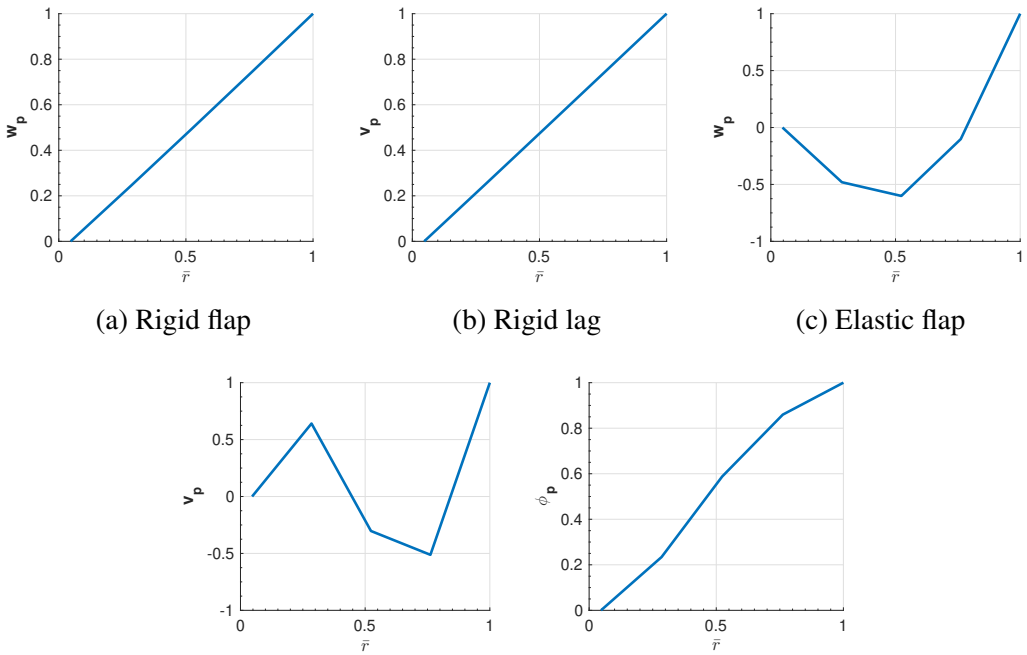

(a) Rigid flap (b) Rigid lag (c) Elastic flap

(d) Elastic lag (e) Elastic torsion

Figure 7.2: Rotating mode shapes used in modal coordinate transformation.

7.1.1 Influence of WOD during approach

Results for the flight segments shown in Fig. 3.1, are considered next. The first set of simulations were performed with the WOD affecting the rotor alone. Subsequently, the influence of WOD on the entire helicopter, including fuselage, empennage and tail rotor, was considered. The vehicle target position was set to $(410, 0, 30)$ ft., which corresponds to a hovering station at a height of 15 ft. from the center of ship deck plane, shown in Fig. 4.1. The approach is initiated at an altitude of 312.3 ft., a value higher than the z_0 value given in Table 3.1, so as to account for the loss in altitude during transition from level flight to descent. The helicopter speed during the level flight part of the approach is 60 knots, or $\mu = 0.14$.

7.1.1.1 WOD effects on rotor alone

The WOD was first assumed to act on the rotor alone. The WOD is a 30-knot wind at three sideslip angles of $0^\circ, 30^\circ$ and -30°, where the sideslip angle is considered to be positive when wind comes from the starboard side, as shown in Fig. 4.4. Each simulation lasted approximately one hour on a 12 core Intel Xeon E5-2609 v3 processor at 1.90 GHz clock-speed.

Time histories of the helicopter position coordinates are shown in Fig. 7.3. The level flight, hover and descent phases of the approach are identified by vertical dashed lines in the plots. The solid vertical line indicates the time when the rotor hub enters the WOD domain. The desired trajectories are denoted as 'ideal' in the figure. The controller is effective in maintaining the trajectory profile in presence of WOD. A slight drift, approximately 1.5 ft., in the final lateral position is noted both with and without WOD. Helicopter attitude angle responses are shown in Fig. 7.4. The WOD influence is evident from the high frequency oscillations, starting at $t = 50.5$ s, when the rotor hub enters the WOD domain. Initial offsets from the desired angular attitude values are noted in the descent phase in Fig. 7.4. The roll and pitch angular attitudes converge to the desired values as the simulation progresses, but the offsets in the yaw angle persist until the end of the simulation.

Time histories of the control inputs generated by the FCS are shown in Fig. 7.5. The high frequency oscillations in lateral cyclic θ_{1c} show that greater control effort is required when WOD is present. The 0° and -30° conditions require greater lateral control than the 30° case. The WOD also induces a larger longitudinal cyclic θ_{1s} input, with the 30° case displaying the largest effort. The θ_0 time history in Fig. 7.5 shows that, compared to the case when WOD is absent, a larger collective input is required for the 0° and -30° conditions. The case of 30° requires the smallest collective changes. Tail rotor collective input time histories follow a trend similar to θ_0. It is noteworthy that the control inputs for the 30° and -30° cases are not symmetric. This is due to the asymmetry in vehicle dynamics. The lack of symmetry implies that vehicle response should be examined for

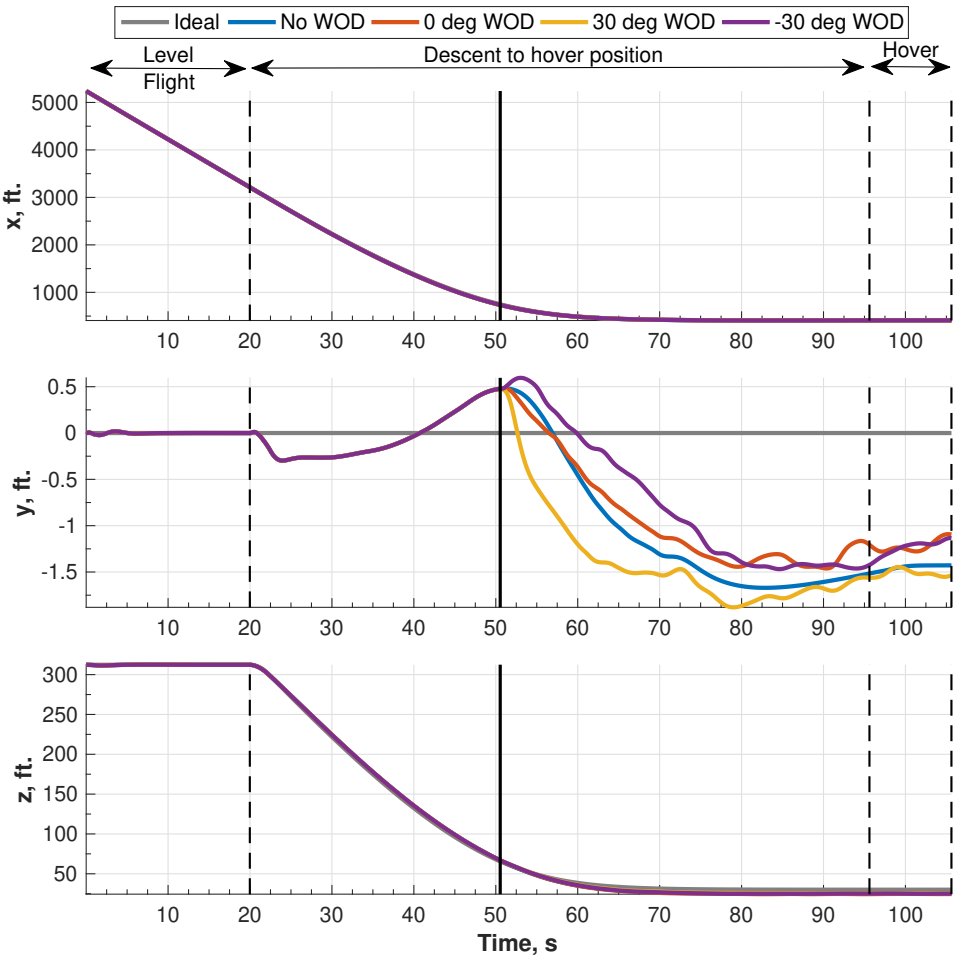

Figure 7.3: Horizontal x, lateral y, and vertical z positions of helicopter CG during approach to a stationary deck, WOD included in main rotor model.

both portside and starboard WOD conditions when establishing SHOLs. The $-30°$ WOD condition appears to be the most demanding in terms of control effort, based on the control input time histories in Fig. 7.5. The additional control effort required in the oblique WOD condition can be attributed to the "cliff-edge" effect [10], whereby winds at an angle induce stronger shear layers that are shed from the edges of the ship structure. The associated WOD velocity components experienced by the vehicle are thus higher, as shown in Fig. 7.6, where magnitudes of the WOD velocities are much higher in the case of $\pm 30°$ compared to $0°$.

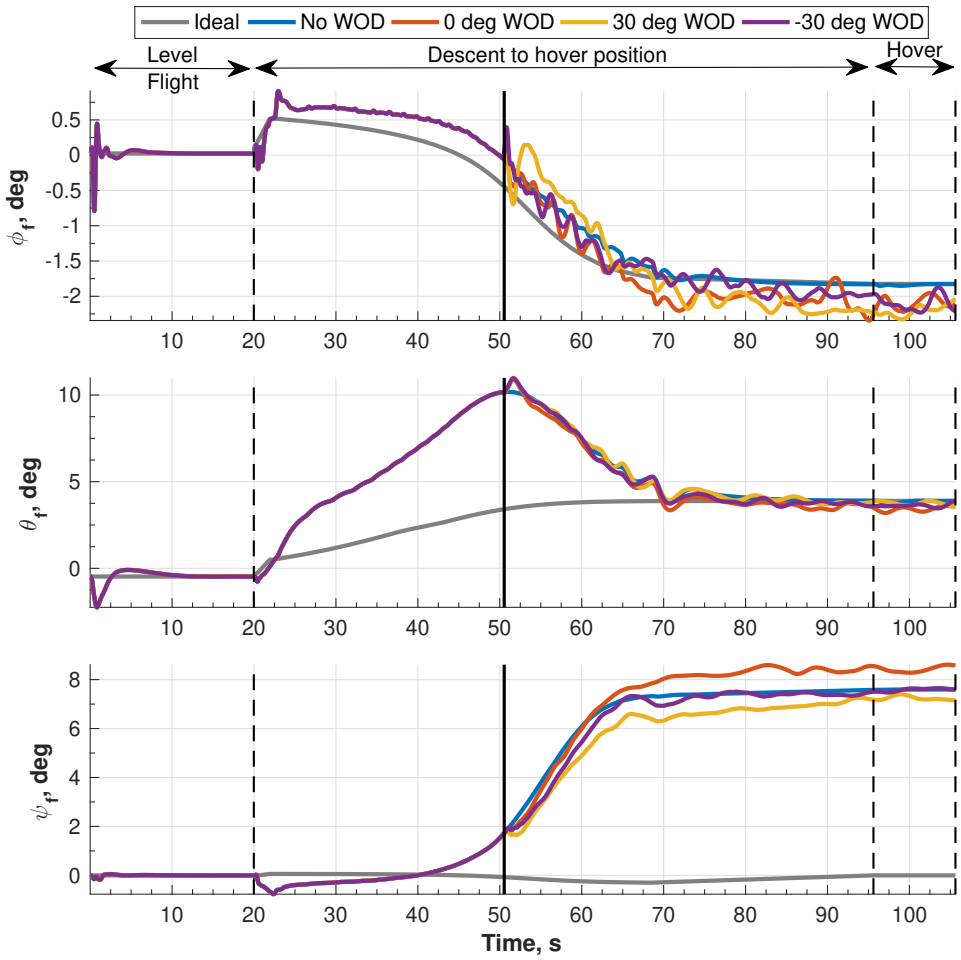

Figure 7.4: Roll ϕ_f, pitch θ_f, and yaw ψ_f angles of fuselage during approach to a stationary deck, WOD included in main rotor model.

7.1.1.2 WOD effects on the entire vehicle

The WOD effect was applied on the entire vehicle consisting of the fuselage, empennage and tail rotor combined with the main rotor. Helicopter approach was simulated with a 30 knot starboard wind at $-30°$, which represents the worst case scenario. Figure 7.7 shows that including WOD effects on the entire helicopter results in larger deviations and oscillations in the helicopter attitude angles. The angles change by up to $4°$ when WOD is included in the additional components. Time histories of the control inputs are plotted in Fig. 7.8. When WOD is included on the entire helicopter, the tail rotor collective input changes by approximately $4°$, while the main rotor control inputs do not display a sig-

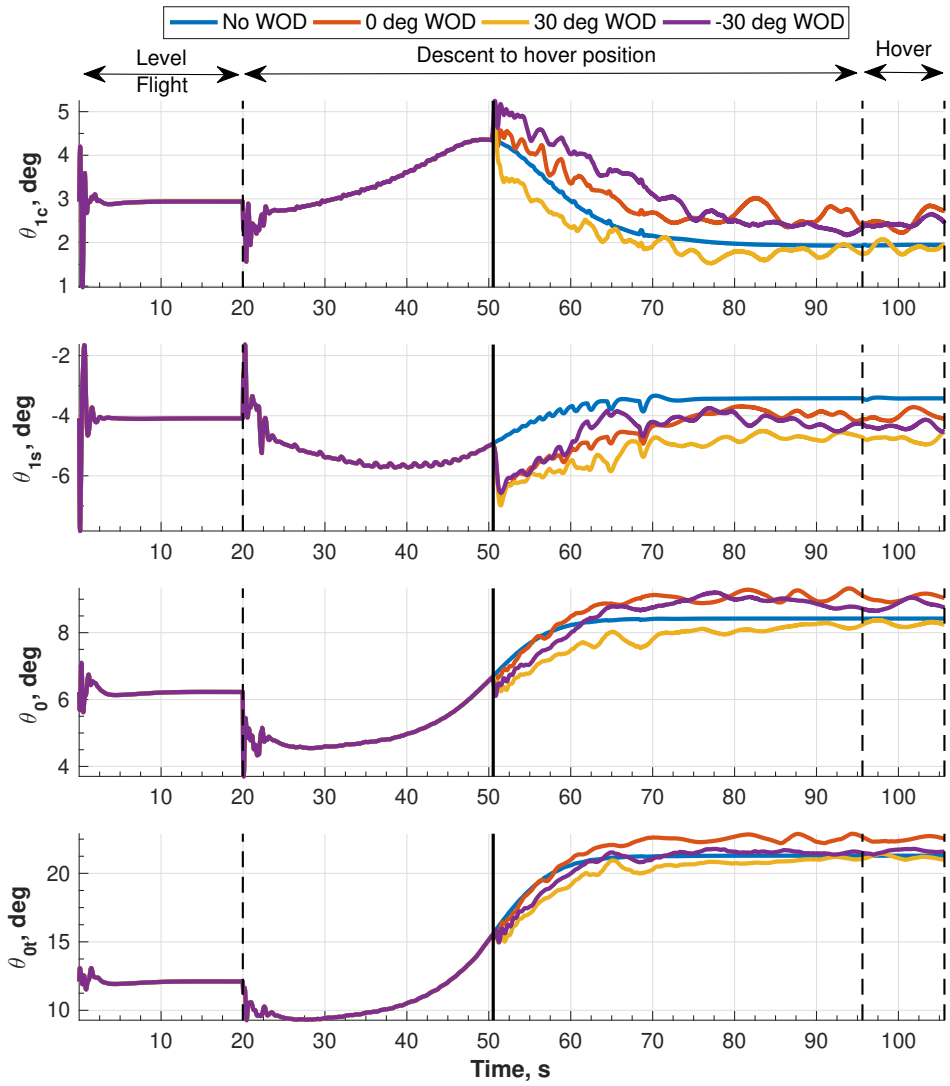

Figure 7.5: Control inputs generated by FCS during the approach to a stationary deck, WOD included in main rotor model.

nificant change. Overall, taking the WOD effects on all the components is important for accurate simulation of the helicopter ship landing dynamics.

7.1.2 Combined WOD and ground effect during hover and landing

Simulation results for hover and landing with ground effect included on the main rotor are presented next. The ground effect is modeled using the scaling factor k_G, described in Section 5.2.1. The effect of WOD is included on all the helicopter components. Only

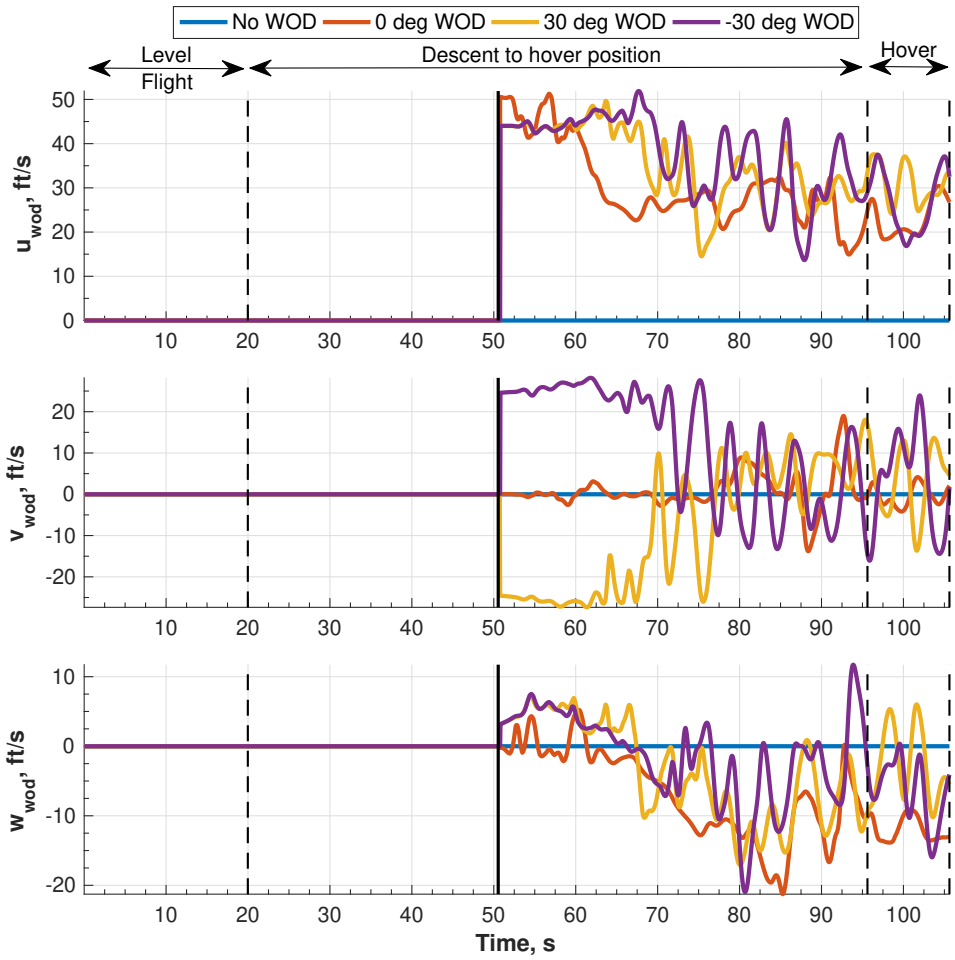

Figure 7.6: WOD velocity components at hub location during approach to a stationary deck, WOD included in main rotor model.

the case of $\beta_{WOD} = -30°$ is considered. Time histories for the CG position coordinates are shown in Fig. 7.9. The response of the baseline case without WOD and ground effect is included for comparison. The vehicle remains stationary after $t = 12$ s, indicating successful landing. Slight drifts of approximately 1.5 ft. from the target value of 410 ft. are evident in the horizontal position for the baseline case. The WOD induces oscillations and offsets in the position coordinates during hover and descent to deck. Adding ground effect causes additional changes in the position coordinates relative to the baseline case. Due to the vehicle weight, the influence of WOD and ground effect on the vertical position is minimal after landing. Figure 7.10 shows the vehicle roll, pitch and yaw responses

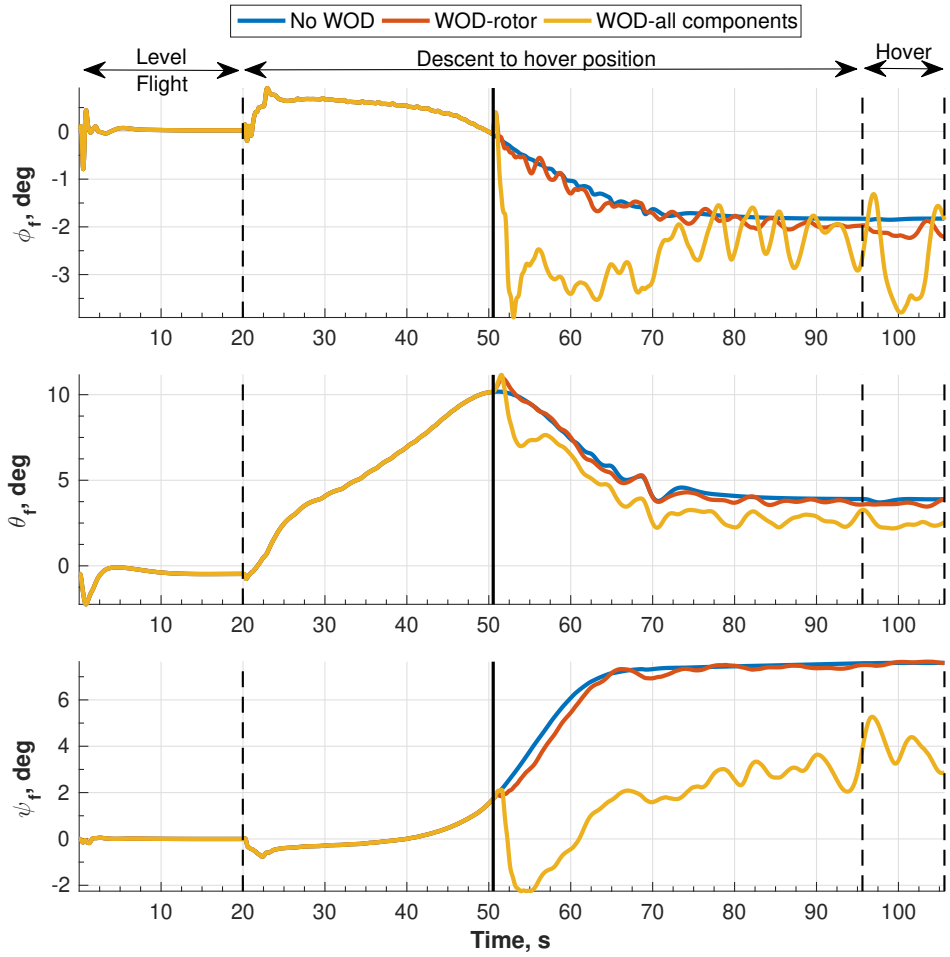

Figure 7.7: Roll ϕ_f, pitch θ_f, and yaw ψ_f angles of fuselage during approach to a stationary deck, WOD included on entire helicopter.

during the hover and landing phases. The WOD induces higher frequency oscillations in CG attitudes, particularly in the roll angle during the hover phase, implying that the WOD can cause the vehicle to spin and roll over during touchdown. Ground effect also induces changes in attitudes during the hover phase. These changes dissipate and the attitudes converge to WOD-only values after landing.

Gear deflections during and after touchdown are shown in Fig. 7.11. Initial transients exist during contact but diminish as simulation progresses. After landing, right, left, and tail gear deflections are 0.3 ft., 0.27 ft., and 0.05 ft., respectively. The right gear deflection is slightly greater than the left due to a small positive roll angle, shown in Fig. 7.10, after

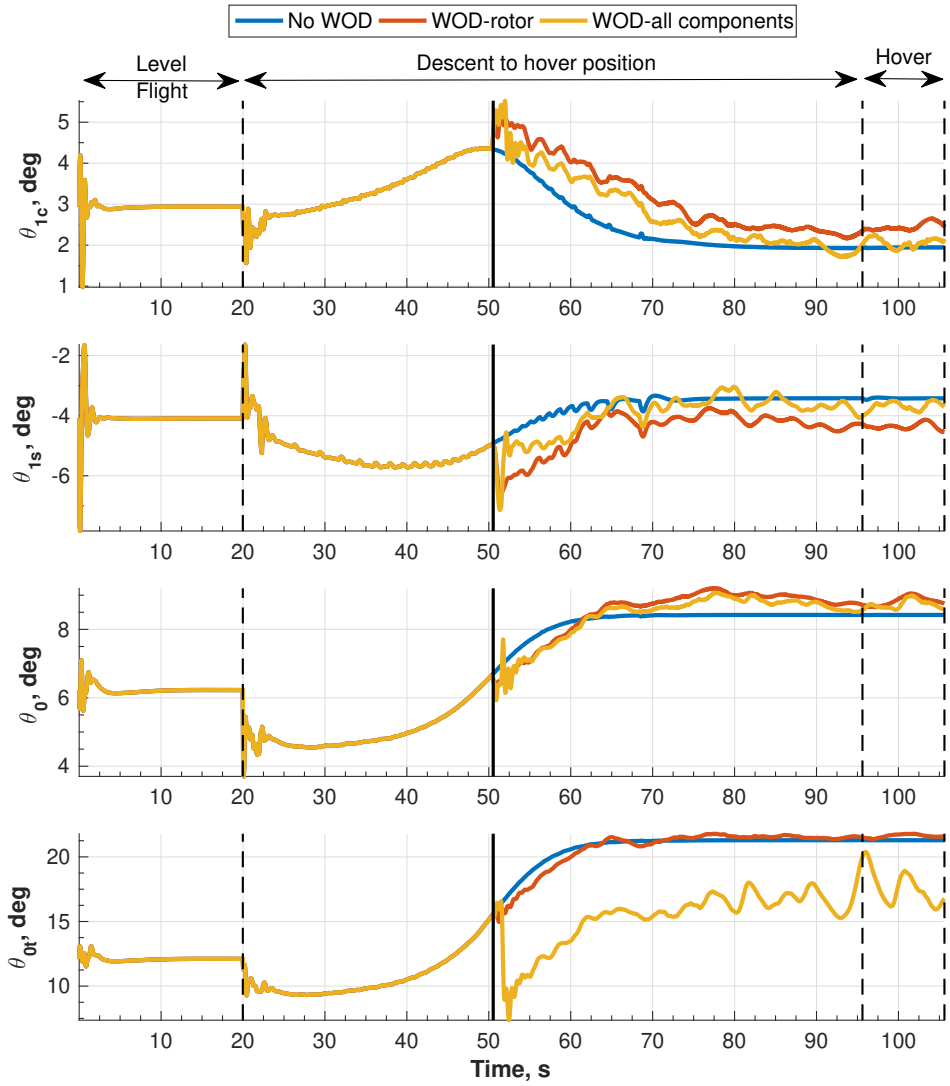

Figure 7.8: Control inputs generated by FCS during approach to a stationary deck, WOD included on entire helicopter.

the vehicle lands. Inclusion of ground effect results in a slight decrease in the final gear deflections. For the cases simulated, the tail gear makes contact first, followed by the main gears 0.1s later. This is a result of the positive pitch angle at $t = 10$ s in Fig. 7.10.

Figure 7.12 shows the control input time histories during hover and landing. In the hover phase, ground effect causes the main rotor collective input to decrease by 8.1%, from 8.6° to 7.9°, relative to the WOD-only case. Ground effect results in a decrease in rotor inflow. As the controller attempts to maintain the main rotor thrust, the collective input

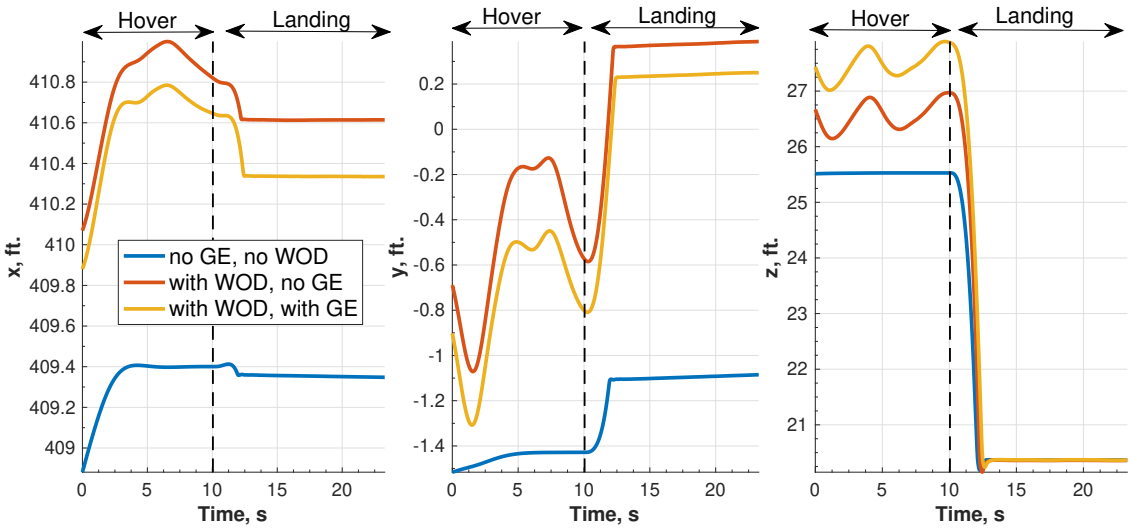

Figure 7.9: Horizontal x, lateral y, and vertical z positions of helicopter CG during hover and landing flight segments with simple ground effect model and WOD included on the entire helicopter, stationary deck.

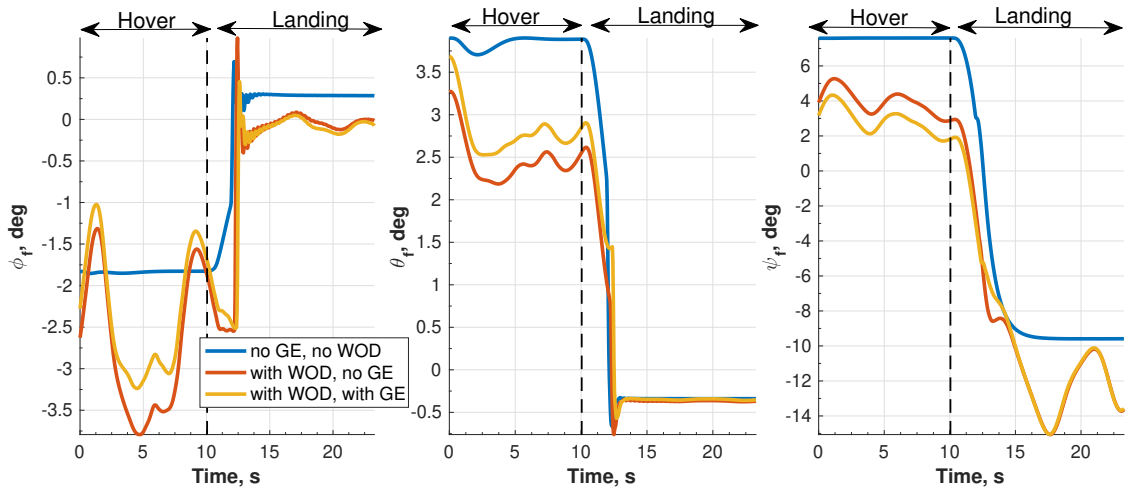

Figure 7.10: Roll ϕ_f, pitch θ_f, and yaw ψ_f angles of fuselage during hover and landing phases with simple ground effect model and WOD included on the entire helicopter, stationary deck.

is decreased to keep the angle of attack constant. Ground effect induces minimal changes in the cyclic inputs. During the landing phase, θ_0 is gradually decreased until touchdown is achieved. After touchdown, the collective input is set to 1°, which corresponds to zero thrust due to the built-in blade twist. The tail rotor collective input follows a similar trend as θ_0. The WOD induces high frequency oscillations in the control inputs during the hover

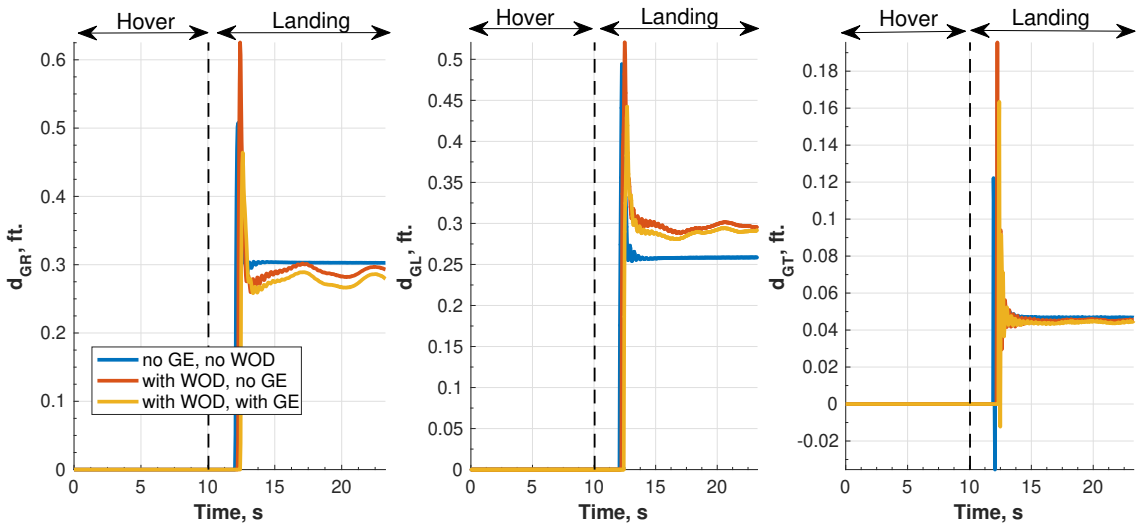

Figure 7.11: Right, left and tail gear deflections during hover and landing phases with simple ground effect model and WOD included on the entire helicopter, stationary deck.

and landing phases.

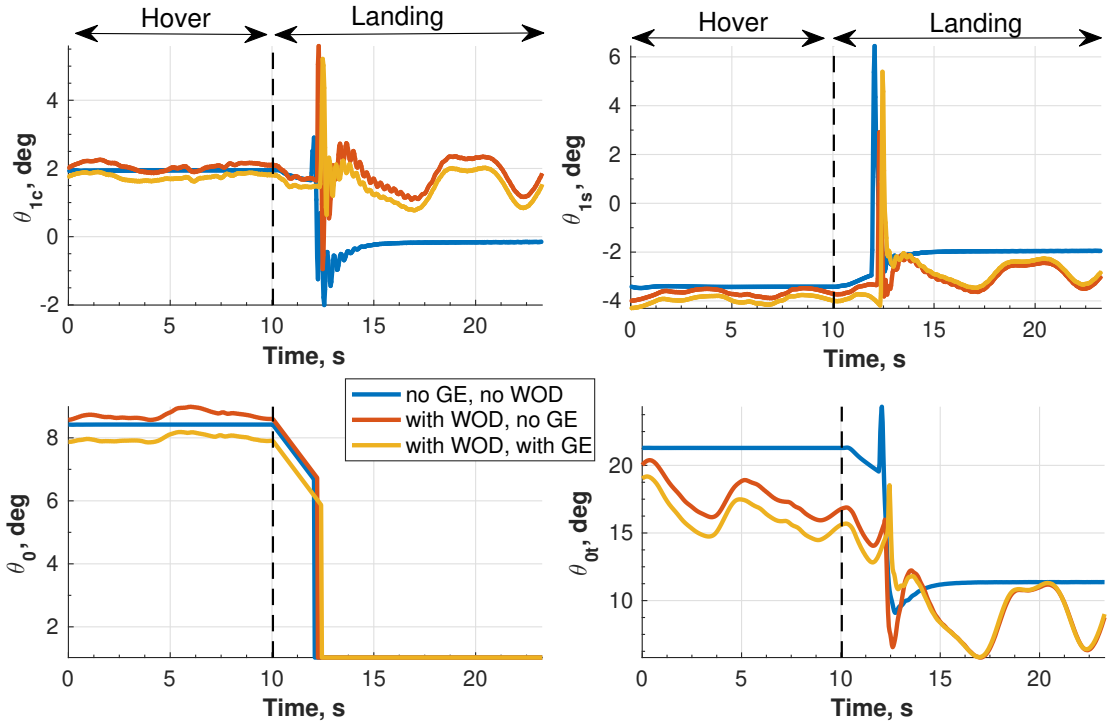

Figure 7.12: Control inputs generated by FCS during hover and landing phases with simple ground effect model and WOD included on the entire helicopter, stationary deck.

The main rotor and tail rotor lift forces, and the combined vertical landing gear reaction

forces are plotted in Fig. 7.13. The tail rotor lift is due to the 20° cant angle, shown in Fig. 7.1. The vertical forces are constant during the hover phase. During the landing phase, the main rotor thrust decreases progressively. Upon touchdown, a sudden decrease in the main rotor thrust is evident. At the same time, the total vertical gear reaction force increases, indicating the transfer of the vehicle weight onto the landing gears. The lift from the tail rotor decreases to approximately 83 lbs. after landing. This is because the tail rotor collective is reduced as less torque is generated by the main rotor once the vehicle weight is transferred onto the gears. Oscillations due to WOD are noticeable in the main and tail rotor lift time histories. The power required during the hover and landing phases are shown in Fig. 7.14. Ground effect results in a 11.3% decrease in power requirement, from 1768 Hp to 1569 Hp, at the onset of the landing phase. Note that the oscillations in the power time histories are due to vehicle dynamics.

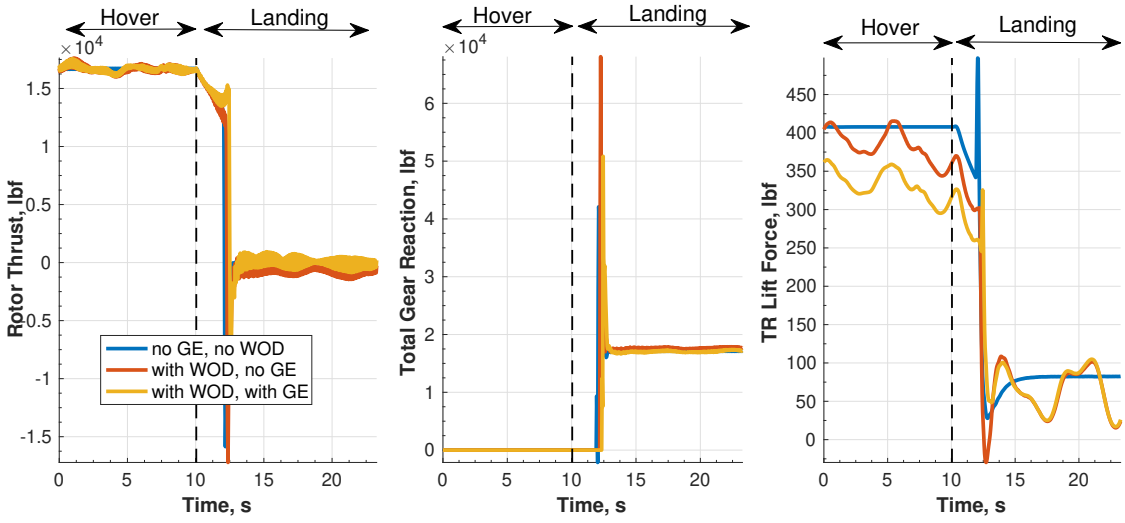

Figure 7.13: Rotor thrust, total vertical gear reaction force, and tail rotor contribution to lift during hover and landing phases with simple ground effect model and WOD included on the entire helicopter, stationary deck.

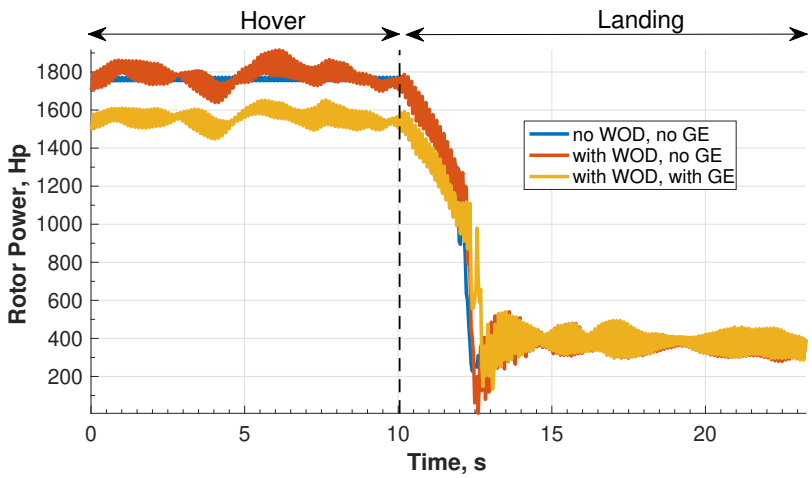

Figure 7.14: Power required during hover and landing phases with simple ground effect model and WOD included on the entire helicopter, stationary deck.

7.1.3 Approach and landing simulation with combined WOD and ground effects

Simulations were performed for combined approach and landing, including all the segments in Fig. 3.1, together with a landing flight segment. Note that the approach simulations in Section 7.1.1 did not take into account the ground effect. Here, both the WOD and ground effect were included. The ground effect is modeled using the k_G factor. Only the -30° WOD condition is considered, and its effect is included on the entire helicopter. The vehicle response is shown in Figs. 7.15 and 7.16. The solid vertical line indicates the time at which the helicopter enters the WOD domain. The time at which the rotor hub enters the region directly above the deck is shown using the dotted vertical line at $t = 63$ s. Note that the vertical position coordinate of the helicopter at $t = 63$ s is 33ft., which corresponds to $z_h/R = 0.85$. The ground effect begins to influence the response as soon as the hub enters the region above the deck, as shown by the CG roll, pitch, and yaw responses are plotted in Fig. 7.15. Similar to the isolated landing simulation shown in Fig. 7.10, the ground effect produces an offset in the state responses, relative to the WOD-only case. Similar trends are noticed in control input time histories plotted in Fig. 7.16. The gain-scheduled controller

is capable of stabilizing and tracking the helicopter reference trajectory through the various phases of the trajectory.

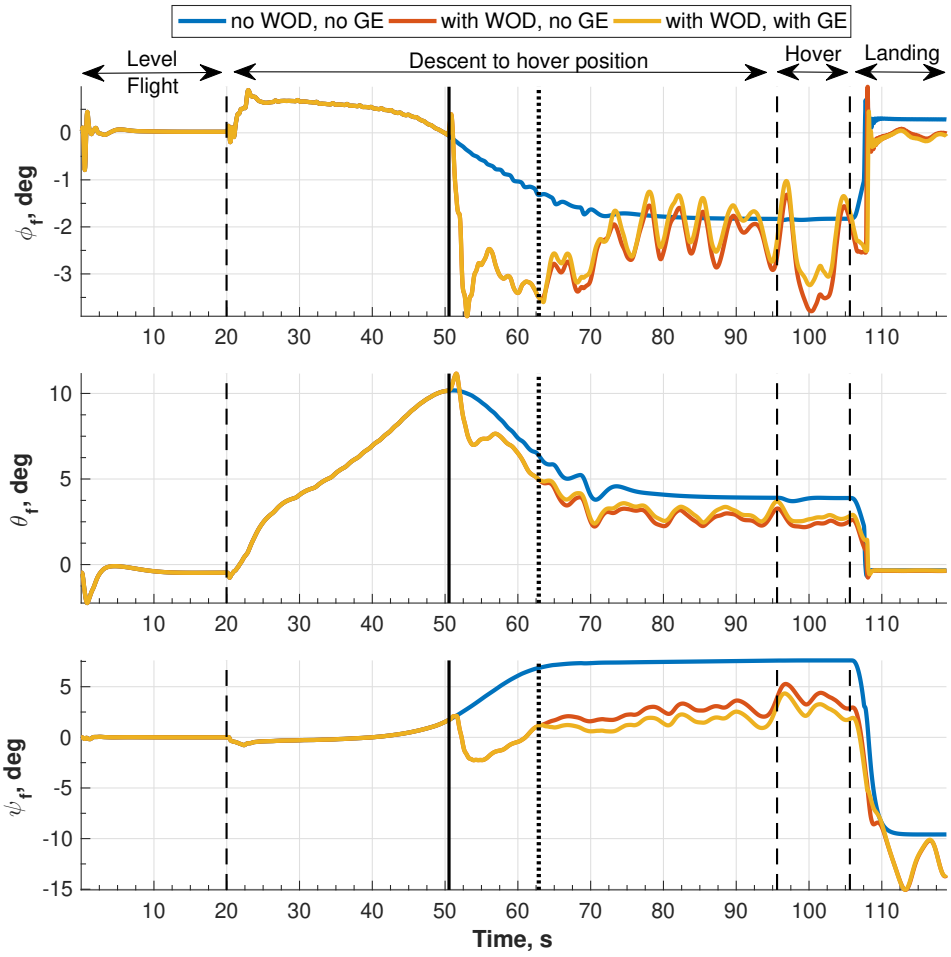

Figure 7.15: Roll ϕ_f, pitch θ_f, and yaw ψ_f angles of fuselage during approach and landing phases with simple ground effect model and WOD included on entire helicopter, stationary deck.

7.2 Ground Effect from Inclined and Moving Decks

Simulations, for hover and landing flight segments, were performed to examine the influence of inclined and dynamic ground planes on helicopter response using the finite-state ground effect model, described in Section 5.2.2. Rotor performance results obtained using the model are first compared with results from literature by considering hover simulations

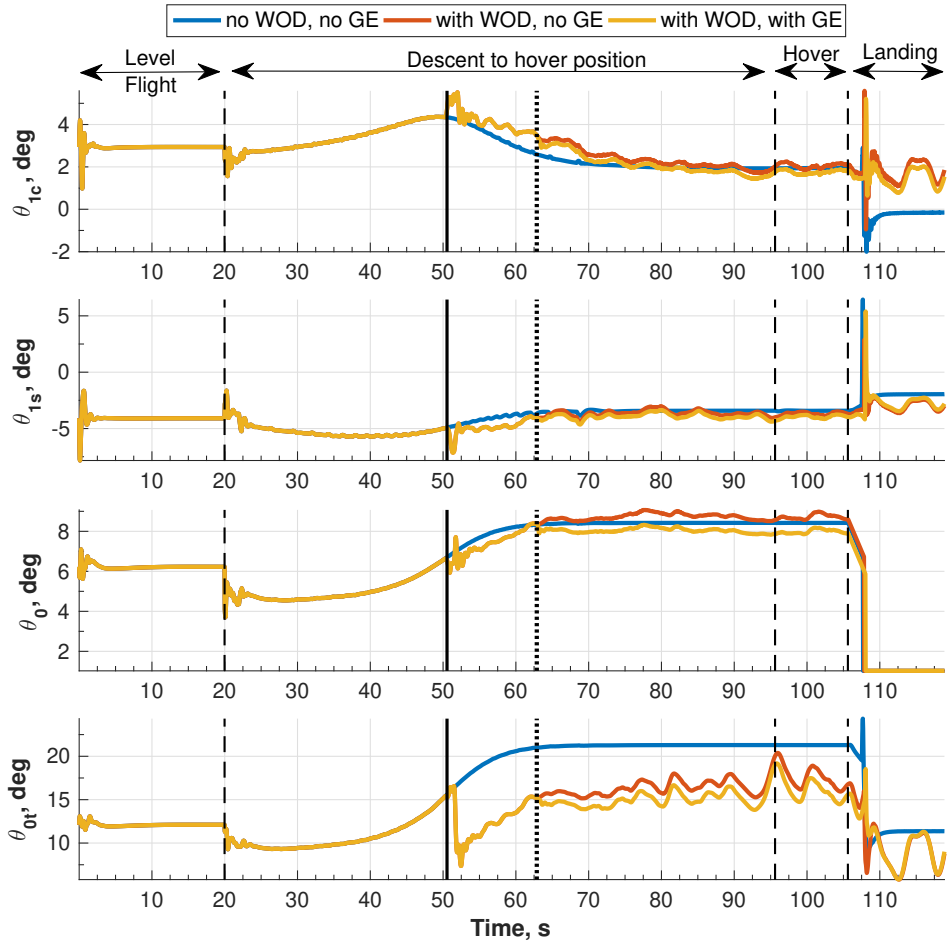

Figure 7.16: Control inputs generated by FCS during approach and landing phases with simple ground effect model and WOD included on entire helicopter, stationary deck.

at various heights above a stationary and level ground plane. Subsequently, the influence of static deck inclination on helicopter response is examined for various deck roll and pitch angles. Next, simulations are performed with the deck excited in isolated sinusoidal motion in roll, pitch and heave DOFs. Finally, the combined influence of WOD and dynamic ground effect during hover and landing is examined for a deck excited in combined roll, pitch and heave DOFs using SCONE data.

7.2.1 Comparison with results from literature

Hover simulations were performed for the helicopter in ground effect at various heights above a stationary and level ground plane using both the Cheeseman and Bennett model and the finite-state ground effect model. The ratio of power in-gound-effect to power out-of-ground-effect for the various heights considered is compared with experimental results in Fig. 7.17. Both models show good agreement with the experiments for heights greater than $1R$. For heights less than $0.5R$, the Cheeseman and Bennett model prediction is inaccurate and quickly approaches zero. The power ratio obtained using the finite-state model remains stable and shows reasonable agreement with experiments for heights less than $0.5R$.

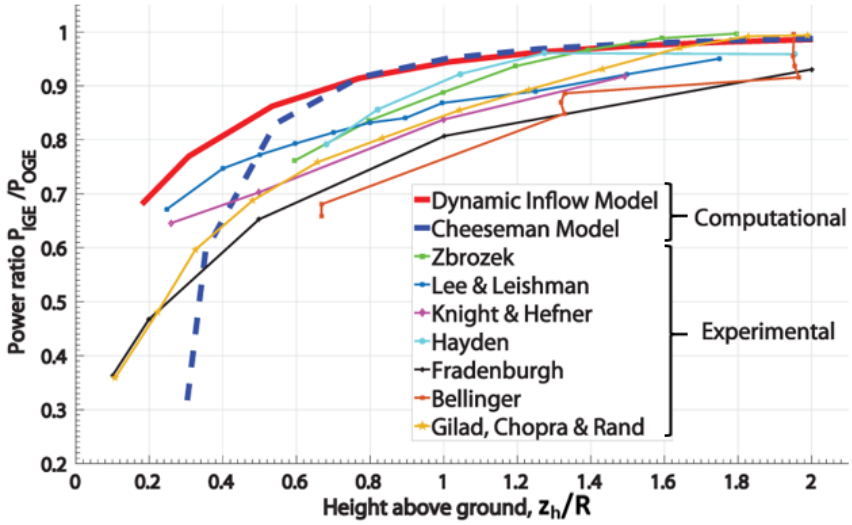

Figure 7.17: Rotor power reduction due to static and level ground effect as a function of height.

7.2.2 Effect of deck inclination

Ground effect due to static deck inclination is considered next. Hover simulation results are presented first, followed by results for landing on the inclined deck.

7.2.2.1 Hover

Hover simulations were performed at $z_h = 0.5R$, with the helicopter $\hat{x}_{hel}$ axis aligned parallel to the deck $\hat{x}_d$ axis, as illustrated in Fig. 7.18. The CG was located 8.7 ft. above the center of the deck. Four deck inclination angles were considered for Γ_{deck} and δ_{deck}: $0°, 10°, 20°$, and $30°$.

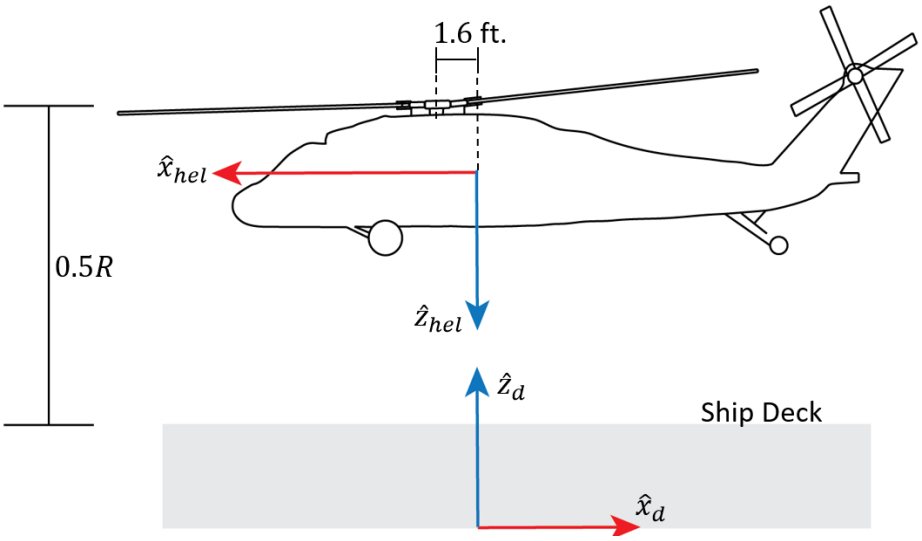

Figure 7.18: Hover configuration during static deck inclination simulations.

Time histories of the effective inflow coefficients $\boldsymbol{\alpha}^{IGE}$ for static deck roll are shown in Fig. 7.19. Since a 3-state He-Peters dynamic inflow model is employed, there are three inflow coefficients α_0^{IGE}, α_c^{IGE}, and α_s^{IGE} corresponding to the average, fore-and-aft and lateral components of inflow, respectively. The baseline case, with no ground effect, is included for comparison. A decrease in the average and lateral components of inflow α_0^{IGE} and α_s^{IGE}, respectively, is noted with increasing roll angle. The $30°$ case produces the greatest change. The coefficients for the $10°$ condition remain close to the $0°$ values. The inflow coefficient α_c^{IGE} does not vary with deck roll angle.

Control input time histories are shown in Fig. 7.20. The ground effect from the rolled deck produces offsets in the control inputs, relative to the $0°$ case. The $30°$ case results in the greatest offsets of approximately $0.5°$ in the longitudinal cyclic and tail rotor collective

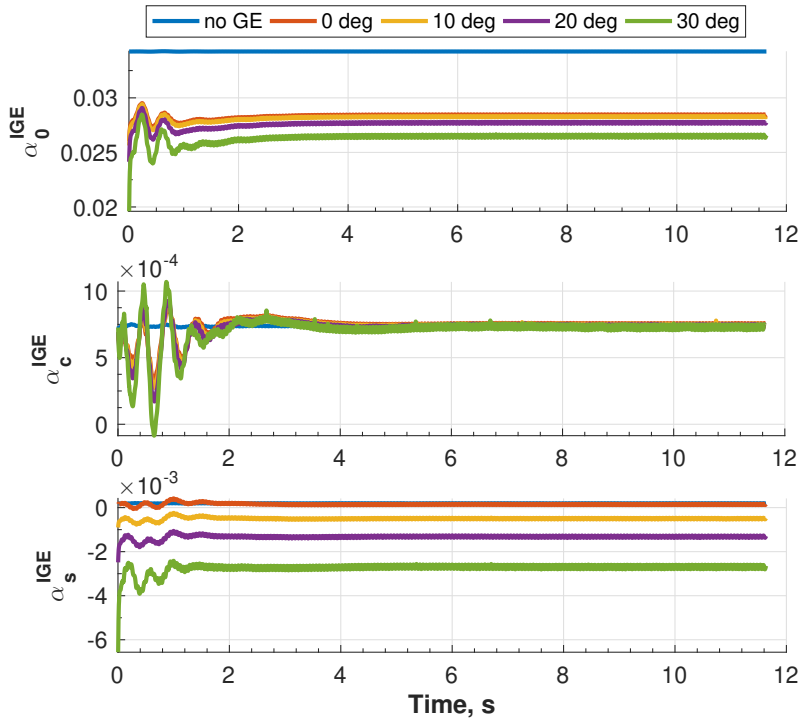

Figure 7.19: Time histories of effective inflow coefficients during hover over a deck inclined at a static roll angle.

inputs, and approximately $0.3°$ in the main rotor collective input. The longitudinal cyclic θ_{1s} is used to control the lateral disturbance in inflow due to static deck roll. This is an interesting finding given that θ_{1s} is normally used to control the longitudinal dynamics of the helicopter. Ground influence on the lateral cyclic input θ_{1c} is minimal.

The power required to sustain the hover flight segment for the various deck roll cases is plotted in Fig. 7.21. The $10°$ case results in approximately the same power requirements as the level deck case, while the $30°$ condition produces a decrease of approximately 5.3% in power requirement, from 1520 Hp to 1440 Hp. Note that the ground effect from the rolled deck causes a rise in the vertical CG position, as shown in Fig. 7.22. This is due to a corresponding increase thrust produced, shown in Fig. 7.23.

Time histories of the effective inflow coefficients during hover over a deck inclined at constant pitch angles are plotted in Fig. 7.24. This time, a change in the average and cosine components of the inflow is noted, while the sine component α_s^{IGE} remains constant. Deck

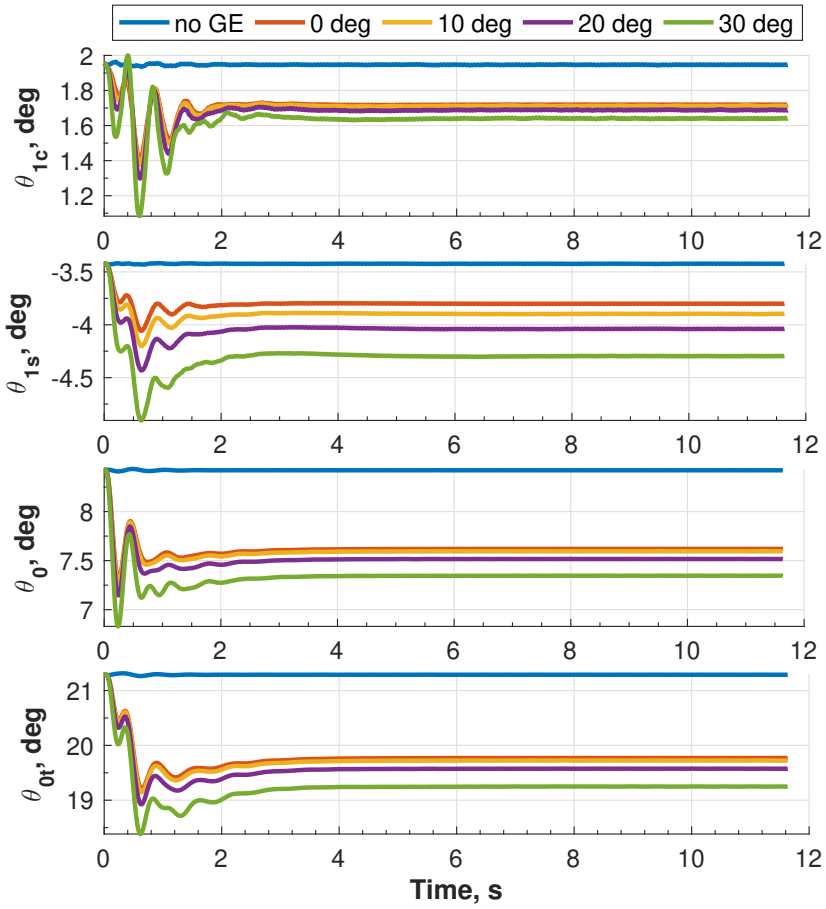

Figure 7.20: Control inputs generated by FCS during hover over a deck inclined at a static roll angle.

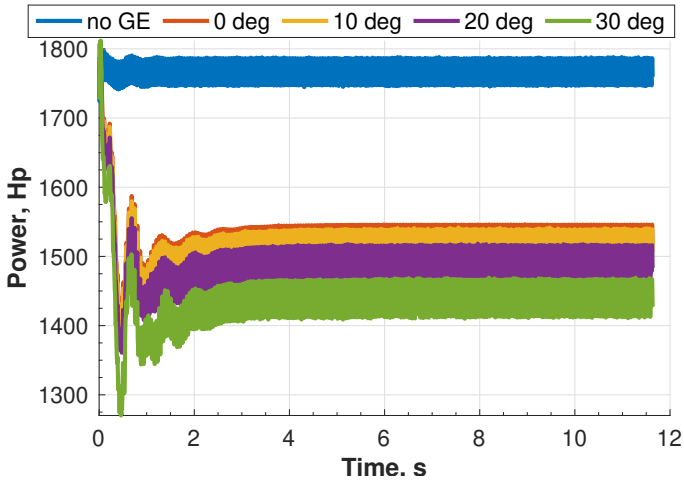

Figure 7.21: Time histories of power required during hover over a deck inclined at a static roll angle.

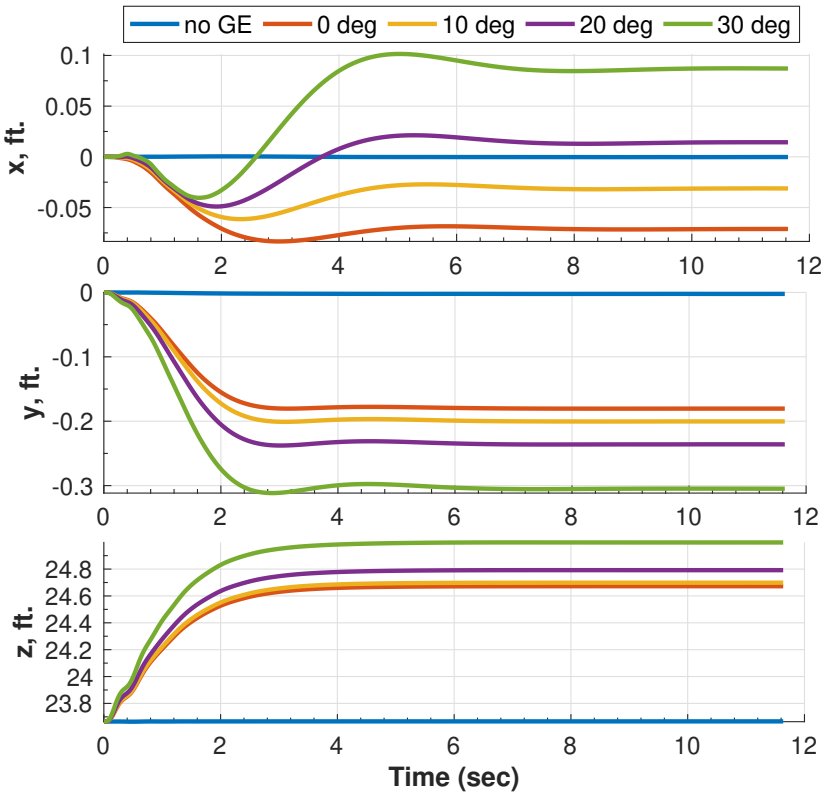

Figure 7.22: Time histories of CG position coordinates relative to the deck frame during hover over a deck inclined at a static roll angle.

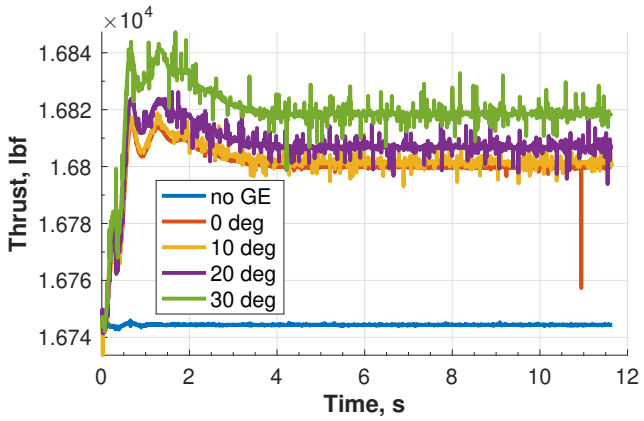

Figure 7.23: Rotor thrust during hover over a deck inclined at a static roll angle.

pitch attitude thus produces a ground effect that affects the longitudinal inflow distribution. The control input time histories are shown in Fig. 7.25. The ground effect due to deck pitch attitude causes a slight increase in the lateral cyclic control input θ_{1c}, with the 30°

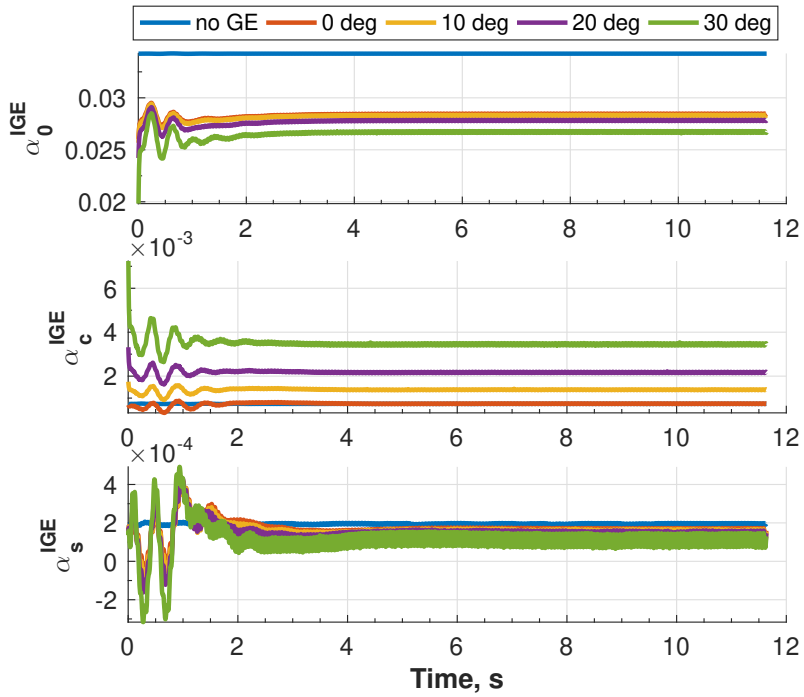

Figure 7.24: Time histories of effective inflow coefficients during hover over a deck inclined at a static pitch angle.

case producing the greatest change of approximately $0.3°$, relative to the $0°$ case. Similar offsets are noted in the main and tail rotor collective inputs. The θ_{1s} input remains relatively unchanged. A 5.3% decrease in power requirement is again noted for the $30°$ condition in Fig. 7.26.

7.2.2.2 Landing

Landing simulations were performed to examine the influence of static deck inclination on landing gear dynamics. After a 10s hover flight segment, based on the configuration depicted in Fig. 7.18, the main rotor collective was progressively reduced to achieve landing. Results are presented for two cases: a) a deck inclined at a constant roll angle of $10°$, and b) a deck inclined at a constant pitch angle of $8°$, illustrated in Fig. 7.27. These angles were found to be the positive limits at which the controller is able to perform a stable landing. The negative limits were $-9°$ for roll attitude, and $-8°$ for pitch attitude.

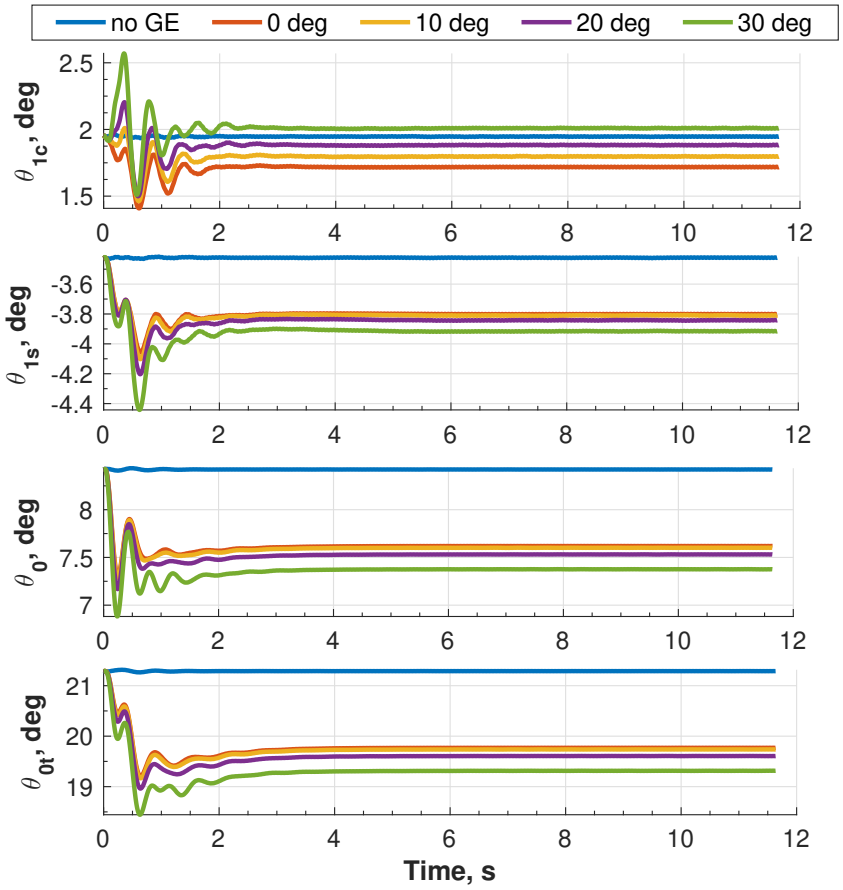

Figure 7.25: Control inputs generated by FCS during hover over a deck inclined at a static pitch angle.

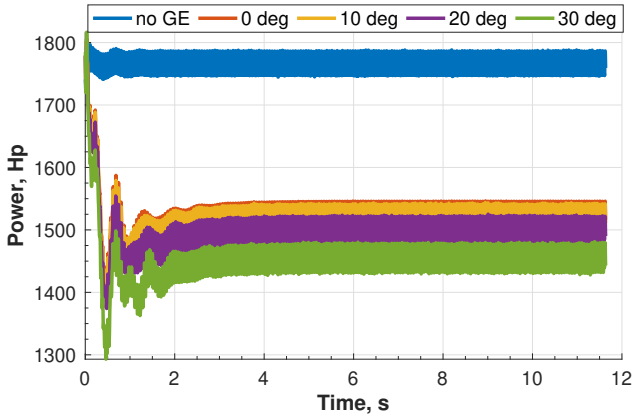

Figure 7.26: Time histories of power required during hover over a deck inclined at a static pitch angle.

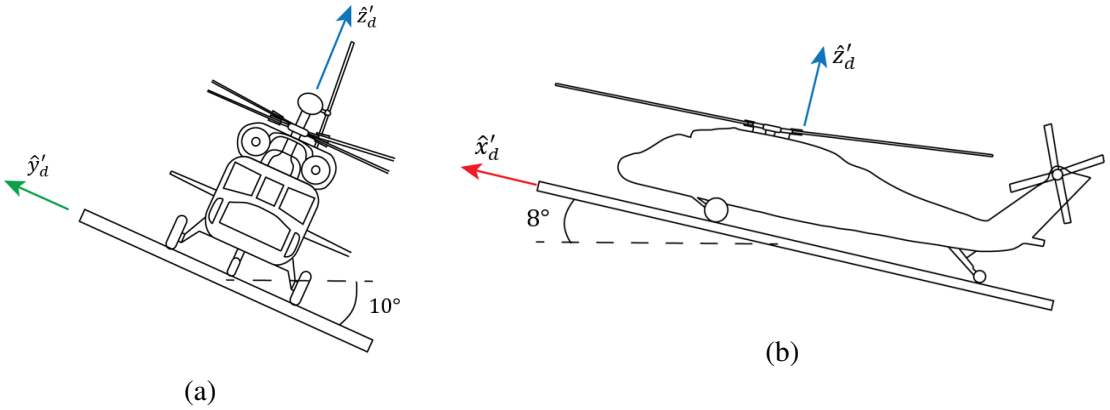

Figure 7.27: Illustration of landing on a deck inclined at a constant (a) roll angle, and (b) pitch angle.

Time histories of the CG roll, pitch and yaw attitudes for a deck inclined at a constant roll angle of 10° are shown in Fig. 7.28. The CG roll angle converges to approximately -10° after landing, thus matching the deck roll angle. The ϕ_f angle is negative because it is defined relative to the helicopter body-fixed frame, which has its positive $\hat{x}_{hel}$ axis in a direction opposite to the positive $\hat{x}_d$ axis, relative to which the 10° deck roll angle is defined. The pitch angle converges to -2.8° after landing, and the yaw angle to -14.2°.

The vertical position coordinates of the three gears and the corresponding points below them on the deck are shown in Fig. 7.29. The gear positions become constant after $t = 12.2$ s, indicating successful landing on the rolled deck. Due to the constant deck roll angle, the point on the deck below the right gear is higher than the deck point under the left gear. The change noted in the deck point under the tail gear between $t = 10.0$ s and $t = 12.2$ s is due to the change in yaw attitude, shown in Fig. 7.28. Gear deflections are plotted in Fig. 7.30. The tail gear makes contact with the deck first at $t = 12.00$ s, followed by the right gear at $t = 12.04$ s, and the left gear at $t = 12.23$ s. After landing, right, left, and tail gear deflections are 0.28 ft., 0.29 ft., and 0.05 ft., respectively. Ground effect causes a slight change of approximately 0.01 ft. in the left gear deflection.

Time histories of the control inputs generated by the FCS are shown in Fig. 7.31. The ground effect from the rolled deck causes the main rotor collective to decrease by 8.3%

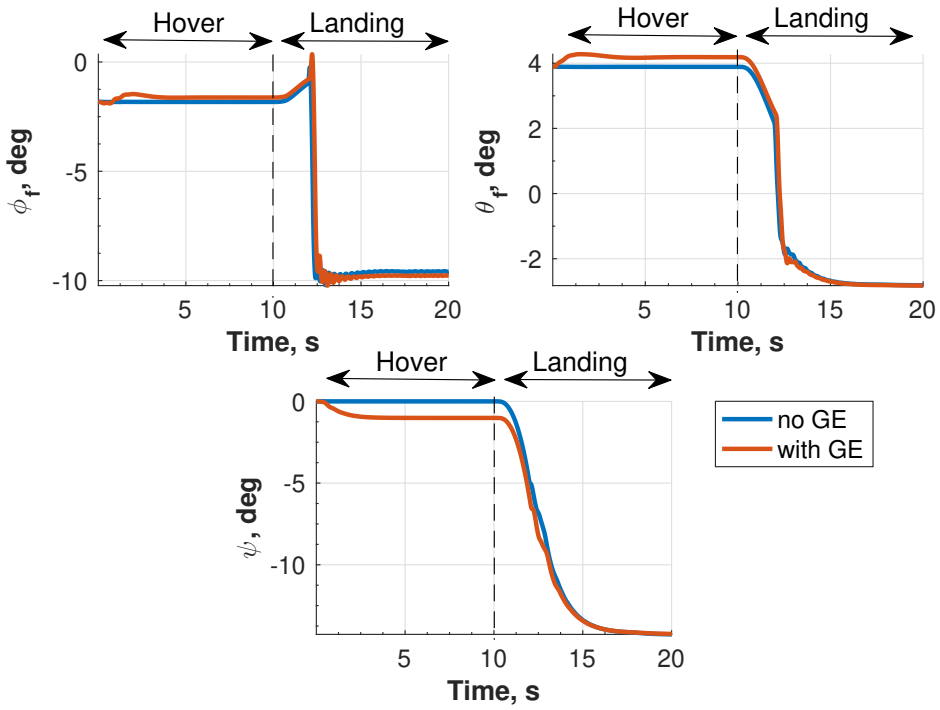

Figure 7.28: Roll, pitch and yaw attitudes during hover and landing flight segments with the deck inclined at a constant roll angle of $10°$.

at the onset of the landing phase, which is close to the 8.6% change noted in the main rotor collective with a level ground plane in Fig. 7.12. The influence of constant $10°$ deck roll angle is thus not significant. The lateral cyclic θ_{1c} changes by approximately $5°$ after landing to counteract the helicopter rolling moment caused by the deck roll angle. The longitudinal cyclic converges to approximately $-0.4°$ after landing.

Results for the deck inclined at a constant pitch angle of $8°$ are discussed next. The CG angular attitudes during the hover and landing flight segments are shown in Fig. 7.32. High frequency oscillations with a magnitude of approximately $0.5°$ are noted in the roll angle in the landing phase. The pitch angle converges to approximately $7.2°$ after landing, closely matching the constant deck pitch angle. The yaw angle converges close to $-18°$.

The vertical position coordinates of the three gears are shown in Fig. 7.33. The deck point below the tail gear is at a height of 11.7 ft. during hover, while the points under the main gears are 15.8 ft. high due to the constant deck pitch angle. The vehicle successfully

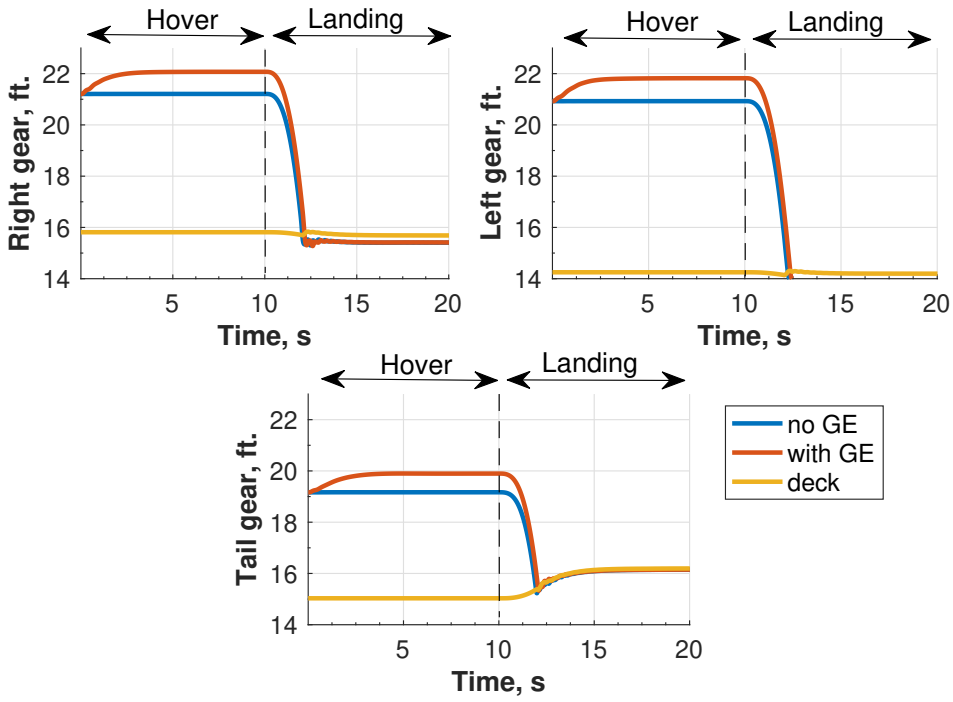

Figure 7.29: Vertical gear positions during hover and landing flight segments with the deck inclined at a constant roll angle of $10°$.

lands at $t = 12.3$ s, as indicated in the figure. The main gears make contact first at $t = 12.0$ s, followed by the tail gear at $t = 12.3$ s.

The control inputs generated by the FCS during the hover and landing flight segments are shown in Fig. 7.34. The high frequency oscillations evident in the lateral cyclic after landing indicates that greater control is required to keep the vehicle stationary on the pitched deck. The longitudinal cyclic θ_{1s} converges to approximately $-7.3°$ after landing to counteract the pitching moment due to the constant deck pitch angle. The change in θ_0 in response to the ground effect from the pitched deck is close to that noted with a level deck, shown in Fig. 7.12. The tail rotor collective converges to approximately $12°$ after landing.

7.2.3 Influence of isolated ground motion

Hover and landing simulations were performed with the deck undergoing isolated sinusoidal motion in roll, pitch and heave DOFs to examine the influence of dynamic ground

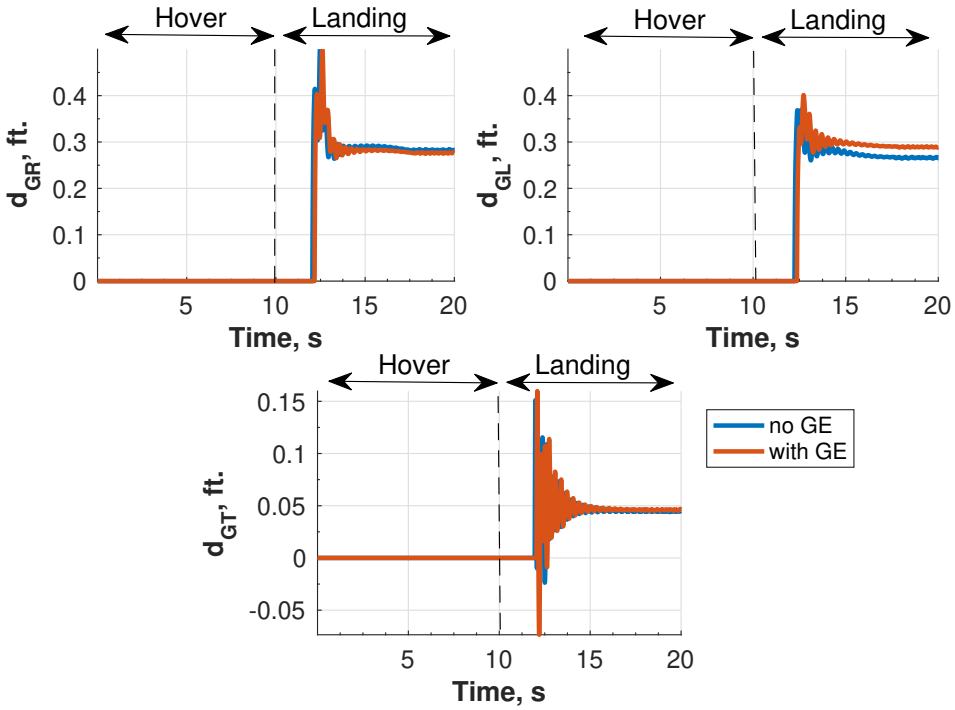

Figure 7.30: Vertical gear positions during hover and landing flight segments with the deck inclined at a constant roll angle of 10°.

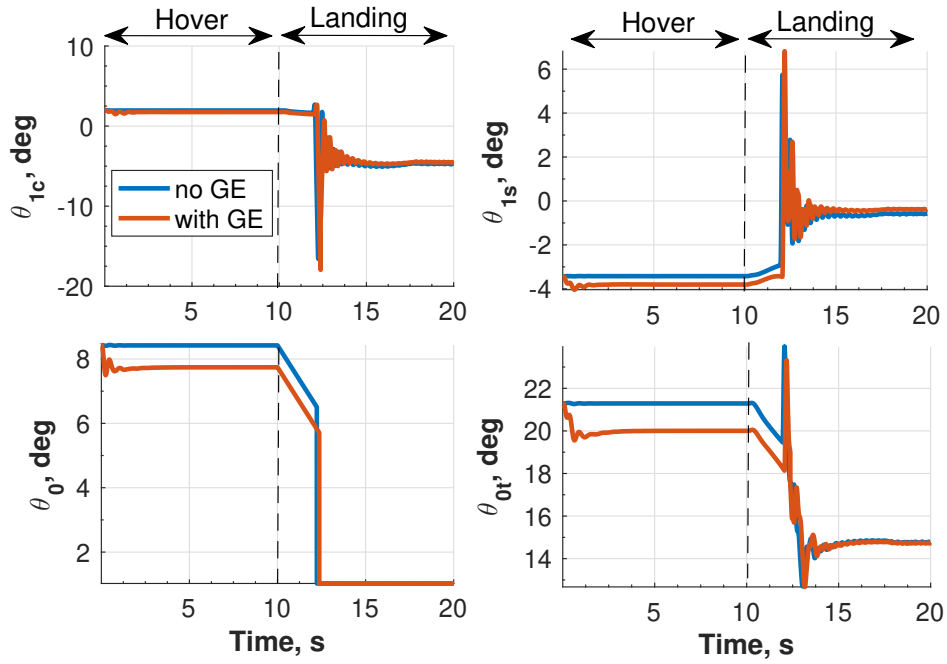

Figure 7.31: Control input time histories during hover and landing flight segments with the deck inclined at a constant roll angle of 10°.

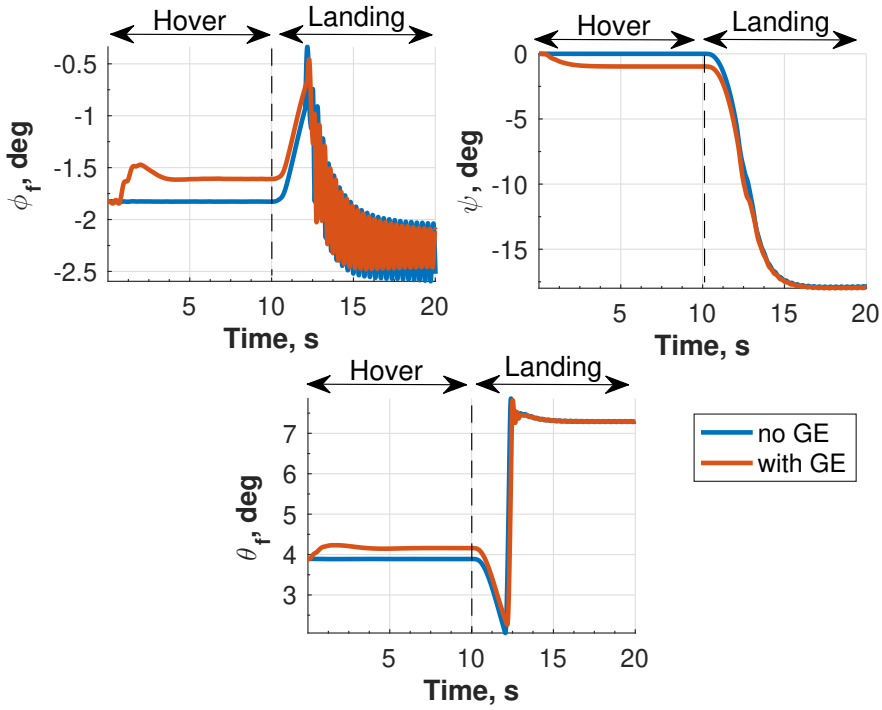

Figure 7.32: Roll, pitch and yaw attitudes during hover and landing flight segments with the deck inclined at a constant pitch angle of $8°$.

effect.

7.2.3.1 Hover

Hover simulations, for roll motion alone, were performed with the rotor at a height of $0.5R$, following the configuration depicted in Fig. 7.18. The deck was excited with a sinusoidal angular motion at 0.1 Hz, which represents the dominant frequency in SCONE ship motion data. Thus,

$$\Gamma_{deck}(t) = \Gamma_{deck} \sin\left(\frac{\pi}{5}t\right), \tag{7.1}$$

and

$$\dot{\Gamma}_{deck}(t) = -\Gamma_{deck}\frac{\pi}{5}\cos\left(\frac{\pi}{5}t\right), \tag{7.2}$$

Four amplitudes were considered for Γ_{deck}: $0°, 10°, 20°$, and $30°$.

Time histories of the effective inflow coefficients $\boldsymbol{\alpha}^{IGE}$ for deck rolling motion, are

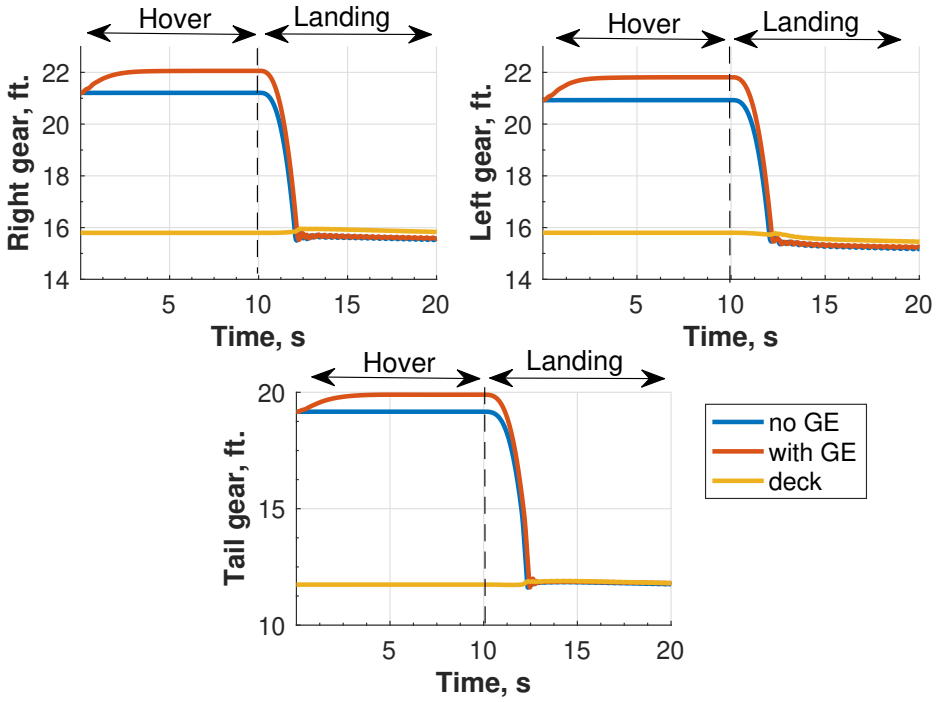

Figure 7.33: Vertical gear positions during hover and landing flight segments with the deck inclined at a constant pitch angle of 8°.

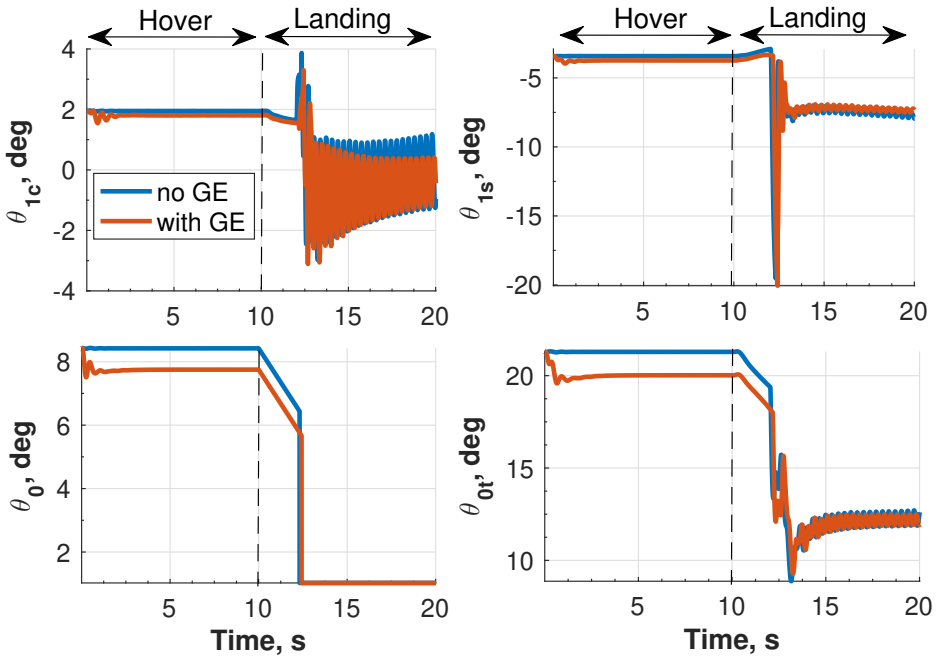

Figure 7.34: Control input time histories during hover and landing flight segments with the deck inclined at a constant pitch angle of 8°.

shown in Fig. 7.35. Harmonic oscillations are evident in the coefficients. The oscillations in the sine component of the inflow α_s^{IGE} occur at a frequency 0.1 Hz, matching the deck excitation frequency. The response has a phase *lead* of approximately $22°$. From Fig. 7.35, deck rolling motion produces fluctuations at twice the excitation frequency in α_0^{IGE}. This is because of the hover configuration employed, where the influence of deck roll on average rotor inflow is the same for both positive and negative values of Γ_{deck}. The amplitudes corresponding to the $30°$ condition are the largest. The influence of deck rolling motion on the α_c^{IGE} coefficient is minimal.

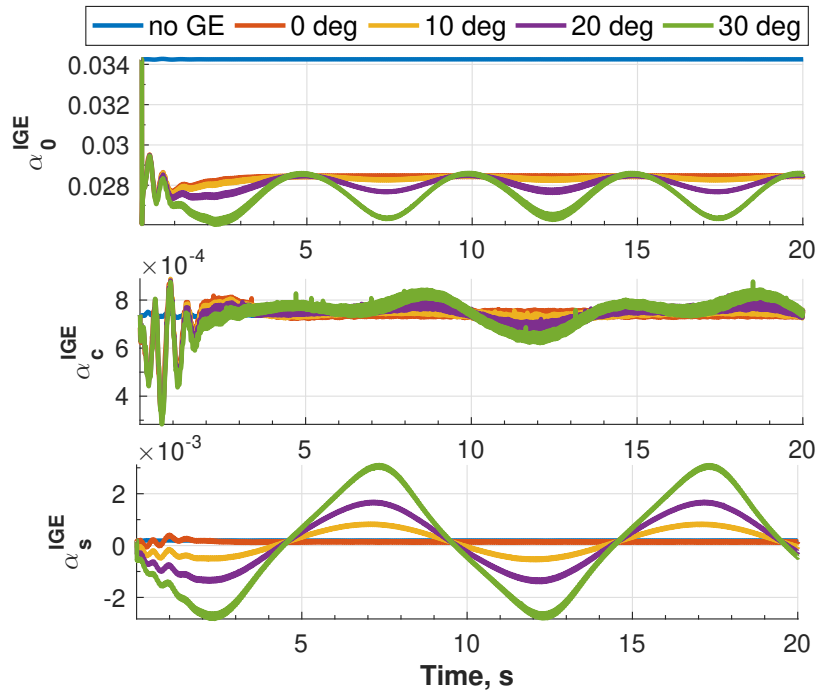

Figure 7.35: Time histories of effective inflow coefficients during hover over a deck excited by roll motion alone.

The control inputs generated by the FCS during hover over a rolling deck are shown in Fig. 7.36. The oscillations in the longitudinal cyclic θ_{1s} occur at a frequency of 0.1 Hz while the remaining inputs have a frequency of 0.2 Hz. The $30°$ deck rolling motion changes the longitudinal cyclic by close to $1°$. The influence on the lateral cyclic is relatively small, while the main and tail rotor collective inputs change by $0.3°$ and $7°$, re-

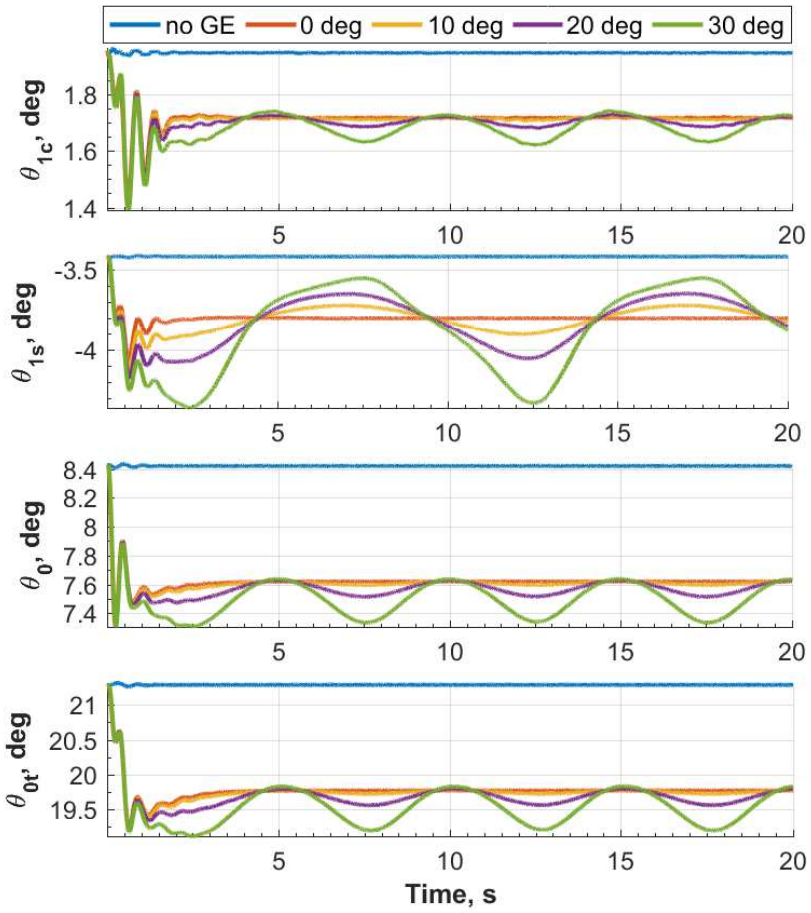

Figure 7.36: Control inputs generated by FCS during hover over a deck excited by roll motion alone.

spectively. Note that the control inputs generated with the deck rolling at 10° remain close to the level deck counterparts. The frequency spectra of the control inputs are plotted in Fig. 7.37. The dominant frequency in the lateral cyclic, and main and tail rotor collective inputs is 0.2 Hz, which is twice the excitation frequency. Note that less dominant motion at 0.1 Hz is noted in θ_{1c}. The dominant frequency in the longitudinal cyclic θ_{1s} response is 0.1 Hz, with less dominant motion at 0.2 Hz. For the 30° deck roll condition, an additional frequency peak at 0.3 Hz is noted in Fig. 7.37. Thus, a larger *amplitude* deck excitation produces a control response with frequencies that are integer multiples of the excitation frequency.

The power required to sustain the hover flight segment over a rolling deck is plotted

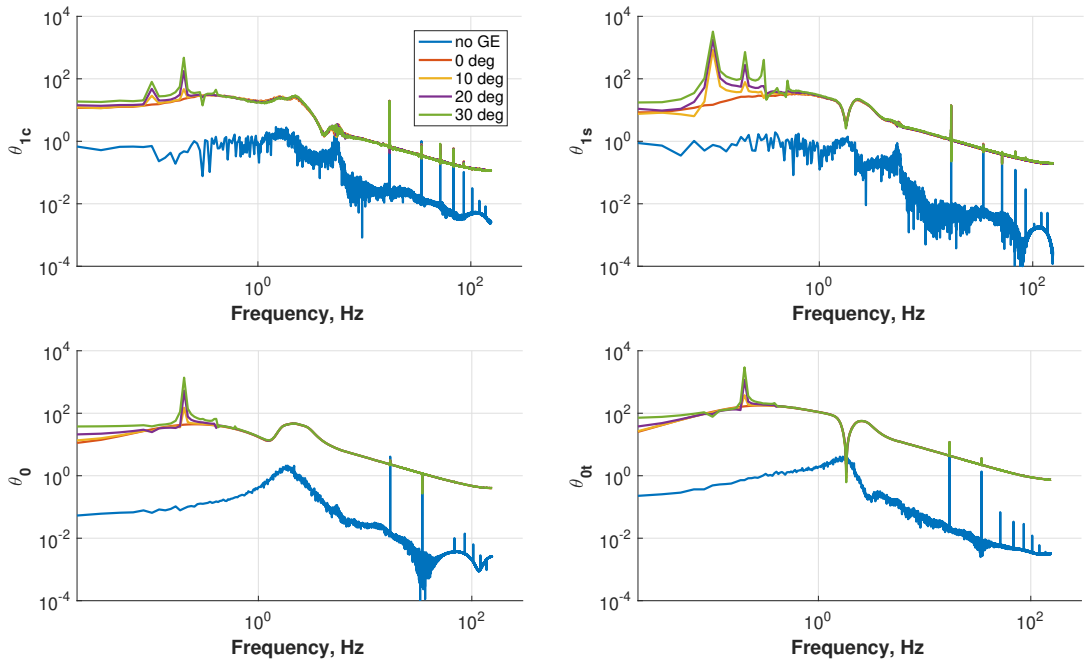

Figure 7.37: Frequency spectra of control inputs during hover over a deck excited by roll motion alone.

in Fig. 7.38. The 10° and 20° roll conditions result in approximately the same power requirements as the level deck case, while the 30° condition causes changes of approximately 7.2% in power requirement. Slight displacements (<0.2ft.) are noted in the CG position coordinates, shown in Fig. 7.39. The change in the vertical displacement is due to the corresponding change in the rotor thrust, plotted in Fig. 7.40.

Results for hover over a deck excited in pitching motion alone are described next. The deck was excited by the following motion:

$$\delta_{deck}(t) = \delta_{deck} \sin\left(\frac{\pi}{5}t\right), \tag{7.3}$$

and thus,

$$\dot{\delta}_{deck}(t) = -\delta_{deck}\frac{\pi}{5}\cos\left(\frac{\pi}{5}t\right). \tag{7.4}$$

Hover simulations were performed at $z_h = 0.5R$ following the previous configuration. The amplitudes considered for δ_{deck} were: $0^\circ, 10^\circ, 20^\circ$, and 30°.

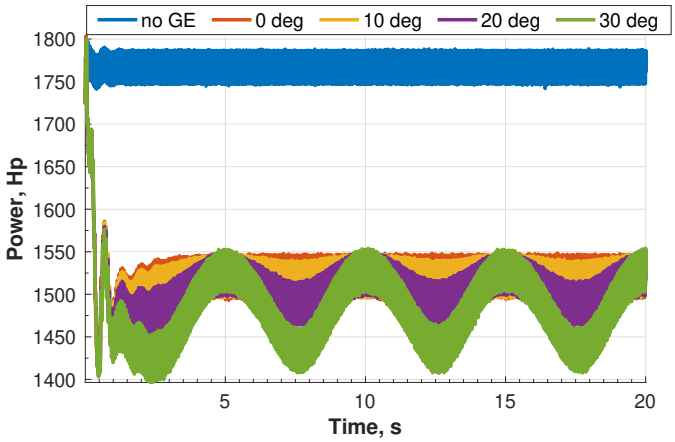

Figure 7.38: Time histories of power required during hover over a deck excited by roll motion alone.

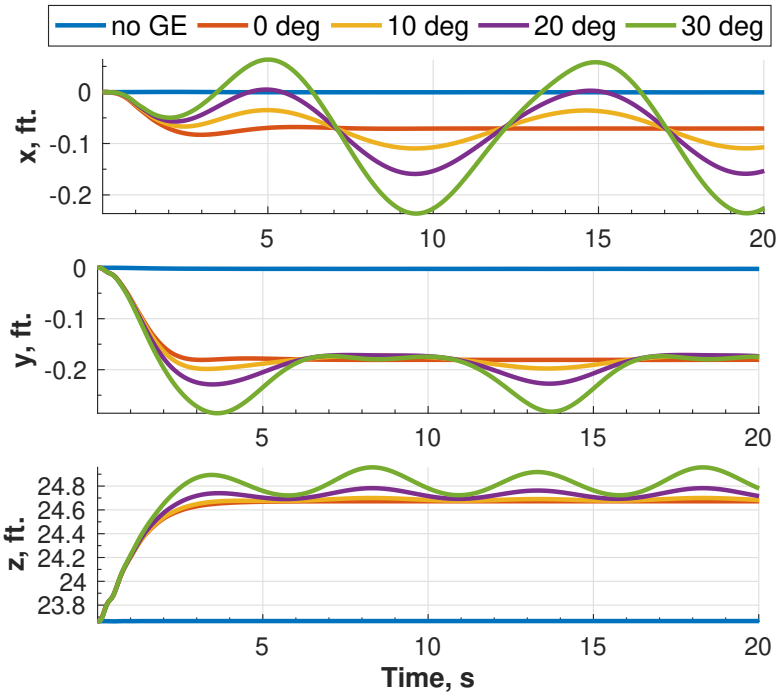

Figure 7.39: Time histories of CG position coordinates relative to the deck frame during hover over a deck excited by roll motion alone.

Time histories of the effective inflow coefficients are plotted in Fig. 7.41. Harmonic oscillations are evident in the average and fore-and-aft coefficients α_0^{IGE} and α_c^{IGE} of the effective inflow. The oscillations in the α_c^{IGE} component have a frequency of 0.1 Hz, while those in the α_0^{IGE} component have a frequency of 0.2 Hz. There is a phase *lag* of

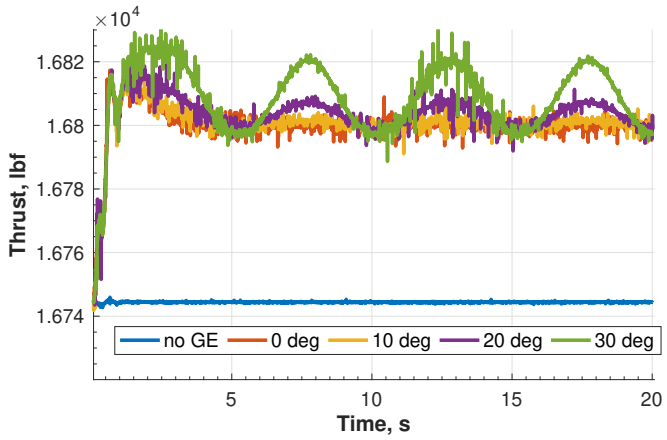

Figure 7.40: Rotor thrust during hover over a deck excited by roll motion alone.

approximately $14°$, relative to the excitation, in the α_c^{IGE} coefficient. The dynamic ground effect from the pitching deck has minimal impact on the sine component α_s^{IGE}.

The control input time histories generated during the hover flight segment are shown in Fig. 7.42. The oscillations in the lateral cyclic have a frequency of 0.1 Hz. The $30°$ con-

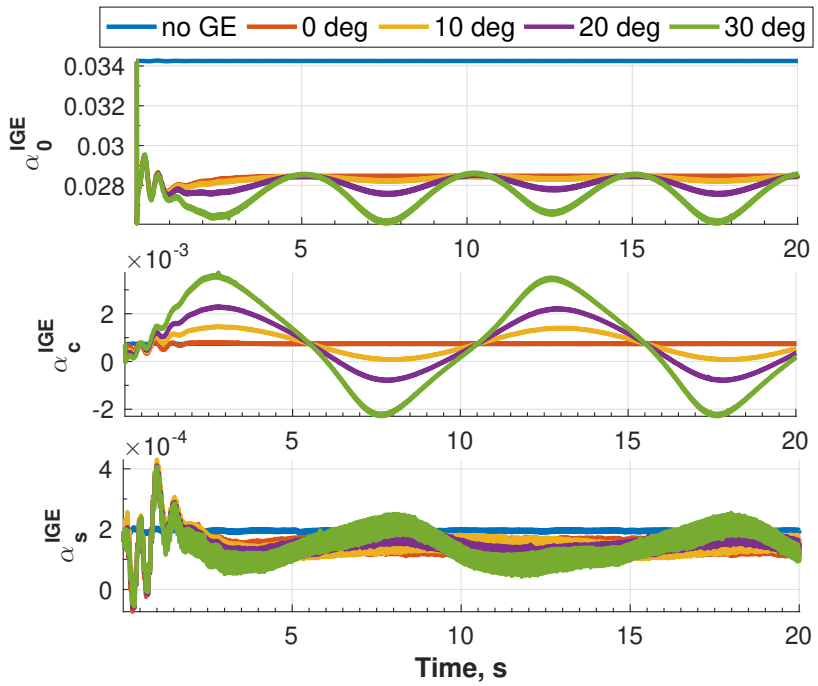

Figure 7.41: Time histories of effective inflow coefficients during hover over a deck excited by pitch motion alone.

dition produces changes of approximately 0.5° in the lateral cyclic, 0.3° in the main rotor collective, and 0.7° in the tail rotor collective, relative to the static, level deck condition. The oscillations in the θ_{1c}, θ_0 and θ_{0t} time histories occur at twice the excitation frequency. The trend noted in the lateral cyclic θ_{1c} points to the existence of multiple dominant frequencies. From the frequency spectra of θ_{1c}, plotted in Fig. 7.43, these frequencies are identified to be 0.1 Hz, 0.2 Hz and 0.3 Hz, with 0.1 Hz being most dominant.

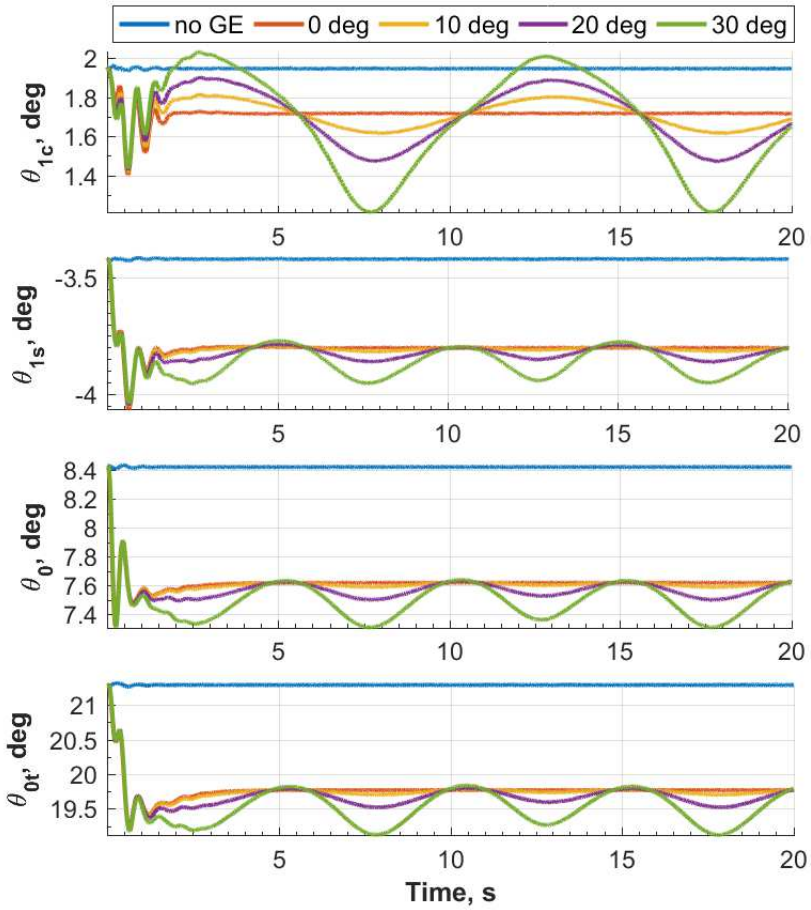

Figure 7.42: Control inputs generated by FCS during hover over a deck excited by pitch motion alone.

Time histories of power required during hover for the various deck pitching conditions are shown in Fig. 7.44. In the 30° pitching condition, changes of approximately 7.2% are noted in the power requirements, relative to the 0° deck condition.

Results for the helicopter in hover over a heaving deck are presented next. Two sinu-

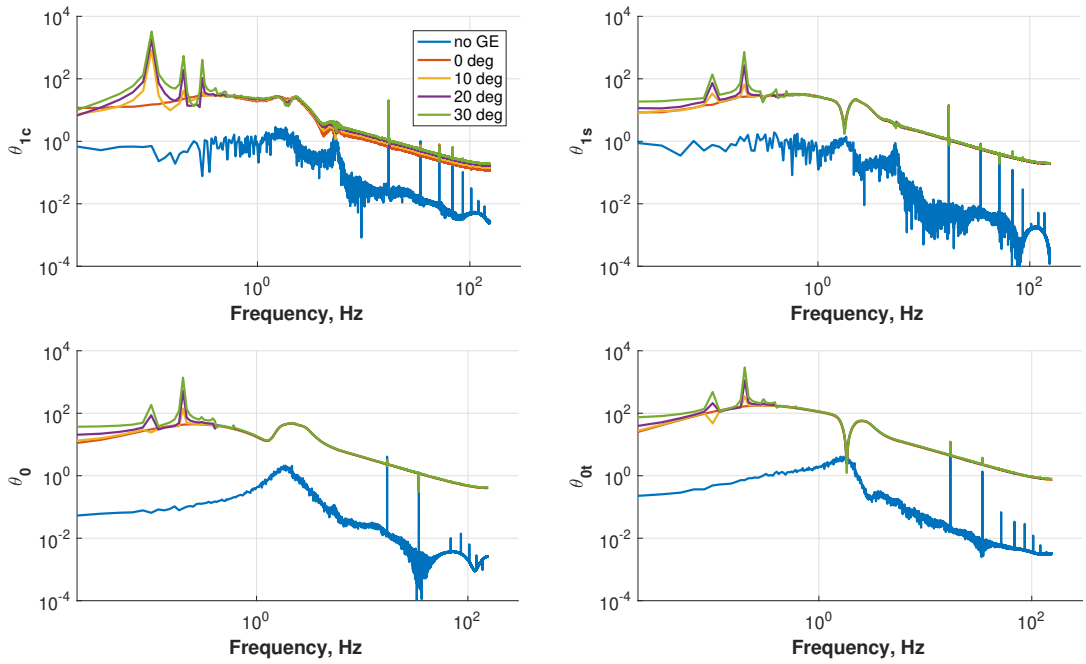

Figure 7.43: Frequency spectra of control inputs during hover over a deck excited by pitch motion alone.

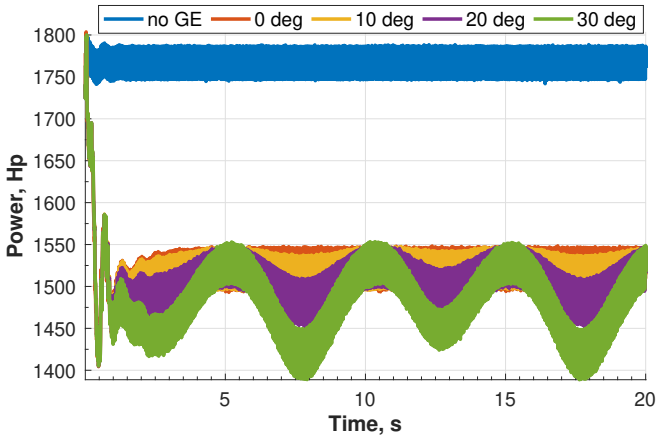

Figure 7.44: Time histories of power required during hover over a deck excited by pitch motion alone.

soidal heave displacements with an amplitude of 5 ft. were considered,

$$z_{dyn}(t) = z_{dyn} \sin\left(\frac{\pi}{10}t\right), \tag{7.5}$$

$$z_{dyn}(t) = z_{dyn} \sin\left(\frac{3\pi}{10}t\right), \tag{7.6}$$

where the first case corresponds to an excitation frequency of 0.05 Hz, and the second to 0.15 Hz. Note that the dominant frequency in SCONE heave motion is 0.15 Hz, as noted in Chapter 6. The hover configuration employed is similar to that depicted in Fig. 7.18, with the only difference being the starting height of the CG, which was set to 12.7 ft., to allow for enough clearance between the landing gears and heaving deck. The ground velocities corresponding to the heave displacement in Eqs. (7.5) and (7.6) are given by

$$\dot{z}_{dyn}(t) = \frac{d}{dt}\left[z_{dyn}\sin\left(\frac{\pi}{10}t\right)\right] = -z_{dyn}\frac{\pi}{10}\cos\left(\frac{\pi}{10}t\right), \tag{7.7}$$

$$\dot{z}_{dyn}(t) = \frac{d}{dt}\left[z_{dyn}\sin\left(\frac{3\pi}{10}t\right)\right] = -z_{dyn}\frac{3\pi}{10}\cos\left(\frac{3\pi}{10}t\right), \tag{7.8}$$

respectively. Note that the ground velocity in the 0.15 Hz heave excitation condition is three times higher than the ground velocity corresponding to the 0.05 Hz excitation condition.

Time histories of the effective inflow coefficients are shown in Fig. 7.45. Deck heaving motion affects the average component of inflow the most, with the 0.15 Hz excitation condition producing the greatest fluctuations. The changes in the cosine and sine components of the effective inflow are small, $O(10^{-4})$. The control input time histories are plotted in Fig. 7.46. High amplitude harmonic oscillations are evident in the figure. The 0.05 Hz and 0.15 Hz deck heaving motions produce changes of approximately 0.3° in the main rotor collective input, relative to the no-ground-effect case. Deck heaving motion also causes the tail rotor and cyclic inputs to change by 0.6° and 0.1°, respectively, relative to the no-ground-effect values. The frequency spectra of the control inputs are plotted in Fig. 7.47. For the 0.05 Hz excitation condition, the responses have a matching dominant frequency of 0.05 Hz. For the 0.15 Hz excitation condition however, two peaks are noted: one at 0.15 Hz, and the other at 0.3 Hz, indicating that a higher *frequency* deck excitation also produces a control response with frequencies that are integer multiples of the excitation frequency.

The power required to maintain the hover flight segment in the presence of a heaving ground plane is shown in Fig. 7.48. Offsets of approximately 7.5% are noted in the power

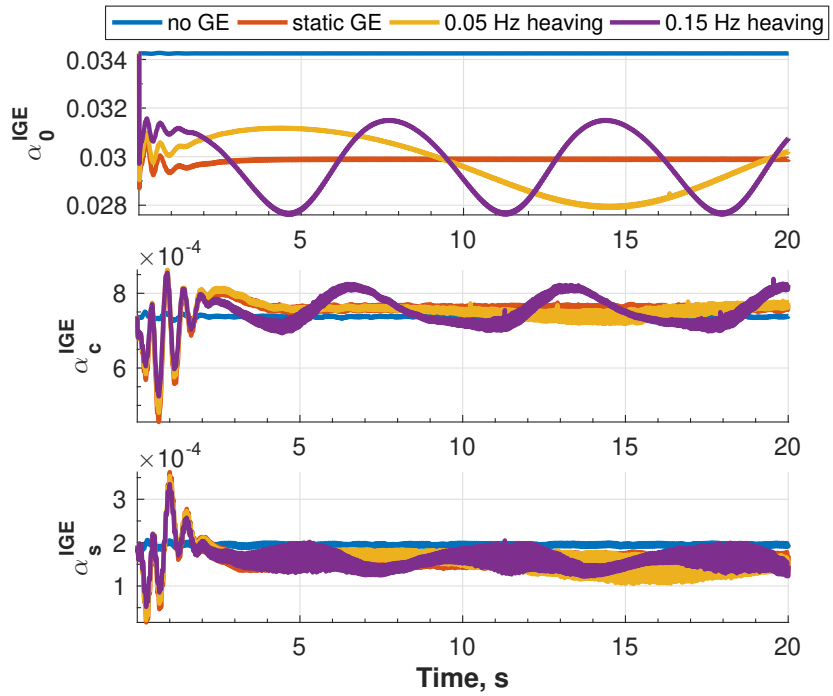

Figure 7.45: Time histories of effective inflow coefficients during hover over a deck excited by heave motion alone.

required for the 0.15 Hz excitation condition, relative to the level ground case. This corresponds to a 17% change when ground effect is not included. Thus, accounting for dynamic ground effect during shipboard operations is important.

7.2.3.2 Landing

The influence of deck motion on helicopter dynamics during landing is considered next. Results are presented for a deck undergoing isolated sinusoidal motion in roll, pitch and heave displacement, given by

$$\Gamma_{deck}(t) = 12^\circ \sin\left(\frac{\pi}{5}t\right), \tag{7.9}$$

$$\delta_{deck}(t) = 8^\circ \sin\left(\frac{\pi}{5}t\right), \tag{7.10}$$

$$\text{and} \quad z_{deck}(t) = 5 \text{ ft.} \sin\left(\frac{3\pi}{10}t\right), \tag{7.11}$$

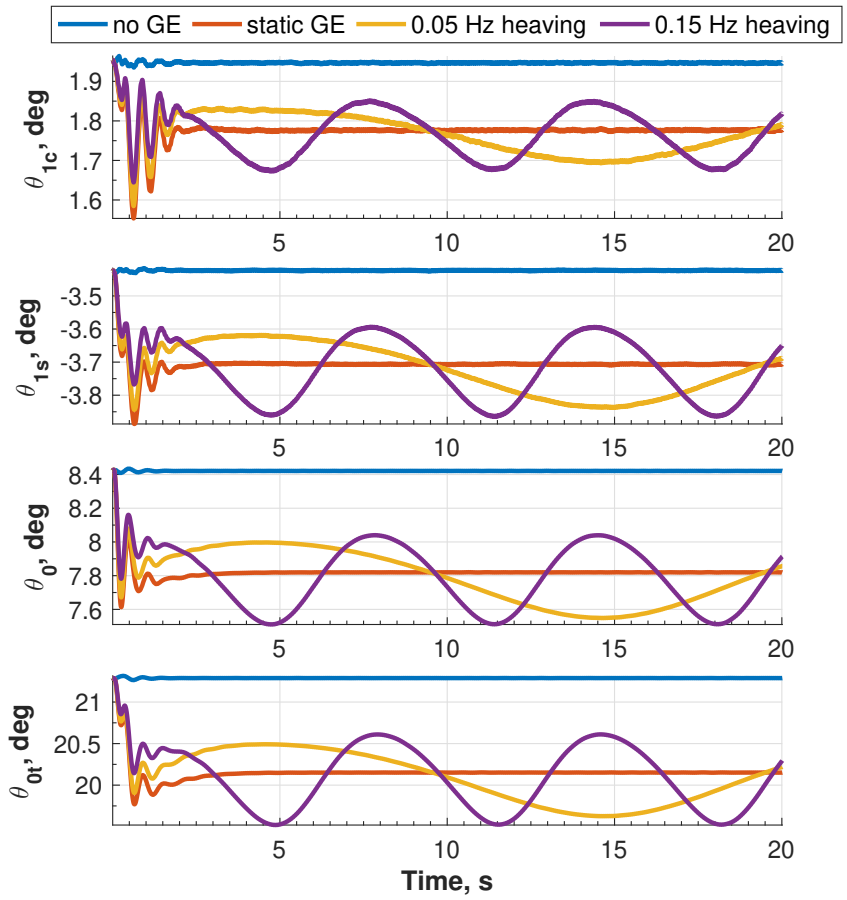

Figure 7.46: Control inputs generated by FCS during hover over a deck excited by heave motion alone.

respectively. The landing flight segment was preceded by a 10s hover flight segment based on the configuration depicted in Fig. 7.18. The initial rotor heights used were $0.5R$, $0.6R$ and $0.8R$ for isolated roll, pitch, and heave motion, respectively. These heights were chosen to allow for enough clearance between the landing gears and the deck during the hover flight segment.

The CG roll, pitch and yaw angular attitudes are plotted in Fig. 7.49 for the deck excited in roll motion alone. After landing, the CG roll angle oscillates harmonically between -12° and 11.8°, matching the deck rolling attitude. Harmonic oscillations are present in the pitch and yaw time histories as well, indicating that the friction based gear reaction forces are not sufficient to keep the vehicle stationary after landing, and that restraining devices should

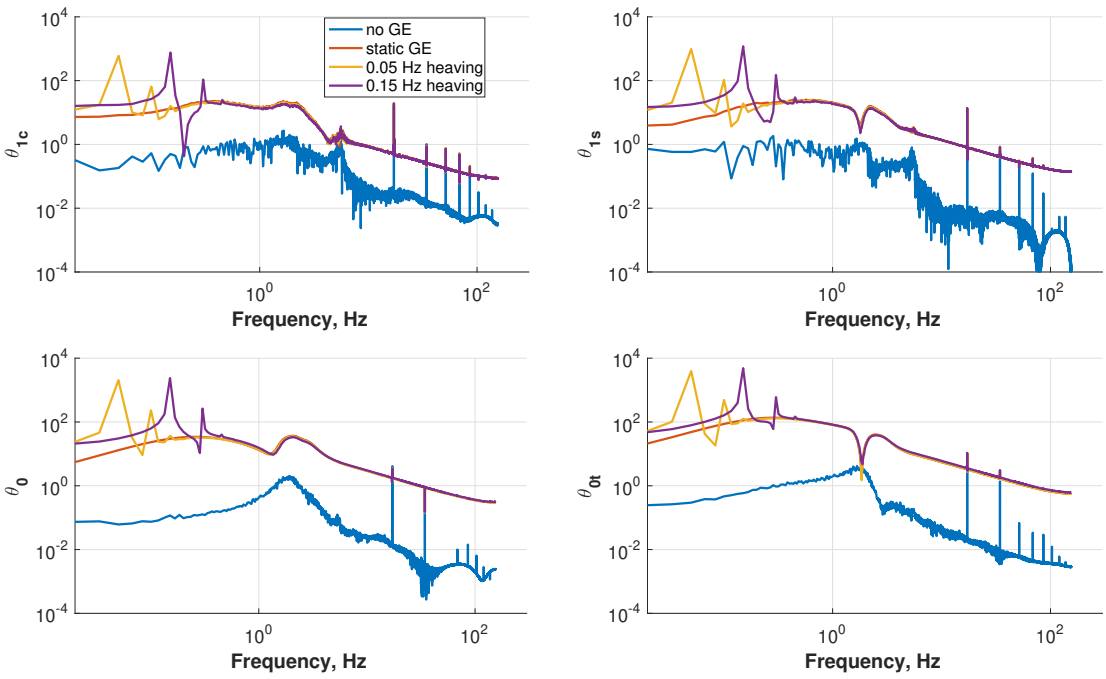

Figure 7.47: Frequency spectra of control inputs during hover over a deck excited by heave motion alone.

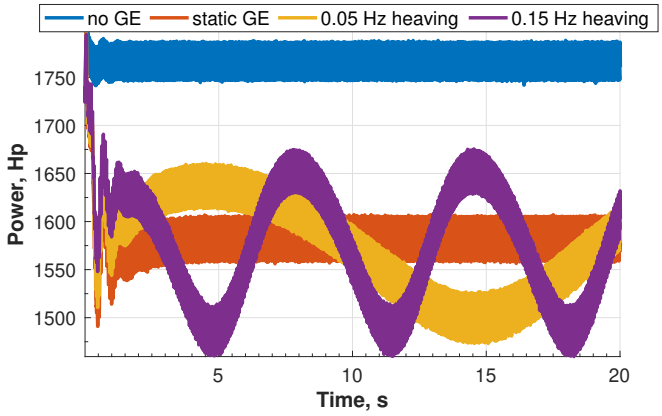

Figure 7.48: Time histories of power required during hover over a deck excited by heave motion alone.

be used. Ground effect is minimal after the vehicle lands.

The vertical positions of the gears are shown in Fig. 7.50. The gear vertical positions match the deck point positions after $t = 12.1$ s, indicating successful landing. The peaks in the right and tail gear positions at $t = 22.4$ s in Fig. 7.50 correspond to the peak in yaw angle in Fig. 7.49. Large yaw angle results in greater displacement of the gears

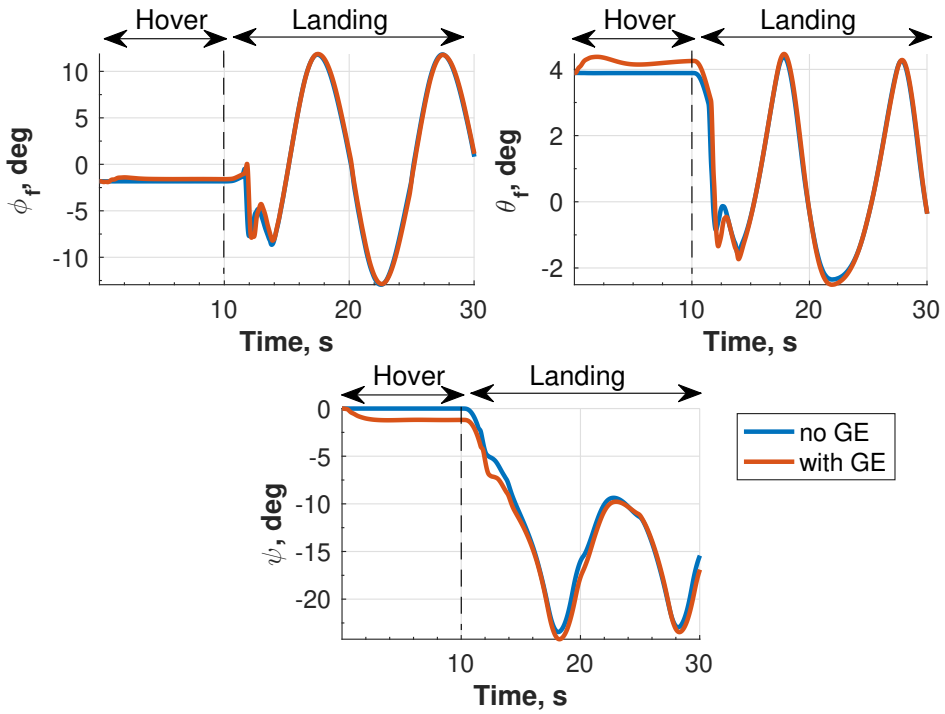

Figure 7.49: Roll, pitch and yaw attitudes during hover and landing flight segments with the deck excited by roll motion alone.

from ship centerline, which in turn enhances the effect of the deck roll angle on the gear positions. Gear deflections during landing are shown in Fig. 7.51. After landing, the main gear deflections vary between 0.15 ft. and 0.45 ft., while those of the tail gear are bounded between 0.035 and 0.086 ft. Upward motion of the deck produces compression in the spring-damper system used to model the gears. Similarly, downward motion results in a relaxation of the system. Hence, the sinusoidal response.

Control input time histories are shown in Fig. 7.52. The influence of ground effect is evident during the hover phase. Large fluctuations of approximately 18° are noted in the lateral cyclic input after the helicopter lands. The longitudinal cyclic and tail rotor collective inputs change by close to 14° after landing. Although the controller is effective in keeping the helicopter on the deck, continuously increasing displacements are noted in the CG horizontal and vertical positions in Fig. 7.53.

Results for the deck undergoing pitching motion alone, described by Eq. (7.10), are

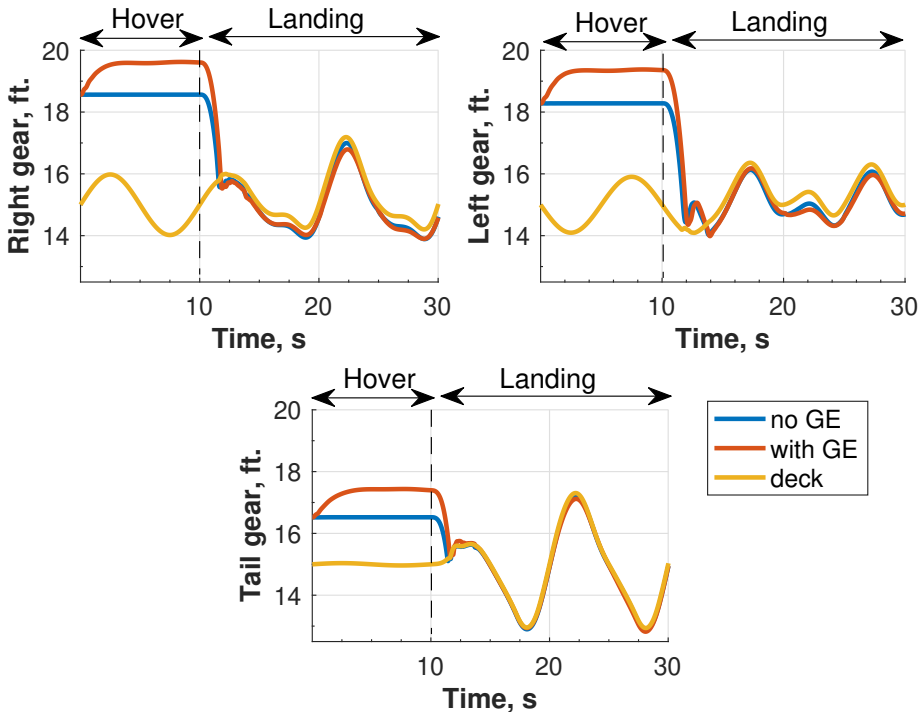

Figure 7.50: Vertical gear positions during hover and landing flight segments with the deck excited by roll motion alone.

considered next. Angular attitudes of the CG during the hover and landing flight segments are shown in Fig. 7.54. After the vehicle lands, the pitch response varies between -8° and 7.2°, matching the deck excitation. Smaller oscillations of approximately 4° are evident in the roll angle. The yaw attitude in Fig. 7.54 displays less variation than that noted in the deck rolling case, shown in Fig. 7.49.

The vertical positions of the gears are shown in Fig. 7.55. The deck point under the tail gear experiences the largest displacements since it is located furthest away from deck pitching axis, as illustrated in Fig. 5.1. The gear vertical positions match the deck point positions after $t = 12.1$ s in Fig. 7.55. The main gears make contact first at $t = 12.1$ s, followed by the tail gear at $t = 12.4$ s. Figure 7.56 shows the time histories of control inputs generated by the FCS. Changes of approximately 3° are noted in the cyclic inputs in the landing phase. The influence of ground motion diminishes after landing, and the responses converge to the no-ground-effect values.

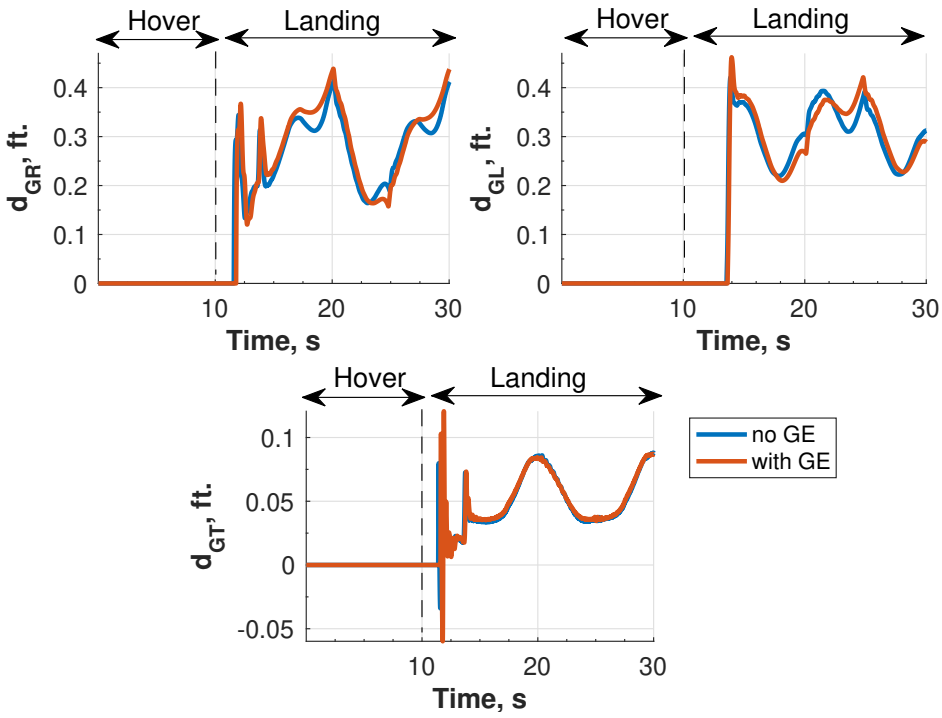

Figure 7.51: Vertical gear positions during hover and landing flight segments with the deck excited by roll motion alone.

Results for landing on a deck excited in heave, described by Eq. (7.11), are discussed next. The vertical positions of the gears are shown in Fig. 7.57. The plots indicate successful landing at $t = 12.3$ s. The tail gear makes contact first at $t = 12.3$ s, followed by the main gears 0.06s later. Large deflections of approximately 0.55 ft. are noted in the main gears in Fig. 7.58. The tail gear deflection remains relatively small, with a maximum value of approximately 0.07 ft. Time histories of the control inputs are plotted in Fig. 7.59. At a rotor height of $0.8R$, dynamic ground effect from the heaving deck produces a small change of approximately 6% in the main rotor collective input at the onset of the landing phase. Variations of approximately 1° and 2° are noted in the lateral cyclic and longitudinal cyclic inputs, respectively, after landing. The tail rotor input remains close to 11° in the landing phase.

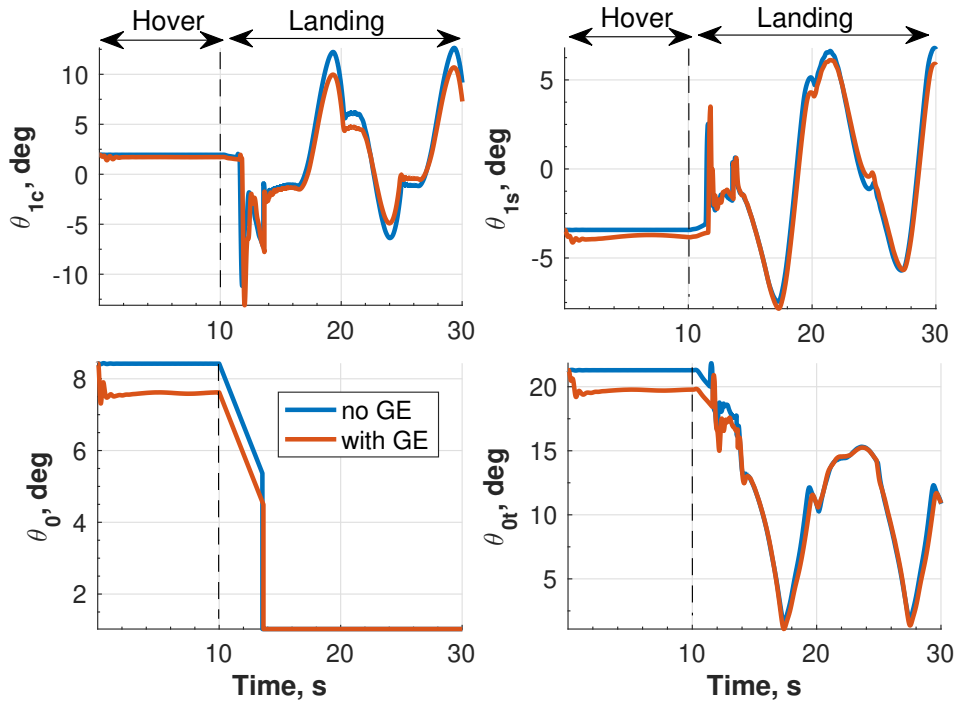

Figure 7.52: Control input time histories during hover and landing flight segments with the deck excited by roll motion alone.

7.2.4 Influence of combined SCONE motion

Hover and landing simulations were conducted with the deck excited in combined roll, pitch and heave motion, using SCONE data corresponding to the "moderate" heave displacement, shown in Fig. 6.6. The CG height during the hover phase was set to 31.7 ft., which is equivalent to $z_h = 0.8R$. Hover and landing flight segments were simulated for 110s and 10s, respectively.

Significant variation in the time histories of power consumption is noted in Fig. 7.60. Power fluctuations are evident in the figure. Changes of up to 14.1% are noted with dynamic ground effect during the hover phase, relative to case with no ground effect. Vertical positions of the gears are plotted in Fig. 7.61. The tail gear makes contact first at $t = 112.6$ s, followed by the main gears 0.1s later.

Time histories of the control inputs generated by the FCS are shown in Fig. 7.62. Ground effect from the moving deck produces slight oscillations of approximately 0.4° in

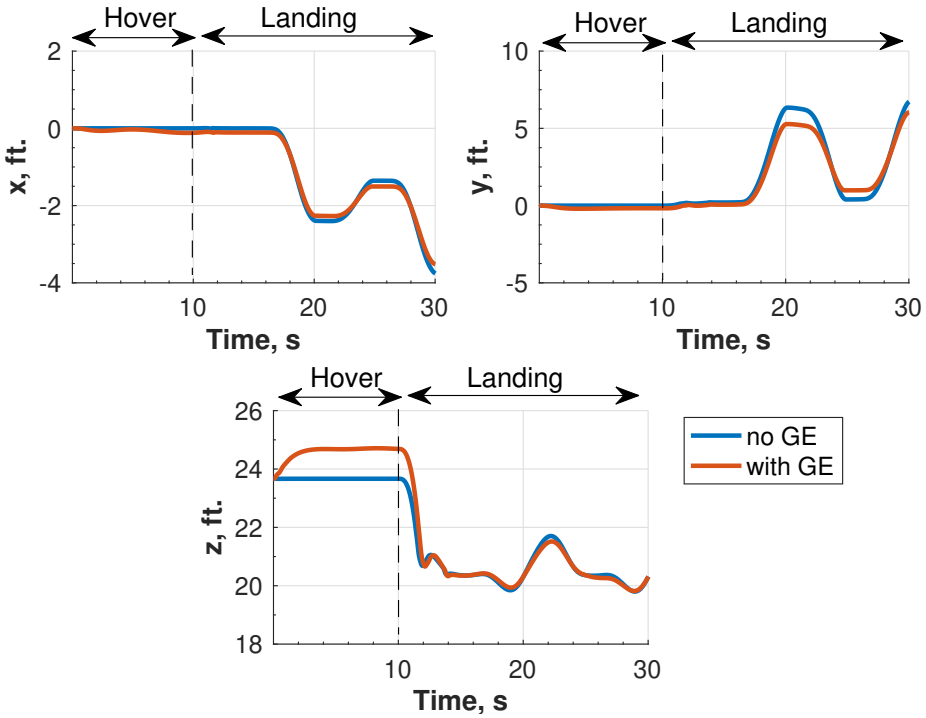

Figure 7.53: Horizontal, lateral and vertical position coordinates of CG during hover and landing flight segments with the deck excited by roll motion alone.

the main and tail rotor collective inputs. From the responses plotted in Figs. 7.60 to 7.62, it can be concluded that the controller was able to reject disturbances from the "moderate" heaving deck motion.

7.2.5 Combined motion and WOD

The combined influence of dynamic ground effect and WOD was examined by conducting hover and landing simulations similar to those in the previous section. The $\beta_{WOD} = -30°$ WOD condition was considered, and its effect was included on the entire helicopter. The position coordinates of the CG during the hover and landing approach are shown in Fig. 7.63. The baseline case with no WOD and ground effect is included for comparison. The inclusion of WOD produces displacements of approximately 1.5 ft., 0.7 ft. and 1.5 ft. in the horizontal, lateral and vertical positions coordinates, respectively, relative to the ground-effect-only case. Note that the offset between the deck and CG position after the vehicle

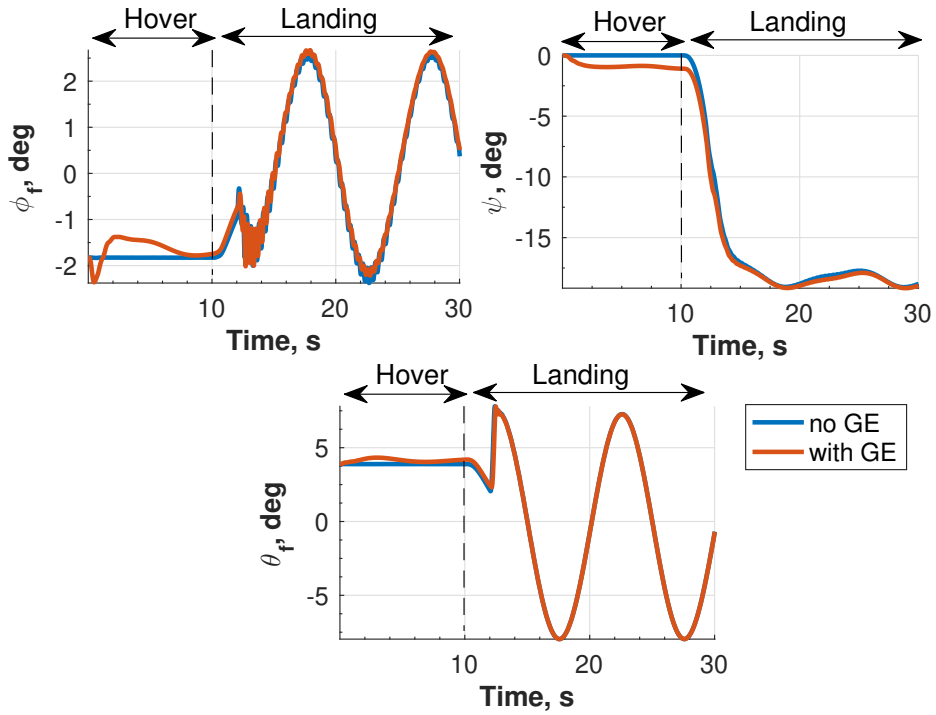

Figure 7.54: Roll, pitch and yaw attitudes during hover and landing flight segments with the deck excited by pitch motion alone.

lands at $t = 112.1$ s corresponds to the z offset of 5.9 ft. between the CG and landing gear contact points, illustrated in Fig. 5.1. The control inputs generated by the FCS during the hover flight segment are shown in Fig. 7.64. High frequency oscillations due to WOD are noted in the control inputs. The inclusion of dynamic ground effect from the combined deck motion induces offsets in the response, relative to the WOD-only case. The greatest change of approximately $0.5°$ is noted in the main rotor collective input. For reference, the WOD velocities at the hub center during the approach and landing flight segments are shown in Fig. 7.65.

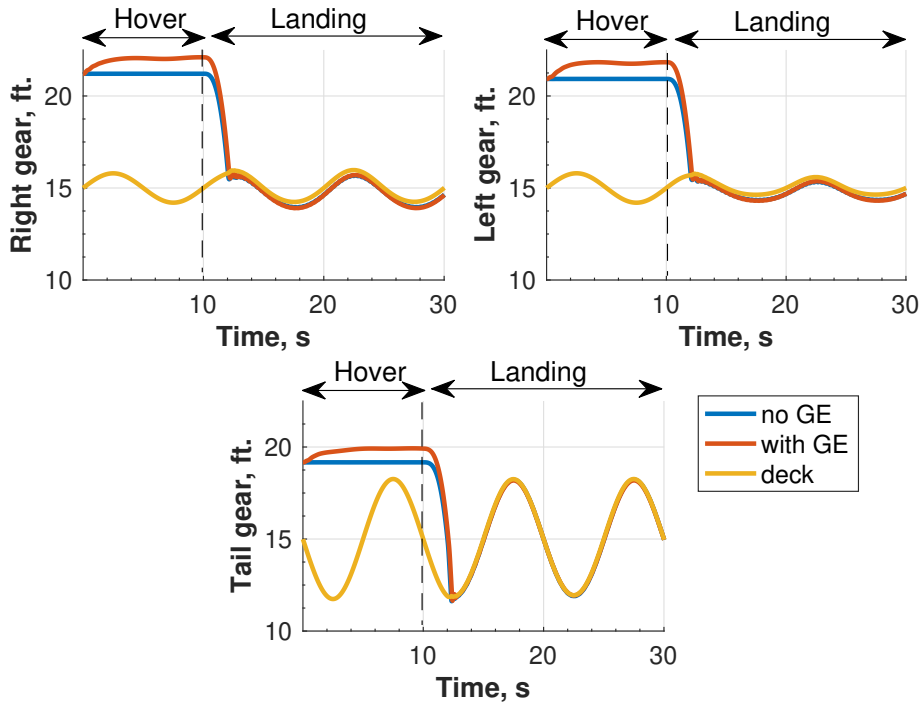

Figure 7.55: Vertical gear positions during hover and landing flight segments with the deck excited by pitch motion alone.

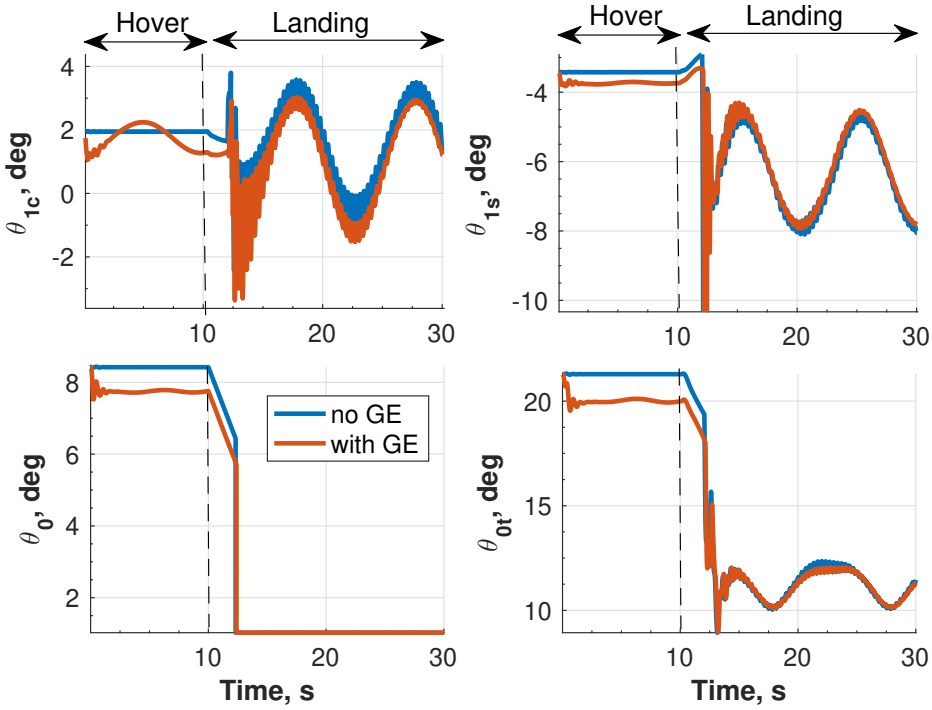

Figure 7.56: Control input time histories during hover and landing flight segments with the deck excited by pitch motion alone.

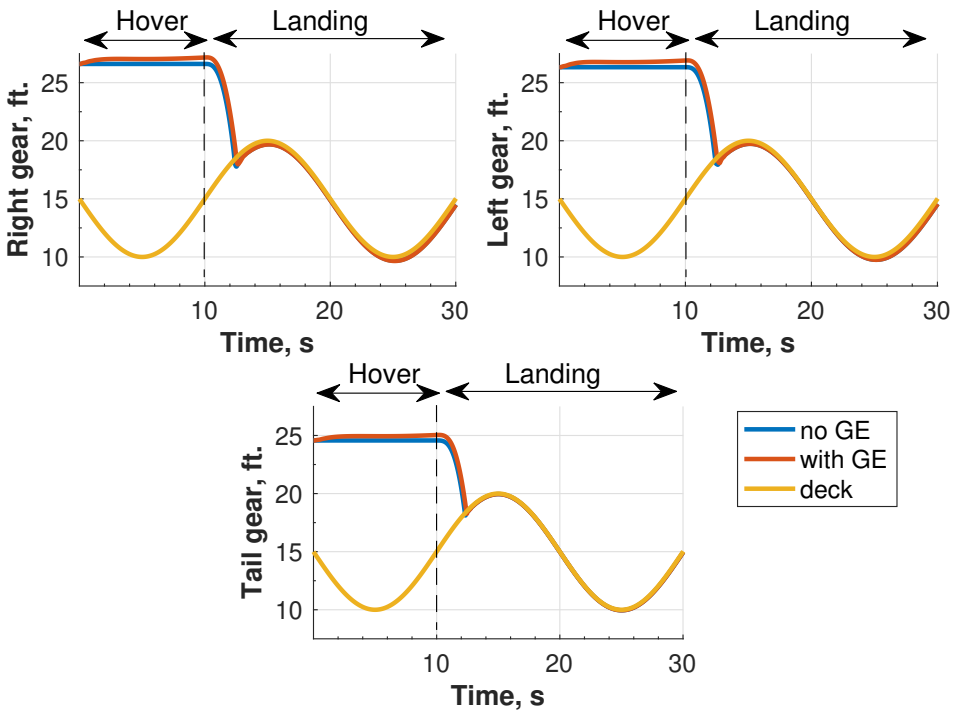

Figure 7.57: Vertical gear positions during hover and landing flight segments with the deck excited by heave motion alone.

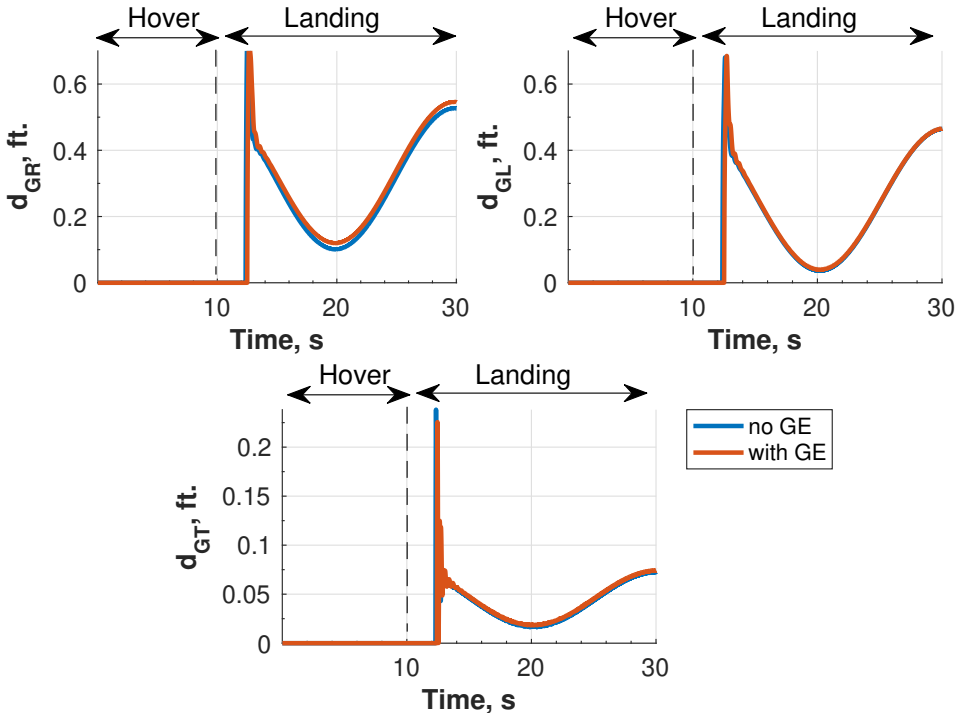

Figure 7.58: Vertical gear positions during hover and landing flight segments with the deck excited by heave motion alone.

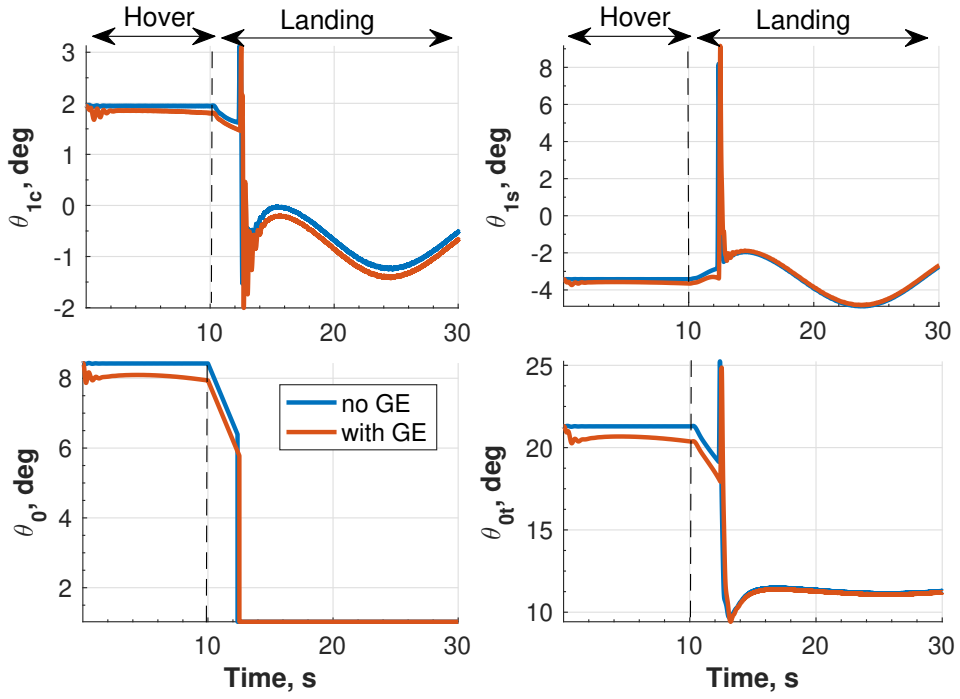

Figure 7.59: Control input time histories during hover and landing flight segments with the deck excited by heave motion alone.

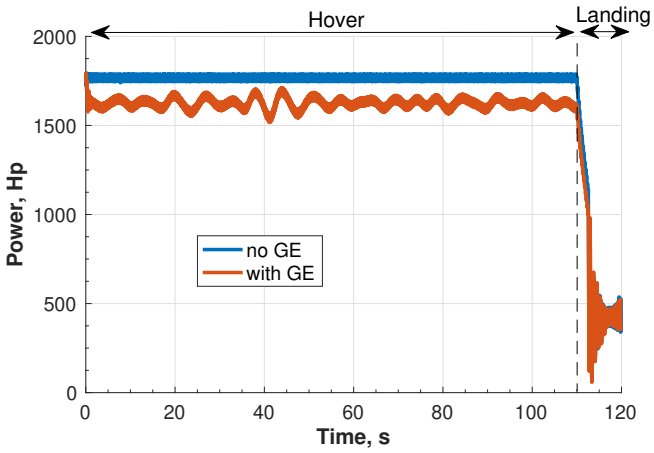

Figure 7.60: Time histories of power required during hover and landing flight segments; deck excited by combined roll, pitch and heave motion using SCONE data for a "moderate" heave condition.

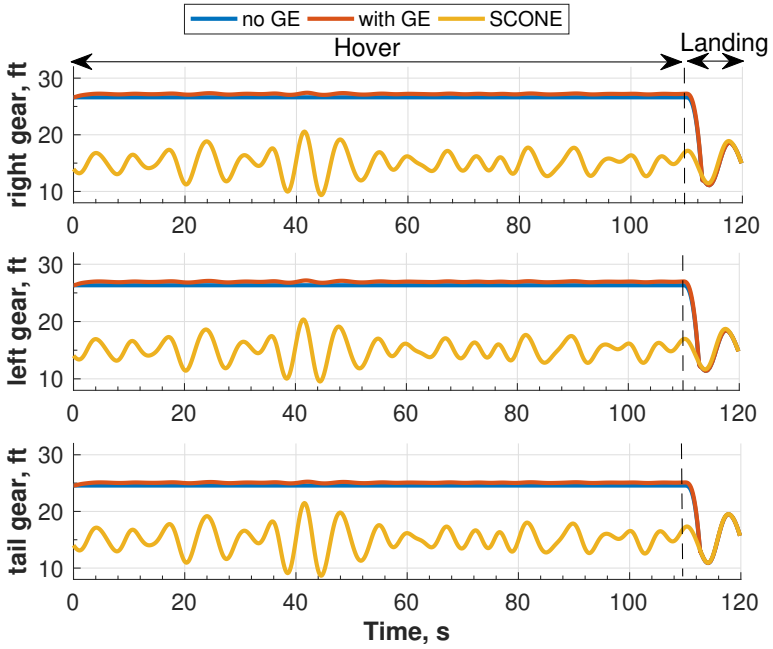

Figure 7.61: Vertical gear positions during hover and landing flight segments; deck excited by combined roll, pitch and heave motion using SCONE data for a “moderate” heave condition.

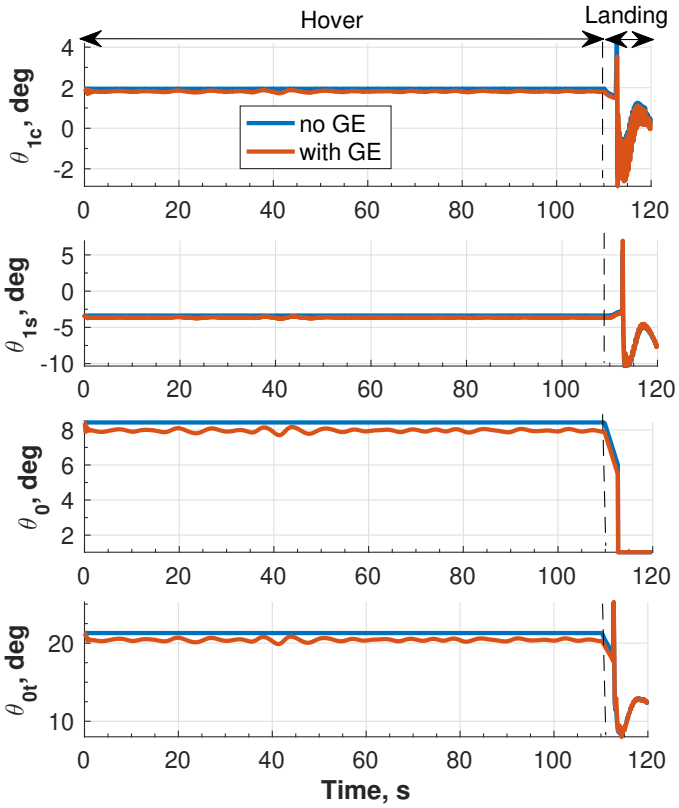

Figure 7.62: Control input time histories during hover and landing flight segments; deck excited by combined roll, pitch and heave motion using SCONE data for a "moderate" heave condition.

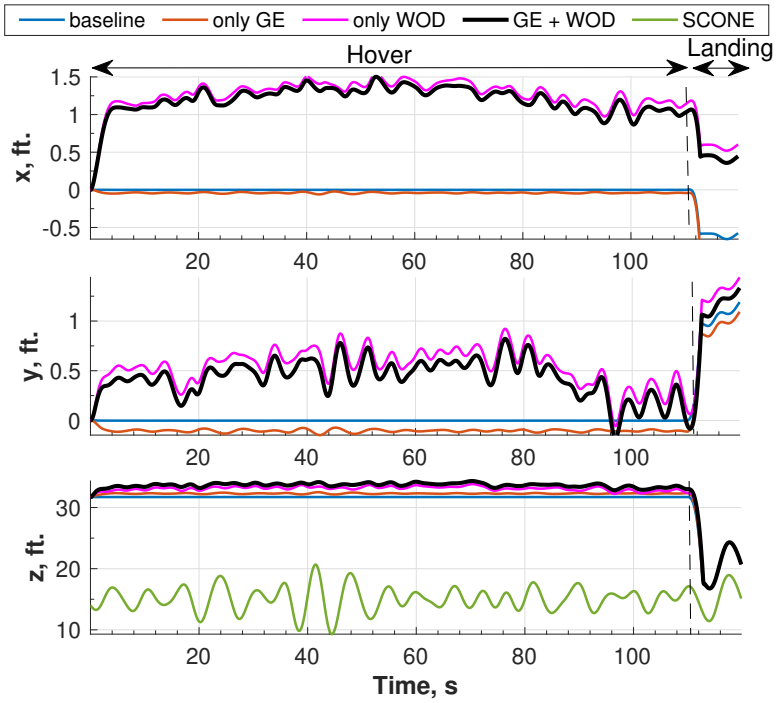

Figure 7.63: Horizontal, lateral and vertical position coordinates of CG during hover and landing flight segments; deck excited by combined roll, pitch and heave motion using SCONE data for a "moderate" heave condition, together with the $\beta_{WOD} = -30°$ WOD condition.

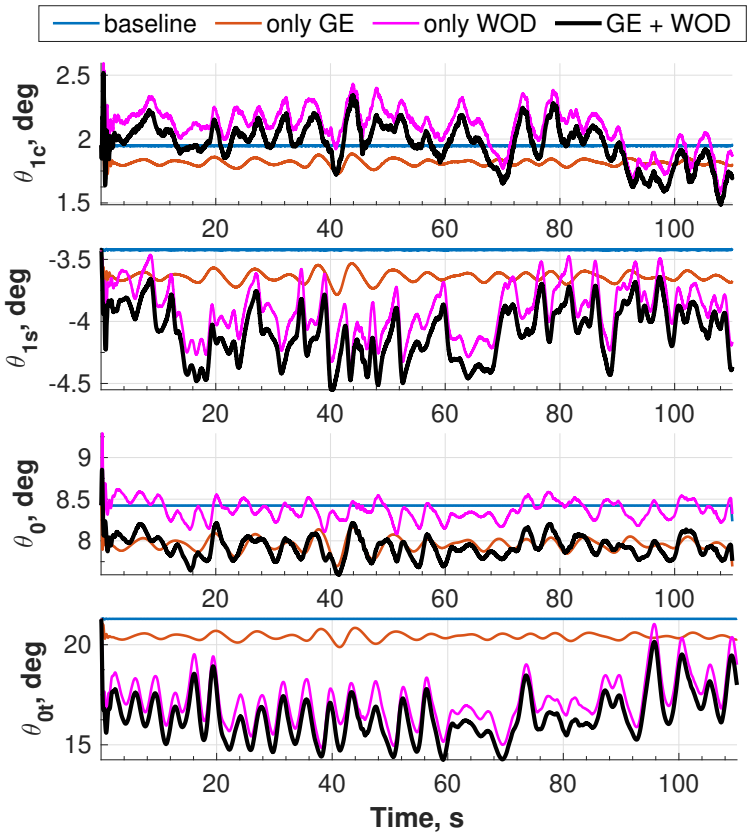

Figure 7.64: Control input time histories during hover and landing flight segments; deck excited by combined roll, pitch and heave motion using SCONE data for a "moderate" heave condition, together with the $\beta_{WOD} = -30°$ WOD condition.

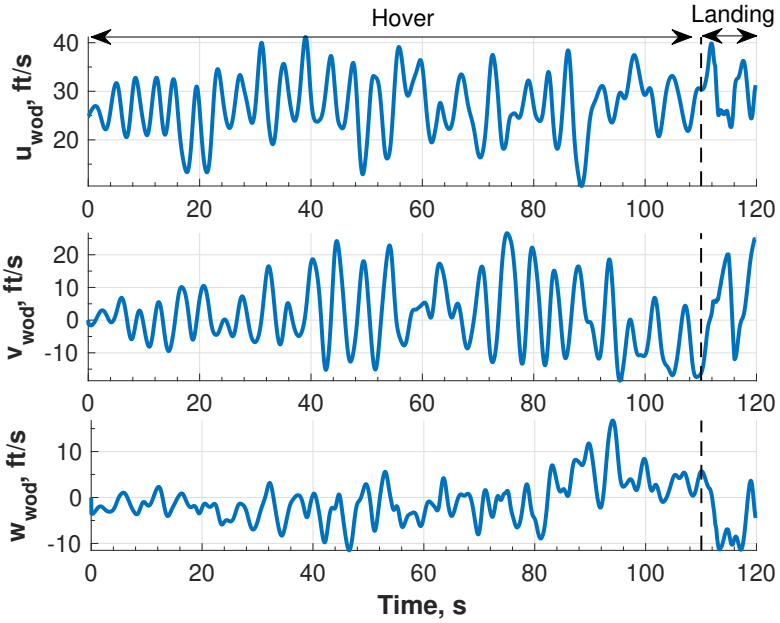

Figure 7.65: WOD velocity components at hub location during hover and landing flight segments for the $\beta_{WOD} = -30^{\circ}$ WOD condition.

CHAPTER 8

Conclusions, Original Contributions, and Recommendations for Future Research

A comprehensive simulation capability for helicopter ship landing, denoted as "HeliUM2-umich", was developed in this dissertation. The capability represents an enhancement over the original HeliUM2 code with provision for a flight control system (FCS), wind-over-deck (WOD), ground effect, and landing gears. A linear-quadratic regulator (LQR) based FCS was used. The WOD was obtained using unsteady Detached Eddy Simulation (DES) of flow over a stationary, full-scale Simple Frigate Shape Version 2 ship. Two main landing gears, and one tail gear were included following the standard UH-60A helicopter configuration. Vertical gear reaction forces were based on linear spring-damper systems, while planar reactions forces were due to friction. Two ground effect models were incorporated: a simple model based on an inflow scaling factor which is valid only for level and stationary ground planes, and a finite-state model that accounts for inclined and moving ground planes. Simulations of approach and landing on a stationary deck were performed in the presence of WOD at various sideslip angles, and the simple ground effect model using a UH-60A helicopter configuration. The difference in vehicle response when WOD is included on the entire helicopter consisting of the fuselage, empennage, main rotor and tail rotor, as opposed to the rotor alone, was also examined. Rotor performance predictions, based on the ground effect models, during hover over a level plane were compared against experimental results. The influence of deck inclination on vehicle dynamics dur-

ing hover and landing flight segments was examined. Hover and landing simulations were also performed to study the influence of a deck undergoing isolated sinusoidal motion in roll, pitch and heave degrees of freedom (DOFs). Vehicle response in-ground-effect with a deck excited in combined roll, pitch and heave DOFs was investigated, using data from the Systematic Characterization of the Naval Environment (SCONE) database, which is representative of actual ship deck motion. The combined influence of WOD and deck motion on helicopter dynamics was examined as well.

8.1 Conclusions

The main conclusions and contributions of this dissertation are summarized next:

1. The gain-scheduled controller is effective in stabilizing and tracking the helicopter reference trajectory throughout the approach. Vehicle response shows that oblique WOD conditions require the largest control effort when compared to the headwind case, due to the cliff edge effect, in which winds from the edges of the ship structure induce higher airwake velocities.

2. High frequency oscillations and drifts induced by WOD are evident in the helicopter response during approach and landing, notably in the angular attitudes, which in turn may induce undesirable effects such as dynamic roll over.

3. Time histories of helicopter control inputs for symmetric portside and starboard WOD cases are not symmetric due to the asymmetry in vehicle dynamics. Thus, both portside and starboard winds should be considered when establishing ship-helicopter operating limits (SHOLs).

4. Greater control effort is required when WOD is included on the entire helicopter, when compared to WOD acting on the rotor alone.

5. The main rotor collective input requirement decreases by approximately 8.1% when the simple ground effect model is included. This results in a decrease of approximately 11.3% in power consumption, a known beneficial effect of operating near ground. Ground effect is important and begins to influence the helicopter response as soon as the rotor hub enters the region above the ship deck. However, the simple model used is not accurate for $z_h < 0.5R$.

6. The finite-state ground effect model shows good agreement with experimental results from literature, even for $z_h/R < 0.5R$.

7. A static roll inclination of the deck produces a disturbance that causes the controller to adjust the longitudinal cyclic input in response. Similarly, a static pitch inclination of the deck results in the FCS adjusting the lateral cyclic input. The ground effect due to static deck inclination becomes significant for inclination angles close to 30°.

8. During hover, if the planes of symmetry of the helicopter and ship deck are aligned, the average component of inflow is independent of the sign of the roll angle. Thus, when the deck is excited by rolling motion alone, the frequency of collective input response is twice the excitation frequency. A similar response is obtained when the deck is excited by pitching motion alone.

9. A harmonic motion of the deck with large amplitude or frequency produces a control response with frequencies that are integer multiples of the excitation frequency.

10. Dynamic ground effect due to deck heaving motion causes an additional change of approximately 7.5% in power requirements, when compared to static ground effect. This is equivalent to a 17% change from the no-ground-effect condition. Thus, it is important to account for dynamic ground effect in helicopter shipboard operations.

11. A realistic landing was achieved on level, inclined and moving decks in the presence of WOD and ground effects using the three landing gear UH-60A configuration.

When considering landing on a level deck, the tail gear touches the deck first followed by the two main gears. When the deck is inclined at a static pitch angle, the main gears make contact before the tail gear. The friction reaction forces from the landing gears are not sufficient to keep the vehicle stationary after landing on a moving deck and thus, restraining devices should be employed.

8.2 Original Contributions Made in this Dissertation

1. Development of a comprehensive first principles, physics based, flight dynamics model of a helicopter with flexible blades, stabilizing controller, and landing gear, capable of actually landing on a moving deck. Such a comprehensive model is not available in the literature.

2. A DES based WOD computational model and its seamless integration in the flight dynamics model.

3. Simulation of a complete helicopter during approach and landing with DES based WOD model.

4. Coupling of a simple static ground effect model with the flight dynamics model to determine the importance of ground effect on landing for the first time.

5. Incorporation of a refined dynamic ground effect model in the flight dynamics model and simulation of landing on a moving deck.

6. Landing simulations combining WOD, dynamic ground effect and SCONE based deck dynamics with combined heave, pitch and roll.

8.3 Recommendations for Future Research

While this study represents a comprehensive investigation of helicopter-ship dynamic interface (DI), additional research on the topic remains to be done.

This study only considered one-way coupling between the WOD and helicopter dynamics. Two-way coupling between the WOD and helicopter flight dynamics should be conducted to determine the accuracy of one-way simulations.

While the gain-scheduled LQR based controller was effective in tracking the prescribed approach trajectory, future research should examine more advanced control strategies such as Model Predictive Control (MPC) that can produce a rich combination of landing approaches. Optimization studies can be valuable for generating approach trajectories that minimize the disturbances due to WOD.

Ground effect due to static deck inclination and motion represents a new area of research. Future research should be performed to further characterize this effect, which was shown to be significant in this study.

APPENDIX A

Associated Legendre Functions

Recurrence relationships used to derive Legendre functions of the first and second kind are given here [93].

$$\bar{P}_{n+1}^{m}(\nu) = \sqrt{\frac{(2n+3)(2n+1)}{(n+1)^2 - m^2}} \left[\nu \bar{P}_{n}^{m}(\nu) - \sqrt{\frac{n^2 - m^2}{4n^2 - 1}} \bar{P}_{n-1}^{m}(\nu) \right], \tag{A.1}$$

$$\bar{P}_{n}^{m+1}(\nu) = \frac{1}{\sqrt{1-\nu^2}} \left[\sqrt{\frac{(2n+1)(n+m)}{(2n-1)(n+m+1)}} \bar{P}_{n+1}^{m}(\nu) - \frac{(n-m)}{\sqrt{(n+m+1)(n-m)}} \nu \bar{P}_{n}^{m}(\nu) \right], \tag{A.2}$$

$$\bar{Q}_{n+1}^{m}(i\eta) = \bar{Q}_{n-1}^{m}(i\eta) - (2n+1) K_{n}^{m} \eta \bar{Q}_{n}^{m}(i\eta), \tag{A.3}$$

$$\bar{Q}_{n}^{m+1}(i\eta) = \frac{1}{\sqrt{1+\eta^2}} [\bar{Q}_{n-1}^{m}(i\eta) - (n-m) K_{n}^{m} \eta \bar{Q}_{n}^{m}(i\eta)], \tag{A.4}$$

where a recurrence relation for K_n^m is given by

$$K_{n+1}^{m} = \frac{1}{K_{n}^{m}} \frac{1}{(n+1)^2 - m^2} = \frac{n^2 - m^2}{(n+1)^2 - m^2} K_{n-1}^{m}. \tag{A.5}$$

A few values of K_n^m with low m + n combinations are shown in Table A.1.

Table A.1: Values of K_n^m

		m				
		0	1	2	3	4
n	0	$\pi/2$				
	1	$2/\pi$	$\pi/4$			
	2	$\pi/8$	$4/3\pi$	$3\pi/16$		
	3	$8/9\pi$	$3\pi/32$	$16/15\pi$	$15\pi/96$	
	4	$9\pi/128$	$32/45\pi$	$15\pi/192$	$96/105\pi$	$105\pi/768$

A.1 Closed-Form Representations

Closed form expressions for the associated Legendre functions of the first and second kind used in this report are provided here.

$$
\begin{aligned}
\bar{P}_0^0(\nu) &= 1 \\
\bar{P}_1^0(\nu) &= \sqrt{3}\nu \\
\bar{P}_2^0(\nu) &= \frac{\sqrt{5}}{2}(3\nu^2 - 1) \\
\bar{P}_3^0(\nu) &= \frac{\sqrt{7}}{2}\nu(5\nu^2 - 3) \\
\bar{P}_4^0(\nu) &= \frac{3}{8}(35\nu^4 - 30\nu^2 - 3) \\
\bar{P}_5^0(\nu) &= \frac{\sqrt{11}}{8}\nu(63\nu^4 - 70\nu^2 + 15) \\
\bar{P}_1^1(\nu) &= \sqrt{\frac{3}{2}}\sqrt{1 - \nu^2} \\
\bar{P}_2^1(\nu) &= \frac{\sqrt{30}}{2}\nu\sqrt{1 - \nu^2} \\
\bar{P}_3^1(\nu) &= \frac{\sqrt{21}}{4}(5\nu^2 - 1)\sqrt{1 - \nu^2} \\
\bar{P}_4^1(\nu) &= \frac{3\sqrt{5}}{4}\nu(7v^2 - 2)\sqrt{1 - \nu^2} \\
\bar{P}_5^1(\nu) &= \frac{1}{8}\sqrt{\frac{165}{2}}(21\nu^4 - 14\nu^2 + 1)\sqrt{1 - \nu^2} \\
\bar{P}_6^1(\nu) &= \frac{\nu}{8}\sqrt{\frac{273}{2}}(33\nu^4 - 30\nu^2 + 5)\sqrt{1 - \nu^2} \\
\bar{P}_2^2(\nu) &= \frac{\sqrt{15}}{2\sqrt{2}}(1 - \nu^2)
\end{aligned}
$$

$$\bar{P}_3^2(\nu) = \frac{\sqrt{210}}{4}\nu(1-\nu^2) \tag{A.6}$$

$$\begin{aligned}
\bar{Q}_0^0(i\eta) &= \frac{2}{\pi}\tan^{-1}\left(\frac{1}{\eta}\right)\\
\bar{Q}_1^0(i\eta) &= 1-\eta\tan^{-1}\left(\frac{1}{\eta}\right)\\
\bar{Q}_2^0(i\eta) &= \frac{2}{\pi}(3\eta^2+1)\tan^{-1}\left(\frac{1}{\eta}\right)-\frac{6}{\pi}\eta\\
\bar{Q}_3^0(i\eta) &= 1+\frac{15}{4}\eta^2-\frac{3\eta}{4}(5\eta^2+3)\tan^{-1}\left(\frac{1}{\eta}\right)\\
\bar{Q}_4^0(i\eta) &= \frac{2}{\pi}\left(1+10\eta^2+\frac{35}{3}\eta^4\right)\tan^{-1}\left(\frac{1}{\eta}\right)-\frac{110\eta}{9\pi}-\frac{70\eta^3}{3\pi}\\
\bar{Q}_5^0(i\eta) &= 1+\frac{735}{64}\eta^2+\frac{945}{64}\eta^4-\frac{15\eta}{64}(15+70\eta^2+63\eta^4)\tan^{-1}\left(\frac{1}{\eta}\right)\\
\bar{Q}_1^1(i\eta) &= \frac{2}{\pi}\sqrt{1+\eta^2}\tan^{-1}\left(\frac{1}{\eta}\right)-\frac{2\eta}{\pi\sqrt{1+\eta^2}}\\
\bar{Q}_2^1(i\eta) &= \frac{3}{2}\sqrt{1+\eta^2}-\frac{3\eta}{2}\sqrt{1+\eta^2}\tan^{-1}\left(\frac{1}{\eta}\right)-\frac{1}{2\sqrt{1+\eta^2}}\\
\bar{Q}_3^1(i\eta) &= \frac{2}{\pi}(5\eta^2+1)\sqrt{1+\eta^2}\tan^{-1}\left(\frac{1}{\eta}\right)-\frac{10\eta}{\pi}\sqrt{1+\eta^2}+\frac{4\eta}{3\pi\sqrt{1+\eta^2}}\\
\bar{Q}_4^1(i\eta) &= \frac{5}{16}(21\eta^2+2)\sqrt{1+\eta^2}-\frac{15\eta}{16}(7\eta^3+3)\sqrt{1+\eta^2}\tan^{-1}\left(\frac{1}{\eta}\right)+\frac{3}{8\sqrt{1+\eta^2}}\\
\bar{Q}_5^1(i\eta) &= \frac{2}{\pi\sqrt{1+\eta^2}}(1+15\eta^2+35\eta^4+21\eta^6)\tan^{-1}\left(\frac{1}{\eta}\right)-\\
&\qquad \frac{14\eta}{\pi}(3\eta^2+1)\sqrt{1+\eta^2}-\frac{16\eta}{15\,\pi\sqrt{1+\eta^2}}\\
\bar{Q}_6^1(i\eta) &= \frac{1}{128\sqrt{1+\eta^2}}\Big[128+2163\eta^2+5460\eta^4+3465\eta^6-\\
&\qquad 105\eta(5+35\eta^2+63\eta^4+33\eta^6)\tan^{-1}\left(\frac{1}{\eta}\right)\Big]\\
\bar{Q}_2^2(i\eta) &= \frac{2}{\pi}(1+\eta^2)\tan^{-1}\left(\frac{1}{\eta}\right)-\frac{2}{\pi}\eta-\frac{4\eta}{3\pi(1+\eta^2)}\\
\bar{Q}_3^2(i\eta) &= \frac{5}{4}+\frac{15}{8}\eta^2-\frac{15}{8}\eta(1+\eta^2)\tan^{-1}\left(\frac{1}{\eta}\right)-\frac{1}{4\pi(1+\eta^2)}
\end{aligned} \tag{A.7}$$

APPENDIX B

General Form of Ground Effect Matrices

The general form of the $\mathbf{A}_G$, $\mathbf{B}_G$, $\mathbf{G}_G$ and $\mathbf{C}_G$ matrices are given here. Using the fundamental and first harmonics $(r, m, l = 0, 1)$, two radial distribution terms for the induced inflow $(j = r + 1, r + 3)$ and the rotor pressure perturbation $(n = m + 1, m + 3)$, and three radial distribution terms for the ground pressure perturbation $(k = l, l + 2, l + 4)$, the general forms of the $\mathbf{A}_G$, $\mathbf{B}_G$, and $\mathbf{G}_G$ matrices from Eq (5.70) are given by

$$[A_G] = \begin{bmatrix} (A_{10}^{00})^{cc} & (A_{12}^{00})^{cc} & (A_{14}^{00})^{cc} & (A_{11}^{01})^{cc} & (A_{13}^{01})^{cc} & (A_{15}^{01})^{cc} & (A_{11}^{01})^{cs} & (A_{13}^{01})^{cs} & (A_{15}^{01})^{cs} \\ (A_{30}^{00})^{cc} & (A_{32}^{00})^{cc} & (A_{34}^{00})^{cc} & (A_{31}^{01})^{cc} & (A_{33}^{01})^{cc} & (A_{35}^{01})^{cc} & (A_{31}^{01})^{cs} & (A_{33}^{01})^{cs} & (A_{35}^{01})^{cs} \\ (A_{20}^{10})^{cc} & (A_{22}^{10})^{cc} & (A_{24}^{10})^{cc} & (A_{21}^{11})^{cc} & (A_{23}^{11})^{cc} & (A_{25}^{11})^{cc} & (A_{21}^{11})^{cs} & (A_{23}^{11})^{cs} & (A_{25}^{11})^{cs} \\ (A_{40}^{10})^{cc} & (A_{42}^{10})^{cc} & (A_{44}^{10})^{cc} & (A_{41}^{11})^{cc} & (A_{43}^{11})^{cc} & (A_{45}^{11})^{cc} & (A_{41}^{11})^{cs} & (A_{43}^{11})^{cs} & (A_{45}^{11})^{cs} \\ (A_{20}^{10})^{sc} & (A_{22}^{10})^{sc} & (A_{24}^{10})^{sc} & (A_{21}^{11})^{sc} & (A_{23}^{11})^{sc} & (A_{25}^{11})^{sc} & (A_{21}^{11})^{ss} & (A_{23}^{11})^{ss} & (A_{25}^{11})^{ss} \\ (A_{40}^{10})^{sc} & (A_{42}^{10})^{sc} & (A_{44}^{10})^{sc} & (A_{41}^{11})^{sc} & (A_{43}^{11})^{sc} & (A_{45}^{11})^{sc} & (A_{41}^{11})^{ss} & (A_{43}^{11})^{ss} & (A_{45}^{11})^{ss} \end{bmatrix}, \tag{B.1}$$

$$[B_G] = \begin{bmatrix} (B_{01}^{00})^{cc} & (B_{03}^{00})^{cc} & (B_{02}^{01})^{cc} & (B_{04}^{01})^{cc} & (B_{02}^{01})^{cs} & (B_{04}^{01})^{cs} \\ (B_{21}^{00})^{cc} & (B_{23}^{00})^{cc} & (B_{22}^{01})^{cc} & (B_{24}^{01})^{cc} & (B_{22}^{01})^{cs} & (B_{24}^{01})^{cs} \\ (B_{41}^{00})^{cc} & (B_{43}^{00})^{cc} & (B_{42}^{01})^{cc} & (B_{44}^{01})^{cc} & (B_{42}^{01})^{cs} & (B_{44}^{01})^{cs} \\ (B_{11}^{10})^{cc} & (B_{13}^{10})^{cc} & (B_{12}^{11})^{cc} & (B_{14}^{11})^{cc} & (B_{12}^{11})^{cs} & (B_{14}^{11})^{cs} \\ (B_{31}^{10})^{cc} & (B_{33}^{10})^{cc} & (B_{32}^{11})^{cc} & (B_{34}^{11})^{cc} & (B_{32}^{11})^{cs} & (B_{34}^{11})^{cs} \\ (B_{51}^{10})^{cc} & (B_{53}^{10})^{cc} & (B_{52}^{11})^{cc} & (B_{54}^{11})^{cc} & (B_{52}^{11})^{cs} & (B_{54}^{11})^{cs} \\ (B_{11}^{10})^{sc} & (B_{13}^{10})^{sc} & (B_{12}^{11})^{sc} & (B_{14}^{11})^{sc} & (B_{12}^{11})^{ss} & (B_{14}^{11})^{ss} \\ (B_{31}^{10})^{sc} & (B_{33}^{10})^{sc} & (B_{32}^{11})^{sc} & (B_{34}^{11})^{sc} & (B_{32}^{11})^{ss} & (B_{34}^{11})^{ss} \\ (B_{51}^{10})^{sc} & (B_{53}^{10})^{sc} & (B_{52}^{11})^{sc} & (B_{54}^{11})^{sc} & (B_{52}^{11})^{ss} & (B_{54}^{11})^{ss} \end{bmatrix}, \tag{B.2}$$

$$[G_G] = \begin{bmatrix} (G_{11}^{00})^{cc} & (G_{13}^{00})^{cc} & (G_{12}^{01})^{cc} & (G_{14}^{01})^{cc} & (G_{12}^{01})^{cs} & (G_{14}^{01})^{cs} \\ (G_{31}^{00})^{cc} & (G_{33}^{00})^{cc} & (G_{32}^{01})^{cc} & (G_{34}^{01})^{cc} & (G_{32}^{01})^{cs} & (G_{34}^{01})^{cs} \\ (G_{21}^{10})^{cc} & (G_{23}^{10})^{cc} & (G_{22}^{11})^{cc} & (G_{24}^{11})^{cc} & (G_{22}^{11})^{cs} & (G_{24}^{11})^{cs} \\ (G_{41}^{10})^{cc} & (G_{43}^{10})^{cc} & (G_{42}^{11})^{cc} & (G_{44}^{11})^{cc} & (G_{42}^{11})^{cs} & (G_{44}^{11})^{cs} \\ (G_{21}^{10})^{sc} & (G_{23}^{10})^{sc} & (G_{22}^{11})^{sc} & (G_{24}^{11})^{sc} & (G_{22}^{11})^{ss} & (G_{24}^{11})^{ss} \\ (G_{41}^{10})^{sc} & (G_{43}^{10})^{sc} & (G_{42}^{11})^{sc} & (G_{44}^{11})^{sc} & (G_{42}^{11})^{ss} & (G_{44}^{11})^{ss} \end{bmatrix}. \tag{B.3}$$

Using the fundamental and first harmonics $(r, p = 0, 1)$, two radial distribution terms for the dynamic induced inflow $(j = r + 1, r + 3)$, and three radial distribution terms for the dynamic ground pressure perturbation $(i = p + 1, p + 3, p + 5)$, a general form for the $\mathbf{C}_G$ matrix in Eq. (5.89) is given by

$$[C_G] = \begin{bmatrix} (C_{11}^{00})^{cc} & (C_{13}^{00})^{cc} & (C_{15}^{00})^{cc} & (C_{12}^{01})^{cc} & (C_{14}^{01})^{cc} & (C_{16}^{01})^{cc} & (C_{12}^{01})^{cs} & (C_{14}^{01})^{cs} & (C_{16}^{01})^{cs} \\ (C_{31}^{00})^{cc} & (C_{33}^{00})^{cc} & (C_{35}^{00})^{cc} & (C_{32}^{01})^{cc} & (C_{34}^{01})^{cc} & (C_{36}^{01})^{cc} & (C_{32}^{01})^{cs} & (C_{34}^{01})^{cs} & (C_{36}^{01})^{cs} \\ (C_{21}^{10})^{cc} & (C_{23}^{10})^{cc} & (C_{25}^{10})^{cc} & (C_{22}^{11})^{cc} & (C_{24}^{11})^{cc} & (C_{26}^{11})^{cc} & (C_{22}^{11})^{cs} & (C_{24}^{11})^{cs} & (C_{26}^{11})^{cs} \\ (C_{41}^{10})^{cc} & (C_{43}^{10})^{cc} & (C_{45}^{10})^{cc} & (C_{42}^{11})^{cc} & (C_{44}^{11})^{cc} & (C_{46}^{11})^{cc} & (C_{42}^{11})^{cs} & (C_{44}^{11})^{cs} & (C_{46}^{11})^{cs} \\ (C_{21}^{10})^{sc} & (C_{23}^{10})^{sc} & (C_{25}^{10})^{sc} & (C_{22}^{11})^{sc} & (C_{24}^{11})^{sc} & (C_{26}^{11})^{sc} & (C_{22}^{11})^{ss} & (C_{24}^{11})^{ss} & (C_{26}^{11})^{ss} \\ (C_{41}^{10})^{sc} & (C_{43}^{10})^{sc} & (C_{45}^{10})^{sc} & (C_{42}^{11})^{sc} & (C_{44}^{11})^{sc} & (C_{46}^{11})^{sc} & (C_{42}^{11})^{ss} & (C_{44}^{11})^{ss} & (C_{46}^{11})^{ss} \end{bmatrix}. \tag{B.4}$$

APPENDIX C

DDG-51 Ship Geometry

The SCONE database [94] contains motion data for a generic surface combatant ship similar to a DDG-51 type destroyer, depicted in Fig. C.1. The principal dimensions of the geometry used are given in Table C.1 [94]. Relevant geometry parameters are defined as follows [96, 97]:

1. *waterline* (WL): the line where the ship hull meets the surface of water;
2. *baseline* (BL): a horizontal line along the length of the ship that passes through the keel;
3. *forward perpendicular* (FP): a vertical line through the intersection of the foreside of the bow with the waterline;
4. *aft perpendicular* (AP): a vertical line through the intersection of the the aft side of the rudder post with the waterline;
5. *beam*: ship width;
6. *draft or draught*: the vertical distance between the waterline and the keel;
7. *longitudinal plane*: a plane that contains both forward and aft perpendiculars;
8. *transverse plane*: a plane along the width of the vessel connecting starboard and portside edges of the ship;

9. *longitudinal center of gravity* (LCG): a point in the longitudinal plane where total weight acts;

10. *vertical center of gravity* (VCG): a point in the transverse plane where total weight acts;

11. *longitudinal center of buoyancy* (LCB): a point in the longitudinal plane the buoyant forces from water act;

12. *transverse center of buoyancy* (CB): a point in the transverse plane where the buoyant forces from water act;

13. *transverse metacentric height* (GM_T): the distance between the VCG and the meta-centre, which is the point where the vertical line through the CB when the ship is level intersects the vertical line through the CB when the ship has listed (rolled) by a small angle.

Table C.1: SCONE ship geometry parameters [94]

Parameter	Value
Length, overall	497.4 ft.
Length, waterline	464.1 ft.
Beam, maximum	69.6 ft.
Beam, waterline	62.6 ft.
Draft, initial	21.4 ft.
Draft, maximum	31.5 ft.
Displaced volume	3.23×10^5 ft^3
Longitudinal center of gravity	234.5 ft. from FP
Vertical center of gravity	4.43 ft above WL
	25.9 ft. above BL
Metacentric height (tranvserve)	5.37 ft.

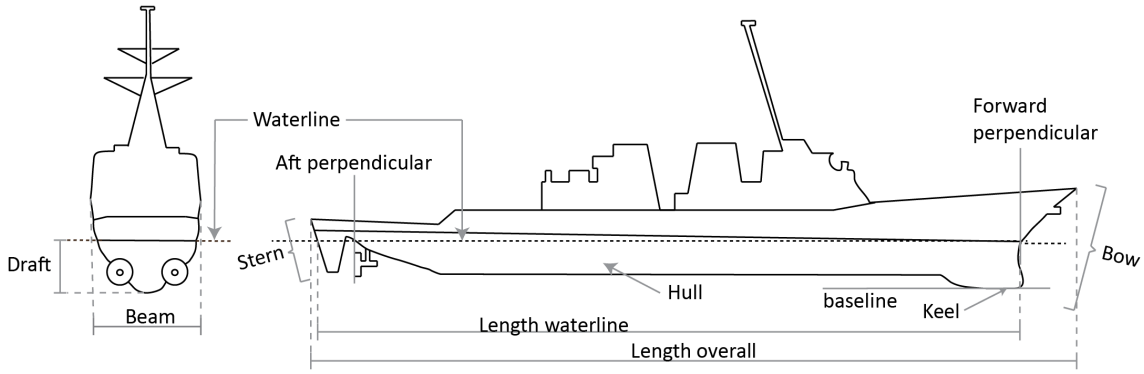

Figure C.1: Illustration of the DDG-51 ship with different parts labeled.

BIBLIOGRAPHY

[1] Forrest, J. S., Owen, I., Padfield, G. D., and Hodge, S. J., "Ship-helicopter operating limits prediction using piloted flight simulation and time-accurate airwakes," *Journal of Aircraft*, Vol. 49, No. 4, July-August 2012, pp. 1020–1031.

[2] Owen, I., White, M. D., Padfield, G. D., and Hodge, S. J., "A virtual engineering approach to the ship-helicopter dynamic interface – a decade of modelling and simulation research at the University of Liverpool," *The Aeronautical Journal*, Vol. 121, No. 1246, Dec 2017, pp. 1833–1857.

[3] Shukla, S., Sinha, S. S., and Singh, S. N., "Ship-helo coupled airwake aerodynamics: A comprehensive review," *Progress in Aerospace Sciences*, Vol. 106, April 2019, pp. 71–107.

[4] Dang-Vu, B., "Shipboard Landing Period Based on Dynamic Rollover Risk Prediction," *Proceedings of the 44th European Rotorcraft Forum*, ERF, Delft, Netherlands, Sep 18-21, 2018.

[5] Tinney, C. E., and Ukeiley, L. S., "A study of a 3–D double backward-facing step," *Experiments in Fluids*, Vol. 47, No. 3, Sep 2009, pp. 427–438.

[6] NATO, *AGARD Conference Proceedings 509 – Aircraft Ship Operations*, Seville, Spain, May 20-23, 1991.

[7] Polsky, S., and Bruner, C., "Time-accurate computational simulations of an LHA ship airwake," *18th Applied Aerodynamics Conference*, Denver, CO, Aug 2000.

[8] Roscoe, M. F., and Wilkinson, H., Colin, "DIMSS - JSHIP's Modeling and Simulation Process for Ship/Helicopter Testing & Training," *Proceedings of the AIAA Modeling and Simulation Technologies Conference and Exhibit*, AIAA, Monterey, CA, Aug 5-8, 2002.

[9] Zan, S., "Experimental determination of rotor thrust in a ship airwake," *Journal of the American Helicopter Society*, Vol. 47, No. 2, April 2002, pp. 100–108.

[10] Lee, D., Sezer-Uzol, N., Horn, J. F., and Long, L. N., "Simulation of helicopter shipboard launch and recovery with time-accurate airwakes," *Journal of Aircraft*, Vol. 42, No. 2, March-April 2005, pp. 448–461.

[11] Hodge, S. J., Zan, S. J., Roper, D. M., Padfield, G. D., and Owen, I., "Time-Accurate Ship Airwake and Unsteady Aerodynamic Loads Modeling for Maritime Helicopter Simulation," *Journal of the American Helicopter Society*, Vol. 54, No. 2, April 2009, pp. 22005–1–22005–16.

[12] Oruc, I., Horn, J. F., Polsky, S., Shipman, J., and Erwin, J., "Coupled flight dynamics and CFD simulations of helicopter/ship dynamic interface," *Proceedings of the 71st Annual Forum of the American Helicopter Society*, AHS International, Virginia Beach, VA, May 5-7, 2015.

[13] Forsythe, J., Lynch, C., Polsky, S., and Spalart, P., "Coupled Flight Simulator and CFD Calculations of Ship Airwake using HPCMP CREATE-AV Kestrel," *53th AIAA Aerospace Sciences Meeting, SciTech*, Vol. 2015, 2015, pp. 1–18.

[14] Healey, J. V., "The Aerodynamics of Ship Superstructures," *AGARD Conference Proceedings 509 – Aircraft Ship Operations, Paper No. 4*, NATO, Seville, Spain, May 20-23, 1991.

[15] Huff, R. W., and Kessler, G. K., "Enhanced Displays, Flight Controls and Guidance Systems for Approach and Landing," *AGARD Conference Proceedings 509 – Aircraft Ship Operations, Paper No. 8*, NATO, Seville, Spain, May 20-23, 1991.

[16] Arney, A. M., J., B., Erm, L. P., and Gilbert, N. E., "A Review of Australian Activity on Modeling the Helicopter/Ship Dynamic Interface," *AGARD Conference Proceedings 509 – Aircraft Ship Operations, Paper No. 20*, NATO, Seville, Spain, May 20-23, 1991.

[17] Carico, D., Reddy, B., and Charles, D., "Ship Airwake Measurement and Modeling Options for Rotorcraft Applications," *AGARD Conference Proceedings 509 – Aircraft Ship Operations, Paper No. 5*, NATO, Seville, Spain, May 20-23, 1991.

[18] Blackwell, J., Arney, A. M., Gilbert, N. E., and Truong, T. T., "Modeling the Helicopter/Ship Dynamic Interface for the Seahawk/FFG-7," *5th Australian Aeronautical Conference: Preprints of Papers*, Institution of Engineers, Australia, 1993.

[19] Ferrier, B., Polvi, H., and Thibodeau, F. A., "Helicopter/Ship Analytic Dynamic Interface," *AGARD Conference Proceedings 509 – Aircraft Ship Operations, Paper No. 15*, NATO, Seville, Spain, May 20-23, 1991.

[20] Lumsden, R. B., Wilkinson, C. H., and D., P. G., "Challenges at the Helicopter-Ship Dynamic Interface," *Proceedings of the 24th European Rotorcraft Forum*, Marseille, France, Sep 15-17, 1998.

[21] Wilkinson, C. H., VanderVliet, G. M., and Roscoe, M. F., "Modeling and Simulation of the Ship–Helicopter Environment," *AIAA Modeling and Simulation Technologies Conference Proceedings, Paper AIAA 2000-4583*, AIAA, Denver, CO, Aug 14–17, 2000.

[22] VanderVliet, G. M., Wilkinson, C. H., and Roscoe, M. F., "Verification, Validation and Accreditation of a Flight Simulator: The JSHIP Experience," *AIAA Modeling and Simulation Technologies Conference Proceedings, Paper AIAA 2001-4061*, AIAA, Montreal, Canada, Aug 6-9, 2001.

[23] Hodge, S. J., Forrest, J. S., Padfield, G. D., and White, M. D., "Determining Fidelity Standards for Maritime Rotorcraft Simulation," *Proceedings of RAeS Conference on Maritime Operation of Rotorcraft*, UK, June, 2001.

[24] Forrest, J. S., and Owen, I., "An investigation of ship airwakes using Detached-Eddy Simulation," *Computers & Fluids*, Vol. 39, No. 4, April 2010, pp. 656–673.

[25] Wilkinson, C. H., Zan, S. J., Gilbert, N. E., and Funk, J. D., "Modelling and Simulation of Ship Airwakes for Helicopter Operations – A Collaborative Venture," *Proceedings of RTO AVT Symposium on Fluid Dynamics Problems of Vehicles Operating Near or in the Air-Sea Interface*, Amsterdam, The Netherlands, Oct 5-8, 1998.

[26] DuVal, R. W., "A real-time multi-body dynamics architecture for rotorcraft simulation," *The Challenge of Realistic Rotorcraft Simulation: RAeS Conference Proceedings*, Vol. 1, London, Nov 2001.

[27] Horn, J. F., Yang, J., He, C., Lee, D., and Tritschler, J. K., "Autonomous Ship Approach and Landing Using Dynamic Inversion Control With Deck Motion Prediction," *Proceedings of the 41st European Rotorcraft Forum*, ERF, Munich, Germany, Sep 1-4, 2015.

[28] Rajmohan, N., Zhao, J., He, C., and Susan, P., "Development of a Reduced Order Model to Study Rotor/Ship Aerodynamic Interaction," *Proceedings of AIAA SciTech Forum 2015 – AIAA Modeling and Simulation Technologies Conference*, AIAA, Kissimmee, Florida, Jan 5-9, 2015.

[29] Alfred, J., Celi, R., and Leishman, J. G., "Rotorcraft Brownout Mitigation through Flight Path Optimization using a High Fidelity Rotorcraft Simulation Model," *Proceedings of the 69th Annual Forum of the American Helicopter Society*, AHS International, Phoenix, AZ, May 21–23, 2013.

[30] Prasad, J. V. R., Comandur, V., Walters, R., and Guerrero, D., "Model Predictive Path Integral Approach for Trajectory Guidance of Rotorcraft Shipboard Landing," *Proceedings of the American Helicopter Society 74th Annual Forum*, AHS International, Phoenix, AZ, May 14-17, 2018.

[31] Horn, J. F., and Bridges, D. O., "A Model Following Controller Optimized for Gust Rejection during Shipboard Operations," *Proceedings of the American Helicopter Society 63rd Annual Forum*, AHS International, Virginia Beach, VA, May 1-3, 2007.

[32] Cooper, J., Horn, J. F., Yomchinda, T., and O'Neill, E. P., "Handling qualities evaluation of an adaptive disturbance compensation system for ship-based rotorcraft," *Journal of the American Helicopter Society*, Vol. 59, No. 2, 2014, pp. 1–12.

[33] Aviation, U. A., and Command, M., *Aeronautical Design Standard ADS-33E-PRF – Handling Qualities Requirements for Military Rotorcraft*, March 2000.

[34] Currey, N. S., *Aircraft landing gear design: principles and practices*, AIAA Education Series, 1988.

[35] Blackwell, J., "A maximum likelihood parameter estimation program for general nonlinear systems," ARL TM 392, 1988.

[36] Blackwell, J., and Feik, R. A., "A mathematical model of the on-deck helicopter/ship dynamic interface," ARL Aero TM 405, Sep 1988.

[37] Smiley, R. F., and Horne, W. B., "Mechanical properties of pneumatic tires with special reference to modern aircraft tires," NACA TN 4110, Jan 1958.

[38] Howlett, J. J., "UH-60A Black Hawk engineering simulation program. Volume 1: Mathematical model," NASA CR-166309, Dec 1981.

[39] Howlett, J. J., "UH-60A Black Hawk engineering simulation program. Volume II: Background Report," NASA CR-166310, Dec 1981.

[40] Linn, D. R., and Langlois, R. G., "Development and experimental validation of a shipboard helicopter on-deck maneuvering simulation," *Journal of Aircraft*, Vol. 43, No. 4, Aug 2006, pp. 895–906.

[41] Léveillé, M. J., "Development of a spacial dynamic handling and securing model for shipboard helicopters," Master's Thesis, Carleton University, Ottawa, Ontario, Sep 2013.

[42] Knight, M., and Hegner, R. A., "Analysis of ground effect on the lifting airscrew," NACA TN, Techincal Report 835, 1941.

[43] Zbrozek, J., "Ground effect on the lifting rotor," British ARC RM, Technical Report 2347, 1947.

[44] Cheeseman, I. C., and Bennett, W. E., "The effect of ground on a helicopter rotor in forward flight," Aeronautical Research Council Report and Memoranda No. 3021, Sep 1955.

[45] Fradenburgh, E. A., "The Helicopter and the Ground Effect Machine," *Journal of the American Helicopter Society*, Vol. 5, No. 4, 1960, pp. 26–28.

[46] Hayden, J. S., "The Effect of the Ground on Helicopter Hovering Power Required," *Proceedings of the 32nd Annual National V/STOL Forum of the American Helicopter Society*, May 10-12, 1976.

[47] Prouty, R. W., "Ground Effect and the Helicopter," *Proceedings of the AIAA/AHS/ASEE Aircraft Design Systems and Operations Meeting*, AIAA Paper 85-4034, Oct 14-16, 1985.

[48] Leishman, J. G., *Principles of helicopter aerodynamics 2nd edition*, Cambridge University Press, 2006.

[49] Gilad, M., Chopra, I., and Rand, O., "Performance evaluation of a flexible rotor in extreme ground effect," *Proceedings of the 37th European Rotorcraft Forum*, Gallarate, Italy, Sep 13-15, 2011.

[50] Tritschler, J. K., Milluzzo, J. I., and Holder, M., John, "Performance Effects of Hover In-Ground-Effect over Sloped Terrain," *Proceedings of the 75th Annual Forum of the American Helicopter Society*, AHS International, Philadelphia, PA, May 13-17, 2019.

[51] Martinez, A., Milluzzo, J., Drayton, S., and Davids, S., "Performance Measurements on Rotors Hovering above Moving Surfaces," *Proceedings of the 75th Annual Forum of the American Helicopter Society*, AHS International, Philadelphia, PA, May 13-17, 2019.

[52] Zhang, H., Prasad, J., Sankar, L., Mello, O., and Funk, J., Jr, "Ground effect simulation model for rotorcraft/ship interaction study," *Proceedings of the American Helicopter Society 51st Annual Forum*, AHS International, Fort Worth, TX, May 1995.

[53] Thomas, S., Amiraux, M., and Baeder, J. D., "Modeling the Two-Phase Flowfield Beneath a Hovering Rotor on Graphics Processing Units," *AIAA Journal*, Vol. 53, No. 8, 2015, pp. 2300–2320.

[54] Saberi, H. A., "Analytical model of rotor wake aerodynamics in ground effect," NASA CR 166533, 1983.

[55] Zhao, J., and He, C., "A viscous vortex particle model for rotor wake and interference analysis," *Journal of the American Helicopter Society*, Vol. 55, No. 1, 2010, pp. 12007–12007.

[56] Prasad, J. V. R., Zhang, H., and Peters, D. A., "Finite State In-Ground Effect Inflow Models for Lifting Rotors," *Proceedings of the American Helicopter Society 53rd Annual Forum*, AHS International, Virginia Beach, VA, May 1997.

[57] Xin, H., Prasad, J., and Peters, D., "Dynamic inflow modeling for simulation of a helicopter operating in ground effect," *Modeling and Simulation Technologies Conference and Exhibit*, 1999, p. 4114.

[58] Xin, H., "Development and validation of a generalized ground effect model for lifting rotors," Ph.D Disseration, Georgia Institute of Technology, Atlanta, 1999.

[59] Peters, D. A., and He, C. J., "Correlation of measured induced velocities with a finite-state wake model," *Journal of the American Helicopter Society*, Vol. 36, No. 3, July 1991, pp. 59–70.

[60] Celi, R., "HeliUM 2 Flight Dynamic Simulation Model: Development, Technical Concepts, and Applications," *Proceedings of the 71st Annual Forum of the American Helicopter Society*, AHS International, Virginia Beach, VA, May 5-7, 2015.

[61] Celi, R., Cheng, R. P., Fusato, D., Kim, F. D., Malpica, C., Ribera, M., Spence, A. M., Theodore, C. R., and Turnour, S. R., "HeliUM—University of Maryland Helicopter Flight Dynamic Simulation Code, Program Documentation," University of Maryland, College Park, March 20, 2008.

[62] Ballin, M. G., "Validation of a Real-Time Engineering Simulation of the UH-60A Helicopter," NASA TM-88360, Feb 1987.

[63] Celi, R., "Aeroelasticity and Structural Optimization of Helicopter Rotor Blades with Swept Tips," Ph.D. Dissertation, University of California, Los Angeles, 1987.

[64] Ribera, M., and Celi, R., "Simulation Modeling of Unsteady Maneuvers Using a Time Accurate Free Wake," *Proceedings of the 60th Annual Forum of the American Helicopter Society*, AHS International, Baltimore, MD, June, 2004.

[65] Celi, R., "Implementation of Rotary-Wing Aeromechanical Problems Using Differential-Algebraic Equation Solvers," *Journal of the American Helicopter Society*, Vol. 45, No. 4, Oct 2000, pp. 253–262.

[66] Sridharan, A., "Simulation Modeling of Flight Dynamics Control and Trajectory Optimization of Rotorcraft Towing Submerged Loads," Ph.D. Dissertation, University of Maryland, College Park, 2014.

[67] Rosen, A., and Friedmann, P. P., "Nonlinear Equations of Equilibrium for Elastic Helicopter or Wind Turbine Blades Undergoing Moderate Deflection," NASA CR-159478, Dec 1978.

[68] Shamie, J., and Friedmann, P. P., "Effect of moderate deflections on the aeroelastic stability of a rotor balde in forward flight," *Proceedings of the 3rd European Rotorcraft Forum*, Aix-En-Provence, France, Sep 7-9, 1977.

[69] Friedmann, P. P., and Straub, F. K., "Application of the Finite Element Method to Rotary-Wing Aeroelasticity," *Journal of the American Helicopter Society*, Vol. 25, No. 1, Jan 1980.

[70] Chandrupatla, T. R., and Belegundu, A. D., *Introduction to Finite Elements in Engineering*, Prentice-Hall, 1991.

[71] Pitt, D. M., and Peters, D. A., "Theoretical Prediction of Dynamic Inflow Derivatives," *Vertica*, Vol. 5, No. 1, 1981, pp. 21–34.

[72] Hohenemser, K. H., and Yin, S.-K., "Some applications of the method of multiblade coordinates," *Journal of the American Helicopter Society*, Vol. 17, No. 3, July 1972, pp. 3–12.

[73] Theodore, C. R., "Helicopter Flight Dynamic Simulation with Refined Aerodynamic Modeling," Ph.D. Dissertation, University of Maryland, College Park, 2000.

[74] Celi, R., "Aeroelastic Effects on Stability and Control of Hingeless Rotor Helicopters," *Proceedings of the 14th European Rotorcraft Forum*, Milan, Italy, Sep, 1988.

[75] Geyer Jr, W. P., Long, K., and Carico, G. D., "American Clearance Process," *RTO AGARDograph 300: Helicopter/Ship Qualification Testing*, Vol. 22, edited by G. D. Carico, R. Fang, R. S. Finch, W. P. Geyer Jr, H. W. Krijns, and K. Long, Feb 2003, pp. 2–17.

[76] Heffley, R. K., "A model for manual decelerating approaches to hover," *Proceedings of the Fifteenth Annual Conference on Manual Control*, AFFDL-TR-79-3134, Nov 1979, pp. 545–554.

[77] Tritschler, J. K., Celi, R., and Leishman, J. G., "Methodology for Rotorcraft Brownout Mitigation Through Flight Path Optimization," *Journal of Guidance, Control, and Dynamics*, Vol. 37, No. 5, 2014, pp. 1524–1538.

[78] Tritschler, J., Horn, J. F., and He, C., "Objective Function Development for Optimized Path Guidance for Rotorcraft Shipboard Recovery," *Proceedings of the AIAA Atmospheric Flight Mechanics Conference*, Dallas, TX, June 22-26, 2015, p. 2395.

[79] Pritchard, J., Tritschler, J., Arteche, D., Allen, J., Bordner, K., and Bumbaugh, J., "A Cueing Set For Piloted Approach And Hover In Simulated Shipboard Environment," *Proceedings of the 74th Annual Forum of the American Helicopter Society*, AHS International, Phoenix, AZ, May 14-17, 2018.

[80] Moen, G. C., Dicarlo, D. J., and Yenni, K. R., "A Parametric Analysis of Visual Approaches for Helicopter," NASA TN D-8275, Dec 1976.

[81] Wolfram, *Mathematica, Version 11.1*, Champaign, IL, 2018.

[82] ANSYS, *ANSYS FLUENT User's Guide, Release 12.0*, Jan 2009.

[83] Wilcox, D. C., "Formulation of the k-ω turbulence model revisited," *AIAA journal*, Vol. 46, No. 11, Nov 2008, pp. 2823–2838.

[84] Spalart, P. R., Jou, W.-H., Strelets, M., and Allmaras, S. R., "Comments on the Feasibility of LES for Wings, and on Hybrid RANS/LES Approach," *Proceedings of 1st AFOSR International Conference on Advances in DNS/LES*, Ruston, LA, Aug 1997.

[85] Menter, F. R., Kuntz, M., and Langtry, R., "Ten Years of Industrial Experience with the SST Turbulence Model," *Turbulence, Heat and Mass Transfer*, Vol. 4, No. 1, 2003, pp. 625–632.

[86] Zan, S., Syms, G., and Cheney, B., "Analysis of patrol frigate air wakes," *PNATO RTO Symposium on Fluid Dynamics Problems of Vehicles Operating near or in the Air-Sea Interface*, NATO RTO, Amsterdam, The Netherlands, 1998.

[87] Zhang, F., Xu, H., and Ball, N., "Numerical simulation of unsteady flow over SFS 2 ship model," *47th AIAA Aerospace Sciences Meeting Including The New Horizons Forum and Aerospace Exposition*, 2009.

[88] Toffoletto, R., Reddy, K., and Lewis, J., "Effect of ship frontal variation on the flow field in the flight-deck region," *Computational Fluid Dynamics 2002*, Springer, 2003, pp. 191–196.

[89] Persson, B. N., Tartaglino, U., Albohr, O., and Tosatti, E., "Rubber friction on wet and dry road surfaces: The sealing effect," *Physical review B*, Vol. 71, No. 3, 2005, p. 035428.

[90] Murakami, Y., "A new appreciation of inflow modelling for autorotative rotors," Ph.D. Dissertation, University of Glasgow, Scotland, 2008.

[91] Joglekar, M., and Loewy, R., "An actuator-disc analysis of helicopter wake geometry and the corresponding blade response," Tech. rep., Rochester University, NY, December 1970.

[92] Chengjian, H., "Development and Application of a Generalized Dynamic Wake Theory for Lifting Rotors," Ph.D Disseration, Georgia Institute of Technology, Atlanta, 1989.

[93] Yu, K., "Development of three-dimensional state-space wake theory and application in dynamic ground effect," Ph.D. Dissertation, Washington University, St. Louis, 2005.

[94] Schwartz, A., "Systematic Characterization of the Naval Environment (SCONE) – Standard Deck Motion Data for a Generic Surface Combatant," Memorandum from Office of Naval Research and Naval Surface Warfare Center – Carderock Division, May 2015.

[95] Shin, Y., Belenky, V., Lin, W., Weems, K., Engle, A., McTaggart, K., Falzarano, J. M., Hutchison, B. L., Gerigk, M., and Grochowalski, S., "Nonlinear time domain simulation technology for seakeeping and wave-load analysis for modern ship design," *Transactions-Society of Naval Architects and Marine Engineers*, Vol. 111, 2003, pp. 557–583.

[96] "Shipbuilding — Principal ship dimensions — Terminology and definitions for computer applications," ISO 7462:1985, Date accessed: June 29, 2019.

[97] Babicz, J., *Encyclopedia of Ship Technology, 2nd edition*, WÄRTSILÄ Corporation, 2015.